Nanosecond Repetitively Pulsed Discharges in Atmospheric Pressure Air

Diane Rusterholtz

▶ **To cite this version:**

Diane Rusterholtz. Nanosecond Repetitively Pulsed Discharges in Atmospheric Pressure Air. Other. Ecole Centrale Paris, 2012. English. NNT : 2012ECAP0054 . tel-00997397

HAL Id: tel-00997397

https://theses.hal.science/tel-00997397

Submitted on 28 May 2014

HAL is a multi-disciplinary open access archive for the deposit and dissemination of scientific research documents, whether they are published or not. The documents may come from teaching and research institutions in France or abroad, or from public or private research centers.

L'archive ouverte pluridisciplinaire **HAL**, est destinée au dépôt et à la diffusion de documents scientifiques de niveau recherche, publiés ou non, émanant des établissements d'enseignement et de recherche français ou étrangers, des laboratoires publics ou privés.

École Centrale Paris

THÈSE

présentée par

Diane Rusterholtz

pour l'obtention du

GRADE de DOCTEUR

Formation doctorale :	Énergétique et Physique
Laboratoire d'accueil :	Laboratoire d'Énergétique Moléculaire et Macroscopique, Combustion (EM2C) du CNRS et de l'ECP

Nanosecond Repetitively Pulsed Discharges in Atmospheric Pressure Air

soutenue le 20 décembre 2012

Jury :	M.	Christophe	Laux	Directeur de thèse
	Mme	Deanna	Lacoste	Co-Directrice
	Mme	Francoise	Massines	Rapporteur
	M.	Michael	Kong	Rapporteur
	M.	Nikolay	Popov	Rapporteur
	M.	Thierry	Callegari	Examinateur
	M.	David	Pai	Examinateur
	M.	Gabi	Stancu	Examinateur

École Centrale des Arts et Manufactures
Grand Établissement sous tutelle
du Ministère de l'Éducation Nationale
Grande Voie des Vignes
92295 Châtenay-Malabry Cedex
Tél : 33 (1) 41 13 10 00
Télex : 634 991 F EC PARIS

Laboratoire d'Énergétique Moléculaire et Macroscopique, Combustion (E.M2.C.)
UPR 288, CNRS et École Centrale Paris
Tél : 33 (1) 41 13 10 31
Fax : 33 (1) 47 02 80 35

Remerciements

Un très grand merci tout d'abord à mes directeurs de thèse Christophe Laux et Deanna Lacoste. Leur complémentarité, leur grande expertise et leur rigueur scientique ont contribué à la réussite de cette thèse. Je remercie chaleureusement Christophe pour son implication, sa grande disponibilité à toute heure, ses nombreux conseils. Je remercie également Deanna pour son implication lors de toutes les campagnes expérimentales, sa grande attention de chaque instant et son humanité.

Je remercie les membres du jury d'avoir accepté d'examiner cette thèse. C'est un grand honneur que m'ont fait Françoise Massines qui a porté la double casquette en présidant également mon jury, Michael Kong et Nikolay Popov d'être les rapporteurs de cette thèse. J'exprime également ma gratitude à Thierry Callegari, David Pai ainsi que Gabi Stancu d'avoir accepté d'en être les examinateurs.

Je remercie la DGA pour le financement de ce travail, ainsi que pour leur constante efficacité dans l'encadrement et pour l'organisation de doctoriales de très grande qualité.

Cette thèse doit également beaucoup à d'autres membres du laboratoire EM2C : tout d'abord les personnels de l'équipe technique, en particulier Yannick Le Teno et Jérôme Beaunier pour leur précieuse aide dans la conception des "pointes", mais aussi Anne-Cécile, Virginie, Nathalie, Erika, Stéphanie, Samira, Sid, Francis, Alain et Adrien. Je garderai un très bon souvenir des conversations autour d'une tasse de thé entretenues avec Anne qui me permettaient de m'évader quelque peu. Merci à Estelle Iacona, Jean Taine, Christophe Laux, Fabien Bellet et Gabi Stancu pour m'avoir permis d'enseigner les transferts thermiques, en français et en anglais, et leur aide lors de la préparation de mes cours. Merci à Laurent Zimmer et Benoît Fiorina de m'avoir permis d'encadrer des TP.

De chaleureux remerciements pour la *running team* : j'ai apprécié que mes camarades de course à pied ralentissent le rythme dans les montées pour m'attendre ! Une pensée également pour les choristes d'Antony - merci à

Monique, Brigitte, Marie-Ange et Christelle, pour leur soutien et pour mes collègues rouennais en particulier Isabelle, Lucie, Georges, Yves et Jean-Marc pour leur compréhension et leur attention dans les derniers mois ce qui m'a permis de terminer ce travail dans les meilleures conditions.

Ces trois ans de thèse ont été très agréables grâce à de nombreux autres thésards et post-doctorants du laboratoire. Les plasmiciens tout d'abord : un grand merci à Florent, en particulier pour son aide lors des derniers mois, mais également à Fabien T. pour nos nombreuses conversations scientifiques ô combien précieuses. Merci également à Da, Carolyn, Megan, François P., Marien, Adrien et Jaroslav. Je n'oublie pas mes co-bureaux: Layal, Alexis, Beto, Kostas, Thomas, Jonas.... et tous les autres thésards et post-doctorants croisés au cours de ma thèse : Alessandro - comment transformer nos galères communes en éclat de rire !, Fred, 1er co-*fire belette*, Vincent L. et nos discussions à propos de la T.T., François D., Thibault, 2ème co-*fire belette*, Laurent S., Théo, Mélanie, Sorour, Diana, Clément, Laurent T., Jean L., Jean C., Tapish, Aurélien sans oublier les "anciens" : Farah, mais également Dave et Julien pour leurs conseils lors de mes débuts en tant qu'expérimentatrice.

Enfin, j'exprime toute ma gratitude à mes amis - merci Guillaume !, ma famille pour leur soutien dans ces années qui demandèrent un grand investissement personnel et pour leur aide pour l'organisation de la journée de soutenance, et enfin à mon conjoint Vincent qui m'a accompagné patiemment et avec enthousiasme, et une bonne implication, durant ce travail. Ton affection et ton soutien m'ont été infiniment précieux.

Abstract

Atmospheric pressure air plasmas have many potential applications in domains such as medical treatment, chemical and biological decontamination, aerodynamic flow control, nanomaterial fabrication, and combustion. Many of these applications require large volume, low power with high chemical reactivity plasmas at a low temperature. These requirements lead to use non-thermal plasmas. One efficient method to produce such plasmas is to use Nanosecond Repetitively Pulsed (NRP) discharges because of the high electron density created for a low power budget compared to other traditional non-thermal atmospheric pressure air plasma generation methods. It was shown that these NRP discharges present three different regimes when increasing the applied voltage: corona, glow, and spark regime at $T_g = 1000$ K. The spark regime has the particularity of creating many active species while increasing the temperature of the gas by about 500-3000 K - depending on the operating conditions. The NRP glow regime has only been observed, so far, for $T_g > 700$ K, but a model predicts the existence of NRP glow discharges at room temperature provided small radius of curvature of the electrode and longer pulse duration (FWHM around 20-30 ns). The goals of this thesis are, first, to validate the two-step mechanism proposed to explain the ultrafast heating observed in NRP spark discharges, and secondly, to experimentally obtain a stable NRP glow discharge at $T_g = 300$ K and to study its properties.

In this thesis, the NRP method was implemented to generate either NRP spark or glow discharges into preheated atmospheric pressure air ($T_g = 300$-1000 K) between two steel electrodes of controlled radius of curvature, placed perpendicularly to the flow or in parallel with the flow. The plasma was created using short (5-30 ns FWHM) high-voltage (up to 8.5 or 14 kV depending on the pulse generator) pulses repeated at frequencies from 1 to 30 kHz for an inter-electrode gap distance from 1 to 8 mm. The radii of curvature of the electrodes studied were from 20 to 500 µm and for some experiments we used a steel plane of 6 mm × 8 mm behind each pin electrode.

In the first part of this thesis, we provide a full set of data on an NRP *reference case* spark discharge. This study complements previous atomic oxygen measurements in order to validate the two-step mechanism proposed to explain

the ultrafast heating observed in NRP spark discharges. We investigated the densities of two excited states of nitrogen - $N_2(B)$ and $N_2(C)$ during and after an NRP spark discharge using absolute Optical Emission Spectroscopy (OES). We performed time-resolved measurements (2-ns resolution) of emission spectra of the NRP *reference case* spark discharge from which we inferred the absolute number densities of $N_2(B)$ and $N_2(C)$. We also measured the radius of the discharge from the density profile of these two species using an Abel inversion of the lateral spectra and we found that they were equal to 450-500 µm for both states. From these measurements, we also deduced the temporal evolution of the gas temperature; it increases from 1500 K to 2400 K within 20 ns, thus confirming ultrafast heating. Synchronizing these measurements with previous atomic oxygen measurements, we have shown that the dissociation of molecular oxygen within the first 20 ns is mainly due to the quenching reactions of $N_2(B)$ and $N_2(C)$, thus confirming the two-step mechanism. The quenching rates of $N_2(B)$ and $N_2(C)$ by O_2 were also determined from the decay times of the density of these species.

In a second part, we investigated whether it was possible to obtain an NRP glow discharge at $T_g = 300$ K. We performed time-resolved imaging (single shot and average images) with an ICCD camera of NRP glow discharges for different electrode radii of curvature and gas temperatures. At $T_g = 1000$ K, we studied the NRP glow discharge for different radii of curvature of the electrodes. We showed that this discharge was identical to the one studied by Pai. We also noticed that for a radius of curvature of the electrode of $R = 50$ µm, the streamer radius decreases during its propagation, whereas for $R = 500$ µm, the radius of the streamer is approximately constant. The influence of the radius of curvature of the tip of the electrode on the limits of existence of the glow regime confirms the model established by Pai *et al* in [1] and confirms that at a given gas temperature T_g, the minimum distance for the existence of the glow regime d_{min} decreases when the radius of curvature of the electrode decreases. We obtained a glow regime at $T_g = 300$ K with small radii of curvature $R = 20$ and 50 µm, as was predicted by Pai *et al* in [1]. However, we added a steel plane (6 mm × 8 mm) behind each pin electrode which modifies the axial Laplacian reduced electric field.

We highlighted the existence of a regime that was not seen by Pai [2] at $T_g = 1000$ K, the so-called NRP Multi-Channel Glow (MCG) regime observed for $300 < T_g < 700$ K. This regime is characterized by the same features as the NRP glow regime - low conduction current, low light intensity, same discharge dynamics, but the streamer can leave the anode on another direction than the inter-electrode direction or several streamers leave the anode within a single discharge.

Finally, in the third part, we performed a parametric study of the existence of the NRP glow regime and of the Multi-Channel Glow regime at $T_g = 300$ K. Decreasing either the inter-electrode gap distance or the length between the plane and the tip of the electrode favors the existence of NRP glow regime rather than NRP Multi-Channel Glow regime. We have also shown that increasing the frequency promotes the NRP glow regime. We have investigated the influence of the flow rate on the nature of the discharge. We show that, when the flow is perpendicular to the discharge axis, the flow has no influence on the nature of the discharge at low frequencies but a strong influence at higher frequencies due to memory effects. In static air at high frequencies, the inter-pulse duration is too small for the evacuation of heat and/or charged particles; NRP glow discharges are privileged. We suggest that the branching structures detected in cases where the model predicted an NRP glow discharge could be due to a low value of the axial Laplacian reduced electric field between the electrodes, and to a highly peaked distribution of the radial electric field.

In conclusion, we have demonstrated the two-step mechanism which explains the ultrafast heating that occurs during and after an NRP spark discharge. This ultrafast heating could have applications in domains such as nanomaterial fabrication or plasma assisted combustion. We have shown the existence of the NRP glow regime at room temperature and the existence of a multi-channel glow regime. Both regimes could be relevant for temperature sensitive applications. The Multi-Channel Glow regime is particularly interesting for applications in which a large volume of gas must be treated. The present work opens up a new range of applications, for which the energy deposited into the plasma, the temperature increase and atomic oxygen production should be investigated further.

Résumé

Les plasmas d'air à la pression atmosphérique ont de nombreuses applications potentielles, telles les traitements médicaux, la décontamination chimique et biologique, le contrôle d'écoulements aérodynamiques, la fabrication de nanomatériaux ou la combustion assistée par plasma. La plupart de ces applications nécessitent des plasmas de larges volumes, à de faibles coûts énergétiques et des températures inférieures à 1000-2000 K. De telles contraintes nécessitent d'utiliser les plasmas hors-équilibre. Les décharges Nanosecondes Répétitives Pulsées (NRP) constituent une méthode efficace pour produire de tels plasmas. En effet, celles-ci créent des densités électroniques élevées pour un coût énergétique faible comparé aux autres méthodes.

Jusqu'à présent, ces décharges NRP existaient sous trois régimes dans l'air à 1000 K. Lorsque l'on augmente la tension, on voit successivement les décharges dites couronne, puis celle dites *glow* et enfin les décharges nommées *spark*. Les décharges de type NRP *spark* ont la particularité de créer des espèces actives en grande quantité tout en chauffant le gaz de façon très importante. Selon les conditions de fonctionnement, une augmentation de 500 à 1500 K en 20 ns a été constatée. Les décharges NRP de type *glow* ont été observées jusqu'à présent uniquement pour une température initiale du gaz supérieure à 700 K. Cependant, un modèle théorique prédit leur existence à température ambiante à condition de diminuer le rayon de courbure des électrodes et d'utiliser des impulsions de tension de durée plus importante (de 20 à 30 ns). Les principaux objectifs de cette thèse sont doubles. Dans un premier temps, il s'agira de valider expérimentalement le chauffage ultra-rapide observé dans les décharges NRP *spark* dans l'air à 1000 K. Le deuxième volet s'attachera à l'obtention et à l'étude expérimentale des décharges NRP *glow* à 300 K.

Dans cette thèse, la méthode des décharges NRP a été mise en œuvre afin de créer des décharges NRP *spark* ou *glow* dans l'air préchauffé ou non à pression atmosphérique entre deux électrodes pointe-pointe, de rayon de courbure contrôlé, en configuration perpendiculaire ou parallèle à l'écoulement. Le plasma était créé grâce à de courtes (de 5 à 20 ns) impulsions hautes tensions (jusqu'à 14 kV) répétées à des fréquences (*Pulse Repetition Frequency*, PRF) variant entre 1 et 30 kHz pour une distance inter-électrode comprise entre 1 et 8 mm. Le

rayon de courbure des électrodes étudiées ici était compris entre 20 et 500 µm et pour certaines expériences, nous avons utilisé une petite plaque métallique (6 mm × 8 mm) derrière les électrodes à des distances comprises entre 1 et 15 mm de la pointe de l'électrode.

Dans la première partie de cette thèse, nous avons fourni un ensemble de données complets sur une décharge NRP *spark* ***de référence***. Cette série d'expériences a été menée dans le but de compléter de précédentes données sur la densité de l'oxygène atomique. Ces expériences avaient été réalisées afin de valider le mécanisme à deux étapes proposé pour expliquer le phénomène de chauffage ultra-rapide supposé dominant dans les décharges NRP *spark*. Nous avons étudié la densité de deux états excités du diazote : $N_2(B)$ et $N_2(C)$ pendant et après une décharge NRP *spark* en utilisant la technique de spectroscopie optique d'émission calibrée en intensité. Nous avons réalisé des mesures résolues en temps, avec une précision de 2 ns, de spectres d'émission obtenus dans une décharge NRP *spark*. De ces spectres, nous avons déduit les densités absolues des espèces $N_2(B)$ et $N_2(C)$. Nous avons également mesuré le rayon de la décharge à partir des profils de densités de ces deux espèces en réalisant une inversion d'Abel des spectres latéraux. Nous avons trouvé que le rayon de la décharge était identique pour ces deux états, et égal à 450-500 µm. A partir de ces mesures nous avons déduit l'évolution temporelle pendant et après l'impulsion de tension de la température du gaz ; celle-ci augmente de 1500 K à 2400 K en 20 ns, confirmant ainsi le chauffage ultra-rapide. En synchronisant ces mesures avec les précédentes données de l'évolution de la densité de l'oxygène atomique, nous avons montré que la dissociation de l'oxygène moléculaire était due dans les 20 premières nanosecondes principalement aux réactions de *quenching* dissociatif de $N_2(B)$ et $N_2(C)$, ce qui confirme le mécanisme à deux étapes. En parallèle, les taux de ces réactions ont été déterminés à partir des temps de décroissance de ces espèces.

Dans une seconde partie, nous avons essayé d'obtenir une décharge NRP *glow* dans l'air à 300 K. Nous avons réalisé des images résolues en temps (images d'une ou de plusieurs décharges) avec une caméra ICCD, pour différents rayons de courbure des électrodes et différentes températures du gaz. Pour $T_g = 1000$ K, nous avons montré que les décharges observées étaient identiques du point de vue dynamique aux décharges observées par Pai *et al* [1]. Nous avons également remarqué que pour un rayon de courbure de $R = 50$ µm, le rayon du *streamer* diminuait lors de la propagation, tandis que pour $R = 500$ µm, ce même rayon était quasiment constant. L'influence du rayon de courbure des électrodes sur les limites d'existence du domaine du régime NRP *glow* confirme le modèle de Pai *et al* [1]; pour une température du gaz donnée, la distance minimum permettant l'existence du régime *glow* d_{min} diminue lorsque le rayon de courbure des électrodes diminue. Nous avons obtenu un régime NRP *glow* à $T_g = 300$ K avec de faibles rayons de courbure ($R = 20$ ou 50 µm), comme Pai

et al l'avait prédit. Cependant, nous avons ajouté un plan en acier (6 mm × 8 mm) derrière chaque électrode ce qui modifie le champ électrique Laplacien au milieu de l'espace inter-électrode.

Nous avons mis en évidence l'existence d'un régime qui n'avait pas été vu par Pai *et al* à $T_g = 1000$ K, que nous avons appelé régime NRP *glow* à plusieurs canaux ou *multi-channel glow*, régime observé pour 300 K $< T_g <$ 700 K. Ce régime est identique au régime NRP *glow* sur plusieurs aspects : très faible courant de conduction, intensité lumineuse faible, dynamique de la décharge identique. Cependant, le *streamer* peut quitter l'anode dans une direction non-axiale, ou bien plusieurs *streamers* quittent l'anode lors d'une seule décharge.

Enfin, dans une dernière partie, nous avons réalisé une étude paramétrique de l'existence du régime *glow* et du régime *multi-channel glow* à $T_g = 300$ K. Diminuer la distance inter-électrode ainsi que la distance entre la pointe de électrode et la plaque métallique arrière privilégie le régime *glow*. Nous avons également montré qu'augmenter la fréquence des impulsions (PRF) favorise le régime *glow*. Nous avons étudié l'influence de la vitesse de l'écoulement sur la nature de la décharge. Lorsque l'écoulement est perpendiculaire à l'axe de la décharge, celui-ci n'a pas d'influence sur la nature de la décharge à basse fréquence ($PRF \approx$ 1-5 kHz) mais a une influence importante à haute fréquence ($PRF \geq$ 10 kHz). Si la décharge est *glow*, arrêter l'écoulement va induire une transition vers une décharge *multi-channel glow*. Ceci est dû aux «effets mémoires» : dans l'air statique à haute fréquence ($PRF \geq$ 10 kHz), la durée entre les impulsions est trop courte pour permettre l'évacuation des particules chargées et de la chaleur. Nous avons suggéré des raisons qui pourraient expliquer cette structure de *branching* que nous avons observé dans des cas où le modèle de Pai *et al* prédisait une structure axiale de la décharge. Ce pourrait être dû à une faible valeur du champ Laplacien axial entre les électrodes et à la variation très abrupte de la composante radiale du champ lorsque l'on s'écarte de l'axe des électrodes.

En conclusion, nous avons démontré que le mécanisme à deux étapes expliquait le chauffage ultra-rapide pendant et après une décharge NRP *spark*. Ce chauffage ultra-rapide pourrait avoir de nombreuses applications dans des domaines tels que la fabrication de nanomatériaux ou la combustion assistée par plasma. Nous avons montré l'existence du régime NRP *glow* à température ambiante et l'existence d'un régime *glow* à plusieurs canaux (*multi-channel glow*). Ces deux régimes sont intéressants pour des applications sensibles à la température : l'énergie par unité de volume du premier régime est plus grande et il serait intéressant pour des applications où les effets doivent être concentrés. Le deuxième régime peut lui être utilisé dans des applications où un large volume de gaz doit être traité. Cependant, cette analyse dépend en grande partie des

différences potentielles entre ces deux régimes en termes d'énergie déposée dans le plasma, de production d'oxygène atomique ou de chauffage du gaz.

Contents

Chapter 1

Introduction

1.1 Motivation

Although atmospheric pressure air plasmas are not as well known as fusion plasmas or TV plasma screen in the general public and in the media, this research domain has great potential for numerous applications that could change everyday's life: health care, the environment, energy, transportation, and manufacturing. This type of plasma could first permit to operate in much easier conditions for applications that are already developed. For instance, to work at atmospheric pressure would eliminate the need of costly low pressure systems. It could also permit to achieve new technological breakthroughs in medical treatment or biological decontamination.

Plasmas are of great interest because of the wealth of their chemical and electrodynamic effects. Various species can be created with high densities: ions, electrons, radicals, and excited species, and these species can promote beneficial reactions. The species produced in the discharge or the post-discharge make them of particular interest for applications where a zone is difficult to reach, such as in medical treatment.

To use them in such applications would imply that they meet key requirements in terms of :

- **high electron number density**: plasma dynamics and efficiency rely mostly on a high number of electrons with a sufficiently high energy. This energy can be transferred by collisions and create new species. Consequently, the electron density is a good indicator of the plasma reactivity.
- **low gas temperature**: many applications such as surface or medical treatment or biological decontamination are sensitive to the temperature. One of the key goal of this thesis is to obtain an efficient NRP glow discharge in air at atmospheric pressure and ambient temperature.
- **significant volume**: the plasma size must be macroscopically developed

in at least one dimension in order to be considered for macroscopic applications.
- **low volumetric power budget**: otherwise the cost would be prohibitive for potential applications.

Cold non-equilibrium plasmas are the most adequate type of plasmas to answer these criteria thanks to the high electron number density created at low gas temperature. However, the use of such plasmas at atmospheric pressure is made difficult because they easily transition to thermal (equilibrium) plasmas, for which the temperature of the gas is high. This "glow-to-arc" transition is mostly due to thermal instabilities. Such plasmas include arc and spark discharges, in which the temperature can increase up to thousands of Kelvins, thus reducing their range of applications.

Several plasma techniques that can be considered always suffer from significant drawbacks. One technique is to insert a current limiting resistor, but this increases the power requirements because of resistive losses. A much more useful technique is to use Dielectric Barrier Discharge (DBD), but in this case, the maximum electron number density in the diffuse regime, which is then a Townsend regime, remains limited to about 10^{10} cm^{-3}, which is not sufficient for many applications. The electron beam technique [3] is in theory the best one, since the ionization efficiency is maximized. However, to obtain such a beam in atmospheric pressure air is a challenge, in particular because of the high heat fluxes created that are not supported - until now - by any window without breaking.

The promising technique considered in this work is the Nanosecond Repetitively Pulsed (NRP) discharge which meets the four requirements previously presented. It consists in applying for a very short time (about 10 ns) a high voltage pulse (about 6-10 kV). The strong applied field accelerates the electrons to high velocity. With a fast (2-5 ns) rise time, the number of collisions at low energy is minimized. To avoid the "glow-to-arc" transition, the field is turned off after only a few nanoseconds. In order to obtain a high average electron number density, the phenomenon is repeated with a sufficient Pulse Repetition Frequency (PRF) from 1 to 30 kHz. Researchers at Stanford University [4] have shown experimentally in 2003 that the NRP glow discharge in atmospheric pressure air at $T_g = 2000$ K meets all the conditions previously detailed. However, they did not extend their study of the glow discharge at gas temperature below 2000 K.

Then, Pai [2] investigated the existence of the NRP glow regime in preheated air at lower temperature from 300 to 1000 K. He established the existence of three regimes of NRP discharges at $T_g = 1000$ K: corona discharges, glow discharges

and spark discharges. He studied the various properties of the NRP spark and glow regimes at T_g = 1000 K and their domains of existence. In particular, he showed that the NRP glow regime only exists for a temperature of the gas greater than 700 K under his experimental conditions of pulse characteristics and electrode geometry. Pai *et al* [1] suggested a model that would explain such a lower limit of existence and showed that the NRP glow regime should exist at room temperature provided one used electrodes with small radius of curvature and longer pulse duration (about 20 ns), and a wider inter-electrode gap.

Furthermore, he also showed that during and after an NRP spark discharge, an ultrafast heating of several hundreds of Kelvins happens within about 20 ns. In order to explain this ultrafast heating, a two step mechanism was proposed [5] and already partly studied [6]:

$$\begin{aligned} N_2(X) + e^- &\rightarrow N_2(A,B,C) + e^- \\ N_2(A,B,C) + O_2 &\rightarrow N_2(X) + 2O + \text{heat} \end{aligned}$$

In this study, the NRP method is implemented to generate either NRP spark or glow discharges in preheated atmospheric pressure air (T_g = 300-1000 K) between two steel electrodes of controlled radius of curvature, placed perpendicular or parallel to the flow. The plasma is created using short (5-30 ns of FWHM) high-voltage (up to 8.5 or 14 kV depending on the pulse generator) pulses repeated at frequencies from 1 to 30 kHz for an inter-electrode gap distance from 1 to 8 mm. Two different pulse generators were used, including one delivering pulses of variable duration. The radii of curvature of the electrodes were from 20 to 500 µm and for some experiments we used a steel plane of 6 $\times$ 8 mm^2 behind each pin electrode.

We analyzed an NRP *reference case* spark discharge - similar experimental conditions to those in [6] - to obtain the gas temperature and the number densities of two species involved in the two-step mechanism proposed: N_2(B) and N_2(C). Then we investigated the existence of the NRP glow regime using a pulse generator delivering variable duration of pulses and electrodes of calibrated radius of curvature.

The two main goals of this thesis can be summarized as follows:

1. validate the ultrafast mechanism observed in NRP spark discharges in atmospheric pressure air at T_g = 1000 K,
2. obtain experimentally a stable NRP glow discharge in atmospheric pressure air at T_g = 300 K and study its properties.

1.2 Scope of the thesis

We first describe in chapter 2 the Nanosecond Repetitively Pulsed discharges used in this work, and their various potential applications in air at low temperature and atmospheric pressure. We also detail the numerous results previously obtained on NRP discharges in preheated air [2], and in particular the properties of the NRP glow and spark regimes, with their domains of existence. We present the two-step mechanism that was proposed [6] to explain the ultrafast heating observed [2], [6] during and after an NRP spark discharge. We analyze the model proposed by Pai *et al* [1] and describe the conditions required to obtain NRP glow discharges at room temperature.

Chapter 3 presents the various plasma reactors and the optical and electrical diagnostics used in this work. The goal of chapter 4 is to validate the mechanism proposed to explain the ultrafast heating. To this end, we present $N_2(B)$ and $N_2(C)$ time-resolved absolute number density measurements obtained with calibrated Optical Emission Spectroscopy on the NRP *reference case* spark discharge at $T_g = 1000$ K. Then, we present measurements of the diameter of the discharge based on the density profile of these two states at different times during and after the high voltage pulse. We also determined the temporal evolution of the gas temperature within the discharge. These measurements added to previous atomic oxygen measurements confirm the mechanism proposed.

The aim of chapters 5 and 6 is to investigate the existence of the NRP glow regime at $T_g = 300$ K. First, we start in chapter 5 by studying with time-resolved ICCD imaging the NRP glow regime at $T_g = 1000$ K with various radii of curvature of the electrodes. Then, we decrease the temperature for various radii of curvature and note that an additional regime with the same characteristics as the NRP glow regime - except the spatial distribution - appears around $T_g = 700$ K: the Multi-Channel Glow regime (MCG). We conclude by demonstrating how to obtain an NRP glow discharge at $T_g = 300$ K.

In chapter 6, we conduct a parametric study of the existence of the NRP glow regime at $T_g = 300$ K. We investigate the influence of the inter-electrode gap distance, the distance between the tip of the electrode and the plane behind, the influence of the Pulse Repetition Frequency and the flow direction and velocity. We conclude on the differences between NRP Multi-Channel Glow and glow regime and the transitions between those regimes.

This work was funded by a DGA (Direction Générale de l'Armement) grant and by the Agence Nationale de la Recherche (ANR) under the *Transformation de l'énergie électrique en PRÉcurseurs actifs par Plasmas froids diffus à la pression Atmosphérique* (PREPA) project grant ANR-09-BLAN-0043.

Chapter 2

Non-thermal Discharges in Atmospheric Pressure Air

2.1 Introduction

In this chapter, we present an overview of non-thermal plasma discharges in atmospheric pressure air with a particular focus on Nanosecond Repetitively Pulsed (NRP) discharges which are at the center of this work. We begin in section 2.2 with an overview of the various applications of atmospheric pressure air plasmas. Then, we present in section 2.3 the several ways to produce such plasmas. In section 2.4, we introduce the plasma generation method that will be used in the present work, Nanosecond Repetitively Pulsed (NRP) discharges, and the results obtained in a pin-pin configuration. In section 2.4.4, we present some of the recent developments using NRP discharges.

Following this presentation, we describe two regimes of operation of NRP discharges: the spark and glow regimes. In section 2.5, we compare the main features of the two NRP discharge regimes: glow and spark regimes in terms of voltage and current measured within the discharge in section 2.5.1, energy deposited into the plasma in section 2.5.2, discharge dynamics in section 2.5.3, and finally gas temperature evolution in section 2.5.4.

Then, we detail two important characteristics of NRP spark discharges in section 2.6. We first explain the importance of the ultrafast heating induced during and after these NRP spark discharges in section 2.6.1. Then, we show recent results about the hydrodynamic expansion of the gas that follows the NRP spark discharge in section 2.6.2. In section 2.7, we show the absolute number density of a few species created by an NRP glow discharge and its potential applications.

Section 2.8 summarizes the domains of existence of the NRP glow and spark

regimes as a function of the Pulse Repetition Frequency (PRF) (Section 2.8.1), the gas temperature (Section 2.8.2) and the inter-electrode gap distance (Section 2.8.3) [1],[2]. Prior to this thesis, the NRP glow regime had been found to exist only at a gas temperature greater than 700 K [1],[2].

In section 2.9, we present the model of Pai *et al* [1] on the coupled influence of the gas temperature and the radius of curvature of the electrodes which explains the various domains of existence of the NRP discharge regimes and the voltage corresponding to the transition between these regimes. We first discuss the Laplacian electric field generated between two point electrodes in section 2.9.1. Then, we detail in section 2.9.2 the transition theory presented in [1]. Finally, using this theory, we predict in section 2.9.3 that the NRP glow regime can be obtained at ambient temperature provided one uses electrodes of small radius of curvature and long duration of the high-voltage pulse.

2.2 Applications of atmospheric-pressure air discharges

Recently, the development of high-pressure low-temperature plasma discharges has opened the way to several applications that used to be limited to low pressure or high temperature domains. We begin with applications in ambient air and then describe applications at higher temperature up to 2000 K.

Although the presented applications do not always use plasmas generated with NRP discharges, this overview highlights the numerous domains of applications where NRP discharges could bring novel contributions. By language abuse, in this section, we will call *plasma* any media where a discharge has created ions, electrons, excited species, or radicals whether the media is neutral or not.

Medical applications

In the near future, medical tools should be less invasive, but remain safe and efficient. Plasma based tools are very promising because they produce active species that efficiently treat many conditions with safe, miniaturizable, low power devices. The species produced by the plasma can also be transported to hard-to-reach areas, thus making plasmas more effective than UV light treatments that require a direct line-of-sight to the target to be treated. As human living cells do not survive temperatures greater than 37-40°C, low pressure or electric shock, atmospheric pressure glow type discharges are necessary. Research in plasma medicine has increased very rapidly in the past decade as discussed in the introductory review recently presented by Kong *et al* [7].

An example of recent advance in plasma medical technology was proposed by Fridman *et al* [8]. They developed a method of direct treatment of living tissue at room temperature and atmospheric pressure, see figure 2.1, that does not

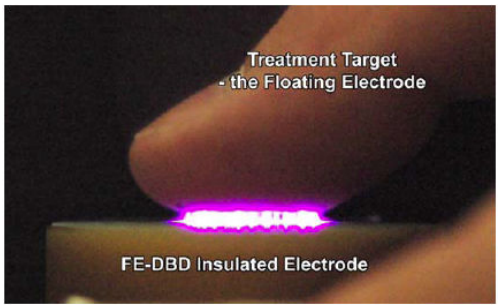

Figure 2.1: Electrically safe non-thermal plasma for treatment of living tissue. Figure taken from [8].

cause any visible or microscopic tissue damage. They used a floating-electrode Dielectric Barrier Discharge (DBD) plasma, and showed that it was electrically safe to human subjects, with a complete tissue sterilization from skin flora within seconds, and blood clot formation in seconds of plasma treatment.

Another promising technique consists in the plasma jets. Recently, Walsh and Kong [9] have developed an air plasma jet generated with NRP discharges, the plasma generation method studied in this thesis. Such a portable plasma jet could be used for etching and polymer surface modification but also for biomedical treatment, particularly wound healing and sterilization. They used a solid state pulser delivering 5-kV pulses of approximately 150-ns FWHM repeated at a frequency of 5 kHz. The plasma jet is created by a central powered metallic needle with 3 mm diameter, held 5 mm from the exit of a conical metallic grounded nozzle. Air was flushed through the nozzle at approximately 10 L/min. The images of figure 2.2 show that, as the discharge current increases, an ionization front propagates through the jet nozzle and continues into the ambient air, with an approximate velocity of 100 km/s.

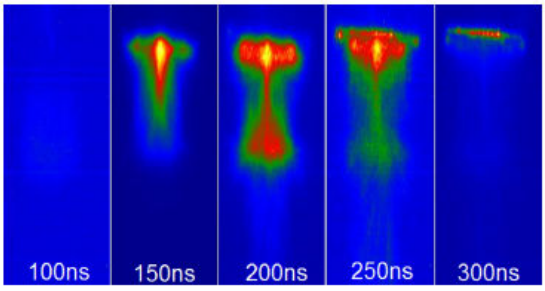

Figure 2.2: 10-ns exposure time images taken during and after the applied voltage pulse. $t = 100$ ns corresponds to the beginning of the current flow. The jet nozzle is at top of image. The air flow is from top to bottom. Figure taken from [9].

Biological decontamination

Methods used to kill harmful bacteria often have side effects, such as a decrease of nutrient content in dairy products resulting from the UHT (Ultra-High Temperature) process. The use of atmospheric air plasmas could be an alternative to sterilization methods. Although the exact mechanism that permits to sterilize is not completely clear, several teams have noted that the active species created by the plasma interfere with membrane cells. Pointu *et al* [10] investigated the surface biological decontamination inside small diameter tubes in atmospheric pressure post-discharges in nitrogen with small additions of O_2. They showed that the $O(^1S)$ metastable state of O had an important biocidal effect. Charged particles can tear apart the cell membrane. The gas heating and UV produced by the discharge could also increase bacteria deactivation.

For example, Machala *et al* [11] tested the deactivation of *Salmonella typhimurium* from contaminated water and surfaces with two types of positive DC discharges (SC Streamer Corona and TS Transient Spark) in a needle-to-plane geometry. They measured oxidative stress by the TBARS method and used different conditions: direct exposure and indirect exposure (water only exposed to neutral species) and showed that the two methods were almost as efficient. However, when contaminated water was only exposed to UV light generated by the discharge, the efficiency of bacteria deactivation was almost null, thus demonstrating the beneficial effect of the plasma treatment.

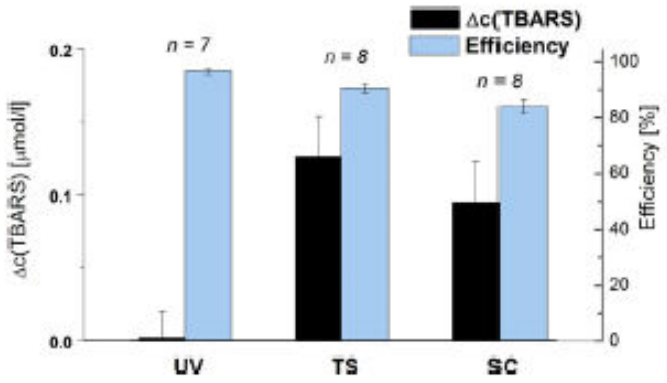

Figure 2.3: TBARS concentration gains and decontamination efficiencies of *S. typhimurium* in water treated by SC and TS with electro-spray, compared with 1 min exposure to UV C (shown with root mean square error, n - number of repeated experiments). Figure taken from [11].

Surface treatment

Low temperature plasmas are widely used for surface treatment, the interest being that the high electron temperature can produce ionization and excitation

while keeping the gas temperature low enough to preserve the material. Using atmospheric pressure air plasmas avoids using pressurized chambers which have a high cost to pressurize and depressurize. However they tend to transition easily into spark discharges, which dramatically increases the gas temperature. The use of DBD prevents this phenomenon. The DBD limits the current, which allows to create large volume plasmas without transitioning into an arc. For example, Massines *et al* [12] have demonstrated using TALIF methods that they could obtain atomic nitrogen densities as high as 3×10^{14} cm^{-3} in a diffuse DBD.

Chemical decontamination

An important issue for industry is the reduction of pollutants, for instance by decomposing them into harmless products. The use of atmospheric air plasmas is particularly appropriate because the energy is mostly transformed into highly energetic electrons. These electrons decompose the pollutants either by direct impact or by the creation of radicals. The decomposition of NO_x has been investigated recently, for instance by Guaitella *et al* in [13]. They treated the inner surface of a Pyrex tube by a capacitively coupled RF plasma at low pressure and studied the oxidation of NO into NO_2 by means of quantum cascade laser absorption spectroscopy in the mid-infrared spectral range. The combination of the plasma discharge with a catalyzer is however often necessary.

Aerodynamic flow control

The field of plasma actuators has been strongly developing in the past 15 years. Compared to mechanical actuators, they can be activated over much shorter timescales. In an electric field, charged particles are accelerated and can transfer their momentum to neutrals through collisions. Placed correctly on an object in a subsonic flow, this force may be used to control the regime of the flow around the profile. Flow control with DBD or DC discharges has been demonstrated, and recently, a maximum induced velocity of 10.5 m.s^{-1} has been achieved by Debien *et al* [14] in a multi-DBD plasma actuator and a maximum velocity of 12 m.s^{-1} was obtained by Colas *et al* [15] with a DC corona discharge. Modeling of DBD actuators has been performed by the LAPLACE group [16] and Likhanskii *et al* [17]. The former showed with a 2D fluid model that the ElectroHydroDynamic (EHD) force is important not only during the positive part of the sinusoidal voltage cycle but also during the negative part of the cycle. During the two phases, the EHD is due to different physical phenomena. In the latter work, they proposed an optimal voltage waveform based on a detailed understanding of the DBD physics: it consists of short (a few nanoseconds in duration) negative pulses repeated at high frequency, combined with a positive DC bias. The Nanosecond Repetitively Pulsed (NRP) discharges they proposed is the generation method used in the present work.

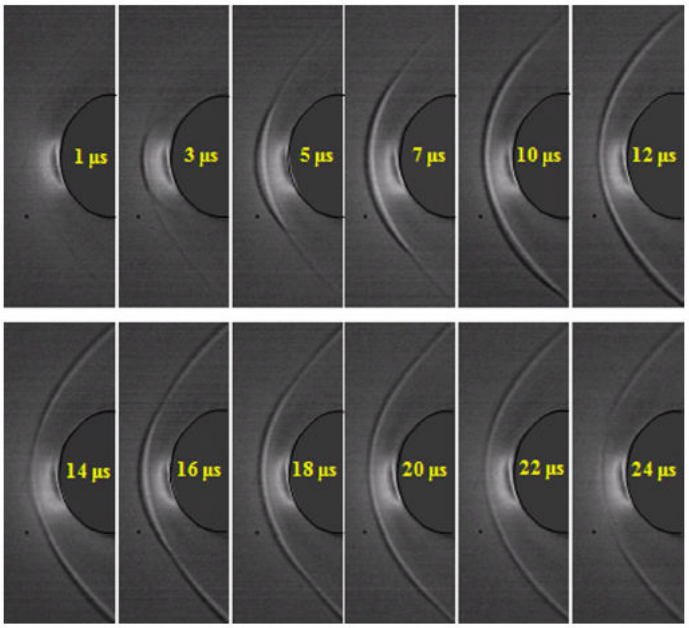

Figure 2.4: Difference of Schlieren signal intensity from the baseline Schlieren signal. Two-pulse burst mode operation at 100 kHz pulse repetition rate and 200 Hz burst repetition rate. The bow shock stand-off distance peaks approximately 5 µs after the first pulse (at $t = 5$ µs) and approximately 4 µs after the second pulse (i.e., at $t = 14$ µs). Figure taken from [18].

Another potentially interesting application of DBDs is for supersonic aerodynamic flow control. One method to modify the bow shock layer that forms ahead of a supersonic aircraft is to add a physical spike at the nose of the aircraft to change the shock into a conical oblique shock. The problem is that the spike suffers from heating and mechanical stress. To circumvent the problems associated with the use of the physical spike, one method is to generate a plasma ahead of the aircraft body. Nishihara *et al* [18] showed the feasibility of hypersonic flow control by low-temperature, repetitive nanosecond pulse discharges using phase-locked Schlieren images of a bow shock perturbation in a Mach-5 air flow at $p = 370$ torr, these images are shown on figure 2.4.

Nanomaterial synthesis

Non-thermal plasmas operating at atmospheric pressure are of great interest for nanomaterial fabrication. The high density may permit a fast synthesis without a vacuum system. In [19], Levchenko *et al* demonstrate the formation of long self-organized carbon connections between Ag nanoparticles on a Si(100) surface in atmospheric pressure Ar + CH_4 microplasmas. Figure 2.5 shows several configurations of carbon connections between Ag nanoparticles. A detailed overview of plasma nanofabrication can be found in [20]. Nanosec-

ond Repetitively Pulsed (NRP) spark discharges in atmospheric pressure air could be of particular interest for nanomaterial fabrication since they create an important quantity of atomic oxygen and excited states of nitrogen. The controled production of atomic oxygen in NRP spark discharges in air could be useful for tailoring metal oxide nanostructures. Preliminary experiments were realized by Pai *et al* [21] with the high-voltage pulse generator presented in section 3.3. They used various experimental configurations and show the several types of nanostructures obtained, including Mo nanoflakes.

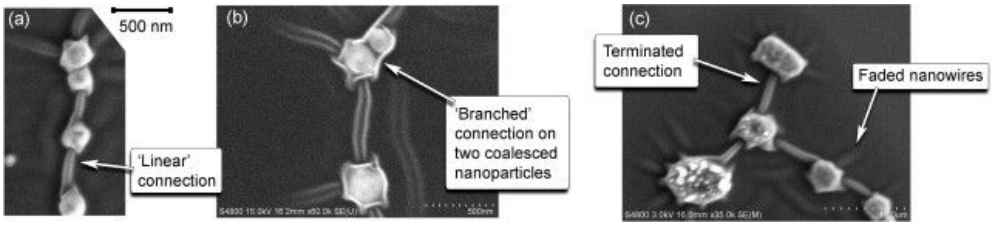

Figure 2.5: Scanning Electron Microscope (SEM) images illustrating various configurations of carbon connections between Ag nanoparticles: (a) linear connection; (b) 'branched' connection based on two coalesced nanoparticles; and (c) terminated connections and 'faded' nanowires which start at the nanoparticle and fade on the surface without reaching other nanoparticles. Figure taken from [19].

Plasma-assisted combustion

Nitrogen oxides are a critical problem in combustion engines. Even more stringent regulations in the aeronautic and automotive industry require breakthrough technologies to reduce the level of these pollutants, and therefore the reduction of NO_x emission has become a crucial issue in combustion research. One path is to reduce the temperature of the flame which reduces the level of NO_x emitted. Working at lower temperature implies to decrease the fuel air equivalence ratio, thus lean flames are increasingly used to reduce the emission of these pollutants [22]. However, lean flames tend to be unstable or difficult to ignite. To solve these problems, one way is to create a plasma in the combustion zone in order to stabilize lean flames. It was shown by Pilla *et al* [23] that lean premixed flames may be stabilized with NRP spark discharges that produce a local increase in heat and active species concentrations. They showed that with an NRP spark discharge of 75 W, stabilization of a 12 kW lean propane-air mixture was possible. The flame region is considerably larger when the plasma is applied, indicating that the combustion is enhanced.

Aleksandrov *et al* [24] simulated the ignition dynamics of a CH_4:O_2:N_2:Ar = 1:4:15:80 mixture by a high-voltage nanosecond discharge. They showed that the addition of nitrogen to the mixture gives rise to new mechanisms for the

production of oxygen atoms via excitation of nitrogen electronic states and their subsequent quenching in collisions with oxygen molecules that become dissociated.

In a recent work, Lacoste *et al* [25] studied the temporal response of 2-kW bluff body stabilized weakly turbulent lean premixed propane-air flame when applying NRP discharges. OH laser induced fluorescence (LIF) measurements have been performed to localize the region of the burnt gases and are shown on figure 2.6. Additional OES measurements were made to determine the rotational temperature in the recirculation zone with and without plasma.

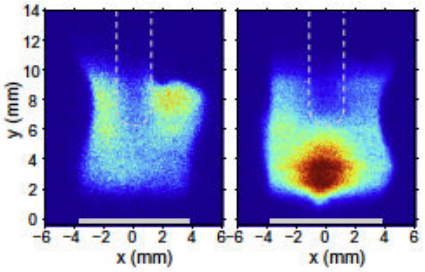

Figure 2.6: OH PLIF images without (left) and with (right) NRP discharges with a power of 12 W and a PRF of 30 kHz, 10 ms after starting the plasma pulses (integration time 50 ns). Figure taken from [25].

We notice from the images of figure 2.6 that the recirculation zone is partly filled with burned gases. However, applying NRP discharges in the burned gases can significantly change the spatial location of a lean premixed flame stabilized over a bluffbody.

For more details on plasma assisted combustion and recent developments, the reader is confered to the review article of Starikovskyi and Aleksandrov [26].

Overview of temperature ranges for applications

We now present an overview of the temperature ranges of the various applications presented in this section. The medical applications are the most sensitive to temperature, as previously explained. The range from 290 to 320 K is safe for patients. Surface treatment and biological decontamination may be performed at temperatures below 500 K. Chemical decontamination applications may go up to 1000 K. Flow control applications must operate from 100 to 2000 K. Finally, combustion applications must operate at higher temperature (around 2000 K) for Plasma Assisted Combustion or lower temperature for ignition.
Non-thermal plasmas are the only viable method for temperature-sensitive applications, and, as will be presented in section 2.4, the NRP discharges are

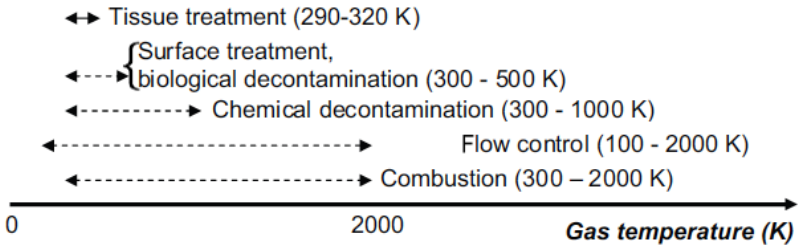

Figure 2.7: Temperatures ranges under which air plasmas must be created for applications presented in this section. Figure taken from [2].

promising candidates because they can create two different regimes of non-thermal discharges at low power cost. The NRP spark regime, which produces active species as well as some degree of gas heating, is important for combustion type applications. The other regime, the NRP glow regime, is promising for applications that do not accomodate any temperature increase, such as surface treatment, medical applications or biological decontamination.

2.3 Methods for producing atmospheric pressure air plasma

Before detailing the NRP discharges strategy in section 2.4, we briefly discuss the various methods for producing plasmas in air at atmospheric pressure. We divide the overview into thermal and non-thermal sources. A more detailed discussion can be found in [2].

2.3.1 Thermal plasma sources

The most direct way to produce thermal plasmas consist in using DC discharges. Another method is to use radiofrequency plasmas with an Inductively Coupled Plasma (ICP) torch for instance, which can create air plasmas up to 10,000 K [27]. Atmospheric pressure air plasmas can also be generated by a microwave generator operating at a frequency of 2.45 GHz, and can create relatively large volume (10 cm^3) plasmas up to 5000 K [28]. Finally, lasers can be used to create plasmas in air via the inverse *Bremsstrahlung* process. Applications include laser-assisted ignition of combustible mixtures.

2.3.2 Non-thermal plasma sources

Non-thermal plasmas can be produced with DC discharges, adding a current-limiting resistor in series with the discharge to prevent the glow to arc transition. They are of great interest because of their strong non-equilibrium ($T_e \gg T_g$) character [27]. Another important source of homogeneous atmospheric pres-

sure air plasma is the Dielectric Barrier Discharge (DBD) [29]. It consists of using plane electrodes separated by a dielectric media, which prevents the arc transition by capacitively limiting the current. Non-thermal plasmas can also be produced by low power RF devices such as the hollow slot microplasmas created by Yalin *et al* [30] or using lasers to generate optically pumped plasmas [31]. A theoretical possibility to create high electron density (up to 10^{13} cm^{-3}) plasma is to use electron beams [3], but this technique has been difficult to implement in practical devices. Finally, atmospheric pressure air plasmas can be created by Nanosecond Repetitively Pulsed (NRP) discharges. This method will be detailed in section 2.4.

2.3.3 Comparison of different methods of air plasma generation

Pai [2] compared the methods in terms of their ability to produce the most reactive plasmas at the lowest possible temperature and power requirements. The electron number density is a good indicator of the plasma effectiveness in terms of chemical reactivity. Figure 2.8 summarizes the gas temperature obtained with various methods, as a function of the electron number density and figure 2.9 shows the corresponding volumetric power required. Note that the graph of figure 2.8 is only for the non-equilibrium regimes, except for thermal plasmas which are shown for comparison. NRP sparks, MHCD (Micro-Hollow Cathode sustained Discharges), filamentary DBDs are not shown.

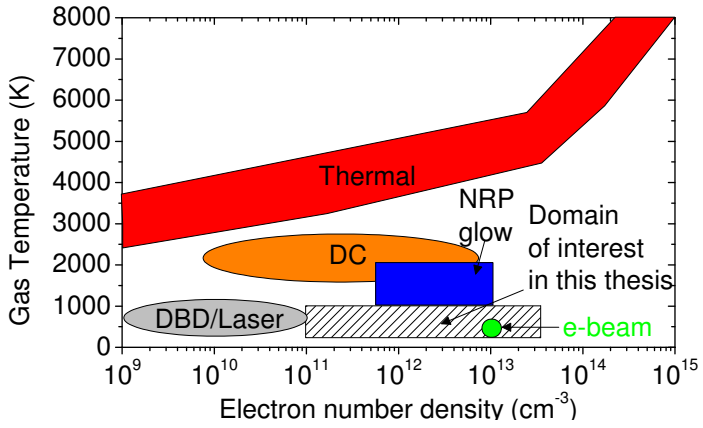

Figure 2.8: Gas temperature of plasmas experimentally generated by the methods mentioned in this section as a function of the average electron number density in air at atmospheric pressure. Figure adapted from [2].

Thermal plasmas create a high number density of electrons but the gas temperature associated is also high, thus preventing them from being useful for biodecontamination or surface treatment. DBD and laser plasmas are more suitable for temperature sensitive applications but the electron density is much lower (up to about 10^{11} cm^{-3}). DC plasmas are the most inefficient - more

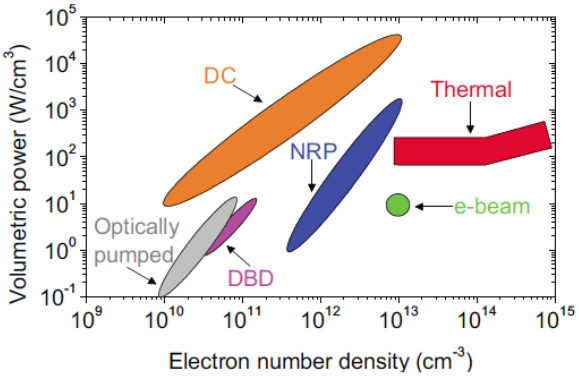

Figure 2.9: Power budgets of plasmas generated by the method mentioned in this section as a function of the average electron number density. Power budget concerns the energy deposited into the plasma, not the total input power of the generator. Figure taken from [2].

than 99 % of the power is lost to N_2 vibrational excitation. As discussed in the next section, NRP glow plasmas have been demonstrated to create relatively high electron number densities (10^{12} cm^{-3}) for one of the lowest power budgets. From figures 2.8 and 2.9, the NRP strategy appears as the most promising way to create a high electron number density with low power consumption at temperatures under 1000 K. Thus, one goal of the present work will be to extend the NRP glow plasma regime to ambient temperature in order to open the way for the use of air plasmas in the temperature-sensitive applications discussed in section 2.2.

2.4 Nanosecond Repetitively Pulsed (NRP) discharges

2.4.1 NRP discharge strategy

Figure 2.10 shows the NRP discharge strategy to generate atmospheric pressure air plasma. First, it is important to ionize efficiently in order to avoid the Glow-to-Arc transition: this leads to apply a very high electric field but stop it just before leading to the Glow-to-Arc transition (which would be the case in a DC discharge with the same electric field), see Figure 2.11. This permits to climb to a reduced electric field greater than 100 Td [1 Td = 10^{-17} V.cm^{-2}], to increase ionization efficiency.

Then, the repetition rate of the pulses is adjusted such that the inter-pulse duration is shorter than the recombination time of active species. The accumulation of various pulses will lead to a high average electron density. The number density of seed electrons before a new pulse will depend greatly on the recombination rate of the electrons during the interpulse. At 2000 K, recombi-

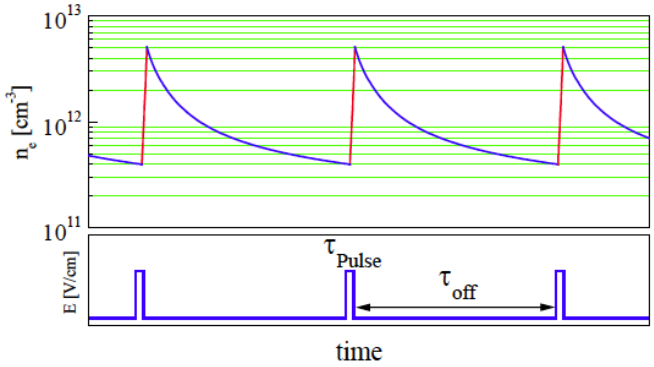

Figure 2.10: The NRP strategy for generating atmospheric pressure air plasma. Electron number density and electric field as function of time for several pulses. Figure taken from [4].

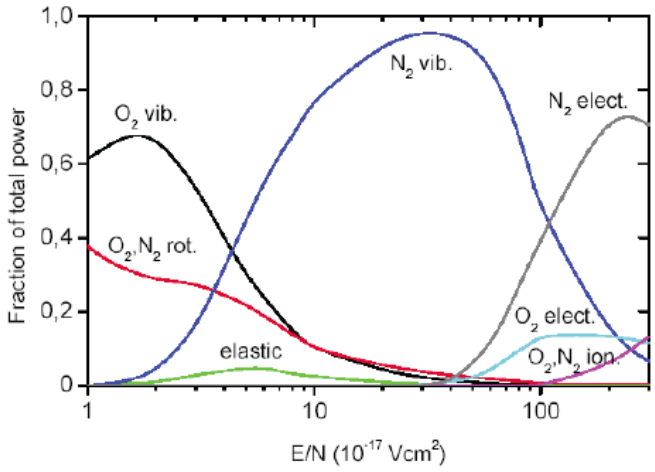

Figure 2.11: Fractions of power dissipated in different modes of excitation for N_2 and O_2 as function of the reduced electric field in Td (1Td = 10^{-17} V.cm^{-2}). Figure taken from [2], [32], and [33].

nation is mainly due to the dissociative recombination of electrons with NO^+ [4]: $NO^+ + e \rightarrow N+O$, whose rate is equal to $k_r = 10^{-7}$ cm^3/s. One can show that the target maximum electron density n_{e1}, the target minimum electron density n_{e0} and the recombination time τ_r are related according to [2],[4]:

$$n_{e0} = \frac{n_{e1}}{1 + k_r \tau_r n_{e1}} \tag{2.1}$$

which leads to a recombination time of 90 µs for $n_{e0} = 10^{11}$ cm^{-3} and $n_{e1} = 10^{12}$ cm^{-3}. Consequently, a PRF of 30-100 kHz was chosen to fulfill the condition previously given.

2.4.2 NRP spark and glow discharges in preheated air at 2000 K

In the early 2000s, the Stanford group [4], [34], and [35] proposed and demonstrated the NRP strategy as an effective way to reduce the power budget needed to obtain a high electron number density in air at atmospheric pressure without heating the gas (hence the term NRP glow discharge). The important parameter to choose is the duty cycle between the duration of the pulse and the time between pulses. In their work, using 10-ns pulses at Pulse Repetition Frequencies (PRF) from 10 to 100 kHz, they showed that a power budget reduction of 2-3 orders of magnitude was possible compared to DC discharges producing an equivalent electron number density of about 10^{12} cm^{-3} [35]. For reasons that will be explained later, all their experiments were performed in air preheated to 2000 K. Figure 2.12 compares the volumetric power needed to create given electron number densities with the two techniques, DC discharges and NRP discharges.

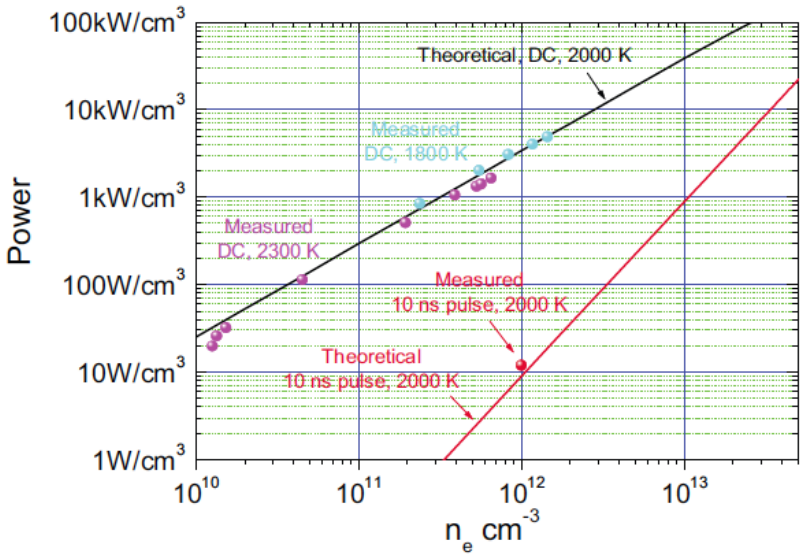

Figure 2.12: Measured and calculated power budget for DC and NRP plasma generation as function of the resulting electron number density. The NRP glow was obtained with a 10-ns, 10-kV, 100-kHz repetitive nanosecond pulse generator. The inter-electrode gap distance was about 1 cm and air was preheated to 2000 K. Figure taken from [34].

Figure 2.13 shows time-resolved images of the NRP glow discharge obtained. From these images, it is clear that the discharge produces a uniform plasma in the gap. Detailed characterization experiments presented in [2], [4], and [36] show that the plasma is non-thermal ($T_g \simeq 2000$ K $\ll T_e \simeq 5$ eV), that there exists a cathode fall region ($V_{cc} \simeq 2$ kV). These observations indicated that the discharge is of the glow type. In this early work, an NRP spark regime was also observed [4] at higher voltage, but this regime was not investigated because it

caused damage to the pulser.

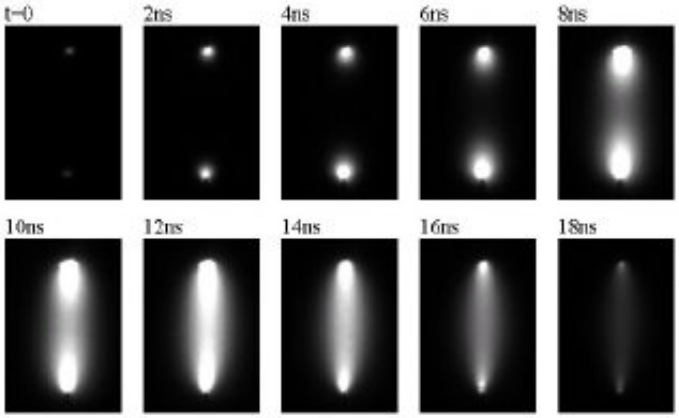

Figure 2.13: Time-resolved images of the NRP glow discharge as a function of time after the beginning of the high-voltage pulse. The inter-electrode gap distance is 1 cm. Figure taken from [4].

2.4.3 NRP spark and glow discharges in preheated air below 1000 K

Following this work, the Ecole Centrale Paris group [1], [2], [36], and [37] investigated the use of NRP discharges in air at atmospheric pressure, at lower temperatures: from 300 to 1000 K. They worked with 10-ns, up to 10-kV positive pulses, repeated from 1 to 30 kHz, applied to steel electrodes in a vertical pin-pin configuration. Under their experimental conditions, they observed two regimes (NRP corona and NRP spark) at temperatures between 300 and 700 K and three regimes (NRP corona, glow and spark) above 700 K. This can be seen on figure 2.28. Figure 2.14 shows images of the three types of NRP discharges. The three regimes are visually identical to their DC counterparts and come in the same order as DC discharges when increasing the voltage: NRP corona discharges, then glow discharge, and finally spark discharges. These three regimes are characterized by different levels of deposited energy, conduction current, and gas heating, as summarized in table 2.1.

Table 2.1: Classification of observed NRP discharge regimes. Table adapted from [1].

Appearance	*Energy deposited per pulse*	*Gas heating*	*Name*
Corona	<10 μJ	≈ 0	NRP corona
Diffuse	10-100 μJ	< 200 K	NRP glow
Filamentary	>100 μJ	2000-4000 K	NRP spark

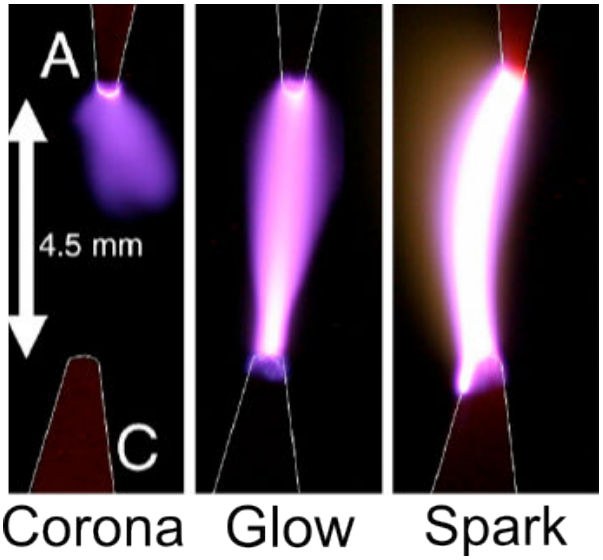

Figure 2.14: Images of the NRP corona, glow, and spark discharges in atmospheric pressure air at 1000 K with PRF = 10 kHz, a gap distance of 4.5 mm, and an air flowrate of 1 m/s. The electrodes are outlined in white. Figure taken from [2].

The NRP glow regime is particularly interesting because it does not heat the gas significantly, much like the corona discharge, yet it produces a significant amount of active species, with much higher energy deposited than in the corona regime. Thus this regime could be of great interest for the development of applications such as surface treatment or biomedical applications, as detailed in section 2.7. On the other hand, the NRP spark regime is also interesting for applications such as plasma assisted combustion. As a result, the properties of NRP glow and spark regimes were studied in depth by Pai *et al* in [1], [36], and [37], and the main results will be summarized in sections 2.5, 2.6, and 2.7.

2.4.4 Other recent methods to produce non-thermal plasmas using NRP discharges

For the sake of completeness, we mention in this section two recent developments using NRP discharges to produce plasmas in air.

NRP discharges with runaway electrons

Shao *et al* [38] studied an atmospheric pressure air discharge in a point-to-plane or point-to-point configuration, created by high voltage pulses of amplitude 12-140 kV and FWHM of 1-40 ns. They have shown that in a wide variety of experimental conditions, a diffuse discharge is ignited due to preionization of the gap by runaway electrons and X-rays. These runaway electrons are produced

near the electrode and in the gap, in response to electric field amplification. This type of NRP discharge clearly operates differently from the discharges studied by the Stanford and Ecole Centrale Paris groups, especially since they rely on runaway electrons and X-rays. We will not address these types of discharges in this thesis.

Multiple array needle-plane configuration

Yang *et al* [39] studied atmospheric pressure air discharges created between multiple array needle electrodes and a plane. The discharges are created with 20 ns rising time up to 24 kV high pulse voltage repeated at a frequency of 150 Hz. They obtained a diffuse discharge plasma with low gas temperature and the plasma volume increases with the increase of the pulse peak voltage, but remains almost constant with the increase of the pulse repetition rate. This kind of diffuse discharge is the type we wish to investigate in this thesis.

2.5 Comparison of the NRP glow and spark regimes

In order to present the main properties of the NRP glow and spark discharges, we have chosen to compare the behaviors of these two regimes in terms of voltage and current measured within the discharge in section 2.5.1, energy deposited into the plasma in section 2.5.2, discharge dynamics in section 2.5.3, and finally gas temperature evolution in section 2.5.4. The results presented in this section were obtained by the Ecole Centrale Paris group [36],[37].

2.5.1 Electrical characteristics

The first different feature of NRP glow and spark discharges are their electrical characteristics. Figure 2.15 shows the typical voltages and currents measured across the electrodes for an NRP glow discharge and an NRP spark discharge.

For an NRP spark discharge, the displacement current is calculated as the current into a capacitor which is subject to the applied voltage. The conduction current is obtained by subtracting the displacement current from the total current. We note that for an NRP spark discharge, the total and displacement currents are rather different: the conduction current is high with a peak at 35 A. This increase of the conduction current corresponds to a steep decrease of the resistance of the plasma. Thus, the voltage pulse shape is distorted, see figure 2.15 (b) top. The details of the determination of the displacement and conduction currents of a typical NRP Spark discharge will be given in section 4.3.

Unlike the NRP spark discharge, for an NRP glow discharge the conduction current is very low, see figure 2.15 (a) bottom, close to the noise current. The

total current is indeed mostly a displacement current. In the case of an NRP glow discharge, the conduction current is found by subtracting the measured total current without plasma from the measured total current with plasma, see section C.2.

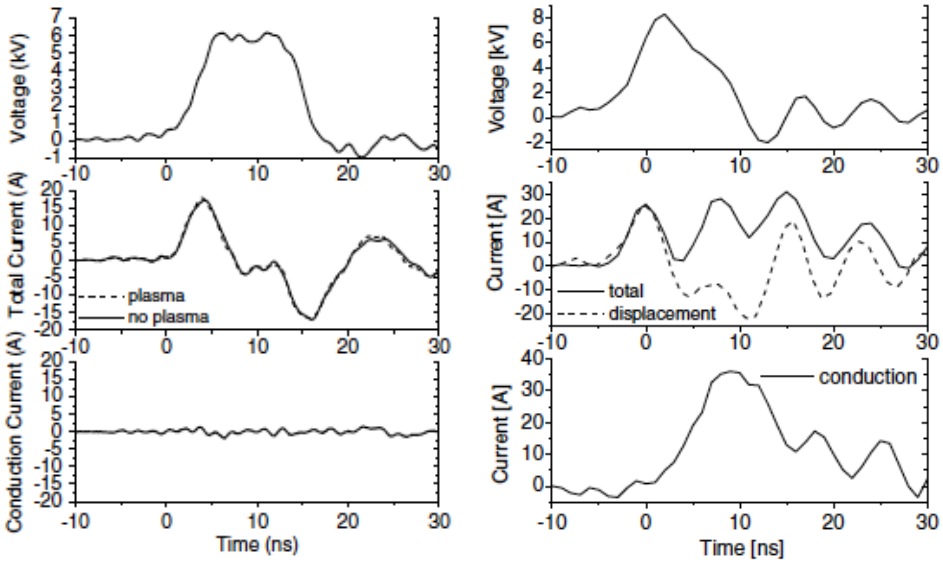

(a) NRP glow **(b)** NRP spark

Figure 2.15: Measured voltage, total current, calculated displacement current and inferred conduction current as a function of time for a typical NRP (a) glow and (b) V_p = 8.3 kV spark discharge.
T_g = 1000 K, d = 5 mm, PRF = 30 kHz and v = 2 m.s^{-1}.

Finally, from the current and voltage measurements of an NRP spark discharge, Pai *et al* [37] deduced the electron number density as a function of time, which can be seen on figure 2.16. The lowest value of the electron number density is about 10^{13} cm^{-3} and the maximum value about 3 $\times 10^{15}$ cm^{-3}.

2.5.2 Energy deposited

From the electrical measurements presented above, it is possible to calculate the energy deposited into the plasma for the two regimes of discharges. For an NRP glow discharge, it is found to be about 10-100 µJ and for an NRP spark discharge, from 150 µJ to 1500 µJ. A more detailed explanation of the method to determine the energy of an NRP spark discharge is given in section 4.3 and for an NRP glow discharge in section C.2. The method to determine the energy is slightly different because the conduction currents at stake are much more important in the case of an NRP spark discharge than in a glow discharge, thus we need to subtract the parasitic losses in the case of a glow discharge.

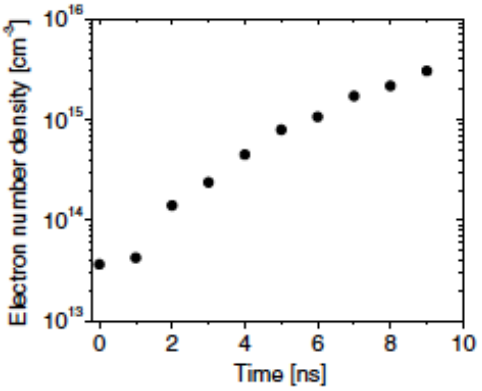

Figure 2.16: Electron number density as a function of time for a typical NRP spark discharge.
T_g = 1000 K, d = 5 mm, V_p = 8.3 kV, PRF = 30 kHz, and v = 2 m.s^{-1}. Figure taken from [37].

Figure 2.17 presents the energy deposited into the plasma as a function of the applied voltage. We clearly see a steep change of slope which corresponds to the transition between the NRP glow and spark regimes.

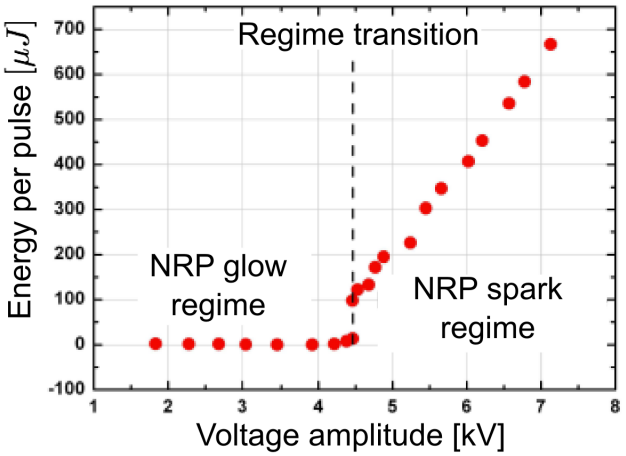

Figure 2.17: Energy deposited per pulse as a function of the voltage amplitude. PRF = 30 kHz, in a propane-air flame of equivalence ratio = 0.8. Figure taken from [40].

2.5.3 Discharge dynamics

Another different behavior is the dynamics of the NRP glow and spark discharges. Figure 2.18 shows the measured emission intensity of N_2(C-B) (0,0) at 337 nm and N_2^+(B-X) (0,0) at 391 nm along the inter-electrode axis of the

NRP glow and NRP spark discharges. For both discharges, time $t = 10$ ns corresponds to the beginning of the high voltage pulse.

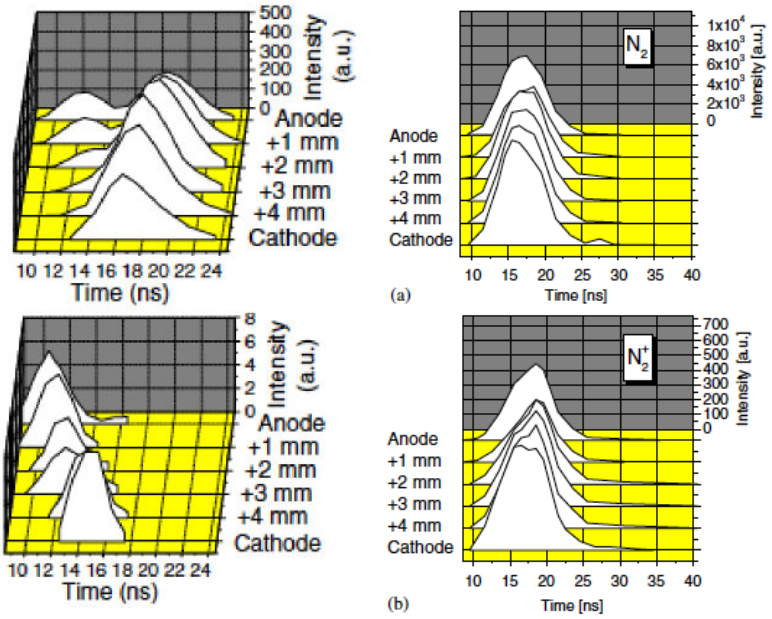

(a) NRP glow **(b)** NRP spark

Figure 2.18: Measured emission intensity of (a) N_2(C-B) (0,0) and (b) N_2^+(B-X) (0,0), along the inter-electrode axis of the NRP (a) $V_p = 6.7$ kV glow and (b) $V_p = 8.3$ kV spark discharge.
$T_g = 1000$ K, $d = 5$ mm, $PRF = 30$ kHz and $v = 2$ m.s^{-1}.

The characteristics are quite different for the NRP regimes. The glow-like regime develops through an initial cathode-directed streamer, followed by a return wave of potential redistribution. The applied electric field is then switched off before the formation of the cathode fall, resulting in an "imminent" glow discharge. We clearly see on the N_2(C-B) (0,0) emission intensity these two distinct phases. These two phases are not seen on the emission traces of N_2^+(B-X) (0,0) because the N_2^+(B-X) (0,0) band at 391 nm is covered by the bands of N_2(C-B) around 380 nm.

The dynamics of the NRP spark discharge are different: both the N_2(C) and N_2^+(B) states emit uniformly across the gap, which is characteristic of a streamerless discharge. The Ecole Centrale Paris group showed that this discharge corresponds to an avalanche ionization in volume [37].

Furthermore, the global intensity of the two regimes are quite different. The intensity of an NRP glow discharge is about 10 times smaller for N_2(C-B) (0,0)

and 100 times smaller for N_2^+(B-X) (0,0) than the intensity of an NRP spark discharge.

2.5.4 Temperature evolution

The last important difference between NRP glow and spark discharges is the temporal evolution of the gas temperature during and after the discharge. In previous work, we performed time-resolved rotational temperature measurements of N_2(C) with a monochromator and ICCD camera system at mid-gap within NRP glow and spark discharges. Pai *et al* deduced the temperature of the gas from the rotational temperature of N_2(C), which is assumed to be equal to the temperature of the gas. This assumption will be discussed in more details in section 4.4.1.2. The rotational temperature of N_2(C) was obtained from the experimental spectra of the (0,0) band. A typical measured spectrum is compared to a spectrum computed with Specair [41], [42] on Figure 2.19 for NRP glow and spark discharges. The NRP spark discharge studied was just above the Glow-to-Spark transition for two different times: t = 7 and 15 ns, and the measurements were obtained with a 2-ns gate width.

The conclusions are different for the two regimes. For an NRP glow discharge with two different applied voltages, V_p = 5.8 and 6.4 kV, the temperature of the gas does not exceed 1200 K for an initial temperature of the gas of 1000 K. The NRP glow discharge does not produce any noticeable gas heating. For the spark discharge studied, we see that the rotational temperature is about 1800-2000K at t = 7 ns which corresponds to the initial stage of NRP spark formation. Then, the rotational temperature increases very rapidly, by 500 K within 8 ns [2], [37]. Unlike the NRP glow discharge, the NRP spark discharge greatly increases the gas temperature T_g.

Figure 2.20 presents the temporal evolution for t = 7-40 ns of the gas temperature. The measurements were made for two different applied voltages V_p = 6.5 and 8.3 kV. In both cases, the temperature increases from 1450-1700 K to more than 3000 K within 20 ns. The time profile of N_2(C-B) (0,0) emission intensity was also added to show that the time of the peak emission occurs before that of the peak temperature for the NRP Spark regime. The explanation we proposed for this ultrafast heating and its applications will be detailed in section 2.6.1. Pai [2] and Pai *et al* [37] also showed that self-absorption was a minor effect for all the experimental spectra used to measure the rotational temperature of N_2(C).

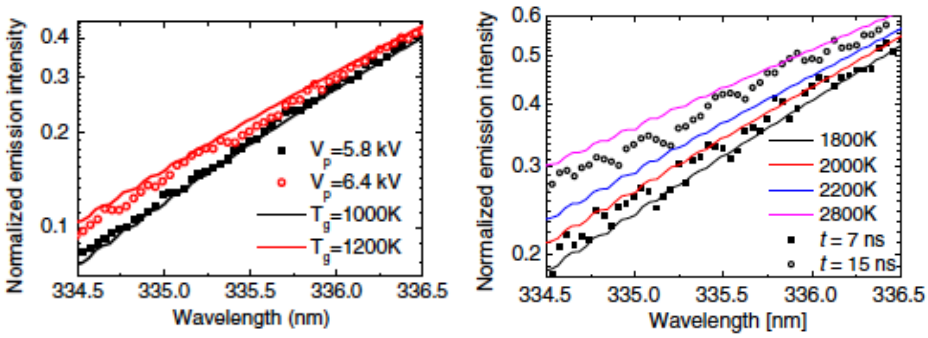

(a) NRP glow **(b)** NRP spark

Figure 2.19: Measured N_2(C-B) (0,0) spectra (symbols) and modeled spectra computed with SPECAIR (lines) of the NRP (a) glow and (b) V_p = 8.3 kV spark discharges. The NRP glow spectra are measured 15 ns after the beginning of the pulse, when the intensity reaches a maximum for two different applied voltages. The NRP spark spectra are measured 7 and 15 ns after the beginning of the pulse. All experimental spectra were measured using a 2-ns gate.
T_g = 1000 K, d = 5 mm, PRF = 30 kHz and v = 2 m.s^{-1}.

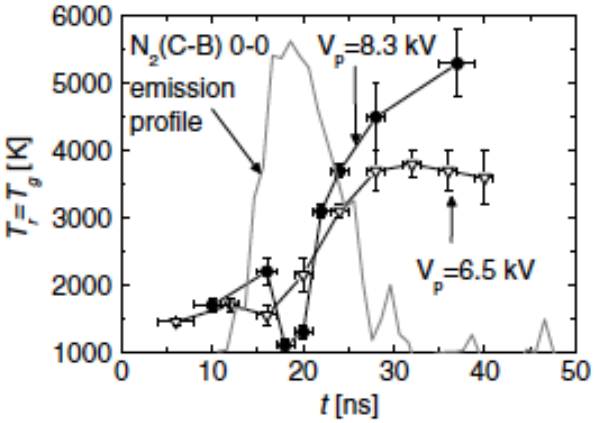

Figure 2.20: Measured gas temperatures at V_p = 6.5 and 8.3 kV (symbols) and time profile for N_2(C-B) (0,0) emission intensity (solid line) for an NRP spark discharge. T_g = 1000 K, d = 5 mm, PRF = 30 kHz and v = 2 m.s^{-1}. Figure taken from [37].

2.6 NRP spark properties and applications

2.6.1 Ultrafast heating through a two-step mechanism during NRP spark discharges

As mentioned in the previous section, ultrafast heating of severals hundreds of Kelvins was detected by Pai *et al* [37] during and after the application of a high voltage pulse creating an NRP spark discharge.

In order to explain this phenomenon, a two-step mechanism was considered, which was first proposed by Popov in 2001 [5]:

$$N_2(X) + e^- \rightarrow N_2(A,B,C) + e^- \quad (2.2)$$

$$N_2(A,B,C) + O_2 \rightarrow N_2(X) + 2O + \text{heat} \quad (2.3)$$

According to this mechanism, the electronically excited molecular nitrogen formed by electron-impact excitation during the pulse dissociates molecular oxygen, thus generating atomic oxygen and heat. This simultaneous ultrafast heating and high concentration of atomic oxygen may have several applications: oxide film deposition [43], aerodynamic flow control, gas treatment, nanomaterial fabrication [44], [45], or plasma assisted combustion [23], [46], and [47]. It is well known [22] that one of the possibilities to reduce nitric oxides in flames consists in using lean premixed combustion systems. However, these systems tend to be unstable at low fuel equivalence ratios. To solve these problems, it was shown [23] that lean premixed flames may be stabilized by a local addition of energy with NRP spark discharges that produce a local increase in heat and active species concentrations.

To validate this mechanism, Stancu *et al* studied the time-evolution of several key species in this mechanism. They implemented Cavity Ring-Down Spectroscopy (CRDS) to measure the density of $N_2(A)$ [6], [48], and time-resolved Two-photon Absorption Laser Induced Fluorescence (TALIF) to measure the evolution of ground state oxygen density [6],[49]. Then, they measured the density of $N_2(B)$ and $N_2(C)$ by Optical Emission Spectroscopy (OES), and used the second positive system of N_2 to infer the temperature of the gas [6], [50].

Figure 2.21 from [49] presents the temporal evolution of the number density of the excited states of N_2 and the atomic oxygen density. The high voltage pulse was also added and, as already mentioned in section 2.6.1, the increase of atomic oxygen starts after the end of the high-voltage pulse. Thus the increase of the number density of O cannot be totally assigned to the dissociation of O_2 by electron impact. Assuming atomic oxygen is mainly produced by Equation (2.3), O number density can be computed using the number densities of $N_2(B)$ and $N_2(C)$ determined experimentally. There is a good agreement between the computed and measured atomic oxygen number density, thus validating the two-step mechanism proposed. However, as will be explained in section 3.5 the

determination of the gas temperature from the spectra of N_2(C-B) must be confirmed, and this is the goal of chapter 4.

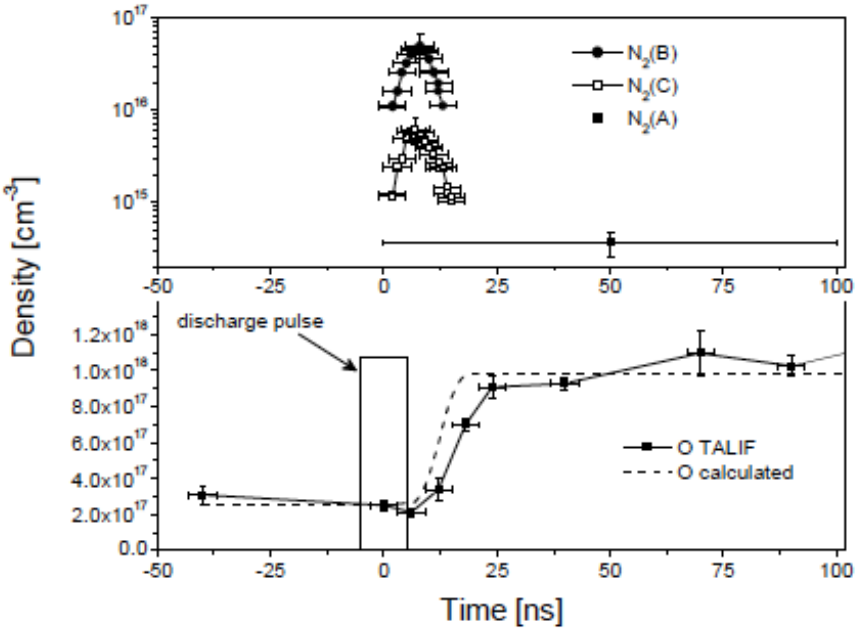

Figure 2.21: Temporal evolution of the densities of N_2(B) and N_2(C) (measured by OES) and O measured by TALIF for an NRP spark discharge. The number density value obtained for N_2(A) is integrated over 100 ns. T_g = 1000 K, d = 4 mm, PRF = 10 kHz, and v = 1.6 m.s^{-1}. Figure taken from [49].

2.6.2 Existence of shock wave during NRP spark discharges

Such an important ultrafast heating as the one highlighted in section 2.6.1 should induce shock waves. Indeed the timescale for reaching pressure equilibrium is about 100 ns for a discharge with a diameter on the order of 100 µm, in air that is initially at $T_g \approx 2000$ K for which the speed of sound is on the order of 1000 m/s. An audible noise is produced by NRP spark discharges. To confirm the production of these shock waves, Xu *et al* [51] led an experimental study of the hydrodynamic expansion following an NRP spark discharge in atmospheric pressure air preheated up to 1000 K. Figure 2.22 shows images, starting from 50 ns after the discharge, of the shock-wave propagation and the expansion of the heated gas channel.

Case 3 corresponds to the similar experimental parameters as in [49]. The images in Case 3 are less contrasted that in Case 1 because of the greater initial temperature of the gas, hence lower gas density. The temporal evolution

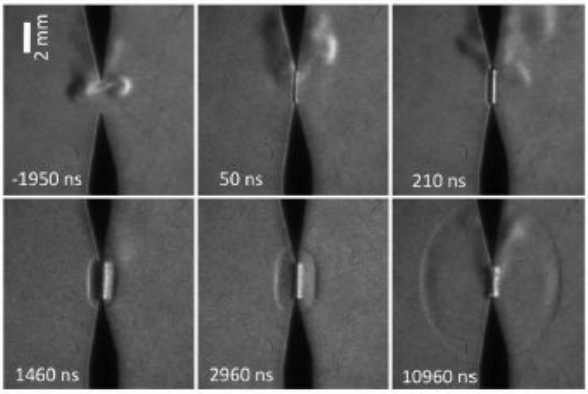

(a) Case 1: $T_g = 300$ K, $d = 2$ mm, $PRF = 1$ kHz and $v \approx 1.6$ m.s^{-1}

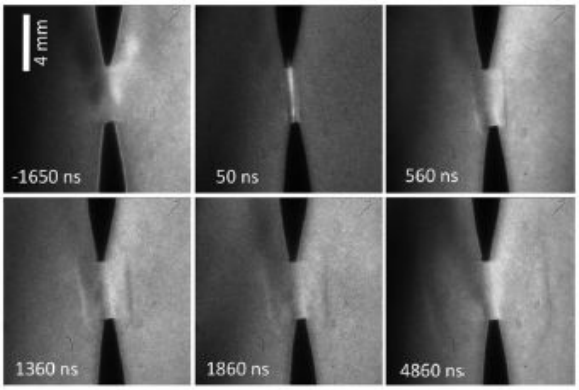

(b) Case 3: $T_g = 1000$ K, $d = 4$ mm, $PRF = 10$ kHz and $v \approx 1.6$ m.s^{-1}

Figure 2.22: Examples of single-shot successive Schlieren images of NRP spark discharges. The exposure time is 20 ns. Time after discharge initiation is written on each image. The minus sign indicates a time before the discharge. Images taken from [51].

of the gas temperature behind the shock-front is estimated from the measured shock-wave velocity by using the Rankine-Hugoniot relationships. Figure 2.23 presents the temporal evolution of the temperature behind the shock-wave. We notice a temperature increase up to 1100 K, 50 ns after the nanosecond pulse. This result confirms the ultrafast heating mechanism of NRP discharges proposed.

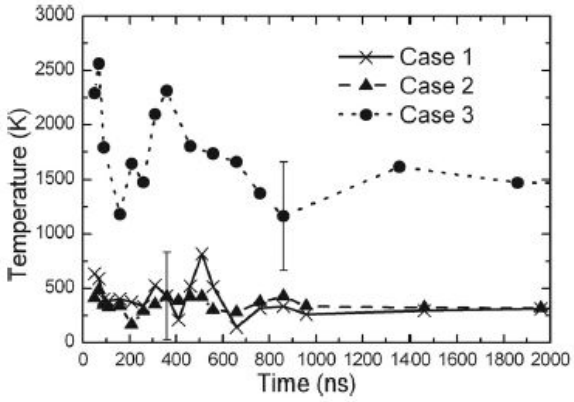

Figure 2.23: Temporal evolution of the temperature behind the shock wave. Figure taken from [51].

2.7 NRP glow properties and applications

Pai *et al* investigated through absolute Optical Emission Spectroscopy the number density of several excited species during and after an NRP glow discharge. Figure 2.24 presents the number density of $N_2(C)$, $N_2(B)$, $N_2^+(B)$, NO(A) and O(3p ^{5}P) measured at mid-gap for a typical NRP glow discharge [36].

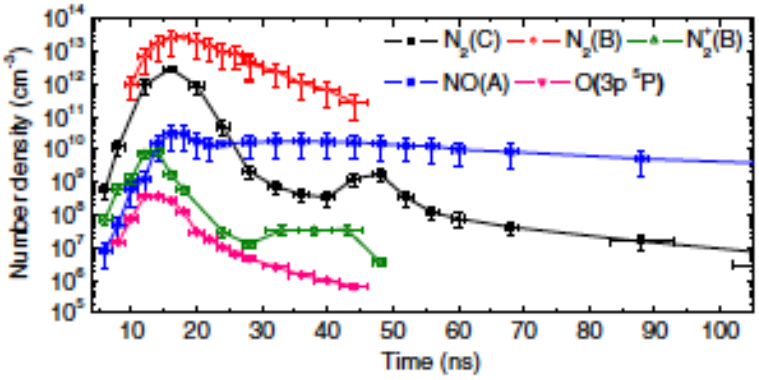

Figure 2.24: Number density of excited species measured at mid gap for a typical NRP Glow discharge.
T_g = 1000 K, d = 5 mm, V_p = 6.7 kV, PRF = 30 kHz, and v = 2 m.s^{-1}. Figure taken from [36].

Stancu *et al* [6] also measured the atomic oxygen production. They showed that the atomic oxygen produced by an NRP glow discharge just below the glow-to-spark transition was about one order of magnitude less than in an NRP spark discharge, but still about 1×10^{17} cm^{-3}.

The advantage of the NRP glow discharges is that they can create relatively large volume, low power, high chemical reactivity and do not increase the temperature of the gas. Thus, NRP glow discharges have a great potential in applications which are sensitive to temperature as detailed in section 2.2 and which need an important number density of atomic oxygen such as *in vivo* medical treatment [52], biodecontamination [11],[53], or surface treatment [29], [54].

2.8 Domains of existence of NRP discharges in atmospheric pressure air for the pin-pin configuration

In this section, we summarize the findings of Pai [2] about the influence of three parameters, namely the Pulse Repetition Frequency PRF, gas temperature T_g, and inter-electrode gap distance d on the discharge regimes. The experimental method used by Pai *et al* is the following: for each parameter studied, the operator watched carefully the discharge and registered the Corona-Glow (C-G) transition voltage and the Glow-Spark (G-S) transition voltage while increasing the voltage from 0 V. The corona regime begins when light is emitted at the anode, and the glow regime when the emission zone extends over the entire gap. The spark discharge is easy to detect because there is a sudden increase of the luminosity of the discharge and a crackling sound becomes clearly audible. All transition voltages were assembled into a "map" of the discharge regimes as a function of the variable parameter (PRF, T_g or d). $\boldsymbol{N}$ represents the "No discharge" domain, $\boldsymbol{C}$ the Corona discharge domain, $\boldsymbol{G}$ the glow discharge domain and finally $\boldsymbol{S}$ the Spark discharge domain.

2.8.1 Influence of PRF on discharge regimes

Figure 2.25 presents the discharge regime map as a function of PRF as investigated by Pai *et al* in [1] and [2] for a fixed gas temperature of $T_g = 1000$ K. The regimes do not depend much on the PRF except that the spark regime is obtained at a lower applied voltage when the PRF increases. We will see later that it can be explained by an increase of the gas temperature T_g with PRF. Pai *et al* also investigated the N_2(C-B) (0,0) emission of the discharge at 337 nm with a Photo Multiplier Tube (PMT) and appropriate filter. Figure 2.26 shows the peak emission intensity of the glow and spark regimes as a function of the applied voltage V_p at mid-gap for PRF from 1 to 30 kHz. The G-S transition occurs fairly smoothly at low PRF, but becomes much more abrupt at high PRF (intensity jumps of about a factor 10 at 30 kHz).

We also note that it is possible to obtain low PRF glow discharges that emit more than high PRF spark discharges. The emission intensity of the glow regime is much more sensitive to the applied voltage V_p than to the PRF. For

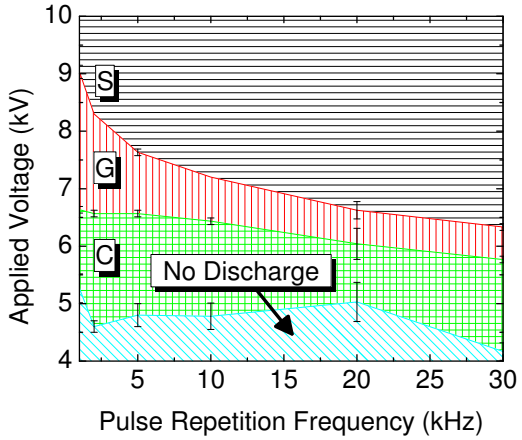

Figure 2.25: Discharge regime map - applied voltage V_p vs PRF. T_g = 1000 K, d = 5 mm, and v = 1.6 m.s^{-1}. Figure taken from [2].

NRP spark discharges, the emitted intensity is almost independent of the PRF.

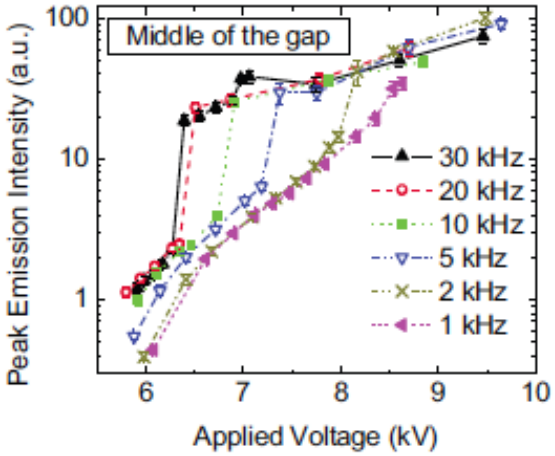

Figure 2.26: Measured N_2(C-B) (0,0) emission intensity peaks in the middle of the discharge gap as a function of V_p for PRF = 1-30 kHz with T_g = 1000 K, d = 5 mm, and v = 1.6 m.s^{-1}.

Finally, Pai *et al* investigated the energy of the discharges as a function of the PRF. The method to determine the energy deposited into an NRP spark discharge will be described in section 4.3. Figure 2.27 shows the measured energy per pulse for glow (hollow) and spark (solid) regimes as a function of the applied voltage V_p for PRF = 1-30 kHz, T_g = 1000 K, d = 5 mm, and v = 1.6 m.s^{-1}. The G-S transition corresponds to a high jump in energy. The

energy deposited per pulse into the plasma is equal to 50 µJ for the glow regime and more than 200 µJ for the spark regime. An interesting feature is that the energy curve for the spark regime shifts upwards when the PRF increases. The shift is also observed for NRP glow discharges, even though the tendency is not as obvious because of the smaller energy at stake. These effects are likely due to gas heating effects at high PRF that increase the conductivity of the plasma column, hence the energy deposited in the plasma.

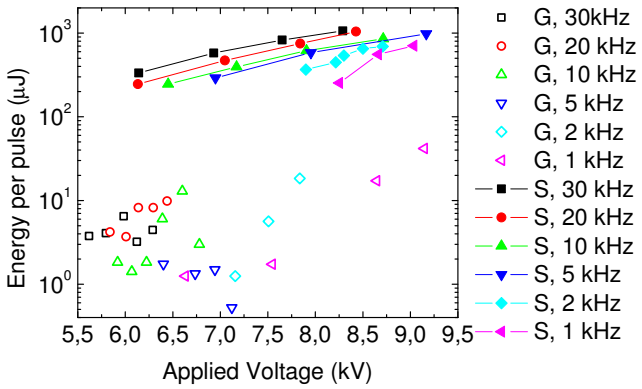

Figure 2.27: Measured energy per pulse for the NRP glow (hollow) and spark (solid) regimes as a function of the applied voltage V_p for PRF = 1-30 kHz with T_g = 1000 K, d = 5 mm, and v = 1.6 m.s^{-1}.

2.8.2 Influence of gas temperature T_g on discharge regimes

Figure 2.28 presents the discharge regime map as function of the gas temperature T_g, with fixed $PRF = 30$ kHz, $d = 5$ mm, and $v = 1.6$ m.s^{-1}, as investigated by Pai *et al* in [1],[2]. There, the regime domains strongly depends on the gas temperature. The NRP glow regime only exists for $T_g > 700$ K and its domain of existence expands with increasing gas temperature. For 300 K$< T_g <$700 K, only the corona and spark regime are observed. The explanation for these domains of existence will be detailed in section 2.9.

Figure 2.29 presents the peak N_2(C-B) (0,0) emission intensity of the glow and spark regimes as a function of the applied voltage at mid-gap for different temperatures $300 < T_g < 1000$ K. We see a jump in emission corresponding to the G-S transition, always of about a factor 10. Finally, figure 2.30 presents the energy deposited per pulse for glow and spark discharges as a function of the gas temperature T_g. The G-S transition corresponds to an important jump in energy which grows with increasing T_g. For a given applied voltage, the energy increases with the gas temperature.

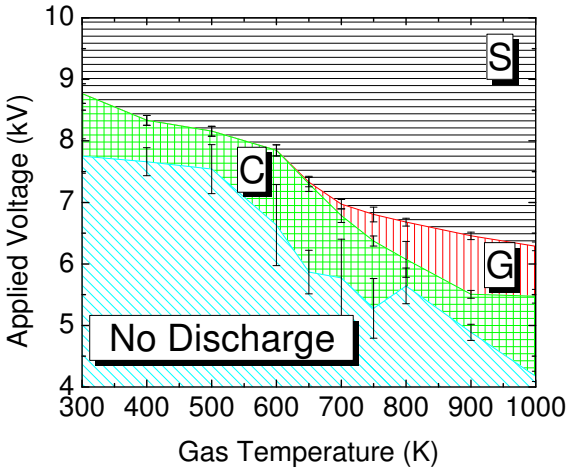

Figure 2.28: Discharge regime map - applied voltage V_p vs gas temperature T_g, with PRF = 30 kHz, d = 5 mm, and v = 1.6 m.s^{-1}.

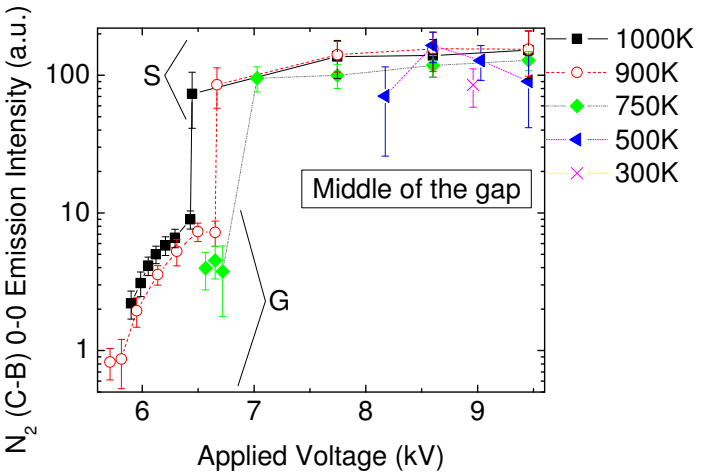

Figure 2.29: Measured N_2(C-B) (0,0) emission intensity peaks in the middle of the discharge gap as a function of V_p for T_g = 300 – 1000 K. d = 5 mm, PRF = 30 kHz, and v = 1.6 m.s^{-1}. Figure taken from [2].

2.8.3 Influence of inter-electrode gap distance d on discharge regimes

Figure 2.31 presents the discharge regime map as a function of the inter-electrode gap distance d, with fixed T_g = 1000 K, PRF = 30 kHz, and v = 1.6 m.s^{-1}, from Pai *et al* ([1] and [2]). Under the critical gap distance d = 3 mm, only the NRP spark regime exists. Thus, figure 2.31 shows the very surprising result that NRP glow discharges cannot exist below a minimum gap distance. This result will be discussed in section 2.9. Figure 2.31 also

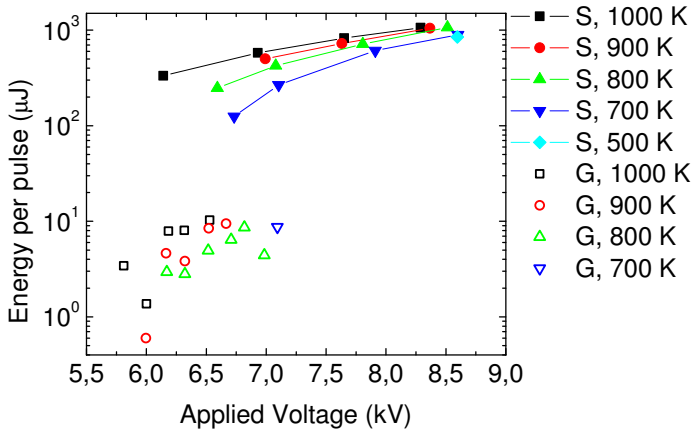

Figure 2.30: Measured energy per pulse for the glow (hollow) and spark (solid) regimes as a function of applied voltage V_p for T_g = 300-1000 K. d = 5 mm, PRF = 30 kHz, and v = 1.6 m.s^{-1}.

shows that there is a maximum gap distance for the existence of the NRP glow discharge. This maximum is determined by the velocity of propagation of a streamer across the gap.

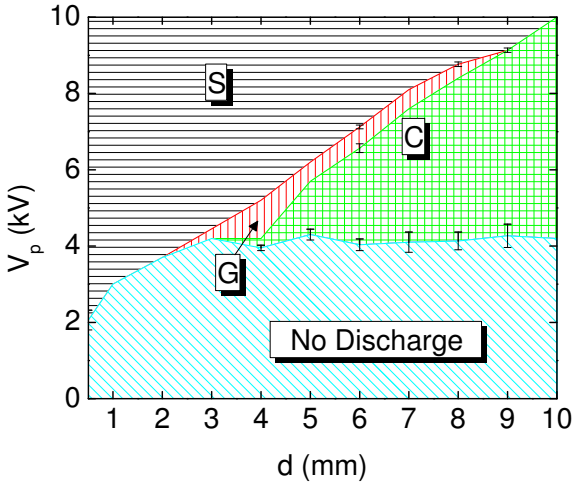

Figure 2.31: Discharge regime map - applied voltage V_p vs inter-electrode gap distance d. T_g = 1000 K, PRF = 30 kHz, and v = 1.6 m.s^{-1}.

Pai *et al* investigated for each gas temperature the minimum and maximum distances for the existence of the NRP glow regime. For instance, at T_g = 1000 K, we can deduce from figure 2.31 that the minimum distance for the existence of the glow regime is 2 mm. Figure 2.32 shows the minimum and maximum distances for a stable NRP glow discharge as a function of the temperature of the gas T_g. It can be seen that the domain of existence of a stable NRP glow

discharge shrinks with decreasing gas temperature. This will be explained in details in section 2.9.

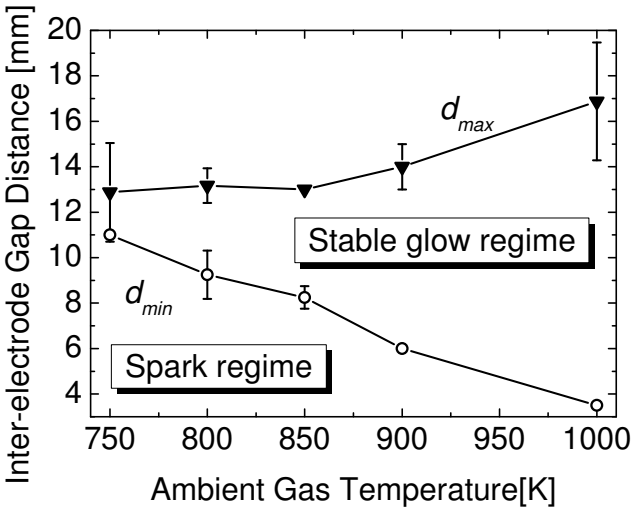

Figure 2.32: Measured range of gap distances that permit stable operation of the NRP glow regime as a function of the gas temperature. PRF **= 30 kHz, and** $v =$ 1.8 m.s^{-1}**. Images taken from [1].**

2.9 Model of the coupled influence of R and T_g on the existence of the glow regime

In section 2.7, we have presented the interest of the glow regime. Pai [2] obtained the glow regime at temperatures from 700 K to 1000 K, see section 2.7 and 2.8. In this section, we detail the model proposed by Pai *et al* [1] which predicts the existence of the glow regime at room temperature at the condition of using electrodes of small radius of curvature, long voltage pulses, and large inter-electrode gap distances.

2.9.1 Laplacian electric field generated by electrodes in a pin-pin configuration

This section presents the influence of the radius of curvature of the electrode tip R and the inter-electrode gap distance d on the Laplacian electric field generated by electrodes in a pin-pin configuration. The electrodes were modeled as two infinite hyperboloid surfaces, as can be seen on figure 2.33. It is a usual assumption because there is an exact solution of the Laplace equation for a potential created in such a geometry. The anode has potential $V = V_p$ and the cathode potential is $V = 0$.

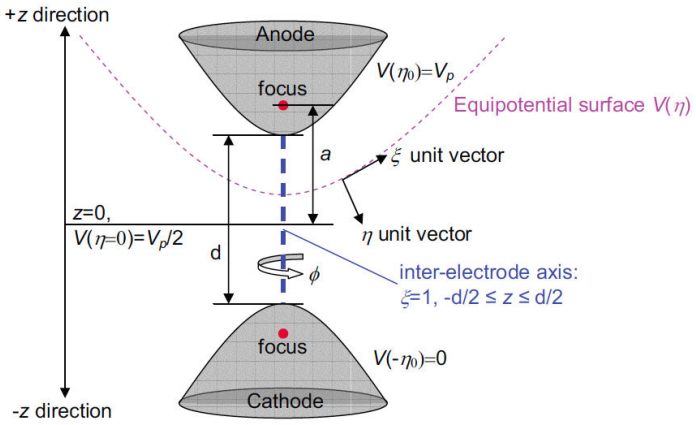

Figure 2.33: Model of the pin-pin electrode configuration of the experiments studied in this thesis, represented by two-sheet hyperboloid and using prolate spheroidal coordinates. Figure taken from [1].

The solution is found using the prolate spheroidal coordinates, and is detailed in [2]. A necessary assumption is to consider the electrodes as infinite hyperboloid surfaces and to place the boundary $V = 0$ infinitely far away, or at least to consider that the gap distance d is small in comparison with the distance between the electrodes and the other conducting surfaces of the experiments. In this case, the axial Laplacian electric field on the inter-electrode axis is nearly symmetric and is equal to:

$$E_L(z) \approx -\frac{V_p}{\ln\dfrac{1+\eta_0}{1-\eta_0}}\frac{a}{a^2-z^2} \tag{2.4}$$

where V_p is the potential of the anode, the cathode is at zero potential, a is the foci distance,

$$a = \left(\frac{d}{2}\left(\frac{d}{2}+R\right)\right)^{1/2}, \tag{2.5}$$

and η_0 represents the equipotential surface of the electrodes:

$$\eta_0 = \left(\frac{d/2}{d/2+R}\right)^{1/2}. \tag{2.6}$$

More information on the model of the potential and electric field created by these electrodes can be found in chapter 6 of Reference [2].

Figure 2.34 shows the Laplacian electric field on the inter-electrode axis $E_L(z)$ calculated for several radii of curvature of the electrodes, which will be experimentally used in chapters 5 and 6. $E_L(z)$ was calculated using Equation (2.4), with an applied voltage $V_p = 10$ kV, and an inter-electrode gap distance

$d = 5$ mm. In the case of a large radius of curvature $R \gg d$, the Laplacian electric field is almost identical to the one between parallel plates:

$$E_L(z) = \frac{V_p}{d} \;=\; 20 \;\; \text{kV/cm}. \tag{2.7}$$

When R decreases, the field enhancement is increased at the electrode tip and becomes progressively more non-uniform. For $R = 20$ µm, the field at the tip is equal to 807 kV/cm compared to 6 kV/cm at mid-gap, which corresponds to a ratio of 134, whereas for $R = 500$ µm, the field at the tip is equal to 71 kV/cm compared to 12 kV/cm at mid-gap, which corresponds to a ratio of 6. The field in the middle of the gap, $z = 0$, decreases slightly, but the effect is much less pronounced. When increasing the radius of curvature from $R = 20$ µm to $R = 500$ µm, the field is divided by 11 at the electrode tip and is only doubled at mid-gap.

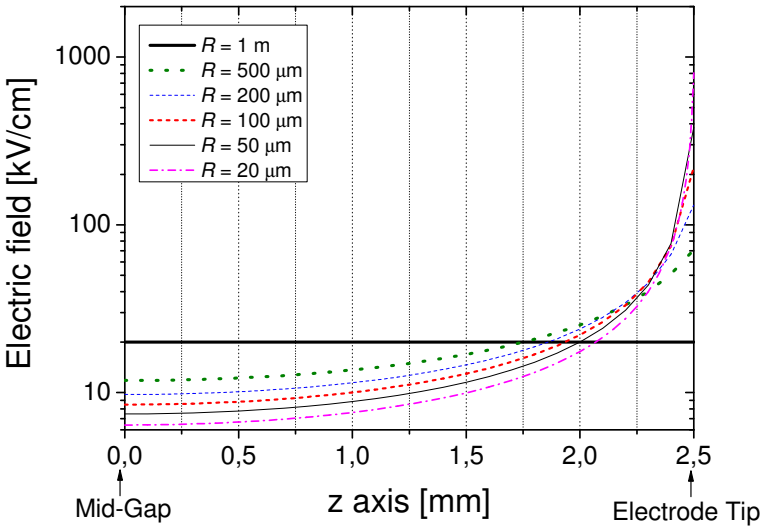

Figure 2.34: Laplacian electric field along the inter-electrode axis with $d = 5$ mm and $V_p = 10$ kV, for several values of the radius of curvature of the electrode tip R. The field is symmetric about $z = 0$.

Figure 2.35 shows $E_L(z)$ calculated for inter-electrode gap distances d using Equation (2.4), with an applied voltage $V_p = 10$ kV, and a radius of curvature of the electrode tip $R = 50$ µm. The distance in the z direction has been normalized by $d/2$ to show how the field non-uniformity varies with d. We notice that the field at mid-gap increases by more than one order of magnitude when d is increased from 2 mm to 15 mm whereas the value at the tip electrode is only multiplied by a factor 1.5. Thus, changing the inter-electrode gap distance has mainly an effect on the mid-gap electric field.

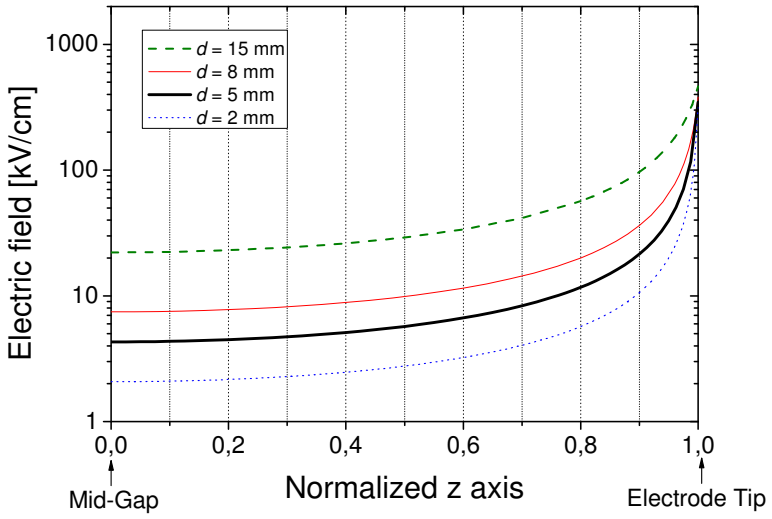

Figure 2.35: Laplacian electric field on the normalized inter-electrode z axis with $R = 50$ µm and $V_p = 10$ kV, for several values of the inter-electrode gap distance d. The field is symmetric about $z = 0$.

The radius of curvature of the electrode tip R has the strongest influence on the electric field near the tip, whereas the gap distance d has the strongest influence on the electric field in the middle of the gap. Thus, for a given applied voltage V_p, by choosing the gap distance and radius of curvature of the electrode, we can tailor the Laplacian electric field profile and, therefore should be able to control the Glow-to-Spark transition. This is the purpose of the next section.

2.9.2 Theory of regime transitions of NRP discharges

This section summarizes the model developed in [1] and recalls its main principles. The dynamics of the glow regime can be divided into three phases. First, an initial cathode-directed streamer - also called positive streamer - creates a conducting channel in the gap. Then, a return wave of potential redistribution leaves the cathode. The structure of the plasma channel is then similar to that of a typical DC glow discharge: most of the gap is occupied by a positive column, and a space charge layer - the streamer head - is situated at the cathode. A conduction phase during which current is driven through the discharge channel constitutes the final phase. It was shown in [1] that the Corona-to-Glow (C-G) and Glow-to-Spark (G-S) transitions can be well described by the theories of simple dielectric breakdown, the AST - Avalanche to Streamer Transition, and the thermal ionization instability.

The NRP C-G transition

Streamer phase - AST The Avalanche-to-Streamer Transition (AST) occurs when the space charge field generated by an electron avalanche becomes comparable with the Laplacian field. The space charge field E_{SC} generated by an electric dipole formed by two spheres with charges $+Q$ and $-Q$, separated by a distance α^{-1}, is given by [55]:

$$E_{SC} = \frac{2eQ\alpha^2}{9\pi\epsilon_0} \equiv K\alpha^2 \tag{2.8}$$

where e is the charge of an electron, Q is the number of charges required for the AST (also known as the ionization integral), ϵ_0 is the permittivity of free space, and α is the first Townsend or ionization coefficient. When a uniform external field E_{unif} is applied, the AST occurs when $E_{SC} = E_{unif}$. In our case, E_L from Equation (2.4) is not uniform. However, one can show that the field is approximately uniform near the electrode tip located at $z = d/2$ [1]. In the conditions of the minimum distance for the existence of the glow regime, $d = d_{min}$ and $V_p = V_{min}$, setting $E_L(z = d/2) \approx E_{unif} = E_{SC}$, and using Equation (2.8) at the AST conditions, it is possible to deduce the ionization coefficient necessary for the AST, α_{AST}, for the experimental conditions studied. In [1], Pai *et al* determined α_{AST} corresponding to the experimental conditions studied, as a function of the gas temperature T_g. In the range T_g = 750-1000 K, α_{AST} is inversely proportional to T_g and only depends on the reduced electric field for a given gas, density [1], and radius of curvature of the electrodes.

By setting $E_L(z = d/2) \approx E_{unif} = E_{SC}$, and using Equations (2.4) and (2.8), and $\alpha = \alpha_{AST}$, we obtain the voltage necessary for the AST, V_{AST}:

$$V_{AST} = K\alpha_{AST}^2 \left[\frac{a^2 - (d/2)^2}{a}\right] \ln\left(\frac{1+\eta_0}{1-\eta_0}\right) \tag{2.9}$$

$$\approx K\alpha_{AST}^2 R \ln\left(\frac{1+\eta_0}{1-\eta_0}\right) \tag{2.10}$$

where the second expression is only valid in the case of sharp tip electrodes, $R \ll d$. A semi-empirical model based on the measurements of the minimum distance for the existence of the glow regime d_{min} and the corresponding voltage V_{min} enables us to determine α_{AST}, and consequently V_{AST}. Note that V_{AST} depends on the radius of curvature of the electrode R.

Conduction Phase - Breakdown During the conduction phase (after the streamer and return wave phases, return phase that redistributes the potential), the field E_{pc} is approximately uniform in the positive column and is given by [56], [57]:

$$E_{pc} = \frac{V_p - V_{cf}}{d} \tag{2.11}$$

where V_p is the applied voltage and V_{cf} the cathode fall voltage. The condition to maintain the positive column during the conduction phase is $E_{pc} > E_{br}$, where E_{br} is the breakdown field. The breakdown field is the electric field necessary to balance ionization and attachment rates in air and it is temperature dependent. It was shown in [58] that $\frac{E_{br}}{N}$, the reduced electric field for breakdown, was approximately constant up to $T_g = 2000$ K. Consequently, we can reasonably scale E_{br} with the gas temperature according to $E_{br} = E_0.300/T_g$, where E_0 is the breakdown field at ambient temperature. Consequently, the breakdown voltage is given by:

$$V_{br} = dE_0\frac{300}{T_g} + V_{cf} \tag{2.12}$$

We should insist on the fact that the transition voltage V_{br} does not depend on the radius of curvature of the electrode R.

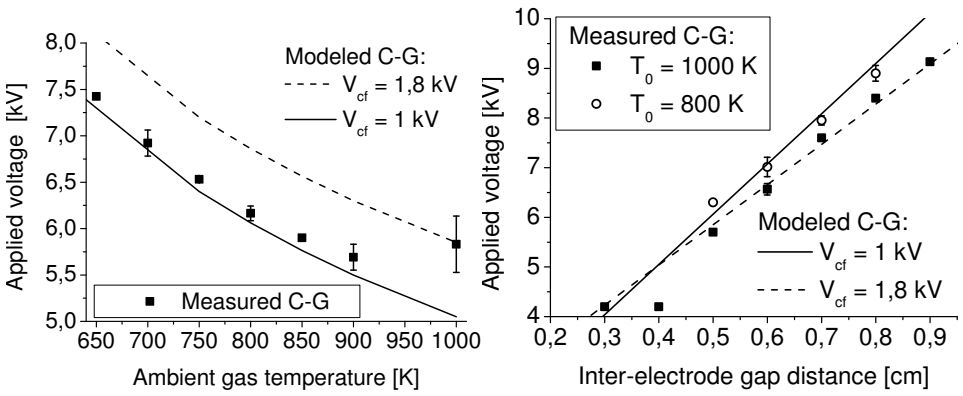

Figure 2.36: Comparison of experimental (symbols) and modeled (lines) C-G transition voltage as a function of (a) the ambient gas temperature T_g and (b) the inter-electrode gap distance d. The theoretical curves were calculated using E_0 = 27 kV/cm. Images taken from [1].

This model was validated in [1]. Figure 2.36 presents the C-G transition voltage V_{CG} as a function of (a) gas temperature T_g for a given distance $d = 5$ mm, and (b) inter-electrode gap distance d for $T_g = 1000$ and 800 K. With the choice $E_0 = 27$ kV/cm, the model fits Pai's data reasonably well, the adjustable variable being the cathode fall V_{cf}. To get the C-G transition, the applied field must be high enough to perform two tasks: initiate the streamer and maintain the plasma during the conduction phase, which can be translated into $V_{CG} = \max(V_{br}, V_{AST})$. In [1], it is the breakdown condition that determines the C-G transition voltage, as it is typically higher than V_{AST}.

The NRP G-S transition

It was shown in [1] that the G-S transition is due to the thermal ionization instability. In the case of Nanosecond Repetitively Pulsed (NRP) discharges, incremental heating occurs because of the high repetition frequency, as long as the gas remains in the discharge gap. Just below the G-S transition, the field in the positive column is

$$E_{pc} = \left(\frac{E}{N}\right)_{GS} N, \tag{2.13}$$

which gives the model for the G-S transition voltage V_{GS}:

$$V_{GS} = \left[\left(\frac{E}{N}\right)_{GS} N\right] d + V_{cf} \tag{2.14}$$

- N is calculated using the elevated temperature of the gas, which takes into account the gas expansion, via heating [1]. This temperature elevation is related to the PRF and the length of the pulse. The model assumes that the heating process is thermodynamically equivalent to a continuous heating process with the same time-averaged volumetric power. In any case, $\Delta T < 200$ K for a glow discharge.
- $\left(\frac{E}{N}\right)_{GS}$ is the G-S transition reduced electric field, and Pai showed that it is constant at all gas temperatures from 300 to 1000 K. In [1] , it was found to be $\left(\frac{E}{N}\right)_{GS} = 144$ Td (35 kV/cm at $T_g = 300$ K and $P = 1$ atm).
- the cathode fall voltage V_{cf}, which is an adjustable parameter. In [1], it was chosen to be 1.9 kV.

The model for V_{GS} fits the experimental data well for the G-S transition when it occurs. Note that V_{GS} does not depend on the radius of curvature of the electrode R.

Existence of the NRP glow regime

Pai noticed that glow regime only exists for $d \geq d_{min}$, and that the value of this minimum distance increases with decreasing gas temperature, see figure 2.32. For $d \geq d_{min}$, the Glow-to-Spark (G-S) transition was observed and for $d < d_{min}$, only the No discharge-to-Spark (N-S) transition was observed.

Figure 2.37 presents the measured transition voltages C-G, G-S and N-S and the modeled transition voltages V_{GS} and V_{AST}. We see that the model for V_{AST} fits the measured N-S transition voltages for $d \leq 2$ mm and that the thermal instability voltage V_{GS} fits the data for the G-S transition voltage for $d > 2$mm. Pai showed that only V_{AST} can explain the existence of this minimum distance. d_{min} corresponds to the limit case when the streamer can initiate and yet the heating during the conduction phase does not lead to the thermal ionization

instability. When $d < d_{min}$, the applied voltage is so high that as soon as the streamer crosses the gap, the G-S transition is triggered after a few pulses by the important Joule heating.

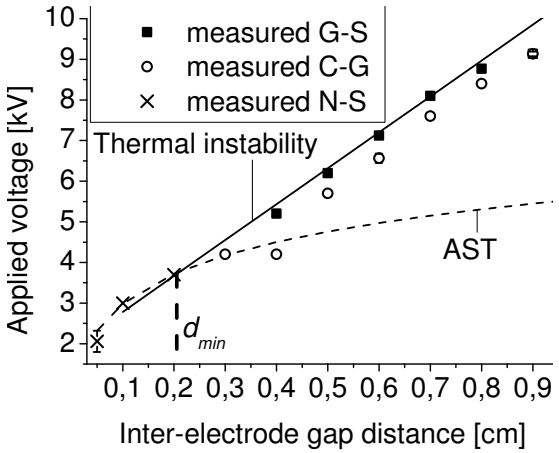

Figure 2.37: Comparison of experimental N-S, C-G, and G-S transition voltage and modeled thermal instability threshold and AST, as a function of inter-electrode gap distance d. T_g = 1000 K, R = 200-250 µm, PRF = 30 kHz, and v = 1.8 m.s^{-1}. Figure taken from [1].

Then, d_{min} corresponds to the abscissa of the intersection of V_{GS} (thermal ionization instability) and V_{AST} in the graph where the transition voltage V is given as a function of the inter-electrode distance d.
By setting $V_{AST} = V_{GS}$ and using Equations (2.10) and (2.14), Pai *et al* [1] derived the equation giving the minimum distance d_{min} for the existence of the glow regime using macroscopic experimental parameters:

$$K\alpha_{AST}^2 R \ln\left[\frac{1+\eta_0(d,R)}{1-\eta_0(d,R)}\right] = \left(\frac{E}{N}\right)_{GS} Nd + V_{cf} \tag{2.15}$$

which is in fact an approximation of the exact criterion obtained using the exact expression of V_{AST} from Equation (2.10), which can be expressed as:

$$K\alpha_{AST}^2 \left[\frac{a^2-(d/2)^2}{a}\right] \ln\left[\frac{1+\eta_0(d,R)}{1-\eta_0(d,R)}\right] = \left(\frac{E}{N}\right)_{GS} Nd + V_{cf} \tag{2.16}$$

In this work, the condition $R \ll d$ will be fulfilled in most cases, except when we will use electrodes of large radius of curvature at the tip R = 500 µm. In that case, we will use the criterion given by Equation (2.16). In any case, the difference between the two criteria is really small.

Pai *et al* noticed that the model of d_{min} fits the experimental value showed on figure 2.37 in their experimental conditions. Consequently, we see that the model predicts that the AST has an influence on the discharge regimes for

the small inter-electrode distances. Since V_{AST} is the only transition voltage influenced by the radius of curvature of the electrode, the radius of curvature has an important influence on the existence of the glow regime for small inter-electrode gap distances. According to the model, V_{CG} and V_{GS} should not depend on the radius of curvature of the electrode. The influence of the radius of curvature on the transition voltages will be investigated experimentally in section 5.5.

Figure 2.38, taken from [1] shows a comparison of the experimental values of Pai *et al* and the model for d_{min} obtained using Equation (2.15) as a function of the gas temperature. The model that best fits the data corresponds to a radius of curvature equal to $R = 250$ µm, which is consistent with the electrodes used in Pai *et al*'s work.

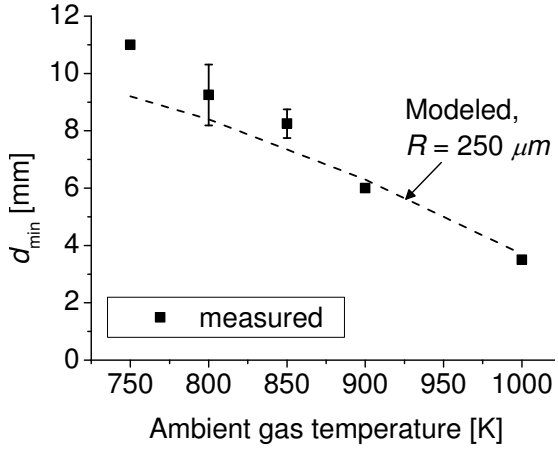

Figure 2.38: Comparison between measured and modeled d_{min} as a function of the gas temperature T_g. $PRF = 30$ kHz, and $v = 1.8$ m.s^{-1}. Images taken from [1].

2.9.3 Existence of the glow regime at $T_g = 300$ K

In this section, we propose to explain why it is important to decrease d_{min} and increase d_{max} to extend the domain of existence of the glow regime to low temperatures. We also detail why R and the duration of the pulse $\Delta\tau$ play a key role to get the glow regime at $T_g = 300$ K.

Decreasing d_{min}

We first examine the importance of the radius of curvature of the electrode tip on the lower limit d_{min} of the domain of existence of the glow regime as a function of temperature. As explained in previous sections, d_{min} is found by solving Equation (2.16). Figure 2.39 presents this minimum distance for

three radii of curvature R = 250 µm, 200 µm, and 100 µm. For a given temperature T_g, we see that d_{min} decreases as R decreases. Consequently, we should decrease the radius of curvature of the electrode to get the glow regime at lower temperatures. This model is based on the empirical values of α_{AST} deduced from the experiments of Pai *et al* [1] for R = 250 µm, and therefore is not fully valid at lower values of R. Nevertheless, the model clearly shows that d_{min} decreases when R decreases. Thus, one possible way to decrease d_{min}, hence to decrease the lower limit of the existence of the glow regime at low temperature, is to decrease R.

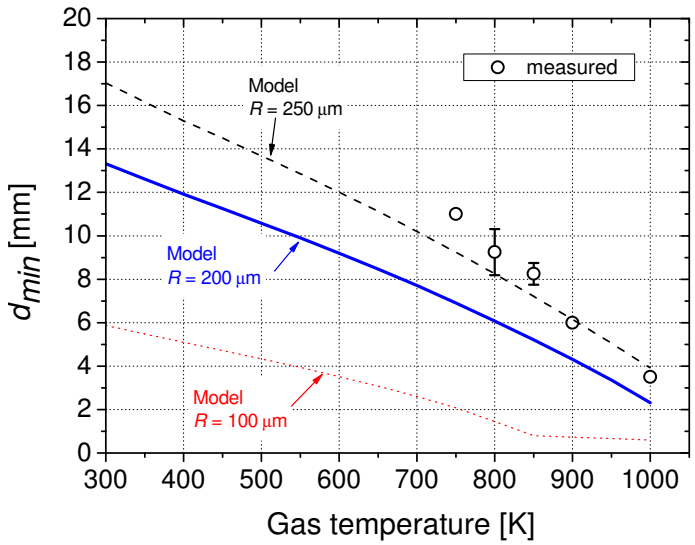

Figure 2.39: Measured d_{min} (symbols) in the experimental conditions of Pai *et al* [1] and modeled d_{min} (lines) for three different radii of curvature R of the electrode tip as a function of the gas temperature T_g. The experimental data were obtained for PRF = 30 kHz and v = 1.8 m.s^{-1} from [1].

Increasing d_{max}

Another parameter studied by Pai *et al* was the maximum distance for the existence of the glow regime. This maximum distance corresponds to the distance that can be crossed by a streamer of velocity v during the pulse duration $\Delta\tau$. In the experiments of Pai *et al* [1], the FWHM of the applied voltage is approximately 12 ns. The streamer velocity scales inversely with gas density [59], so if we consider that the streamer velocity is given by the following equation

$$v = v_0 \frac{T}{T_0}, \tag{2.17}$$

where T is the temperature of the gas, and $v_0 = 10^8$ cm/s is the velocity of the streamer at T_0 = 1000 K, we can deduce the maximum distance d_{max} for the

existence of the glow regime. Figure 2.40 shows d_{max} for three different pulse durations $\Delta\tau$. The symbols represent the experimental data for d_{max} taken from [1] and the lines the model detailed above. The longer the pulse, the longer the maximum distance for a given temperature T_g. Thus, one possibility to increase d_{max} would be to increase the FWHM of the voltage pulse.

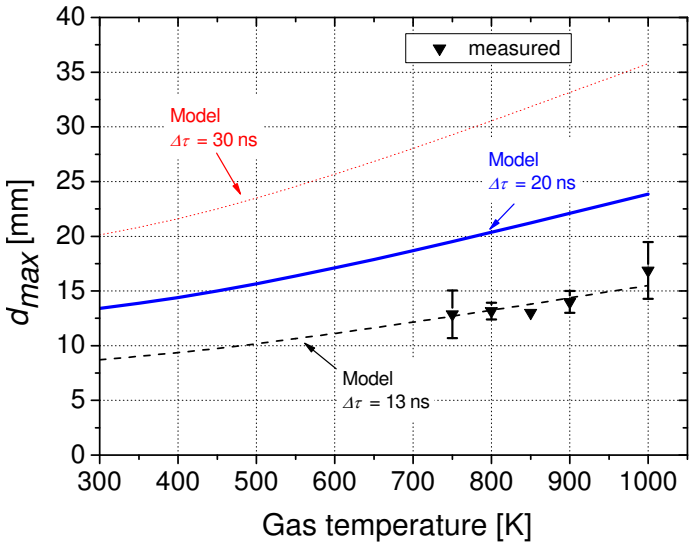

Figure 2.40: Measured d_{max} (symbols) in the experimental conditions of Pai *et al* [1] and predicted d_{max} (lines) for three different durations $\Delta\tau$ of the voltage pulse as a function of the gas temperature T_g. The experimental data were obtained for PRF = 30 kHz and v = 1.8 m.s^{-1} from [1].

These models suggest how to obtain the glow regime at lower temperatures than Pai, see figure 2.41. The domain of existence of the glow regime obtained in [1] and [2] was limited to 700-1000 K due to the crossing of the lower limit d_{min} and the upper limit d_{max}. Increasing the duration of the pulse $\Delta\tau$ and decreasing the radius of curvature R of the electrode tip, the model predicts that we could extend the domain of existence of the glow regime to lower temperatures.

Figure 2.42 presents the predicted domain of existence of the glow regime with R = 100 µm and $\Delta\tau$ = 20 ns. At T_g = 300 K, we have d_{min}=5.9 mm < d_{max}=13.4 mm. Thus, the glow regime could be obtained in principle with these parameters.

There is however one additional consideration to take into account. If the duration of the pulse is increased, the thermal ionization instability may occur if the distance is kept constant. To prevent the spark discharge, we should increase the inter-electrode gap distance and also the applied voltage V_p in order to maintain a sufficient electric field. Our original pulse generator being

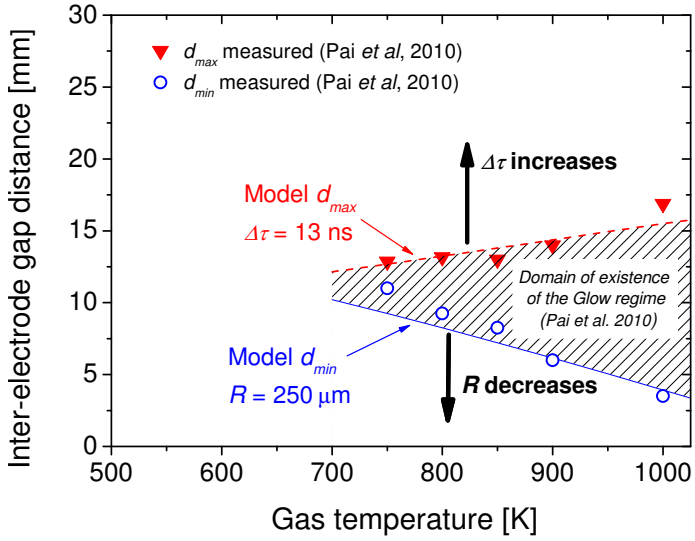

Figure 2.41: Measured (symbols) and predicted (lines) range of gap distances that permit stable operation of the glow regime, as a function of the gas temperature, with PRF = 30 kHz and v = 1.8 m.s^{-1}. Experimental data taken from [1].

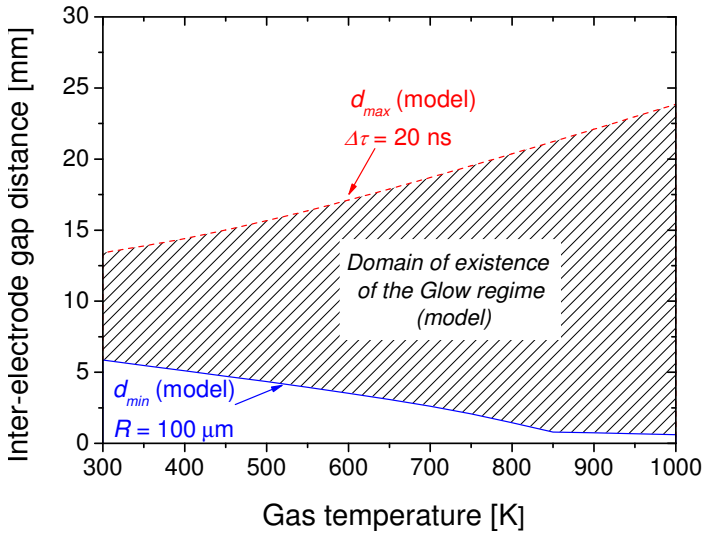

Figure 2.42: Predicted range of gap distances for the existence of the glow regime, as a function of gas temperature T_g, for R = 100 µm and a duration of the voltage pulse $\Delta\tau$ = 20 ns. PRF = 30 kHz.

limited to $V_p \leq 8.6$ kV and $\Delta\tau = 10$ ns, a new pulse generator able to deliver voltage pulses of variable duration up to 50 ns, up to $V_p = 20$ kV, was acquired. This pulser will be characterized in section 3.3.

The results of this preliminary analytical study of NRP discharges properties will be experimentally tested in chapters 5 and 6. In the following chapter, chapter 3, we present the experimental set-up used in the experiments.

2.10 Conclusions

In this chapter, we have presented several features of NRP discharges in atmospheric pressure air plasma and how they could meet the requirements of several applications. We have presented the various applications of atmospheric pressure air plasmas, detailing the several ways to produce such plasmas and showing how the NRP were the only discharges that could in particular meet the requirements of large temperature range for high electron density and low power budget. We have shown a few recent developments of NRP discharges, and detailed the previous results [1], [2], [36] and [37] about the pin-pin configuration studied in preheated air. The various properties of the two relevant discharge regimes were exposed: the NRP spark and glow discharges. We have shown the regime transition with respect to the Pulse Repetition Frequency, the temperature of the gas, and the inter-electrode gap distance. In particular, to date the NRP glow regime has been found to exist only at a temperature of the gas greater than 700 K. Finally, we have presented the model of Pai *et al* [1] on the coupled influence of the gas temperature and the radius of curvature of the electrode which explains the various domains of existence of the three NRP discharge regimes and the transition voltages. This model also predicts the existence of the NRP glow regime at ambient temperature provided the use of small electrode radius of curvature and long duration of the high-voltage pulse.

Chapter 3

Experimental Setup

3.1 Introduction

In this chapter we present the experimental setup used in this work and the main characteristics of the various components. In section 3.2, we present the plasma generation system and the various diagnostics used. Section 3.3 details the main characteristics of a new pulser, called Pulser 2, that creates high-voltage pulses of variable duration. Section 3.4 describes the various electrodes we used. Sections 3.5 and 3.6 detail the experimental setup for the Optical Emission Spectroscopy (OES) measurements and the main characteristics of the monochromator and ICCD camera used. The calibration procedure of the spectra obtained in OES is explained in section 3.7, and the synchronization of the ICCD camera used in OES and imaging is detailed in section 3.8. Finally, we investigate the influence of the position of the voltage probe on the electrical measurements for NRP glow and spark discharges in section 3.9.

3.2 Plasma generation and measurements system

In this section, we present the plasma generation system and the various measurement systems used. Figure 3.1 shows a diagram of the experimental setup for plasma generation, the electrical measurement system, and one of the measurement systems we used for direct imaging of the discharges.

Air heater

The discharge is generated in a vertical airflow that can be preheated from 300 to 1000 K by a resistive heater Osram Sylvania 8 kW Hot Air System, see figure 3.2. A Sierra Instruments Smart Trak digital mass flow meter calibrated for air regulates laboratory grade air from 5 atm to 1 atm. Its flow rate can be adjusted from 0 to 30 NL/min. Then, air flows into the resistive heater where it passes through a ceramic heating coil. The metal tube flows air vertically

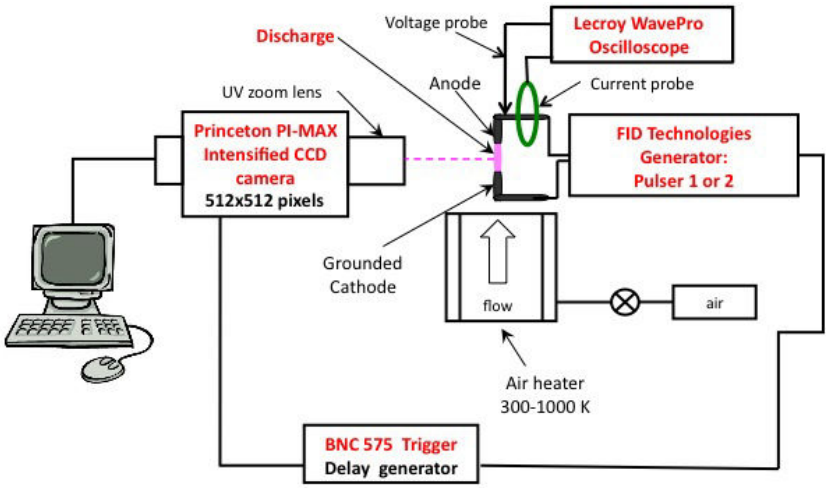

Figure 3.1: Schematic diagram of the experimental setup. The imaging system with ICCD camera is shown. The details of operation of the high-voltage generator and CCD camera are explained further in the chapter.

from the bottom to the top. Its internal diameter is 1.5 cm and its external diameter 2.5 cm.

Electrode assembly

Two electrode configurations are used. The first configuration studied is the axial configuration where the flow is along the direction of the inter-electrode axis, see figure 3.2. The electrode assembly is mounted on two orthogonal micrometric translation stages allowing horizontal movement. Another z-translation stage allows to move both electrodes vertically above the air heater exit. In this configuration, experiments were done with the cathode 1 mm above the air heater exit. Another z-translation stage permits to move the anode from the cathode so as to vary the inter-electrode gap distance d. This axial configuration will be used for the study of ultrafast heating following an NRP spark discharge in air in Chapter 4 and the study of the influence of R (electrode radius of curvature) and T_g (gas temperature) on discharge regimes and properties in Chapter 5.

The second configuration studied is the transverse configuration where the flow direction is orthogonal to the direction of the inter-electrode axis, see figure 3.3. As for the axial configuration, the electrode assembly can be translated in the horizontal plane in two orthogonal directions, and on the vertical z-axis. The inter-electrode gap distance d can be adjusted with another micrometric translation stage. As the air heater exit is grounded, we did not place the high-voltage electrode in contact with the air heater exit. In all experiments,

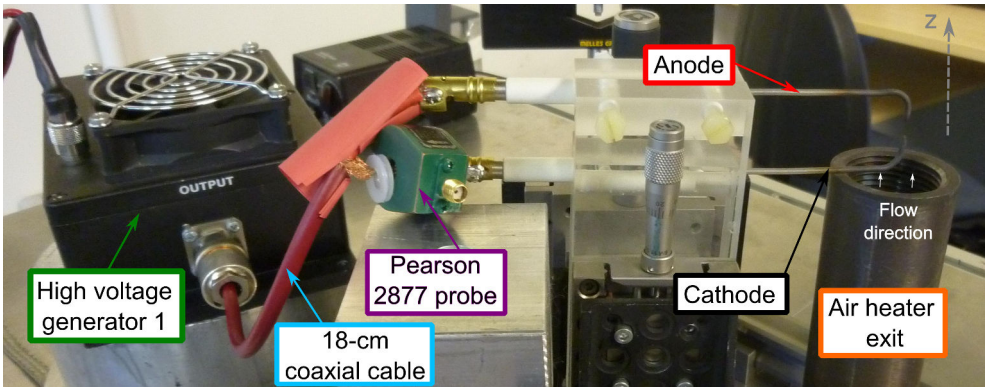

Figure 3.2: Photo of air heater exit and electrode assembly in axial configuration.

the center of the bottom electrode was placed 15 mm above the output of the air heater. This transverse configuration is used for the parametric study of the glow regime at $T_g = 300$ K in Chapter 6.

High-voltage pulse generation

Plasma is generated by applying nanosecond high-voltage pulses between two pin electrodes. The various types of electrodes used in this work are described in section 3.4. High-voltage pulses are produced by two different high-voltage pulse generators.

The first pulse generator is a FID Technology FPG 10-30MS pulser that produces pulses with rise/fall times of 5 ns, a flat top of 10 ns at greater than 90% of the maximum voltage, and amplitudes up to +10 kV into an open circuit. The output of the pulse generator is connected with a 18-cm coaxial cable to the electrodes. The coaxial cable is split about 4 cm from the electrode, the core joining the anode and the sheath the cathode, as shown in figure 3.2. This pulse generator will be called in this work Pulser 1 (P1), and was already described in more details in [2].

A second pulse generator Pulser 2 (P2), FID Technology FPG20-30MKS50, is used. A complete description of this pulse generator will be given in section 3.3. The main characteristic of Pulser 2 is that it can be used on two independent channels that deliver pulses of variable pulse duration. As announced by the manufacturer, Channel 1 delivers pulses of duration 20-50 ns, and Channel 2 pulses of duration 5-11 ns. A detailed study of the pulse duration will be done in section 3.3. The rise/fall time of Channel 1 is 15 ns and that of Channel 2 is 5 ns. Two knobs on the front panel permit to adjust respectively the **Pulse Width** (PW) and the **Amplitude** of the pulses. Both channels produce pulses

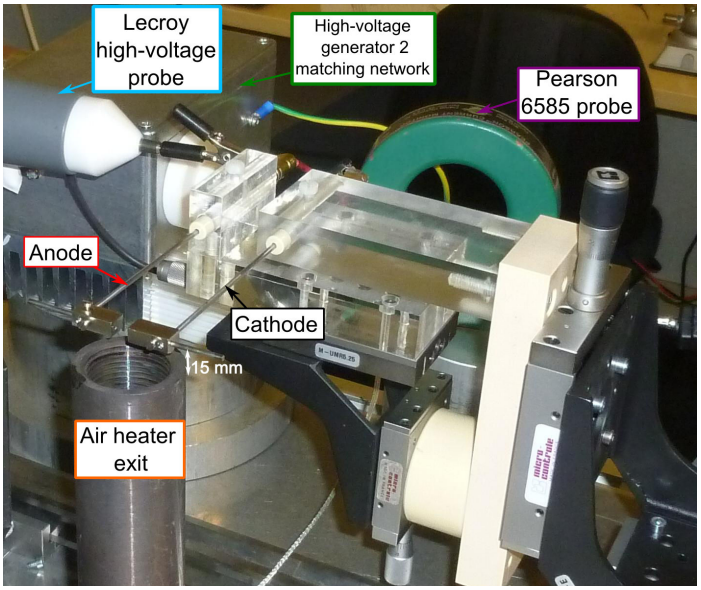

Figure 3.3: Photo of the air heater exit and electrode assembly in the transverse configuration.

of amplitudes up to +20 kV into an open circuit, at frequencies from 1 Hz to 30 kHz. The main characteristics of the two pulsers are presented in table 3.1 following our characterization work.

Table 3.1: Pulser 1 and Pulser 2 main characteristics

Pulser	Pulser 1	Pulser 2	
		Channel 1	Channel 2
Output impedance [Ω]	75	100	100
Voltage amplitude into an open circuit [kV]	≈ 9	≈ 20	≈ 20
FWHM [ns]	12	5 -11	20 - 52
Pulse width at 90 % [ns]	4	2 - 4	9.5 - 35
Rise time [ns]	5	5	15
Frequency [Hz]	1 - 30,000		

Electrical measurements

Measurements of the voltage applied across the electrodes V_p are obtained using 100-MHz bandwidth Lecroy PPE 20 kV high-voltage probes connected to the 1 MΩ input impedance of the oscilloscope. Their ability to measure the nanosecond high-voltage pulses was already investigated by Pai in [2]. When needed, we added a Lecroy attenuator 10:1 to the voltage probe. The dis-

charge current, also called total current I_{tot}, see section 6.8, is measured using two different Pearson coil current monitors. For Pulser 1, we used a Pearson model 2877 Rogowski-type current probe, located after the break of the 18-cm coaxial cable connecting the pulse generator to the electrodes, on the grounded electrode side, as can be seen on figure 3.2. To measure current using Pulser 2, a Pearson model 6585 current probe was placed around the ground cable connecting the cathode to the matching network of the pulse generator. This can be seen on figure 3.3. Section 3.3 further describes the matching network of Pulser 2. Both probes are connected to the ground via flat braided wire. The characteristics of the two probes are detailed in table 3.2. Both Pearson probes are connected to the attenuator and the scope via a Pasternack double shielded flexible RG142B/U coaxial cable. The use of this cable minimizes the noise captured via the wire.

Table 3.2: Pearson coil characteristics

Model number	*Output [V/A]*	*Maximum peak current [A]*	*Useable rise time [ns]*	*3 dB cutoff low frequency [Hz]*	*± 3 dB cutoff high frequency [MHz]*
2877	1	100	2	300	200
6585	1	500	1.5	400	250

Both probes have a current-to-voltage ratio of 1 A to 1 V when plugged on the 1-MΩ channels of the scope. A low-voltage 50-Ω impedance attenuator, Barth Model 2-20, with a 20 dB (÷ 10) attenuation, 0-20 GHz bandwidth, and 20 ps output rise time is connected between the cable that leads to the Pearson probe and the oscilloscope. To minimize signal reflections, we connect the Pearson probes using an additional BNC straight 50 Ω plug terminator on the 1MΩ input impedance of the scope to match the Pearson probe impedance. Consequently the effective current-to-voltage ratio is 2 A to 1 V in this configuration.

Two different oscilloscopes were used to record the signals from the various probes: a 350-MHz (maximum 1 or 2 Gs/s) Lecroy Wavesurfer 434 or a 1-GHz (maximum 10 or 20 Gs/s) Lecroy Wavepro 7100A oscilloscope. Except when mentioned otherwise, all voltage and current measurements recorded with the oscilloscopes are averaged over 100 samples. For measurement made with the 1-GHz Lecroy Wavepro 7100A oscilloscope, the maximum voltage that we could monitor was 16 kV. Using Pulser 2, the applied voltage could be as high as 18-20 kV, consequently, we used an additional Lecroy D 9010 (÷ 10) high impedance divider between the Lecroy high-voltage probe and the 1-MΩ input impedance of the scope.

Light collection

For optical emission spectroscopy, we used two 90° off-axis parabolic UV-grade MgF_2-coated aluminum mirrors of 50 mm diameter (Janos technologies). Those mirrors collect light from the plasma and focus it into the front entrance slit of the monochromator. Mirrors are placed in mirror mounts (Ultima U200-A38) with adjustment knobs allowing 3-D movement. A schematic diagram of the experimental setup is described in section 3.5. Each mirror is positioned on $x-y-z$ translation stages in order to align them independently. A diaphragm is placed before the first collecting mirror to adjust the solid angle and to reduce spherical aberrations. This permits to control the intensity of light collected in the monochromator. In order to isolate specific transitions and discard second order diffraction, we used interference filters positioned on the optical path just before the entrance of the monochromator.

Monochromator and ICCD camera

For the experiments presented in chapter 4, calibrated optical emission spectroscopy measurements were made using a monochromator fitted with an ICCD camera. The light emitted from the discharge was collected and entered an Acton SpectraPro 2500i monochromator for spectral analysis before final detection by an intensified Princeton Instruments PI-MAX CCD camera. Further details about the monochromator and ICCD camera subsystem are given in sections 3.5, 3.6, 3.7, and 3.8.

ICCD camera for imaging

For the experiments presented in chapters 5 and 6, direct visualization of the discharge was realized using an ICCD camera. The light emitted from the discharge was collected via a UV Nikkor 105 mm zoom lens and entered an intensified Princeton Instruments PI-MAX CCD camera. The camera model was identical to the one used with the monochromator except that the imaging CCD was a 512 × 512 px array. The zoom lens was focused without the discharge in order to visualize the image of the electrodes on the CCD when those were lit with an external lamp. The camera was mounted on a tripod. The camera was used in imaging mode in order to visualize the discharge. The operation of the PI-MAX ICCD camera will be described in section 3.6 and the synchronization procedure will be presented in section 3.8.

3.3 Characterization of the high-voltage pulse Generator 2

In this section, we present the FID Technology FPG20-30MKS50 pulse generator, called Pulser 2 (P2) in this thesis, and detail its main properties. As

mentioned in section 3.2, the width and amplitude of the pulses produced by Pulser 2 can be adjusted. The duration of the pulses delivered by both channels will be studied in more details further. Typical waveforms of voltage delivered on pin-pin electrodes can be seen on figure 3.4 and are compared to the voltage delivered by Pulser 1. The pulses delivered by Pulser 2 on Channel 2 are shorter than those delivered by Pulser 1 for all Pulse Widths. The pulses delivered by Pulser 2 on Channel 1 are much longer than those delivered by Pulser 1 for all Pulse Widths. The waveforms shown on figure 3.4 correspond to a pulse width in the middle of the range of pulse widths attainable for Channel 2 (full range 5 to 11 ns) and to a minimum width on Channel 1. The characteristics of these waveforms results are given in table 3.3.

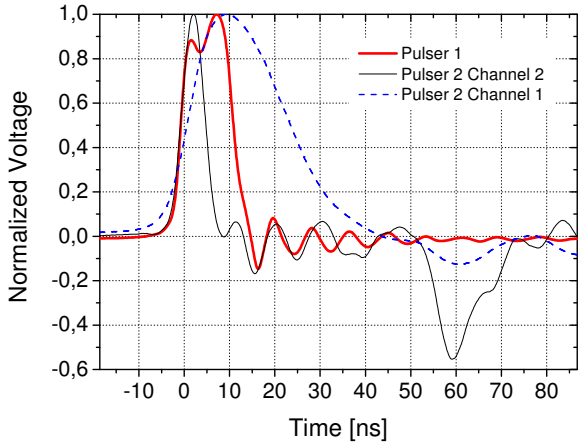

Figure 3.4: Measured normalized voltage delivered by Pulser 1 (thick red), Pulser 2 Channel 2 (thin black), and Pulser 2 Channel 1 (dash blue) in a typical glow discharge.

Table 3.3: Pulse Width at 90% and 50% amplitude of the waveforms shown in figure 3.4 for Pulser 1 and Pulser 2. Pulse Width for Pulser 2 is adjusted to the middle of the pulser range for Channel 2 and to the minimum for Channel 1.

Pulser	Pulse Width at 90% [ns]	Pulse Width at 50% [ns]
Pulser 1	4.0	11.8
Pulser 2 Channel 2 (intermediate PW)	2.3	5.7
Pulser 2 Channel 1 (minimum PW)	9.8	22.9

The curves on figure 3.4 are representative of the shapes of all pulses produced by Pulser 1 and Pulser 2 Channels 1 and 2. We note that the rise times of Pulser

1 and Pulser 2 Channel 2 are always similar and tend to be much shorter that those of Pulser 2 Channel 1.

Figure 3.5 shows a block diagram of the high-voltage pulse generator system. The pulse generator can be triggered either by its own pulse delay generator, or by a Berkeley Nucleonics Corporation (BNC) Model 575 digital pulse/delay generator delivering pulses of duration 80 ns and amplitude 5 V.

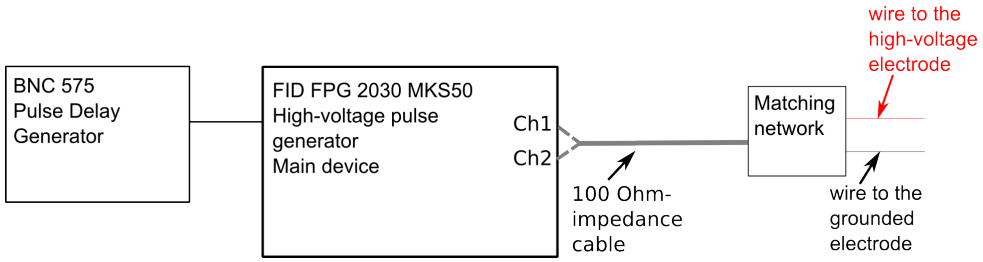

Figure 3.5: Block diagram of the high-voltage pulse generator 2

The output channels of the pulse generator are connected to a 5-m cable of characteristic impedance 100 Ω. At the end of the cable, a matching network permits to avoid reflections to go back into the pulser. This would put too much power into the pulser and potentially lead to its destruction. Figure 3.6 shows measured voltage waveforms after the 100 Ω-cable when no matching network is connected (thick blue) and at the output of the matching network with no external load (thin red). We see that the matching network reduces the amplitude of the reflected pulse by more than a factor 2. Consequently, we will use the pulse generator with the matching network in the present work.

First, we determine the characteristic output impedance of the pulser. We connect the output of the matching network on two test resistors. We measure the voltage across the resistors with the Lecroy high-voltage probes previously described in section 3.2. We work at low frequency (1 Hz) not to burn the resistors used. Figure 3.7 shows the measured voltages across two test resistors and across an open circuit. The voltage amplitude on the test resistor of $R_{load} = 100\ \Omega$ is divided by two compared to the amplitude of the voltage measured on an open circuit, which confirms that the characteristic impedance of the pulser is $Z = 100\ \Omega$.

At high frequency such as 10 kHz, the voltage does not go to zero in the inter-pulse. As shown in figure 3.7, at 1 Hz, the inter-pulse residual voltage is null on an open circuit, whereas at 30 kHz, it is approximately equal to 1.3 kV (see figure 3.6). This had not been observed on Pulser 1. It turns out that the internal electric circuits of both pulse generators are different and do

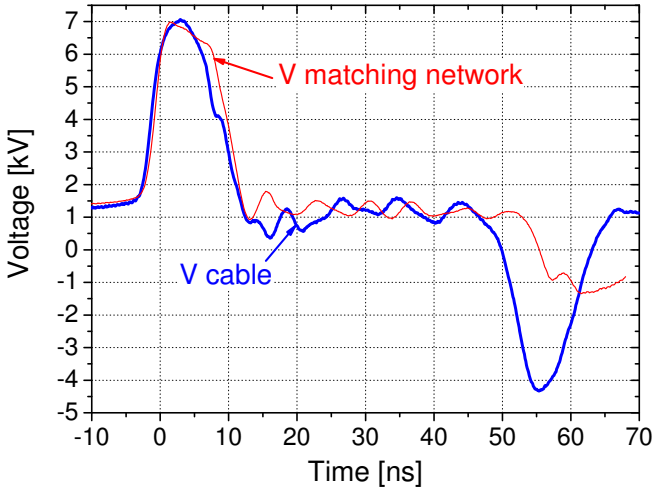

Figure 3.6: Measured voltage waveforms at the end of the 100 Ω-cable when no matching network is connected (thick blue) and at the output of the matching network (thin red) on an open circuit. Pulser 2, Channel 2, PRF = 30 kHz.

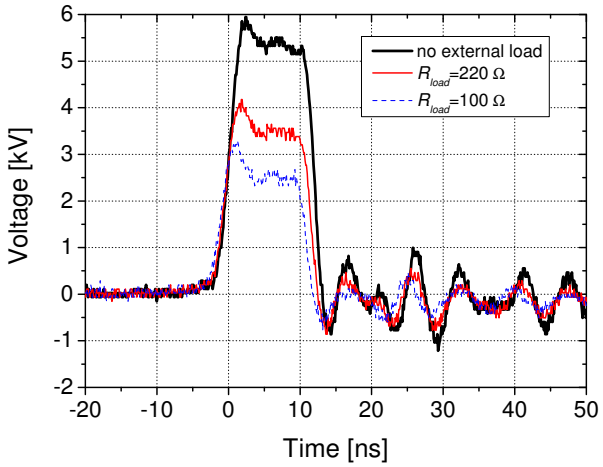

Figure 3.7: Measured high-voltage pulse generator 2 Channel 2 voltage waveforms for various loads. PRF = 1 Hz. Waveforms are single shot samples.

not discharge in the same way between pulses. Consequently, we study the value of the inter-pulse residual voltage with respect to several parameters: pulse frequency PRF, load, and voltage amplitude. Figure 3.8 shows voltage waveforms measured for different PRFs on Channel 2.

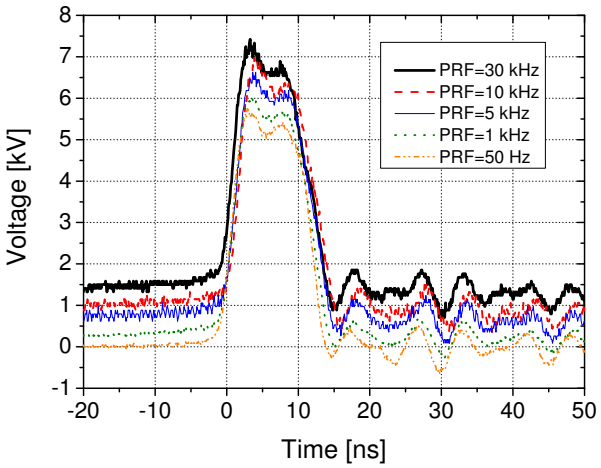

Figure 3.8: Measured voltage waveforms on an open circuit with Pulser 2 Channel 2 for various values of the pulse frequency. Waveforms are single shot samples.

The inter-pulse residual voltage increases with the frequency, from zero at 50 Hz up to 1.5 kV at 30 kHz. When no impedance load is connected to the output of the pulse generator, energy is not dissipated, so at high PRF it appears as an additional DC voltage. Thus, for a given frequency, the inter-pulse residual voltage increases with increasing voltage amplitude. Finally, we investigate the influence of the number of pulses in a burst of pulses on the inter-pulse residual voltage. A burst of a variable number of pulses is followed by a pause of variable duration. We vary the number of pulses from 10 to 10,000 and the duration of the pause from 900 to 6,000 pulses. In each case, for a number of pulses lower than 100-200, the inter-pulse residual voltage is negligible, and the voltage increases with the number of pulses. This confirms that this inter-pulse residual voltage is related to the average energy delivered by the pulser.

We intended to used this pulse generator to create NRP glow discharges at T_g = 300 K. For such discharges, the load is quite similar to an open circuit because the equivalent plasma resistance is very high. Consequently in such conditions, the inter-pulse residual voltage becomes significant.

In addition, preliminary tests showed that the discharge transitions were quite different from those obtained using Pulse Generator 1 under similar conditions. We inferred that this inter-pulse residual voltage might be the cause of this awkward behavior. In order to eliminate the residual voltage, we added a Murata capacitor of capacitance C= 1000 pF $\pm$ 20% and maximum voltage

15 kV in between the positive output of the matching network and the anode. This capacitor is shown on figure 3.10. We checked that the capacitor did not change the shape of the main pulse while still removing the inter-pulse residual voltage, as can be seen on figure 3.9. We then compared the voltage required to obtain NRP glow discharges at $T_g = 300$ K. The way to obtain a glow discharge at $T_g = 300$ K will be described in chapters 5 and 6. It can be also be seen that the capacitor slightly increases the ringing pulses. The second pulse amplitude goes from 40% to 57% of the first pulse amplitude when adding the capacitor, see figure 3.9. This increase is not significant and does not change the discharge regimes. Consequently, in the rest of this work, we will always use Pulser 2 with a capacitor of capacitance C= 1000 pF between the high-voltage output of the matching network and the anode of the reactor.

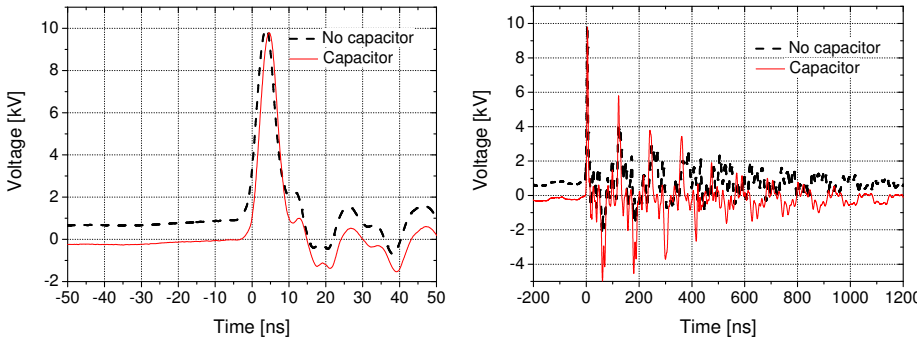

Figure 3.9: Measured voltage waveforms with Pulser 2 Channel 2 with (thin red) and without (dash black) a capacitor C= 1000 pF at the anode for a typical glow discharge at $T_g = 300$ K. The way to obtain a glow discharge at $T_g = 300$ K will be described in chapters 5 and 6. (a) corresponds to a zoom of the waveforms of (b).

Figure 3.10 shows a picture of the Pulser 2 with the matching network and the additional capacitor on the high-voltage output. The amplitude and pulse width adjusting knobs are visible on the front panel. The 100-Ω cable is connected to the main device on the rear panel (not visible on the picture).

Finally, we investigated the output characteristics of the high-voltage pulse generator by varying independently the amplitude and the pulse width. Originally, this pulser was acquired to investigate the influence of the pulse duration on the existence of the glow regime at low temperature, see section 2.9.3. However, we found out that the pulse width and amplitudes could not be varied independently. Thus, we begin by a characterization of the pulse width and amplitude. The first test consisted in increasing the pulse width while keeping the amplitude constant on Channel 2, see figure 3.11 (a). This was done on an open circuit. Changing the pulse width from its minimum to maximum value

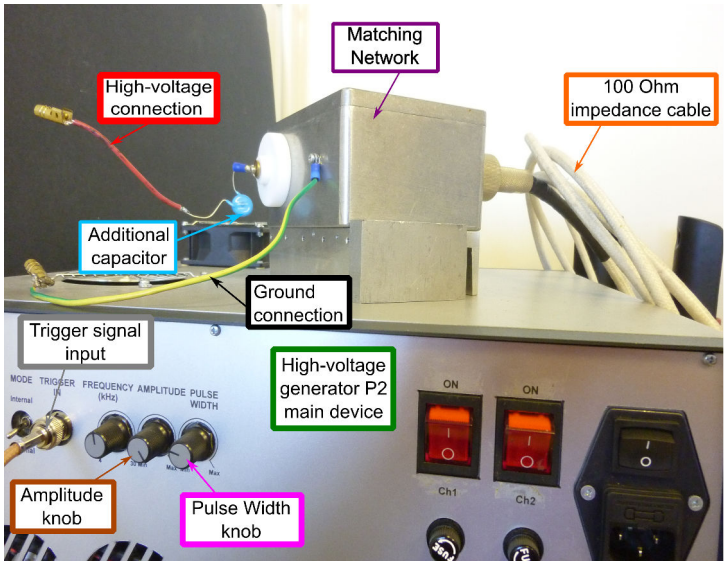

Figure 3.10: Pulser 2 connected circuit components.

results in an increase of the voltage by 2 kV, the maximum of the voltage pulse increasing from 4 to 6 kV. Conversely, we also increased the amplitude while keeping the pulse width constant for several pulse widths on Channel 1. Figure 3.11 (b) shows the voltage waveforms obtained keeping the pulse width at 3/4 of its scale, with a matching load of $R_{load} = 100\ \Omega$ (Kanthal 888 AS 101 KDS resistor). We progressively increased the voltage amplitude from its minimum value to its maximum value. The duration of the pulse at half-maximum decreases when the amplitude increases. For the minimum amplitude, the FWHM is equal to 40.5 ns, whereas for the maximum amplitude, it is equal to 24.7 ns, which corresponds to a 40% reduction. This is consistent with the fact that there is a maximum average power that can be delivered by the pulser. When we try to increase the voltage amplitude too much, the pulser has to shrink the duration of the pulse.

Consequently, we investigated the variations of the maximum output voltage as a function of the pulse width on a matched load $R_{load} = 100\ \Omega$ on both channels. Figure 3.12 shows the evolution of the maximum value of the output voltage as a function as the pulser FWHM for several positions of the pulse width knob. Each symbol colors corresponds to a given position of the pulse width knob. These measurements were made in burst mode with 80 applied pulses followed by a pause of 800 pulses at a frequency of 10 kHz. A range of pulse FWHM of 5-11 ns is reachable with Channel 2, and 15-20 ns to 52 ns is reachable with Channel 1. However, as was shown on figure 3.12, the maximum output voltage and the FWHM are not independent. Increasing the voltage decreases the pulse duration at high amplitude. Furthermore, there is a domain of FWHM from

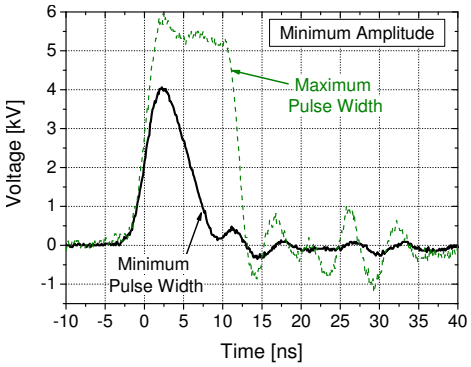

(a) Channel 2, Minimum amplitude, minimum pulse width (solid black) and maximum pulse width (dash green), PRF=1 Hz

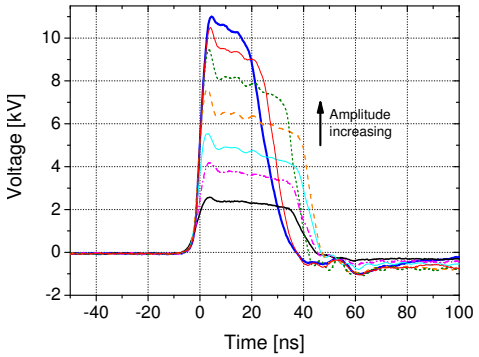

(b) Channel 1, pulse width= 3/4 of its scale and increasing amplitude. Burst mode: 80 ms, pause 800 ms, PRF=10 kHz

Figure 3.11: Measured single-shot voltage waveforms with Pulser 2 (a) Channel 2 on an open circuit and (b) Channel 1 on a resistor R_{load} = 100 Ω. When the pulse width increases, the voltage amplitude increases. When the voltage amplitude increases, the pulse width decreases, all the more at high voltage. Waveforms on figure (a) are single shot samples.

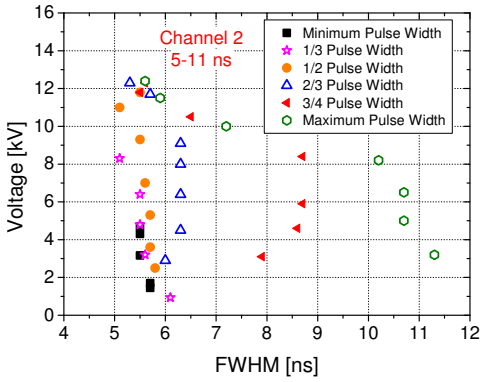

(a) Channel 2

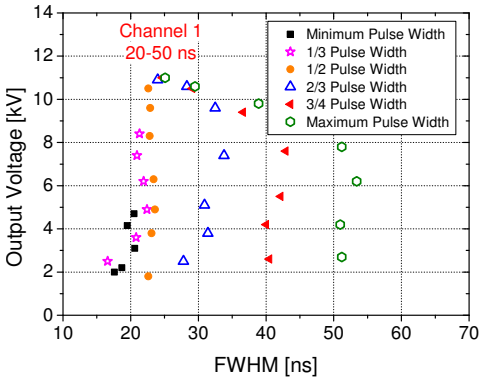

(b) Channel 1

Figure 3.12: Maximum values of the output voltage as a function of the FWHM for several positions of the pulse width knob for (a) Channel 2 and (b) Channel 1 on a Kanthal 888AS 101 KDS resistor load R_{load} = 100 Ω. Each symbol colors corresponds to a given position of the pulse width knob. Measurements were made in burst mode with 80 pulses applied followed by a pause of 800 pulses at a frequency of 10 kHz.

11 ns to 15-20 ns that cannot be reached with this pulse generator. Fortunately, this corresponds to the FWHM of Pulser 1.

As was shown on figure 3.4, the rise time of Pulser 1 is identical to the rise

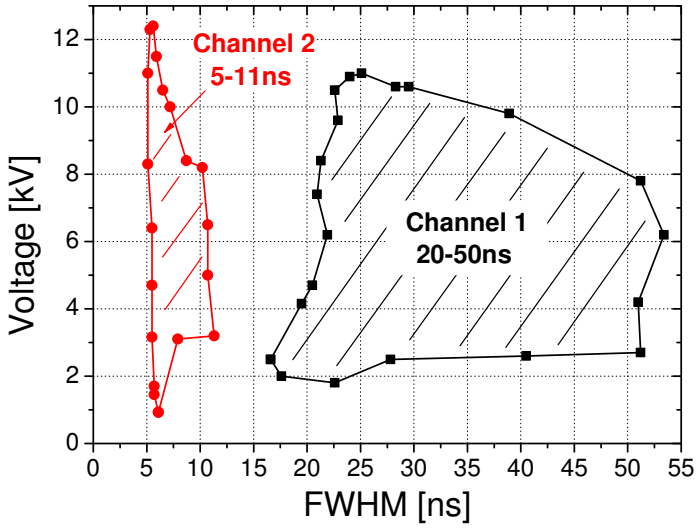

Figure 3.13: Reachable domain of maximum values of the output voltage of Pulser 2 as function as the FWHM on a resistor load $R_{load} = 100\ \Omega$.

time of Pulser 2 Channel 2. Consequently, when we need to work in closeby conditions as with Pulser 1 but with higher voltage, we will use Pulser 2 Channel 2 since the maximum voltage reachable with Pulser 2 is 20 kV in an open circuit. However, we will have to keep in mind that the pulse duration is slightly shorter in this setting.

In section 2.9.3, we saw that increasing the duration of the pulse to a FWHM of approximately 20 ns while increasing the inter-electrode gap distance to 6-10 mm at about 10 kV could be a method to increase the maximum distance of existence of the glow regime, and thus to obtain the glow regime at $T_g = 300$ K. However, we see that it is difficult with Pulser 2 to keep a constant value of the FWHM, particularly at high voltages. Consequently, we will not make a systematic study of the existence of the glow discharge as a function of the pulse duration as was planned in section 2.9.3 but concentrate on the influence of the radius of the electrode on the NRP glow discharge regime while decreasing gas temperature, see chapters 5 and 6.

In this section, we have investigated the main properties of Pulser 2. We detailed the main components of the pulser and emphasized the importance of the matching network to avoid reflections of the main pulse. We confirmed that the output impedance of the pulser is 100 Ω. We noticed the existence of an inter-pulse residual voltage, that might be disturbing when studying glow discharges. We added a capacitor between the high-voltage output of the matching network and the anode, and we checked that this capacitor eliminated the residual voltage while not affecting the shape of the pulse. Finally, we studied the maximum

voltage as a function of the FWHM and showed that it is not easy to work at constant FWHM at high output voltages. Thus, we will not use Pulser 2 to study glow discharges with long pulse durations (FWHM = 30 ns), but mainly use it to obtain voltages higher than 9 kV (up to 14 kV), since the maximum voltage attainable with Pulser 1 is 8.6 kV.

3.4 Electrodes

We used several types of electrodes. The first type is the same as that previously used by Pai in [2], *Delmo* refractory stainless steel electrodes. They are manufactured with a cylindric shape at the tip. To obtain a sharp pin, we hand sharpened them with a grinder, to make them as symmetric as possible to the naked-eye. The radius of curvature obtained is approximately 200-250 µm. Then we bend them in order to get a pin-pin configuration, so as to obtain the geometry shown in figure 3.2. This kind of electrode is used for the study of the ultrafast heating following an NRP spark discharge in air in chapter 4 and in section 5.3 to show the different NRP discharges at T_g = 1000 K.

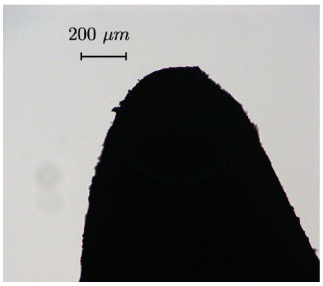

Figure 3.14: Typical home-made sharpened *Delmo* electrode. Image taken with a BX51 Olympus microscope.

However, as can be seen on figure 3.14, images obtained with an optical Olympus BX 51 microscope indicate that the shape of the electrode is not symmetric, and that there are salient, prominent angles likely to enhance the development of streamers. To validate the strategy presented in section 2.9.3, a smooth surface and a calibrated radius of curvature of the electrodes are needed. Thus, we have ordered *Delta Precis* custom-made stainless steel electrodes of radii of curvature 50, 100, 200 and 500 µm. The actual radii of curvature of the manufactured electrodes were 58, 116, 204 and 508 µm. A picture of an electrode of nominal radius of curvature R = 100 µm is shown on figure 3.17 (a). The electrodes are made with a portion of sphere tangentially linked to a cone of angle at the summit around 9°. The height of this part is around 8 mm and is

followed by a cylinder of diameter 2 mm. The salient angle between the cone and the cylinder is smoothed. These electrodes are held by a metallic cube, itself was fixed on a straight section of a *Delmo* electrode, see figure 3.15.

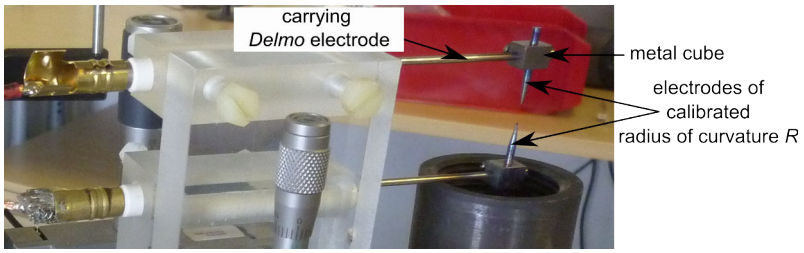

Figure 3.15: Photo of the experimental setup used to maintain the *Delta Precis* and *Axfil* electrodes above the preheated air flow.

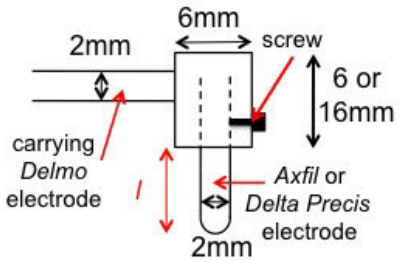

Figure 3.16: Schematic side-view of the experimental setup to maintain the *Delta Precis* and *Axfil* electrodes above the preheated air flow.

Two different types of cubes are used, both of the same area $A = 48$ mm^2 perpendicular to the axis of the electrodes, but of different lengths in the direction of the axis of the electrode, in order to be able to vary the inter-electrode gap distance d without bending the carrying electrode. The introduction of this cube introduces a new parameter in the experiment, namely the length l between the tip of the electrode and the cube. This length can be adjusted from 1 to 15 mm using the set-screw on the side. The influence of this parameter on the nature of the NRP glow discharge will be studied further in section 6.4. We also used *Axfil* electrodes, of radius of curvature around 20 µm. However, their shape is not as symmetric as the shape of the *Delta Precis* electrodes, as can be seen on figure 3.17 (b). The diameter of the base cylinder is also 2 mm, and the metal is stainless steel, as for the *Delta Precis* electrodes.

Even though the model described in section 2.9 was for electrodes of hyperboloid shape, the present electrodes are very close in terms of shape (see figure 3.18). Therefore, they are adequate to test the model, as will be done in section 5.5. The characteristics of the various electrodes used in the present work are summarized in table 3.4.

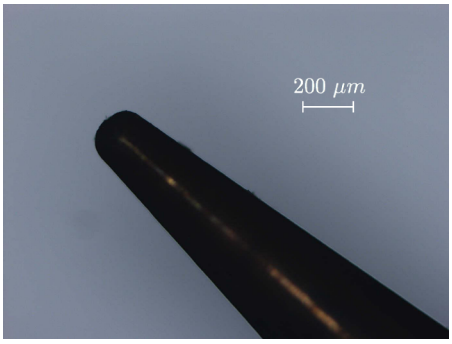

(a) R=100 µm *Delta Precis* electrode

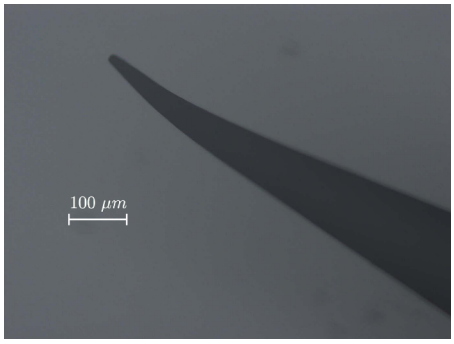

(b) R=20 µm *Axfil* electrode. The electrode is not perfectly symmetric

Figure 3.17: Photos of two types of electrodes used in this work. Photos taken with a BX51 Olympus microscope.

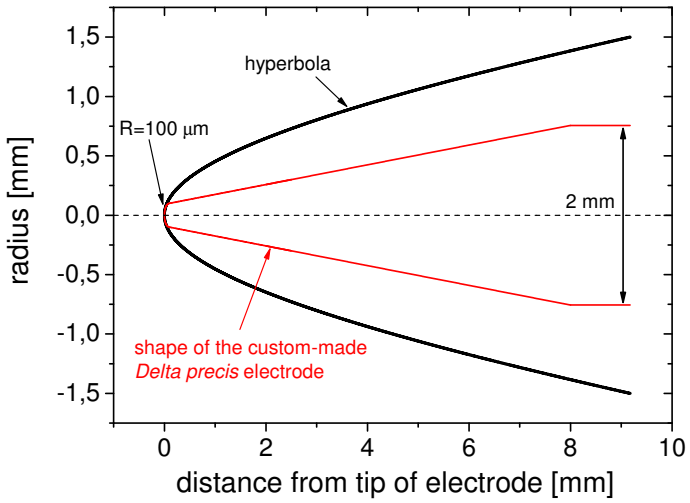

Figure 3.18: Cross section of the custom-made *Delta precis* electrode of radius of curvature at the tip R = 100 µm (thin red) and corresponding hyperbola of same radius of curvature at the tip (thick black).

Table 3.4: Electrodes characteristics

Electrode	*Delmo*	*Delta Precis*	*Axfil*
R [µm]	≈ 200	58, 116, 204, 508	20
Total length [mm]	-	20	38
Mounting technique	bent at 90°	metallic cube holder	
Configuration	pin	pin with plane behind	

3.5 Experimental setup for Optical Emission Spectroscopy (OES) measurements

Previous measurements of Optical Emission Spectroscopy (OES) had been performed on an NRP spark discharge in [6] and [48]. However, the experimental setup implemented in these works used an optical fiber between the plasma and the side entrance of the monochromator, which can introduce uncertainty, for example, in terms of the spatial resolution, and hence on the quantitative determination of densities.

Figure 3.19 shows a schematic view of the light path from the discharge to the side entrance of the monochromator in the previous setup.

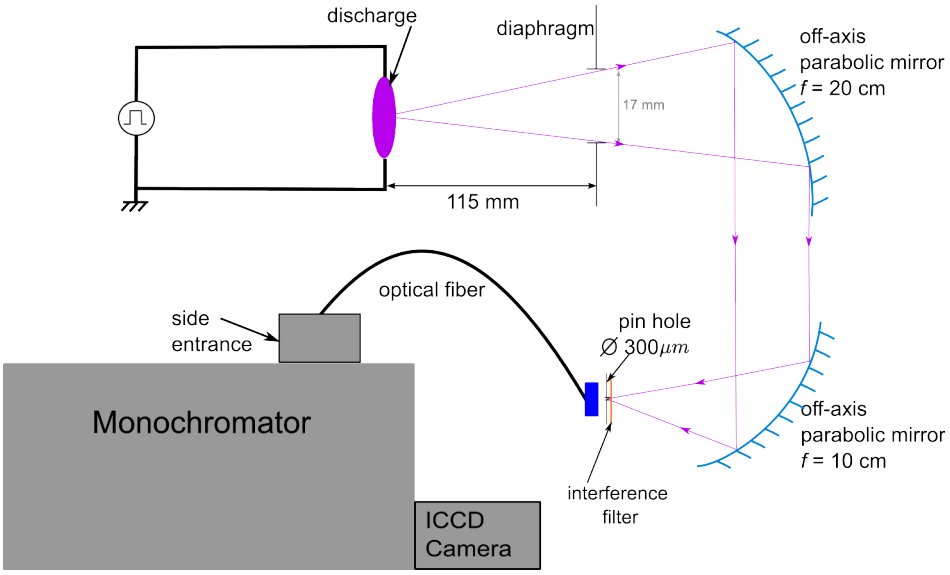

Figure 3.19: Diagram of the previous experimental setup used for OES in reference [6].

The experiments performed in that configuration needed to be confirmed for the following reason. At the entrance of the optical fiber, after the two off-axis parabolic mirrors, a pinhole of diameter 300 µm had been placed. Since the magnification of the system was 1/2, the resulting spatial resolution was 600 µm. One concern is that this size is actually larger than the size of the discharge (the diameter of the NRP spark discharge had been previously measured to be around 350 µm [6]). Thus the spatial resolution was insufficient to determine the discharge radius accurately.

Furthermore, the 2-mm tungsten filament used for intensity calibration is wider than this diameter of 600 µm, see figure 3.20. A correct calibration procedure must use a reference calibration signal of the same surface as the luminous signal

studied (see section 3.7). Consequently, the calibration procedure accuracy was not warranted and the absolute densities inferred from the spectra obtained by OES might be biased. In addition, the optical fiber we used was composed of 18 fibers, which can introduce variations in the system response.

To eliminate these problems, we decided to remove the optical fiber between the plasma and the entrance of the monochromator and to build a new fiberless optical train. This setup is much more delicate to align, but offers increased accuracy, spatial resolution and reliability for the quantitative measurements envisaged. Figure 3.21 shows a diagram of the experimental setup used for the Optical Emission Spectroscopy measurements performed in this work.

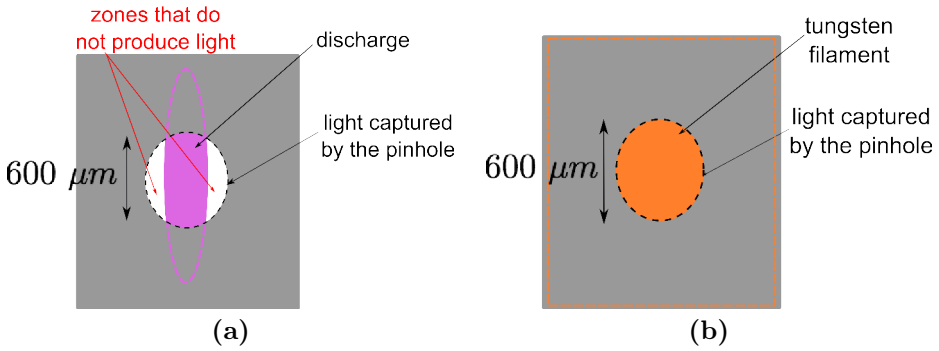

Figure 3.20: Portions of (a) discharge and (b) tungsten filament detected with the 300-μm diameter pinhole system.

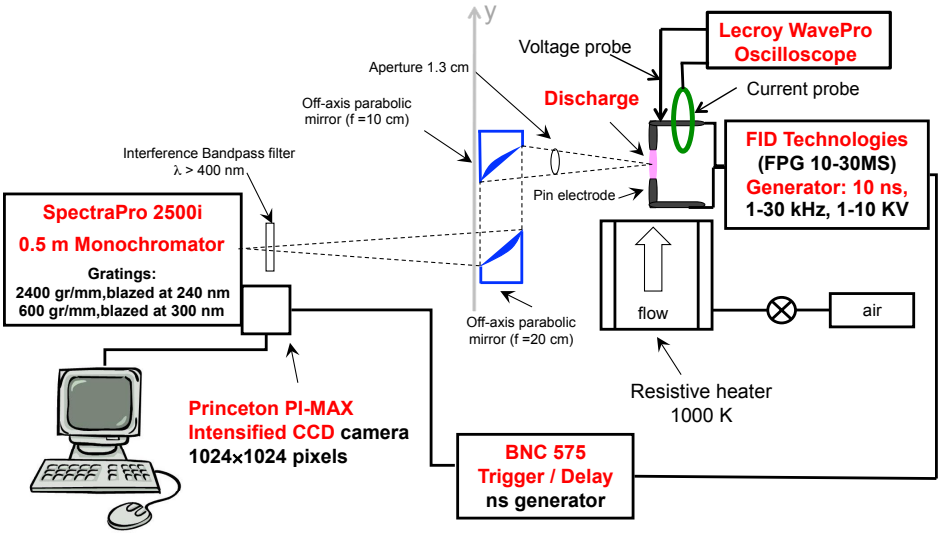

Figure 3.21: New experimental setup for Optical Emission Spectroscopy measurements

To further improve the measurements, in particular the spatial resolution, additional changes were made. Specifically, we exchanged the positions of the two off-axis parabolic mirrors in the optical path. The collecting mirror is now the 10-cm focal length Off-Axis Parabolic (OAP) mirror and the focusing mirror the 20-cm focal length OAP mirror. Thus the system magnification is now 2. Light is now sent directly onto the front entrance slit (100 µm wide, 14 mm height) of the monochromator. The optical system is positioned to collect light perpendicular to the plasma channel. Thus, the lateral spatial resolution is 50 µm horizontally. This is significantly lower than the value of the diameter of the discharge. The slit height being 14 mm, the vertical resolution is 7 mm. Consequently, we are not in the situation of figure 3.20 anymore, but in a situation where the whole diameter watched within the system will be entirely covered by the discharge. Thus, the calibration procedure will be adequate. Furthermore, the improved spatial resolution is sufficient to resolve the discharge diameter. We adjust vertically the discharge so that the image of the plasma is centered on the middle of the entrance slit.

The changes from the previous system have other consequences. The solid angle that is accessible to the system is larger since the collecting mirror has a smaller focal length $f = 10$ cm. Reducing the focal length of the collecting mirror by two increases the solid angle by four, thus increasing the amount of light collected into the monochromator. Consequently, the signals obtained will have a better signal-to-noise ratio. It is important to optimize the f number ($f\#$) of the imaging optics and the spectrometer. The f number of the imaging optics is defined as $f\#_{\text{optics}} = f'/D'$ where f' is the OAP mirror focal length and D' the maximum diaphragm diameter (1.3 cm in this work). The f number of the spectrometer is defined as $f\#_{\text{ spectrometer}} = f/D$ where f is the spectrometer aspheric mirror focal length and D the mirror diameter. In this work, we have $f\#_{\text{optics}} = 10/1.3 = 7.69 \approx f\#_{\text{ spectrometer}} = 50/6.5$, thus the f number of the spectrometer was matched to the f number of the imaging optics in order to optimize the optical system.

When necessary, we place an interference filter at the entrance of the monochromator just before the entrance slit to prevent the second order diffraction of wavelength from 200 to 400 nm to appear on top of the first order diffraction above 400 nm. We were careful to mask any direct light coming from the discharge from getting into the monochromator as this would bias the measurements. Finally, we monitored the electrical parameters using the probe described in section 3.2 to synchronize the OES measurements and the NRP discharges. The synchronization of the high-voltage pulse generator and the ICCD camera will be described in section 3.8.

3.6 Monochromator and ICCD camera

The spectroscopic measurements presented in this thesis were performed with an Acton SpectraPro 2500i monochromator of the Czerny-Turner type, and its main characteristics are described in table 3.5. A schematic diagram of the spectrometer is shown on figure 3.22. Light emitted by the discharge is focused to the front entrance slit of the monochromator by the optical train described in section 3.5 and shown on figure 3.21. As previously mentioned, the f numbers are matched. Light is first reflected off the collimating spherical mirror and is then diffracted by one of the gratings placed on a turrett. The various wavelengths are selectively diffracted. The second spherical mirror focuses light on the CCD array. A calibration procedure in wavelength can be performed with a standard mercury lamp for each grating. This permits to set the correspondence between each pixel of the CCD and the resulting wavelength. We use two different gratings in this work, a 600 gr/mm grating blazed at 300 nm and a 2400 gr/mm blazed at 240 nm. The larger the groove density, the larger the angle of diffraction for a given wavelength. Consequently, for the same width of CCD array (1024 px), the wavelength range observable is narrower with the higher resolution grating. The window observed with 600 gr/mm is 40 nm whereas with the 2400 gr/mm grating, the window is only 9-nm wide. The 2400-gr/mm grating was used in order to maximize the spectral resolution.

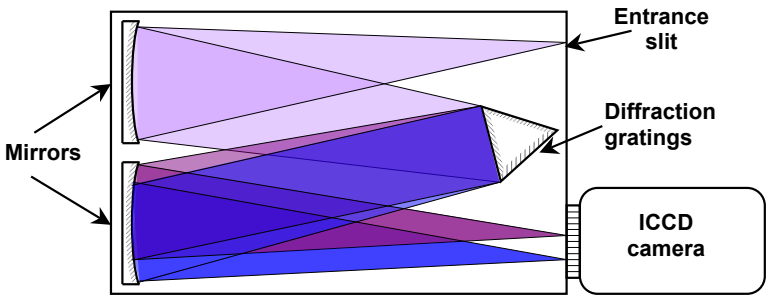

Figure 3.22: Schematic view of the light path in monochromator until the ICCD camera.

The PI-MAX camera is an intensified CCD camera that can be used in either spectroscopy mode or imaging mode. In this section, we describe the use of the camera in the spectroscopy mode, see reference [60]. The user interface is WinSpec. The principle of data acquisition is the following. An incident photon arrives on the photocathode and releases one electron via the photoelectric effect. Each electron is accelerated in the Micro-Channel Plate (MCP), and creates more electrons, resulting in an amplification of the signal - provided high voltage is applied to the intensifier. The resulting electrons strike the

Table 3.5: Specifications and nominal settings used in all measurements for the monochromator-ICCD camera system

SpectraPro2500i Monochromator		
Optical path	180 °	
Mirrors	Original polished aspheric	
Focal length	50 cm	
Slit	14 mm high, 100 μm wide at front entrance	
Diffraction grating	600 gr/mm	2400 gr/mm
Blazing	300 nm	240 nm
Resolution	0.40 nm	0.08 nm
Princeton PI-MAX Intensified CCD camera		
Image intensifier	Micro-Channel Plate (MCP)	
Mode	Gate mode	
CCD array dimension	1024 × 1024 pixels	
Shutter type	Electronic	
Gain	255	
Temperature control	Peltier-effect cooler at -20 °C	
Minimum Gate Width	2 ns	
Princeton Instruments ST-133 controller with Programmable Timing Generator (PTG) Module		
IST-133 timing mode	Internal sync	
PTG Trigger	External	
Operating Mode	Gate mode	

phosphor coating, which causes a release of visible photons that are transferred on the surface of the CCD array. While the photons impact the CCD, they create charges in the corresponding pixel as long as the intensifier is gated on. When the intensifier is gated off, during the read-out phase, accumulated charges are converted into voltage, that is digitally stored. Even when no photon impacts the photocathode, thermal electrons may be generated into the CCD and create so-called dark noise. This dark noise can be reduced by cooling the CCD array. Peltier-effect is used to cool the CCD down to -20°C. To summarize, the integration of a signal of interest on the CCD array constitutes the *exposure phase*. It is followed by the second phase, the *read-out phase* of the CCD, which is the transfer of the integrated signal from the array for storage.

During exposure, CCDs are sensitive to light impacting them and collect charges proportionally to the number of photons detected. The intensifier is used in Gate Mode. It can be switched on at a chosen gate delay triggered by the triggering signal. This mode is particularly relevant to synchronize the PI-MAX camera with the high-voltage pulse generator, as will be described in section 3.8. The time of exposure corresponds to the Gate Width duration when high

voltage is applied to the intensifier. A sequence of several gates can be applied during the exposure time. Each CCD pixel will accumulate charges each time voltage is applied at the intensifier during the gate. A timing diagram of camera operation in Gate Mode is shown on figure 3.23. To summarize, the intensifier controls the amount of light that passes through the system (during a gate width) and that each CCD pixel "sees" during the exposure time.

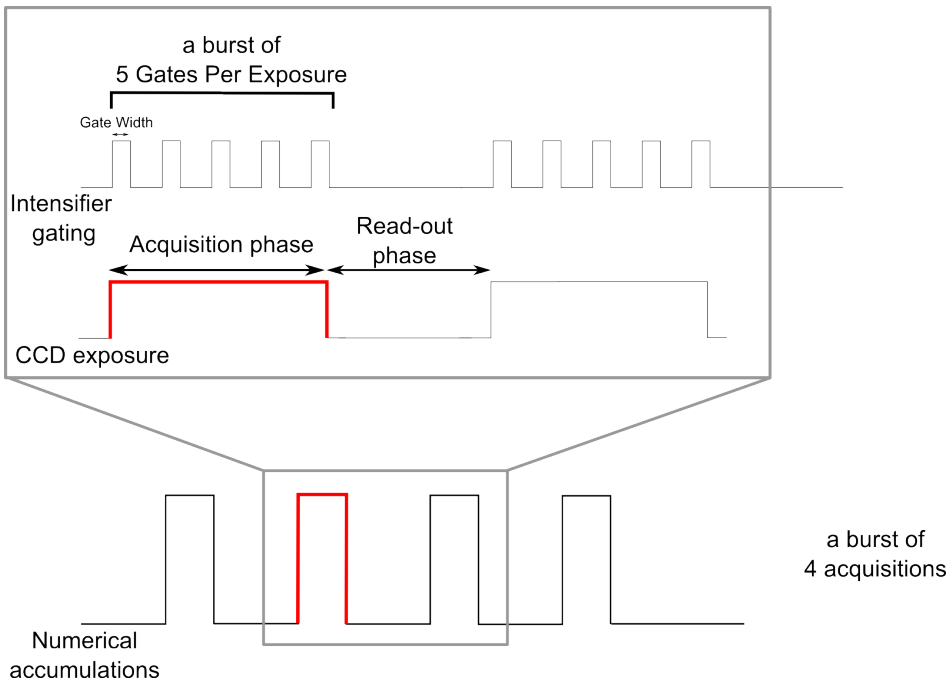

Figure 3.23: Timing diagram for the PI-MAX ICCD camera.

The number of gates during an exposure of the CCD array will be called Gates Per Exposure (GPE) and can be chosen by the operator. Increasing the number of Gates Per Exposure will increase the Signal to Background ratio (S/B) since dark noise mainly results of the activation of the CCD array. Exposure is followed by the read-out phase during which the CCD is emptied and data are stored. The use of a high number of Gates Per Exposure is particularly useful for low repetitive signals such as those produced by the NRP discharges that we will study.

One possibility to improve the Signal-to-Noise ratio (S/N) is to average the signal by repeating the succession of exposure and read-out phases. This succession of exposure and read-out phases will be called an "accumulation" (or numerical accumulation) and the number of accumulations can be chosen by the operator as well. Consequently, to perform a measurement in Gate Mode, the operator must specify the Gate Width (GW), the Gate Per Exposure (GPE), the Gate Delay (GD) and the number of accumulations. GPE are chosen to

maximize S/B without saturating the CCD and damaging the camera. The number of accumulations is chosen to maximize S/N for a reasonable experiment time.

An additional parameter must be chosen, the Range Of Interest (ROI). As previously mentioned, the height of the slit entrance is about 14 mm and the image through the optical system of the 4-mm-high plasma discharge is 8 mm. Consequently, we have adjusted the discharge vertically so as to center its image on the slit entrance. Moreover, since we are interested in the temperature in the mid-gap of the discharge, we limited the ROI to a plasma zone of typically 500 µm centered on the middle of the discharge. Thus, we chose a ROI of typically 75 pixels.

The synchronization between CCD exposure and read-out and the intensifier gating is controlled by the Princeton Instruments ST-133 controller with Programmable Timing Generator (PTG) Module. The settings of the PTG and ST-133 are summarized in table 3.5. The PTG receives an external trigger signal, controls the intensifier gating and directs the ST-133 to control the CCD exposure and read-out phases at appropriate times. This is possible when the ST-133 is set to "Internal Sync". More details on the synchronization procedure of the PI-MAX camera and the NRP discharge can be found in section 3.8.

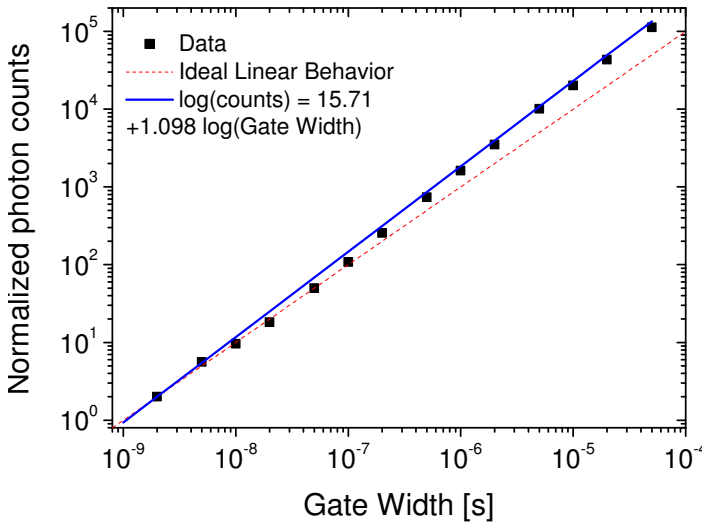

Figure 3.24: Measured photon count as a function of the Gate Width (symbols), with a log-log fit (solid blue line) and comparison with ideal linear behavior (dashed red line).

For a constant light source in front of the spectrometer and ICCD camera sys-

tem, we should see a linear dependence of the signal measured on the camera as a function of the duration of the Gate Width or the number of GPE. For example, if x photons are counted during a 2-ns Gate Width (minimum Gate Width possible for this system), $2x$ photons should be counted during a 4-ns Gate Width or for 2 GPE of Gate Width 2 ns. Unfortunately, reality deviates slightly from the ideal case. Figure 3.24 and 3.25 shows the counted number of photons collected as a function of the Gate Width and GPE. These measurements were obtained by measuring the emission of a stabilized radiation source OL 550 tungsten filament lamp, varying the Gate Width with a fixed number of GPE and numerical accumulations for figure 3.24, and varying the GPE for fixed Gate Width and numerical accumulations for figure 3.25. The other parameters (ROI, Gain) were kept constant. This procedure of calibration of the accumulation rate of the CCD array had already been performed by Pai in [2] for the same ICCD camera. The results found turn out to be very similar to those obtained by Pai a few years ago, thus indicating that the characteristics of the CCD camera system remain very stable over long periods of time.

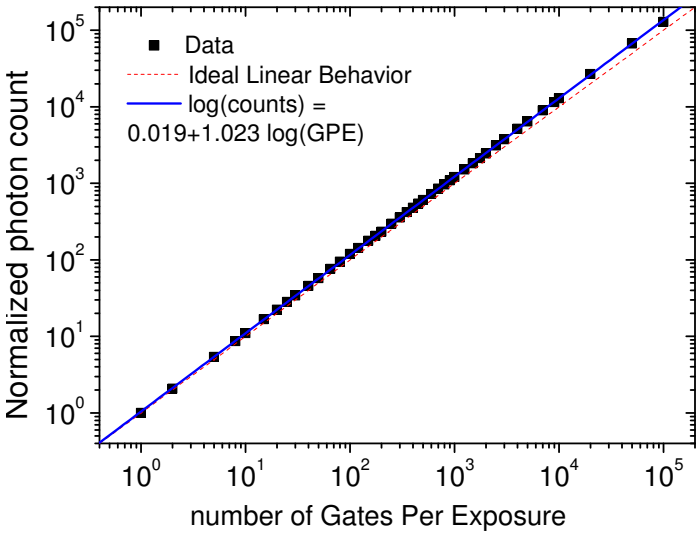

Figure 3.25: Measured photon count as a function of the number of Gates Per Exposure (symbols), with a log-log fit (solid blue line) and comparison with the ideal linear behavior (dashed red line).

For a given intensity of the tungsten filament, a limited range of Gate Widths is accessible. Consequently, when the signal is close to the saturation limit, a second measurement in exactly the same conditions is taken at either a reduced lamp intensity or for fewer GPE. The ratio of both measurements is used to normalize the second measurement realized at reduced lamp intensity or for fewer GPE. Several values of Gate Width from 2 ns to 50 µs were investigated. We also repeated the procedure from 1 to 100,000 GPE.

Figures 3.24 and 3.25 show that the camera is nearly ideal for small Gate Widths and small numbers of GPE. However, the behavior deviates from linearity significantly for high Gate Widths. The deviation is less marked for high numbers of GPE. In both cases, the fits given on the figures account for the real behavior of our system at the time of our experiments.

We will use these fits to scale our measurements for different GW and GPE, so as to simplify the calibration procedure, as detailed in section 3.7.

3.7 Calibration in absolute intensity of the spectrometer and ICCD camera system

This section presents the procedure for calibration in absolute intensity of the spectrometer and ICCD camera used for Optical Emission Spectroscopy measurements in chapter 4. Each component of the optical detection system has its own spectral response: the CCD response varies with wavelength and so does the mirror's response, etc. The grating response depends much on the wavelength, with a peak at the blazed wavelength. Both gratings we used are blazed in UV, where the response of the ICCD and mirrors is the lowest. Consequently, the overall response of our system must be determined experimentally.

To acquire the absolute system response in the range 350-800 nm, we used a standard radiance system: an Optronic Laboratories OL550 tungsten ribbon-filament lamp with calibration traceable to NIST standards, when operated with 15.000 A and approximately 5 V. The spectral radiance I_λ of a surface area $\mathcal{A}$ that emits spatial power Φ_λ over solid angle Ω at normal incidence in the wavelength range $\Delta\lambda$ is given by:

$$I_\lambda = \frac{\Phi_\lambda[W]}{\Delta\lambda\ [nm]\ \cdot \mathcal{A}\ [\mathrm{cm}^2]\ \cdot \Omega\ [sr]} \tag{3.1}$$

This formula is true as long as we consider small $\mathcal{A}$ and Ω at normal incidence, which will be the case in all our experiments. The instrumental broadening of the spectrometer is expressed by the spectral width $\Delta\lambda$. The instrumental broadening is different for the two gratings used. We measured it using a Thorlabs HRP 120 He-Ne laser at 632 nm for the slit width used in our study (100 µm) for both gratings. The slit function of the 600 gr/mm grating is shown on figure 3.26. The profile is approximately a Gaussian of FWHM equal to 0.400 nm. For the 2400 gr/ mm grating, an additional correction must be taken into account.

In chapter 4, we will investigate spectra around 380 and 660 nm. The slit function of the spectrometer and ICCD camera is obtained at 632 nm. This means that we need to take into account the variations of the linear dispersion

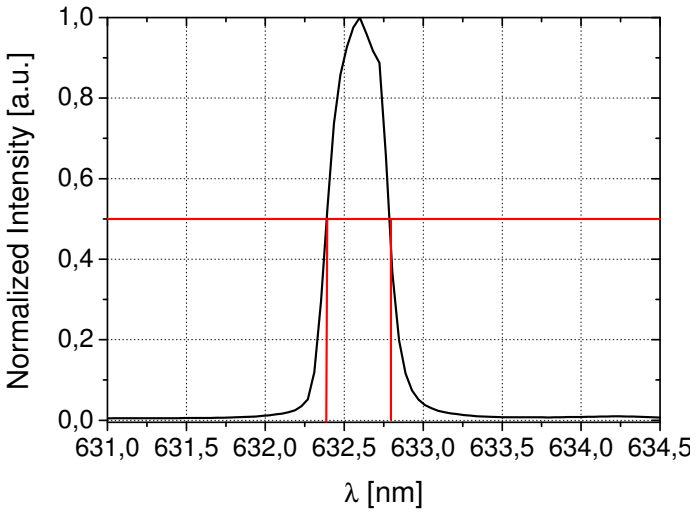

Figure 3.26: Measured slit function of the SpectraPro monochromator with the 600 gr/mm grating used in this study. The FWHM of this Gaussian profile is approximately 0.403 nm.

of the system with wavelengths. The reciprocal linear dispersion is given by [61]:

$$\frac{d\lambda}{dx} = \frac{\lambda}{2f}\left(\tan\Phi + \sqrt{\left(\frac{2d}{m\lambda}\cos\Phi\right)^2 - 1}\right) \tag{3.2}$$

where f represents the focal length of the monochromator (0.50 m), d the spacing between the grooves of the grating, m the order of dispersion, and Φ half the angle between the lines joining the center of the grating to the centers of the two mirrors of the monochromator. Φ equals to 9.0 ° for the SpectraPro spectrometer used in this work, and all measurements were done at first order (m=1).

Figure 3.27 shows the reciprocal linear dispersion curves for both gratings used in this study. For the 600 gr/mm grating, the curve is approximately constant over 300-800 nm. In contrast, for the 2400 gr/mm grating, $d\lambda/dx$ changes significantly over 300-800 nm. Consequently, to obtain the spectral broadening around 380 nm, we need to dilate the abscissa of the slit function measured at 632 nm in the following way:

$$\lambda_{\text{dilated}} = \lambda_{\text{measured}} \cdot \frac{(d\lambda/dx)_{\ 360\ \text{nm}}}{(d\lambda/dx)_{\ 632\ \text{nm}}} \tag{3.3}$$

Figure 3.28 shows a comparison of the measured slit function and the slit function after the dilatation procedure. The dilatation procedure multiplies the

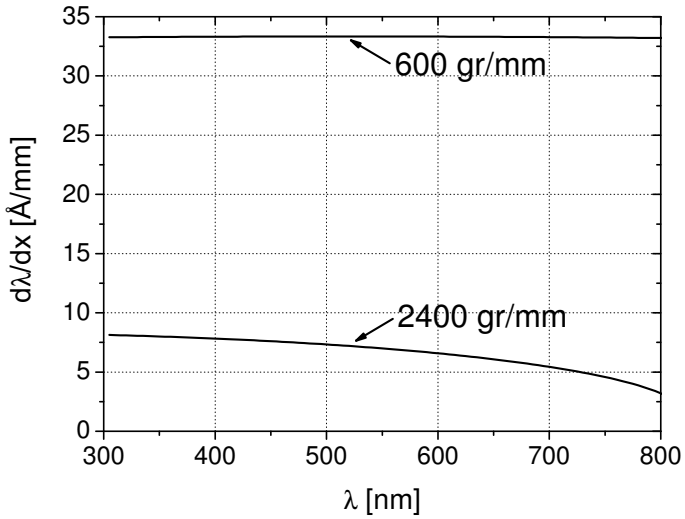

Figure 3.27: Reciprocal linear dispersion of the two gratings used with the SpectraPro spectrometer.

FWHM by a factor 1.25, thus giving a FWHM of 0.104 nm. This value will be used for all experiments performed with the 2400 gr/mm grating. Once we know the spectral resolution $\Delta\lambda$, we can determine the system response in intensity.

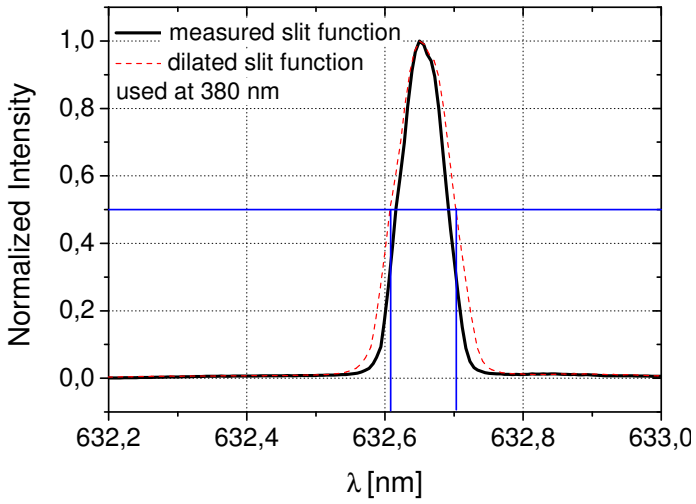

Figure 3.28: Measured (thick black solid) slit function and dilated (thin red dashed) slit function of the SpectraPro spectrometer with the 2400 gr/mm grating used in this study. The dilated slit function takes into account the variation of linear dispersion with wavelength. The FWHM obtained is 0.104 nm and will be used for measurements in the range 300-400 nm.

Since the absolute system response depends on the collection area and solid angle, we must place the tungsten lamp exactly at the focal point of the collecting mirror (same location as the discharge) and work with the same solid angle. The discharge diameter is approximately equal to 500 µm and the tungsten filament is 2 mm wide. As the imaged region is approximately 50 µm wide, i.e. smaller than the plasma and the tungsten filament, the problem mentioned in section 3.5 will not appear here, which validates the calibration procedure.

Calibration should be done with the same experimental settings for the ICCD camera as during the discharge emission measurements. However, the calibration tungsten lamp emission around 380 nm is very low. Thus, we increased the GPE (to 20,000 for instance) in order to have a good Signal-to-Background Ratio (see section 3.6), keeping all other parameters constant. Then we used figure 3.25 to correct the calibration signal for the appropriate number of GPE.

3.8 Synchronization of the ICCD camera with the discharge

In this section, we present the synchronization of the high voltage pulse generator creating the discharge with the ICCD camera controlled by the PTG. For the two diagnostics used - OES with spectrometer and ICCD camera, and imaging with ICCD camera, we used an intensified Princeton Instruments PI-MAX CCD camera with a Programmable Timing Generator (PTG), as described in sections 3.2 and 3.6. For both techniques, the synchronization procedure is identical.

Figure 3.29 shows a block diagram of the devices used. Synchronization was controlled by a Berkeley Nucleonics Corporation (BNC) 575 digital pulse delay generator, which triggered both devices. The synchronization procedure was already described in [2].

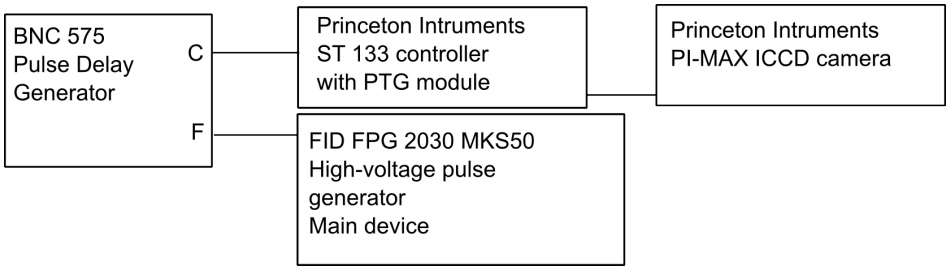

Figure 3.29: Block diagram of the synchronization scheme for ICCD camera and high-voltage pulse generator.

The PI-MAX camera is triggered by Channel C of the BNC 575 pulse delay generator with a TTL signal sent to the "Ext. Trig. In" input of the PTG

that initiates the required PI-MAX gating and readout cycle. The total delay between the TTL signal and the photocathode gating, called $\Delta\tau_{cam}$, depends on several parameters: the cable delay between the BNC pulse delay generator and the PTG, the internal delay of the PTG controller, and the Gate Delay, which can be changed by the operator. Channel F delivers the high voltage pulse generator trigger signal, either for Pulser 1 or 2. Pulser 1 requires a 10-V, 100-ns square-signal and Pulser 2 a 5-V, 80-ns square signal. The high-voltage generation delay following its trigger signal may be different and changes slightly for the two pulsers. It also depends on the PRF, see [2]. There might be an additional delay between the high-voltage pulse and the plasma emission. Finally, the optical path, which was about 3 m for OES and 40 cm for direct visualization, adds an optical path delay that depends on the diagnostics used. The total delay between the trigger signal and the arrival of light on photocathode will be called $\Delta\tau_{dis}$. Figure 3.30 presents a time diagram of the synchronization of the PI-MAX camera with the high-voltage generator.

The initial delay between Channel C and Channel F was set to 0. What is relevant to control is the delay between the photocathode gating and the arrival of light on the photocathode, that is to say the difference between $\Delta\tau_{cam}$ and $\Delta\tau_{dis}$. This is performed by adjusting the Gate Delay (GD) of the photocathode. For each experiments, we determined the Gate Delay that synchronized the photocathode gating and arrival of light on the photocathode. We first started with a Gate Width (GW) longer that the inter-pulse duration ($GD > 1/PRF$). In this case, a discharge is always observed during the photocathode gating. The Gate Width is then reduced down to 2 ns by dichotomy. The procedure is summarized on figure 3.31. Let's assume an initial GW of τ ns. GW is divided by two while keeping the Gate Delay constant. Two cases may happen: either the signal is still present and the procedure can be repeated (case 1) or no light is detected (case 2), and then we increase the gate delay by $\tau/2$ to detect light again. When the Gate Width becomes small (50 ns), the light intensity may decrease, meaning that the photocathode gate only captures part of the discharge. In this case, the Gate Delay must be either increased or decreased by a few nanoseconds to capture the whole discharge.

This procedure is applied until it is possible to see light during a 2-ns GW. Then, the GD is reduced until we see no light. We have then obtained the GD that corresponds to the start of the discharge. The emission of the discharge can then be studied in time using a 2-ns GW and increasing by 1 or 2-ns step the GD, or we can integrate the light of the whole discharge using a longer GW (20 ns for Pulser 1, 25 ns for Pulser 2 Channel 2 and 50 ns for Pulser 2 Channel 1).

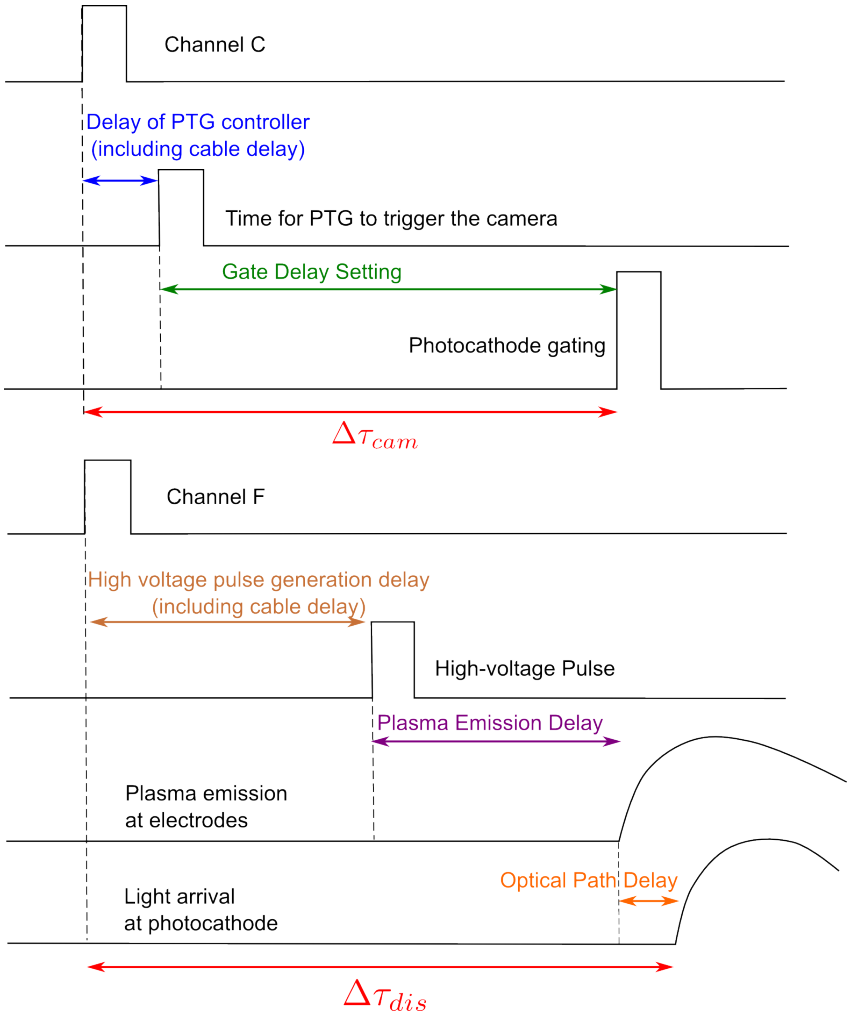

Figure 3.30: Time diagram of the synchronization of the PI-MAX ICCD camera photocathode with high-voltage pulse generator.

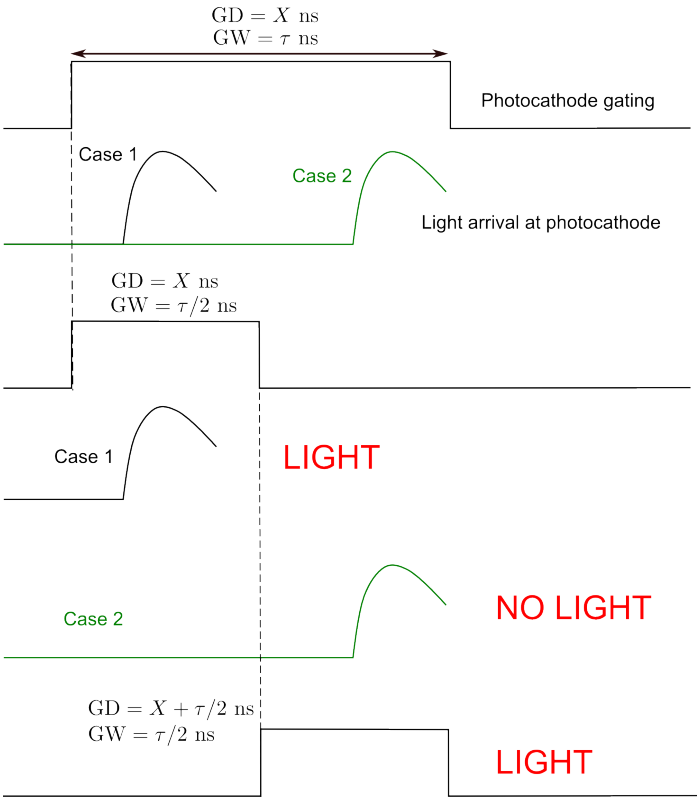

Figure 3.31: Description - with a time-diagram of photocathode gating and light arrival at the photocathode - of the method for the determination of the Gate Delay corresponding to the beginning of the discharge emission.

3.9 Influence of the probe position on the voltage measurements

In this section, we study the influence of the voltage probe position on the measurements of discharge voltage during application of the high voltage pulse. The voltage was measured with a Lecroy PPE20 kV high-voltage probe, as detailed in section 3.2. Because the tips of the electrodes were hot when working in preheated air, it was not possible to position the high-voltage probe at the tip of the electrode but rather at the electrode terminal located about 15 cm from the electrode tip. The inductance of the 15-cm long electrodes (about 1 mH/m) could affect the measured voltage. Since the conduction current in both regimes is quite different, it could have a different influence on the role of the inductance of the electrodes. Thus, we investigated separately the influence of the position of the probe on the two regimes studied in this work: NRP glow and NRP spark discharges.

3.9.1 Influence of the position of the high-voltage probe for glow discharge voltage measurements

First, we investigated the influence of the position of the probe on the measured voltage waveform in typical glow discharges obtained with Pulser 2. The various positions studied are indicated on figure 3.32.

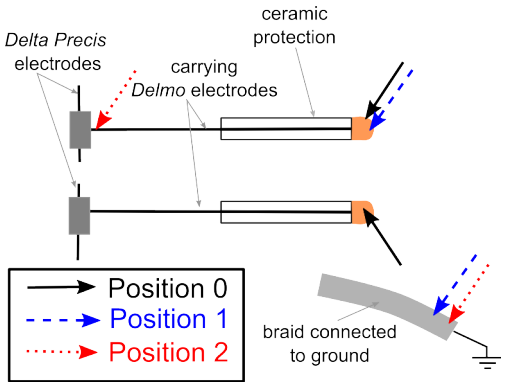

Figure 3.32: Schematic view of the three positions investigated for the influence of the high-voltage probe location on the voltage waveform during a glow discharge.
The probe tip can either be attached to the anode terminal (position 0 and 1) or the extremity of the carrying electrode (position 2) and the ground tip of the probe can be attached to the cathode terminal (position 0) or the ground braid (position 1 and 2).

We compared position 0, where the probe tip was attached to the anode terminal and the ground tip to the cathode terminal, position 1, where the probe tip was attached to the anode terminal and the ground tip to the ground braid and

position 2, where the probe tip was attached to the extremity of the carrying electrode and the ground tip to the ground braid. Position 0 is the only possible position for the voltage probe when experiments are done using preheated air.

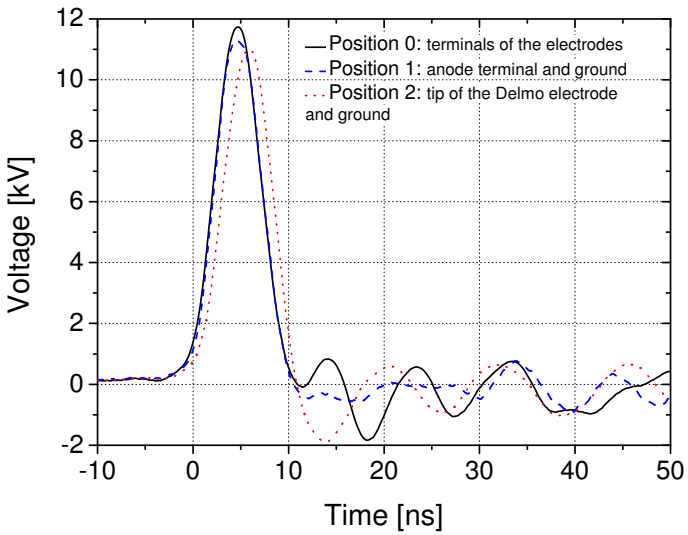

Figure 3.33: Voltage waveforms measured at different positions on the electrodes of the high-voltage probe for a typical NRP glow discharge.

Figure 3.33 shows the comparison of the voltage waveforms from a typical glow discharge at $T_g = 300$ K (see chapter 5), the voltage probe being at the different positions previously described. We can see that the voltage waveforms aspect are very similar whatever the position of the probe. The ringing due to the probe loading is slightly attenuated when the ground tip is connected to the ground braid. Consequently, we have taken the voltage measurements for the glow regime in position 0, whether working in preheated air or not.

3.9.2 Influence of the position of the high-voltage probe for spark discharge voltage measurements

During an NRP spark discharge, the conduction current can increase up to 35-40 A, thus the influence of the electrode inductance might be important and create an additional voltage that might influence the measured voltage depending on the position of the voltage probe. In this subsection, we investigate the influence of the position of the probe on the voltage and current waveforms and on the calculated energy of a typical spark discharge.

To investigate the position close to the electrode tip, we worked in ambient air. Consequently, we worked with Pulser 1 with an inter-electrode gap distance of $d \approx 2$ mm and increased the voltage up to 7 kV to obtain a spark discharge. We

investigated positions 0 and 1 and we also measured the voltage when the tips of the probe were in the middle of the electrode joint, after the ceramic protection (position 3), and when they were at the end of the electrodes (position 4). These various positions are summarized in figure 3.34.

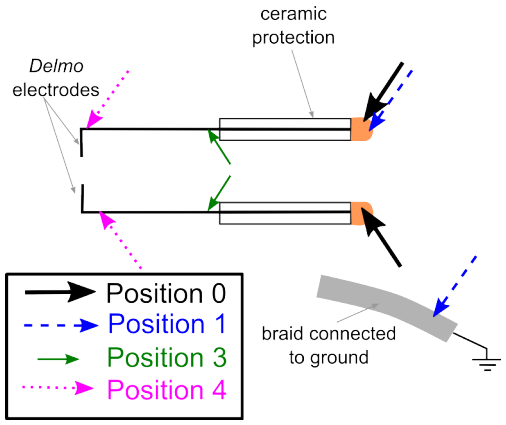

Figure 3.34: Schematic view of the four positions investigated for the influence of the high-voltage probe location on the voltage waveform during a spark discharge.
The probe tip can either be attached to the anode terminal (position 0 and 1), the middle (position 3) or the extremity of the anode (position 4) and the ground tip of the probe can be attached to the cathode terminal (position 0), the ground braid (position 1), the middle (position 3) or the extremity of the cathode (position 4).

First of all, we notice on figure 3.35 (a) that when placing the ground tip of the high-voltage probe on the ground braid, the ringing of the measured current is reduced. The various voltage waveforms measured, see figure 3.35 (b), clearly show that the voltage waveforms are slightly different when the voltage is measured at the end of the electrodes close to the plasma, or at the electrode terminal.

However, we determined the energy deposited into the plasma using probes in positions 0 and 4 (see section 4.3 for details on energy measurements). Figure 3.36 shows that even though the voltage waveforms are slightly different in the two positions, the energy is 805 ± 5 µJ in both cases. Thus, because in preheated air the terminal of the electrode is the only location possible for the high-voltage probe, we will always place the high-voltage probe at this location (position 0) in the present study.

In this section, we have shown that the voltage waveforms measured at the electrode terminals are similar to those measured across the NRP glow discharge. For the NRP spark discharge, the voltage waveforms differ somewhat, but the energy measurements are within 0.1%.

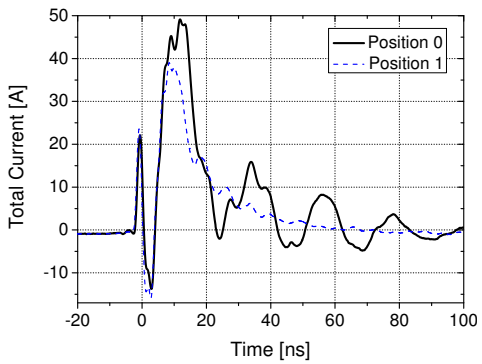

(a) Current waveforms measured for positions 0 and 1

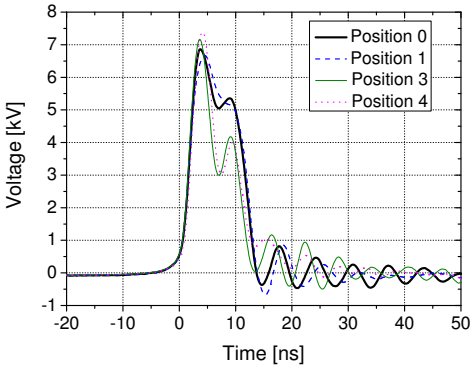

(b) Voltage waveforms measured for positions 0, 1, 3, and 4

Figure 3.35: Electrical measurements for different positions of the high-voltage probe for a typical NRP spark discharge.

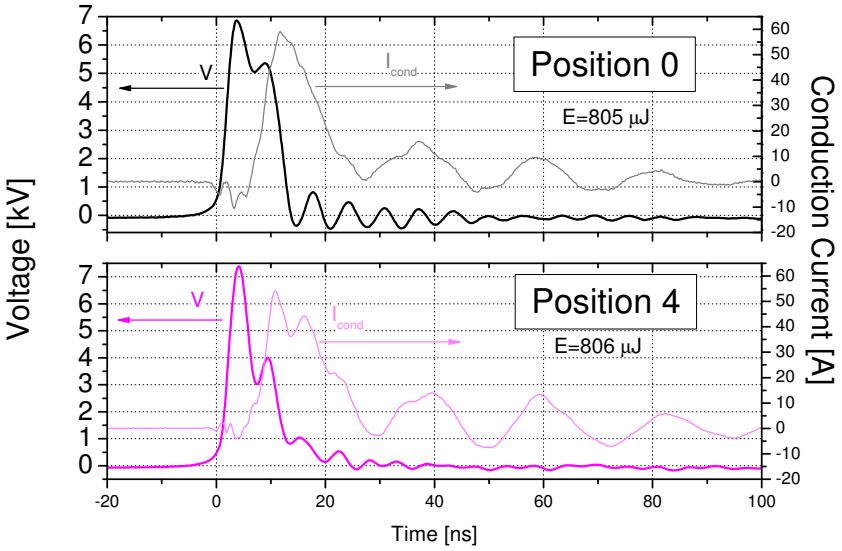

Figure 3.36: Voltage, current and energy determined using the voltage waveforms measured at position 0 (top) and position 4 (bottom).

3.10 Conclusions

In this chapter we have presented the experimental setup used in the present work and the main characteristics of the various components. In section 3.2, we have presented the plasma generation system and the various diagnostics used. The main characteristics of Pulser 2 were detailed in section 3.3 and the various electrodes used in section 3.4. We have discussed in sections 3.5 and 3.6 the experimental setup for the Optical Emission Spectroscopy measurements and the main characteristics of the spectrometer and ICCD camera used. We explained the calibration procedure of the spectra obtained by OES in section 3.7, and the synchronization of the ICCD camera with the discharge in section 3.8. Finally, in section 3.9, we have shown that the position of the probe had no influence on the voltage waveforms measured during a glow discharge, and that the position of the probe did not influence the energy determined during a spark discharge.

Chapter 4

Ultrafast Heating following an NRP Spark Discharge in Air

4.1 Introduction

In this chapter, we have investigated the ultrafast heating of the gas by NRP spark discharges in preheated air to provide validation data for the two-step mechanism described in section 2.6. In section 4.2, we describe the "*reference case*" that we study in this chapter and which corresponds to the same experimental settings as in [6]. Most of the work focus on the use of Optical Emission Spectroscopy calibrated in intensity to study the first and second positive systems of N_2 in an NRP spark discharge corresponding to the *reference case*.

First, in section 4.3, we determine the energy deposited in the discharge to verify that we are in the *reference case*. Then we detail the method used to determine the rotational and vibrational temperatures of $N_2(C)$ and $N_2(B)$ from the emission spectra obtained in section 4.4. In section 4.4.1.1, we determine the rotational temperature of $N_2(C)$ and in section 4.4.1.2, we show that the rotational temperature of $N_2(C)$ corresponds to the gas temperature. In section 4.4.2, we show spectra of N_2(C-B) obtained in a wider spectral range and determine the vibrational temperature of $N_2(C)$. To determine the absolute densities of these excited states, we investigate the plasma diameter in section 4.5.

In section 4.6.1, we show the absolute densities deduced from the emission spectra and we discuss the validity of the results. We synchronize the time-evolution of the densities of $N_2(C)$ and $N_2(B)$ with TALIF atomic oxygen measurements [6] and electrical measurements. In section 4.6.2, we deduce the temperature dependence of the quenching rates of the $N_2(C)$ and $N_2(B)$ states which are key controlling rates in the two-step mechanism. Finally, in section 4.7, we

determine the time-evolution of the electron number density at the beginning of the high voltage pulse.

4.2 Description of the *reference case*

In order to validate experimentally the two-step mechanism presented in section 2.6.1, Stancu *et al* investigated the densities of the key species involved in the mechanism. The number density of $N_2(A)$ was studied with Cavity Ring-Down Spectroscopy (CRDS) in [6] and [48]. The number density of the ground state of atomic oxygen was studied with time-resolved Two-photon Absorption Laser Induced Fluorescence (TALIF) [6], [49]. Finally, the number densities of $N_2(B)$ and $N_2(C)$ were studied with Optical Emission Spectroscopy (OES) and the gas temperature was deduced from the rotational temperature of the second positive system of N_2 (see section 4.4.1.2) [6], [50].

However, as detailed in section 3.5, the OES measurements of $N_2(B)$ and $N_2(C)$ number density temporal evolution must be confirmed, in particular because of the uncertainties in the calibration procedure due to the previous use of an optical fiber and a large pinhole. That is why we implemented new OES measurements without any optical fiber with better spectral and spatial resolution, see section 3.5 and 3.6 for details about the experimental setup. Hence, to use the previous TALIF atomic oxygen number density measurements, we worked in the ***reference case*** corresponding to these measurements. In the whole chapter, the experimental parameters correspond to this *reference case*. It corresponds to an NRP spark discharge in preheated to $T_g = 1000$ K air. The air was flowing at $v = 2.6$ m.s^{-1} parallel to the electrodes (see figure 3.2), and the inter-electrode gap distance was fixed at $d = 4$ mm. The pulse repetition frequency was set at $PRF = 10$ kHz and the applied voltage was set to $V_p = 5.7$ kV.

4.3 Electrical characterization

In this section, we study the electrical characterization of the NRP spark discharge studied in this chapter - the *reference case* and determine the energy deposited into the discharge to verify the correspondence with the atomic oxygen measurements [6]. The method to determine the energy of an NRP spark discharge was detailed in [2]. When a plasma is observed in a pin-pin configuration, the measured total current I_{tot} corresponds to two different terms:

$$I_{tot} = I_{disp} + I_{cond} \tag{4.1}$$

I_{disp} corresponds to the displacement current related to the equivalent capacitance that constitute the electrodes. The conduction current I_{cond} is important

only in the case of an NRP spark discharge where a conducting channel is established between the electrodes; the conduction current can increase up to 40-60 A [2]. In order to measure the displacement current, we record current and voltage traces in ambient air, while keeping the same settings of the experiments - in particular the applied voltage on the electrodes - when no discharge is observed. In this case, the measured current is only a displacement current.

$$I_{disp} = C\frac{dV_p}{dt} \tag{4.2}$$

Figure 4.1 presents the measured total current and the calculated displacement current. Synchronization of I_{disp} and I_{tot} in such conditions gives the delay between the current and voltage. By convention, time $t = 0$ ns is defined as the time when the rising edge of the pulse measured by the voltage probe reaches 50 % of its maximum value. The capacitance of the electrodes is calculated by matching the amplitudes of the derivative of the applied voltage and of the total current. In our case we find $C = 8.7$ pF.

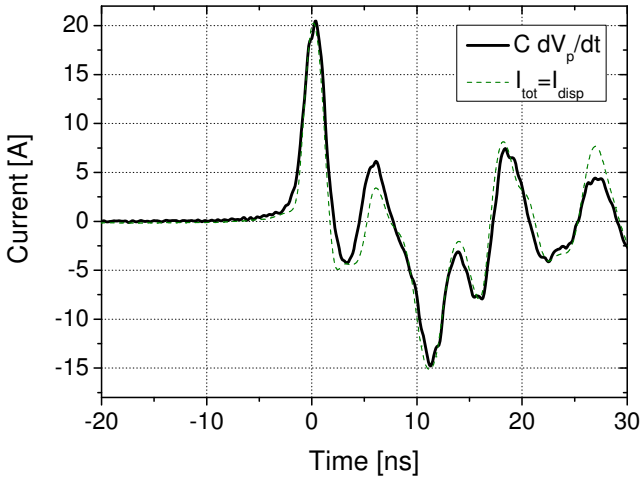

Figure 4.1: Measured current waveform (dash green) in ambient air with no plasma discharge, and capacitive displacement current calculated from the applied voltage (thick black). The capacitance of the electrodes deduced from matching the amplitudes of the waveforms is $C = 8.7$ pF.

The value of the electrode capacitance C and the delay between current and voltage waveforms determined when no plasma is present is intrinsic to the electric circuit. We use its value to determine the conduction current $I_{cond} = I_{tot} - I_{disp} = I_{tot} - CdV_p/dt$ from the measured total current and voltage for the NRP spark discharge studied. Figure 4.2 shows the measured current waveform, the calculated displacement current and the resulting conduction current of the

NRP *reference case* spark discharge. The amplitude of the conduction current is about 35 A.

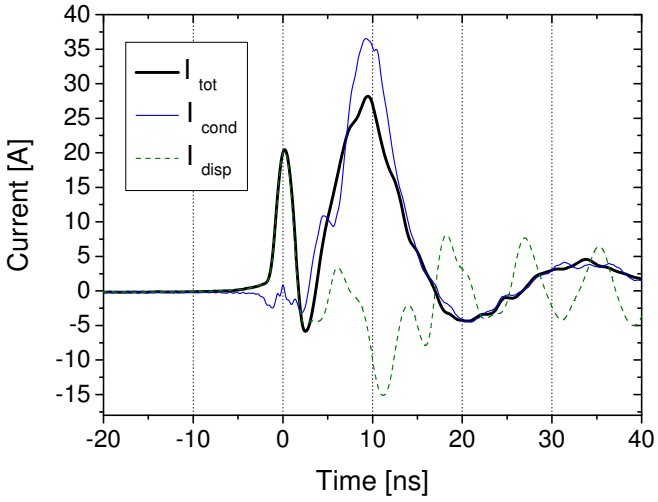

Figure 4.2: Measured current waveform (thick black) in the NRP *reference case* spark discharge, capacitive displacement current calculated from applied voltage (dash green), and resulting conduction current (thin blue).

The total energy deposited within the discharge is obtained by multiplying the measured voltage and conduction current waveforms to obtain the power, which is then integrated in time over the pulse duration to yield the energy.

We can deduce from the measured voltage the value of the reduced electric field E/N. For an NRP spark discharge, a good estimation is to consider that [2], [57]:

$$\frac{E}{N} = \frac{V_p}{d \cdot N} \tag{4.3}$$

where V_p is the measured applied voltage, d the inter-electrode gap distance and N is the number density of the gas. N can be deduced from

$$N = \frac{P}{k_B T} \tag{4.4}$$

where P is the pressure, T the temperature, and k_B the Boltzmann constant. Although air is preheated to 1000 K, the initial gas temperature is about 1500 K due to the heating from previous pulses, see section 4.4.1.1. Furthermore, we consider that during the first 40 ns after the beginning of the high-voltage pulse, the volume of the discharge is approximately constant - the timescale being small compared to the hydrodynamic timescale (few hundreds of nanoseconds)

[51]. Hence, we can deduce the profile of the reduced electric field E/N in Td (1 Td = 1 $\times 10^{-17}$ V.cm^2) from the profile of the applied voltage using equations (4.3) and (4.4).

Figure 4.3 shows, for the NRP *reference case* spark discharge, the measured applied voltage and corresponding reduced electric field E/N, conduction current and calculated energy per pulse deposited into the plasma. The value obtained is 650 $\pm$ 50 µJ, which corresponds to the same value as in the discharge studied by Stancu *et al* [6], for the atomic oxygen density measurements.

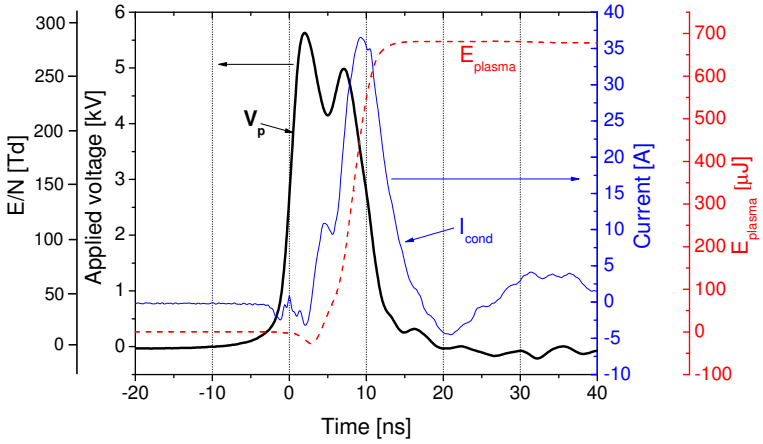

Figure 4.3: Measured applied voltage and corresponding reduced electric field E/N (thick black), conduction current (thin blue) and calculated energy deposited per pulse (dash red) in the NRP *reference case* spark discharge.

4.4 Temperature measurements

The aim of this section is to determine the rotational and vibrational temperatures from the calibrated spectra of N_2(B) and N_2(C) via the emission of the $N_2(B^3\Pi_u$ - $A^3\Sigma_u^+)$ and $N_2(C^3\Pi_u$-$B^3\Pi_g)$ electronic systems of N_2, also called the first and second positive systems of N_2, respectively. First, we will detail how we obtained the rotational temperature of N_2(C) in section 4.4.1. Then, we describe the method we employ to determine the vibrational temperature of N_2(C) in section 4.4.2.

4.4.1 Rotational temperatures

In section 4.4.1.1, we describe the experimental procedure we led to obtain the rotational temperature of N_2(C), then in section 4.4.1.2 we explain why it is

a good approximation of the gas temperature and finally, in section 4.4.1.3 we present additional $N_2(C)$ rotational temperature data.

4.4.1.1 Rotational temperature of $N_2(C)$ and $N_2(B)$

We use the 2400 grooves/mm grating to study the second positive system of N_2 to maximize the spectral resolution. For the first positive system, a 600 grooves/mm grating is used since the accessible wavelength range is from 610 nm to 710 nm, i.e. much larger than the 9-nm window of the 2400 gr/mm grating. As was explained in section 3.5, we need to add a Melles Grillot 03FCG 061 longpass interference filter absorbing light for $\lambda < 420$ nm in order to suppress the second order of diffraction. The emission of the vibrational bands (3,0) to (11,8) of $N_2(B \rightarrow A)$ is recorded between 610 and 710 nm. The temporal evolution of the emission of $N_2(B)$ and $N_2(C)$ is recorded every 2 ns during the high voltage pulse and until 25 ns afterwards, with a temporal window of 2 ns. We align our system in order to measure the emission from the center of the discharge on a 500-µm height. As the spatial resolution of the system is small (50 µm), we carefully check the spatial stability of the discharge by monitoring the intensity for a given set of parameters and ensuring it does not vary by more than 10% over the course of the measurements. This procedure was applied for all measurements presented in this chapter.

An important step after acquiring any spectrum is to subtract the straylight. For any wavelength, the signal recorded by the CCD can come either from the light diffracted by the grating, but it can also come from light that enters by the entrance slit into the monochromator, and arrives on the CCD by another path. This light is not diffracted (i.e. can have any wavelength) and should not be taken into account into the measured spectrum. A way to determine the straylight is to set the grating at 160 nm in the VUV where room air O_2 absorbs all radiation. Consequently, the signal measured in this setting corresponds only to straylight. For all the spectra considered in this work, we checked that the signal over straylight ratio was much greater than one. Once we obtain the resulting spectra, we calibrate them in intensity. The calibration procedure was described in section 3.7. We should be careful to calibrate in intensity with a filter when the emission was recorded with a filter, for $N_2(B)$ for instance. This procedure to obtain calibrated spectra will be used in this whole chapter.

Typical calibrated spectra of N_2(B-A) and N_2(C-B) are presented on figure 4.4 in black symbols. The vibrational bands are indicated. The experimental spectra were fitted with Specair 2.3 [41] ,[42] and are presented in solid red lines. We note that the simulated spectra correspond quite well to the experimental spectra for both transitions. Atomic lines of O at 615 nm, and H at 656 nm can also be seen on the $N_2(B \rightarrow A)$ spectrum.

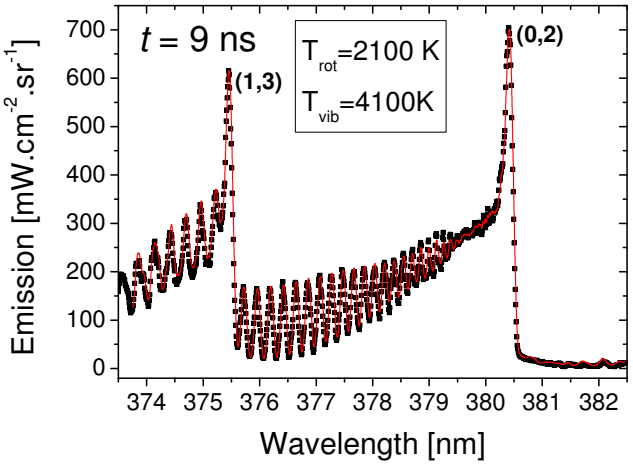

(a) $N_2(C \rightarrow B)$ spectra

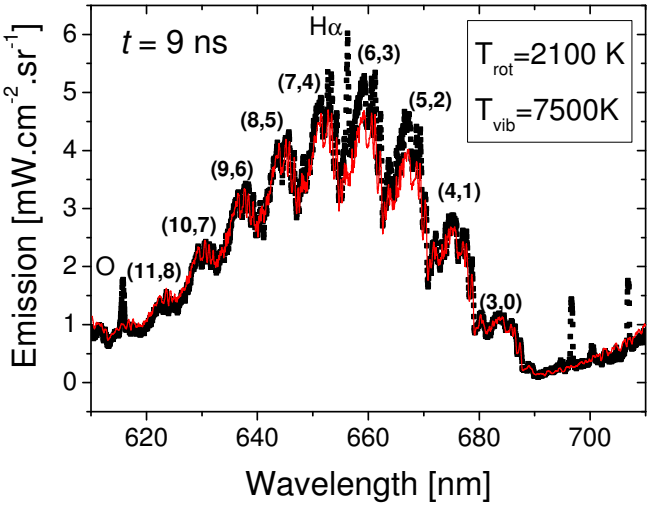

(b) $N_2(B \rightarrow A)$ spectra

Figure 4.4: Experimental calibrated spectrum (black symbols) and Specair simulated spectrum (solid red line) of (a) $N_2(C \rightarrow B)$ (0,2) and (1,3) vibrational bands and (b) $N_2(B \rightarrow A)$ Δv = -3 series between 610 and 710 nm. Experimental spectra integrated for 2 ns at the maximum of emission of the NRP *reference case* spark discharge.

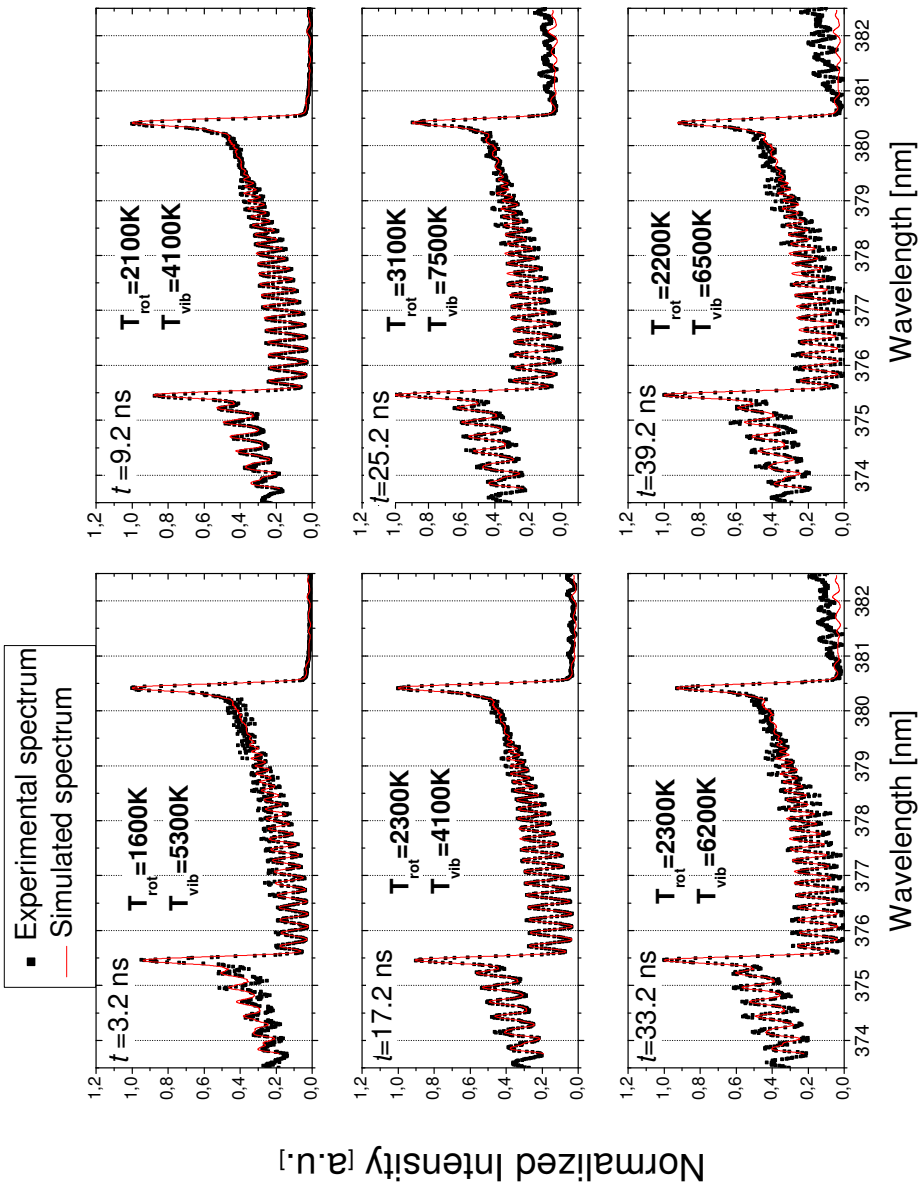

Figure 4.5: Experimental (black symbols) and simulated spectra (red lines) obtained for various times t, integrated for 2 ns. Experimental spectra obtained with the 2400 gr/mm grating and calibrated in intensity.

From these calibrated spectra, we can deduce the vibrational, rotational and electronic temperatures of the emitting state at every time t. Typical $N_2(C)$ spectra obtained at different times t during and after the high voltage pulse are presented on figure 4.5. The time-evolution of the rotational temperature of $N_2(C)$ is shown on figure 4.6. The rotational temperature of $N_2(B)$ is assumed to be equal to the rotational temperature of $N_2(C)$ due to the fast translational-rotational equilibrium, see section 4.4.1.2. There is a large increase of rotational temperature, $\Delta T = 1000$ K within 20 ns, which confirms the ultrafast heating.

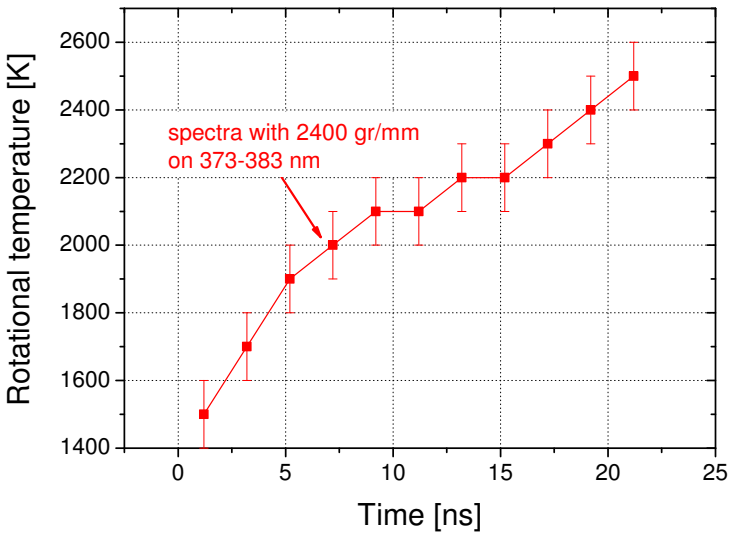

Figure 4.6: Time-evolution of the rotational temperature of $N_2(C)$ obtained from emission spectra of figure 4.5 with the 2400 gr/mm grating.

It is important to determine precisely the rotational temperature of $N_2(C)$ to validate the two-step mechanism because it is a good marker of the temperature of the gas at atmospheric pressure. The goal of the next section is to verify this assumption.

4.4.1.2 Validity of the gas temperature measurement

In this section, we investigate the conditions for which the rotational temperature of $N_2(C)$ is representative of the gas temperature.

We first examine the usual assumption at atmospheric pressure:

$$T_{rot}N_2(C) = T_{rot}N_2(X) = T_{trans}N_2(X) \tag{4.5}$$

During the pulse from $t = 0$ ns to $t = 12$ ns, $N_2(C)$ is populated primarily by electron-impact excitation of the ground state of N_2:

$$N_2(X) + e^- \quad \rightarrow \quad N_2(C) + e^- \tag{4.6}$$

Table 4.1: Rotational constants, characteristic rotational temperature and rotational quantum number of the maximum of the Boltzmann rotational distribution of various N_2 electronic states.

State	$Be[cm^{-1}]$ [63] [64]	$\theta_{rot}[K]$	J_{max}
$N_2(X)$	1.99824	2.9	16
$N_2(A)$	1.4539	2.1	18
$N_2(B)$	1.63772	2.4	17
$N_2(C)$	1.82677	2.6	17

Then, according to recent simulations [62], when the reduced electric field becomes relatively weak ($E/N <$ 80-100 Td), the main reaction populating N_2(C), until about $t = 20$ ns, becomes:

$$N_2(B) + e^- \quad \rightarrow \quad N_2(C) + e^- \tag{4.7}$$

Finally, for $t > 20$ ns, the pooling reactions

$$N_2(A) + N_2(A) \quad \rightarrow \quad N_2(B) + N_2 \tag{4.8}$$

$$N_2(A) + N_2(A) \quad \rightarrow \quad N_2(C) + N_2 \tag{4.9}$$

become predominant. The rotational distributions of the B and C states are approximately identical because the rotational constants of these states are similar (see table 4.1). Figure 4.7 shows the evolution of the rotational distribution of various electronic states of N_2 and we see that the various distributions have very close maxima. The Boltzmann population distribution of each state is given by [63]:

$$n(J) = \frac{(2J+1)\exp(-J(J+1)\frac{\theta_{rot}}{T_{rot}})}{Q_{rot}} n_{N_2} \tag{4.10}$$

where Q_{rot} is the rotational partition function and J the rotational quantum number. As shown in table 4.1 and figure 4.7, the maximum of this distribution is located at nearly the same J for the different nitrogen electronic states. Thus, when the C state is populated by electron-impact excitation of N_2(X) or N_2(B), its rotational distribution is close to the rotational distribution of the X or B state. In contrast, when pooling reactions (4.8)-(4.9) become important (after $t = 20$ ns), the population distribution of the C state is likely to be distorted from a Boltzmann distribution. Thus, the N_2(C) rotational temperature may not be as closely representative of the rotational temperature of the gas past $t = 20$ ns.

Finally we come to question of whether the rotational temperature of the N_2(C) state is representative of the gas temperature for times $t = 0$ - 20 ns. We recall that the rotational-translational relaxation time τ_{RT} is given by [65]:

$$\tau_{RT} = Z_{RT}\tau_0 \tag{4.11}$$

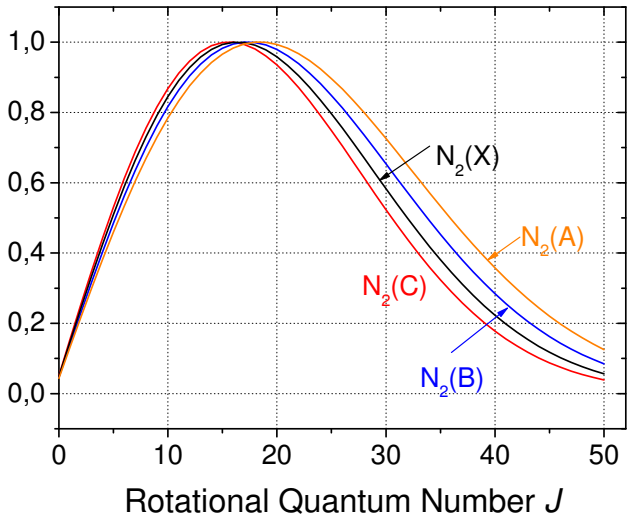

Figure 4.7: Evolution of the rotational distribution of various electronic states of N_2 as function of rotational quantum number J.

and the mean time between collisions by [64]:

$$\tau_0 = \left[10^{10} \sqrt{\frac{300}{T[K]}} P[atm] \right]^{-1} \tag{4.12}$$

where τ_0 is the inverse of the collision frequency (in s), and Z_{RT} is the number of collisions needed for rotational relaxation. In pure nitrogen, Z_{RT} increases with the temperature but reaches a plateau at 1500 K, according to Capitelli *et al* [65] and Brau *et al* [66]. In a recent model, Park [67] proposed slightly different values, with a linear increase (see table 4.2). During the discharge, the pressure of the gas increases proportionally with the temperature because the process of energy deposition is very fast, and therefore, the discharge volume does not expand. Using the parameters of table 4.2, we show that the rotational relaxation time is 2-4 ns in the time interval t = 0-20 ns. This value is small compared to the timescale of variation of the rotational temperature of $N_2(C)$. Thus we can expect that the measured rotational temperature is equilibrated with T_{gas}.

Table 4.2: Influence of the gas temperature on the rotational-translational relaxation time ([65], [66], and [67])

t [ns]	T_g [K]	P [atm]	τ_0 [ns]	Z_{RT}(N_2-N_2) [65], [66]	Z_{RT}(N_2-N_2) [67]	τ_{RT} [ns] [65], [66]	τ_{RT} [ns] [67]
0	1500	1	0.22	10	15	2.2	3.4
9	2000	1.3	0.19	12	20	2.3	3.9
20	2400	1.6	0.18	13	24	2.3	4.2
25	2600	1.7	0.17	13.5	26	2.3	4.4

4.4.1.3 Additional $N_2(C)$ rotational temperature data

Because the temperature profile is still increasing at $t = 20$ ns on figure 4.6, we looked for a way to determine by how much the temperature continues to increase after 20 ns. To this end, we may use a peculiar feature of our pulser: by construction this pulser produces a secondary pulse about 270 ns after the main pulse, as can be seen from the voltage shown on figure 4.8. This secondary pulse is sufficiently strong to produce excitation of $N_2(C)$ by electron and therefore to obtain additional measurements of the rotational temperature at 270 ns.

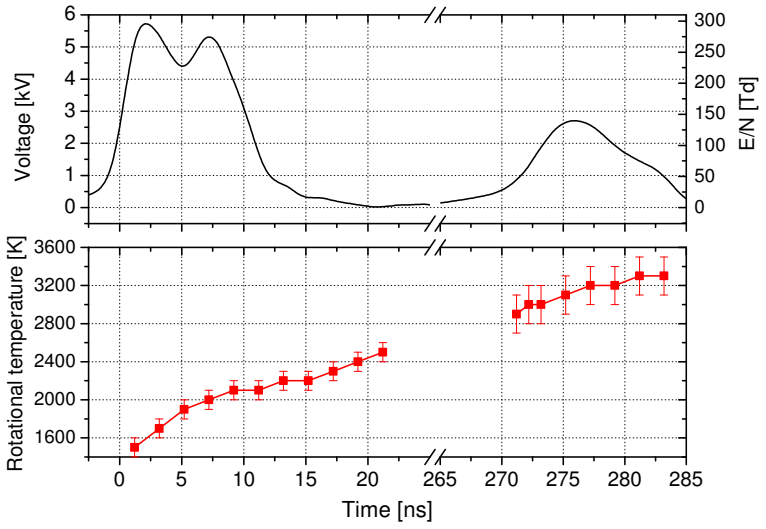

Figure 4.8: Time-evolution of the rotational temperature of $N_2(C)$ (bottom) obtained from experiments with 2400 gr/mm, synchronized with main and secondary high-voltage pulses (top) with the corresponding reduced electric field E/N.

At the very beginning of the secondary pulse, the measured temperature should be very close to the gas temperature resulting from the fast heating process. Thus, this secondary pulse provides useful additional data on the ultrafast

heating process.

4.4.2 Vibrational temperature

The aim of this section is to determine the vibrational temperature of $N_2(C)$ performing the same OES measurements with the lower-resolution grating. We investigate the same vibrational bands using the 600 gr/mm grating.

Indeed, in [2], Pai showed spectra of NRP glow and spark discharges and noticed the presence of $N_2{}^+$ within both discharges. The $N_2^+(B \rightarrow X)$ (0,0) transition bandhead being at 391.14 nm, this species could encroach on the $N_2(C \rightarrow B)$ (0,2) band at 380 nm. The 600 gr/mm grating has a much wider window (40 nm) than the 2400 gr/mm grating (9 nm). We analyzed the $N_2(C \rightarrow B)$ (0,2) band at 380 nm with the two gratings 2400 gr/mm and 600 gr/mm. The spectra obtained with the two gratings gave similar rotational temperatures on $N_2(C)$, with similar intensity of the $N_2(C \rightarrow B)$ (0,2) bandhead peak at 380 nm. However, with the 600 gr/mm grating, we see more bands, the (0,3) (1,4) (2,5) (3,6) and (4-7) from the Δv = -3 system, and the (0,2) (1,3) and (2,4) bands from Δv = -2. Typical spectra are shown on figure 4.9 for different times t. The simulated spectra are obtained using only the N_2(C-B) transition for the red spectrum. For figure 4.9 (c), we add the $N_2^+(B \rightarrow X)$ transition (dash green spectrum). The bands are indicated on figure (c). From $t > 19$ ns, the structure of the spectrum changes significantly, the base line increases, and this effect cannot be only due to the $N_2^+(B \rightarrow X)$ transition. To determine the origin of this spurious structure, we started by acquiring a survey spectrum over a wide wavelength range 150-900 nm. The goal is to find what other species are present in the spectra that could produce the bands superimposed to the spectra of $N_2(C \rightarrow B)$ and $N_2^+(B \rightarrow X)$ in figure 4.9 at $t >$ 19 ns.

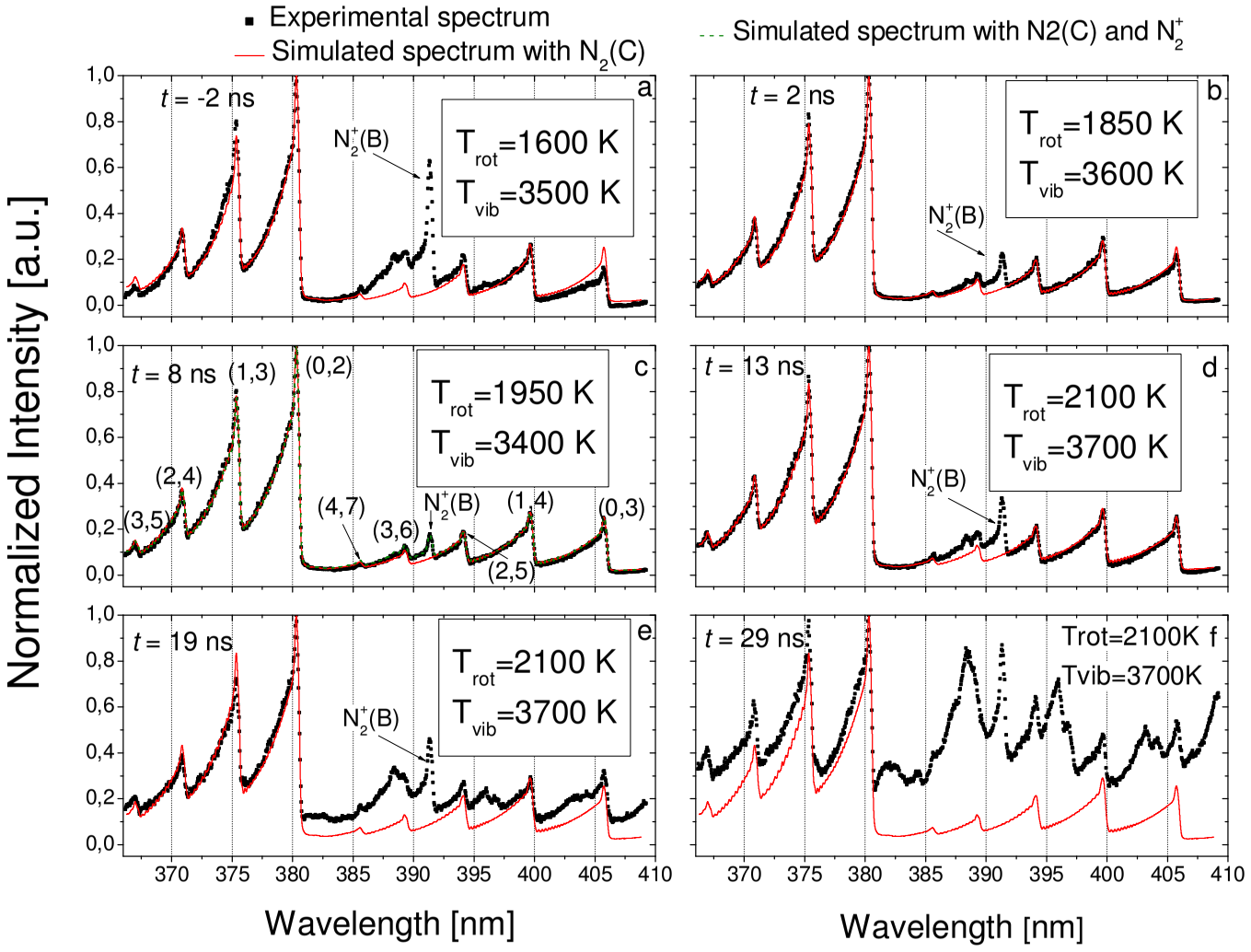

Figure 4.9: Experimental (black symbols) and simulated spectra (red lines) of N_2(C-B) obtained for different times t, integrated for 2 ns. Experimental spectra are obtained with the 600 gr/mm grating and calibrated in intensity. For $t <$ 19 ns, the experimental spectra are well fitted by $N_2(C \rightarrow B)$ and $N_2^+(B \rightarrow X)$. For $t >$ 19 ns, additional species appear.

Emission spectrum of NRP spark discharges from 150 to 900 nm

In this section, we investigate the whole spectrum of the NRP *reference case* spark discharge from 150 nm to 900 nm (highest wavelength detectable by the spectrometer) at $t = 30$ ns. Figure 4.10 shows a complete spectrum from 150 to 900 nm recorded at time $t = 30$ ns for a duration of 2 ns. As we only needed a qualitative identification of the species, these spectra were not calibrated in absolute intensity neither in relative intensity, i.e. they were not corrected for the uneven pixel response across the CCD array. We used several filters in order to discard the second order diffraction:

- from 360 to 650 nm, a UV Melles Grillot 03 FCG 121 WG 305 longpass color glass filter which absorbs light for $\lambda < 280$ nm,
- from 650 to 800 nm, a Melles Grillot 03 FCG 061 longpass interference filter absorbing light for $\lambda < 420$ nm,
- from 830 to 900 nm, a Melles Grillot 03 FCG 089 longpass color glass filter which absorbs light for $\lambda < 550$ nm.

We see that the pixels that record data at low wavelengths have a higher response than the pixels that record data at higher wavelengths. This causes discontinuities between the various windows. We adjusted each recorded spectrum from the various windows to approximately match them in intensity.

The emission for $\lambda < 200$ nm is not negligible, we identify in particular the presence of the NOγ transition. Since we recorded the spectra of figure 4.9 without any filter, the spurious light on figure 4.9 (f) is actually the second order of the vibrational bands of NO that are not totally absorbed by air. We see that for $\lambda < 185$ nm, the CCD does not detect anything, all radiation is absorbed by air but for 185 nm $< \lambda <$ 200 nm, we actually see the emission of NO. This had not been observed in [6] or [2], because the authors of that work used an optical fiber that cut all UV light. Consequently, the spectra were not altered by NOγ. Furthermore, this effect is seen when the spectra studied are of weak intensity, which is the case when $t > 20$ ns, where the intensity of $N_2(C \rightarrow B)$ (0,2) is 200 times less than the intensity at the peak of emission ($t = 9$ns). In the previous work of [6], the spectra were captured until $t \leq 25$ ns, so this effect was not as strong as in our work.

In conclusion, we have understood why we had additional structures on the spectra of figure 4.9. These structures clearly affect the determination of the rotational and vibrational temperatures of N_2(C) and must be suppressed. In the following section, we investigate the N_2(C-B) spectra with a UV filter in order to discard the second order diffraction.

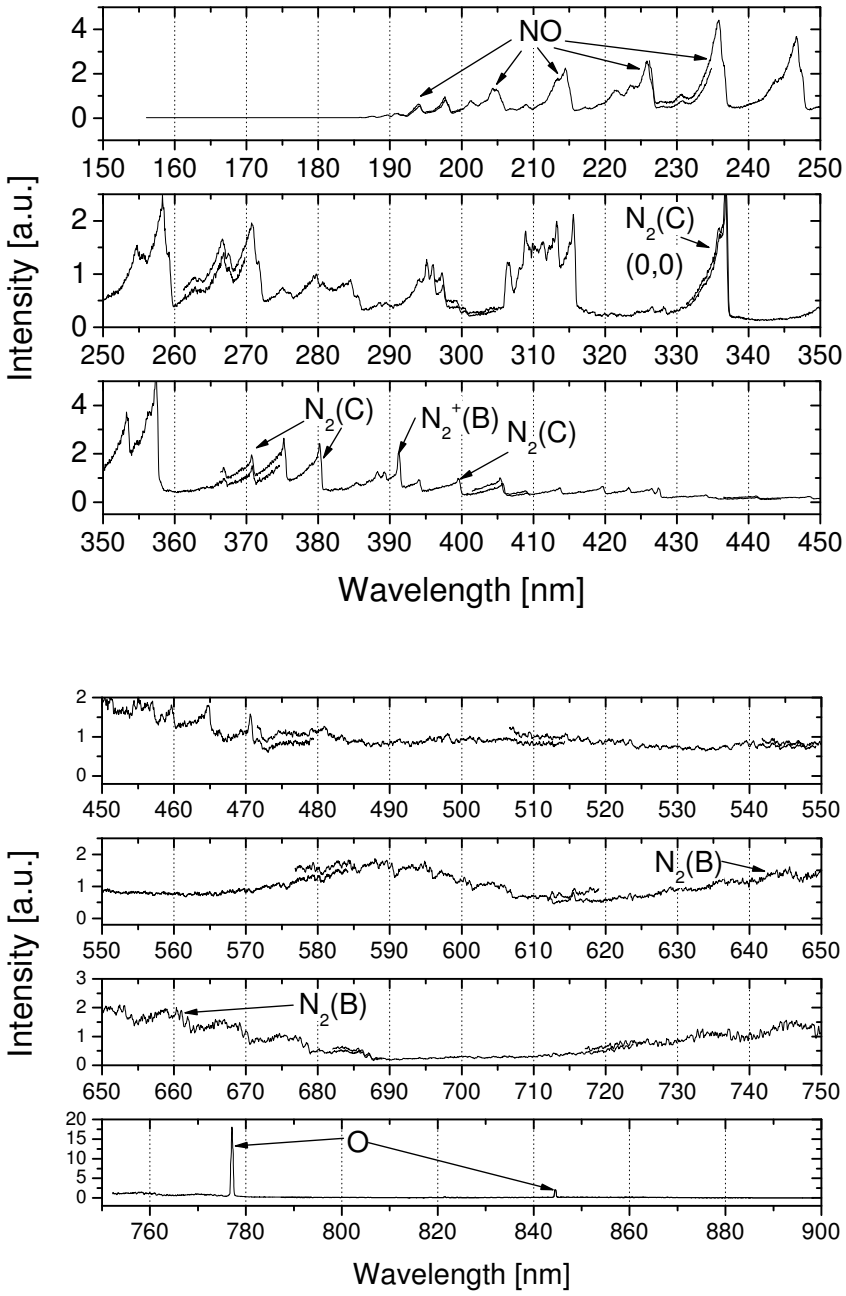

Figure 4.10: Emission spectra integrated for 2 ns from 150 to 900 nm at $t = 30$ ns. Spectra are obtained on different 40-nm wide windows with 600 gr/mm grating and are not calibrated in intensity.

Spectra obtained with 600 gr/mm grating and UV filter

We capture time-resolved spectra of $N_2(C \rightarrow B)$ and calibrate them in intensity, working with a UV Melles Grillot 03 FCG 121 WG 305 longpass color glass filter that absorbs light for $\lambda < 280$ nm. The filter is placed just in front of the entrance of the monochromator. We compare the normalized spectrum with and without this filter. For $t < 20$ ns, the spectra are similar, which confirms the results of section 4.4.1.

Typical experimental and simulated spectra are shown on figure 4.11. The simulated spectra are calculated using the $N_2(C \rightarrow B)$ and $N_2^+(B \rightarrow X)$ transitions. We note that we do not see the second order of NOγ anymore for $t > 20$ ns. However, for $t = 21.1$ ns and $t = 31.1$ ns, we see that there is still a slight discrepancy between the experimental and calculated spectra around 380-385 nm. This might be due to the presence of a small portion of the second order of NOγ which not completely attenuated by the filter. Consequently, we will not take into account the spectra obtained for $t > 20$ ns for the determination of the temperatures of $N_2(C)$.

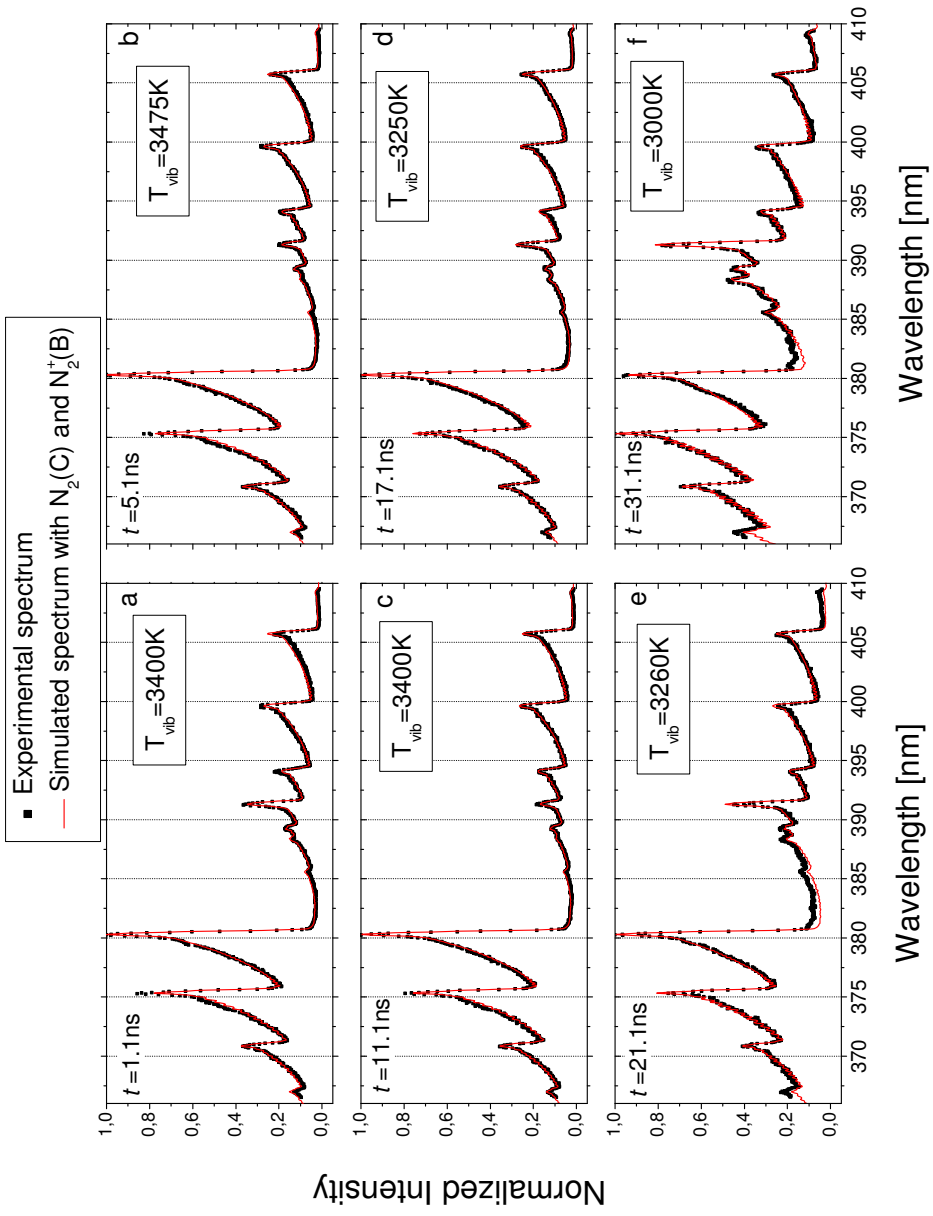

Figure 4.11: Experimental (black symbols) and simulated spectra (red lines) obtained for different times t, integrated for 2 ns. A UV Melles Grillot 03 FCG 121 WG 305 longpass color glass filter absorbing light for $\lambda < 280$ nm is used. Experimental spectra are obtained with the 600 gr/mm grating and calibrated in intensity.

From the spectra of figure 4.11, since we see several bands of $N_2(C)$, we can determine the vibrational temperature of $N_2(C)$, which is approximately constant, around 3200 ± 300 K. It is interesting to note that all five levels of the C state of N_2 follow a Boltzmann distribution at all times, because the spectra are well fitted with a Boltzmann distribution of the populations. Figure 4.12 shows the time evolution of the vibrational temperature of $N_2(C)$ taken from the spectra of figure 4.11. Figure 4.13 shows the time-evolution of the vibrational temperature of $N_2(B)$ taken from the spectra obtained in section 4.4.1.

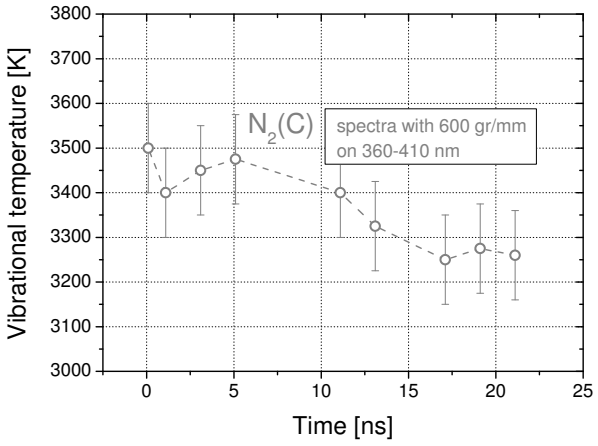

Figure 4.12: Time-evolution of the vibrational temperature of $N_2(C)$ obtained from experiments presented in this section (dash grey) with the 600 gr/mm grating and UV filter, see figure 4.11.

To summarize this section, the gas temperature increases by about 1000 K in 20 ns. This increase of temperature is consistent with Popov [62] who predicts a temperature increase of about 700 K, and with our previous measurements [50]. An even higher temperature increase of 2500 K was also previously reported by Pai *et al* [37] (but those measurements were made with a higher applied electric field).

Such a fast temperature elevation suggests that there should be a fast pressure increase within the plasma, which should create a shock wave. Such a shock wave has been observed in Xu *et al* [51]. These results indicate that nanosecond pulses can produce ultrafast heating, here at a rate of 5×10^{10} K/s.

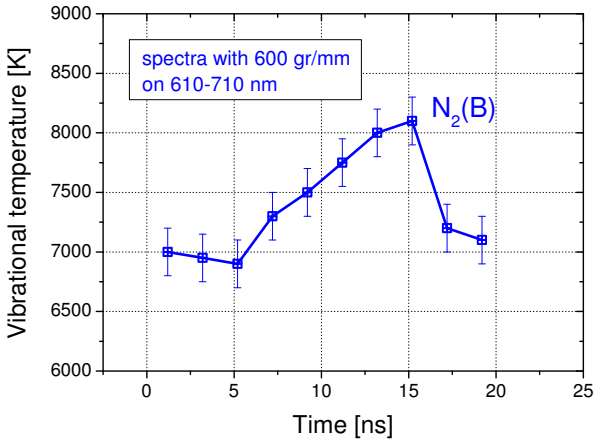

Figure 4.13: Time-evolution of the vibrational temperature of N_2(B) obtained from experiments presented in section 4.4.1 with the 600 gr/mm grating.

4.5 Plasma Diameter

We can also determine the absolute densities of the emitting states from the simulated spectra provided we know the length of column of the emitting region. The density deduced is quite sensitive to this parameter, so the column length should be determined precisely. The diameter of the NRP spark discharge has been determined in [6] from the emission of the second positive system of N_2. We also wanted to determine whether the first positive system had the same spatial extension. To this end, the N_2(C-B) emission spectra were obtained with the 2400 gr/mm grating and N_2(B-A) emission spectra with the 600 gr/mm grating.

To determine the spatial extent of the plasma, we use two different methods: an accurate method, *method 1* and an approximate (and faster) method, *method 2*. We will describe both methods and show that they give similar results on one case, thus justifying the use of *method 2* to determine the diameter of the discharge. For both methods, we assume the plasma to be axisymmetric.

Accurate method - *Method 1*

Scans of the $N_2(C \rightarrow B)$ spectra over the spectral range 373-392 nm were recorded at 20 lateral positions, i.e. every 100 µm on a total width of 2 mm at peak intensity (t = 9 ns) using a 2-ns gate. We then performed an Abel inversion at every wavelength of the calibrated spectra to obtain the spectra at each radial position within the discharge. The resulting local Abel inverted spectra have units of mW/cm^3.sr. Using Specair again, we deduced the radial

profile of the density of $N_2(C)$, as shown in figure 4.14 (a). For $r = 0$ - 0.250 mm, the rotational and vibrational temperatures of $N_2(C)$ remain approximately at constant values of 2100 K and 3900 K, respectively, as shown on figure 4.14 (b). The diameter of the plasma is considered to be equal to the measured FWHM of the $N_2(C)$ density radial profile. It is approximately equal to 0.450 mm. We note that the measured diameter is about ten times larger than the spatial resolution (50 µm) of our optical system, thus justifying why we resorted to such a high spatial resolution.

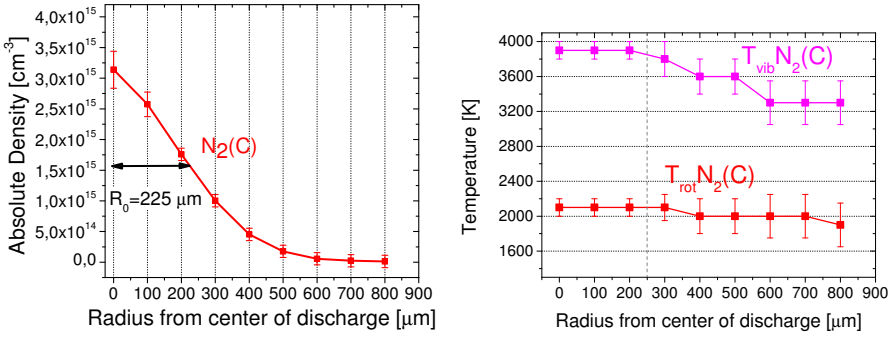

Figure 4.14: (a) Radial profile of $N_2(C)$ density obtained with *method 1*. (b) Radial profiles of the vibrational and rotational temperatures of $N_2(C)$ obtained with *method 1*. The densities and temperatures are obtained by fitting with Specair the Abel-inverted calibrated spectra measured at $t = 9$ ns.

Approximate method - *Method 2*

A much quicker method to estimate the diameter of the discharge - *method 2* - is to make a lateral scan of the intensity at just one fixed wavelength, and to perform an Abel inversion of the lateral profile of intensity at that fixed wavelength to get the local intensity at that wavelength. The result is very similar since we find 0.440 mm for $N_2(C \rightarrow B)$ at the maximum of emission ($t = 9$ ns). This second method was used to determine the diameter of the plasma using the $N_2(C \rightarrow B)$ (0,2) emission at 380 nm, and the $N_2(B \rightarrow A)$ emission at 667 nm at different times with respect to the high-voltage pulse ($t = 9$ ns, $t = 15$ ns, and $t = 23$ ns).

The various measured values of the plasma diameter are given in table 4.3. They are slightly larger, by 22%, than the value of our previous work [6]. Note that the diameters deduced from the $N_2(B)$ and $N_2(C)$ profiles are almost identical, 7% greater for $N_2(B)$, at the maximum of emission, as shown in figure 4.15. Then these two diameters slightly increase (by less than 20%), for $t = 15$ ns and $t = 23$ ns, in the decreasing part of the temporal profile.

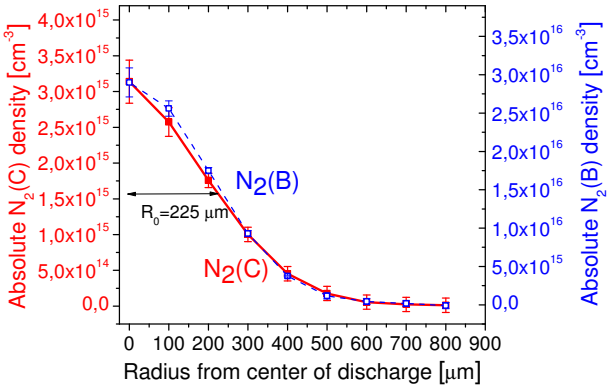

Figure 4.15: Radial profile of $N_2(C)$ and $N_2(B)$ density at $t = 9$ ns. $N_2(C)$ density is obtained with *method 1* and $N_2(B)$ density is obtained with *method 2*.

Table 4.3: Discharge diameter, based on the spatial distribution of $N_2(C)$ and $N_2(B)$
***Method 2*: Abel inversion of the lateral intensity profile at fixed wavelength.**
***Method 1*: Density profile using Abel inversion of the lateral intensity at every wavelength.**

Electronic States	FWHM [µm]			
	$t = 9$ ns (max of emission)		$t = 15$ ns	$t = 23$ ns
	Method 2	*Method 1*	*Method 2*	*Method 2*
$N_2(C)$	440 ± 20	450 ± 20	520 ± 20	520 ± 20
$N_2(B)$	470 ± 20	-	530 ± 20	

We then determined the time-resolved absolute densities of both $N_2(B)$ and $N_2(C)$ from measurements along the line-of-sight, passing through the center of the discharge and assuming a 450-µm column length. What is important to note is that at the maximum of emission, $t = 9$ ns, the $N_2(C)$ density found using *method 1* at the center of the discharge, 3.4×10^{15} cm^{-3}, is very close to the one found using *method 2*, 3.1×10^{15} cm^{-3}, which corresponds to the local density at $r = 0$ mm. This additional argument comforts the relevance of our method of measurements of the absolute densities of the species in the center of the discharge.

4.6 Absolute density measurements and resulting quenching rates

4.6.1 Absolute density measurements

From the calibrated spectra obtained in section 4.4.1.1, knowing the width of the plasma determined in section 4.5, we are able to determine the time-evolution of the absolute densities of $N_2(C)$ and $N_2(B)$. Our results agree with previous experiments [6] (after correcting the column length, previously estimed as being 350 µm, to the current value of 450 µm). Figure 4.16 shows the time-evolution of the absolute densities of $N_2(C)$ and $N_2(B)$ synchronized with the high-voltage pulse, and the previous values obtained in [6]. First, the densities of $N_2(C)$ and $N_2(B)$ increase due to excitation by electron impact of the ground state of N_2, then the densities decrease due to the quenching reactions by O_2 and N_2. Finally, from $t = 20$ ns onward, there is a change of slope due to the onset of pooling reactions, see section 4.4.1.2.

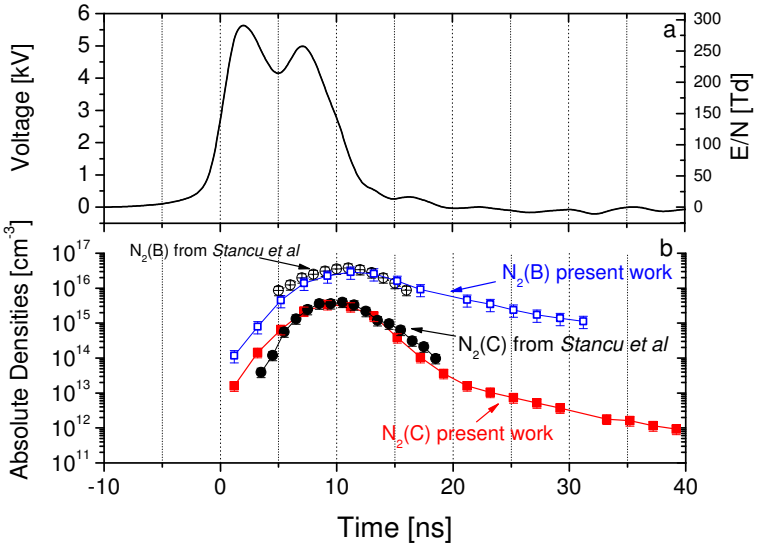

Figure 4.16: (a) Voltage measured across the discharge and (b) Temporal evolution of $N_2(B)$ and $N_2(C)$ densities compared with previous experiments from [6]. Densities determined using *method 2*.

In order to validate the two-step mechanism, it is important to obtain precise values of the $N_2(B)$ and $N_2(C)$ densities. Thus, an important check is to compare the sensitivity of the absolute densities of $N_2(C)$ and $N_2(B)$ to the rotational temperature. Figure 4.17 shows the time-evolution of the absolute densities of $N_2(C)$ and $N_2(B)$ using different assumptions. The red square symbols show the density evolution using the rotational temperature deduced from the fitting procedure with Specair, explained in section 4.4.1.1. The purple

stars represent the density deduced using the intensity of the bandhead of the (0,2) vibrational band. The profiles are scaled in absolute density using the Specair fitting procedure only at maximum of emission $t = 9$ ns. Both curves coincide for $t < 20$ ns, and remain close even for $t > 20$ns.

For the two methods used, we observe a clear change of slope around $t = 20$ ns, that we interpret as the onset of pooling reactions (Equations (4.8) and (4.9)) which create $N_2(C)$ and $N_2(B)$ excited states. These reactions start to be important after the end of the pulse when the density of $N_2(A)$ has increased enough.

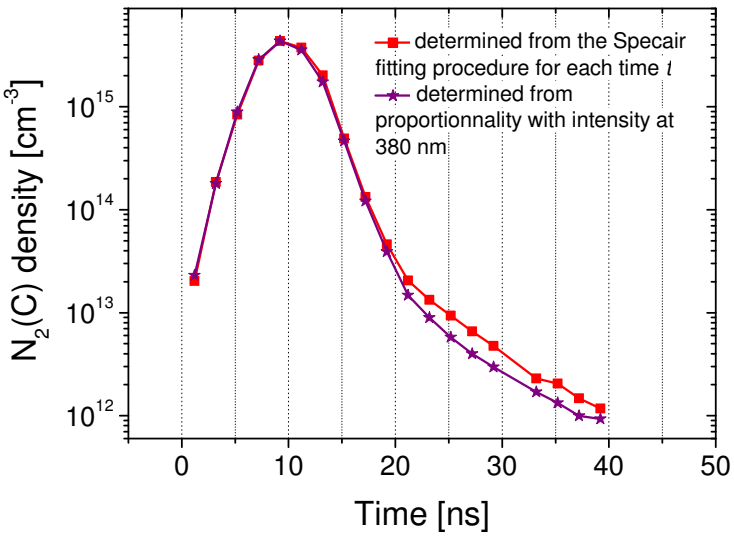

Figure 4.17: Time-evolution of the absolute density of $N_2(C)$ deduced using two different methods. The method that gives the red squares is more accurate because it takes into account the temperature variations with time. Both methods give similar results for $t < 20$ ns and are within 50% of each other for $t > 20$ ns.

Furthermore, we can synchronize the $N_2(B)$ and $N_2(C)$ absolute density measurements with the TALIF absolute measurements of the density of atomic oxygen ([6] and [49]) which are reproduced in figure 4.18(d). These results confirm that O formation only occurs after the formation of $N_2(B)$ and $N_2(C)$; the rapid increase in O density coincides with the decay of the $N_2(B)$ and $N_2(C)$ density. We also notice that the temperature continues to increase after the end of the pulse. Both facts contribute to validate the two-step mechanism presented in section 2.6.1.

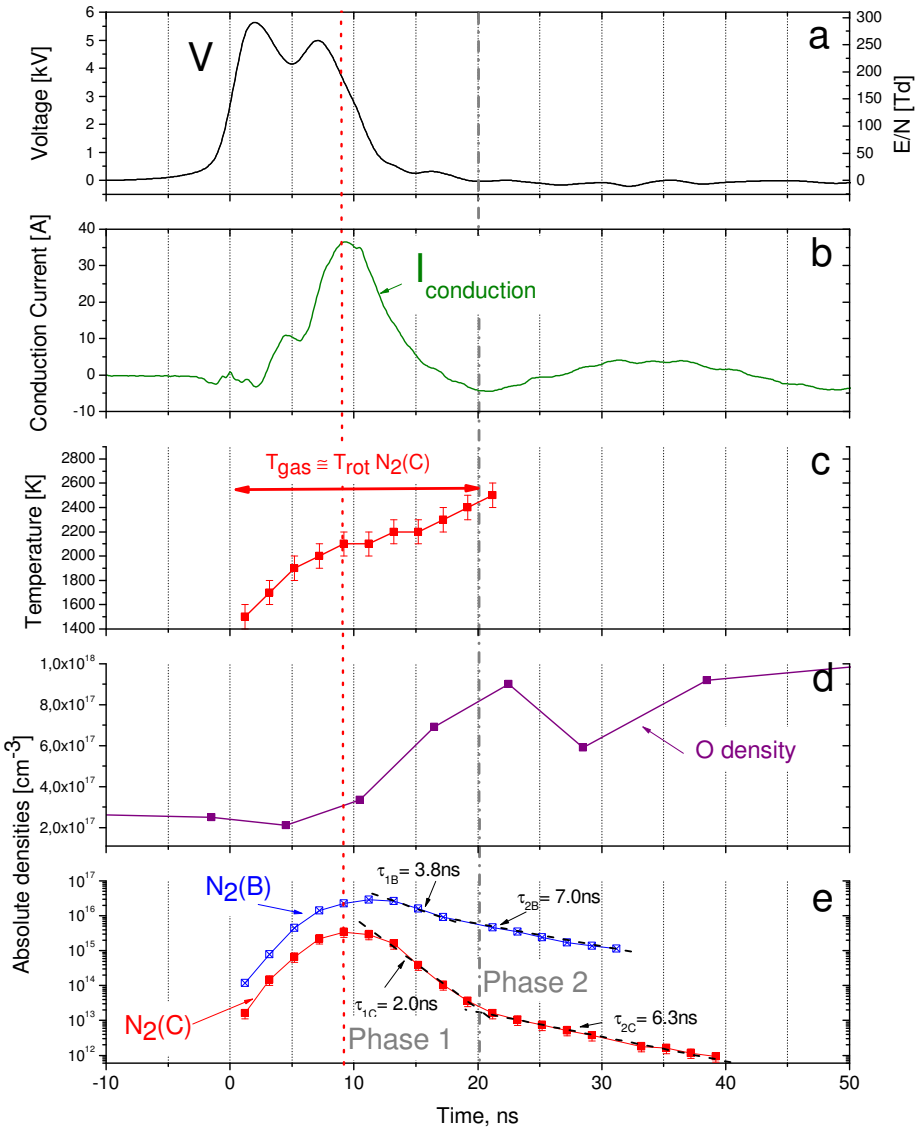

Figure 4.18: (a) High voltage pulse and corresponding reduced electric field; (b) Conduction current; (c) $N_2(C)$ rotational temperature (d) O absolute density measured by TALIF [6], [49] (e) $N_2(B)$ and $N_2(C)$ absolute density.
NRP *reference case* spark discharge : T_g = 1000 K, d = 4 mm, V_p = 5.7 kV, PRF = 10 kHz and v = 2.6 m.s^{-1}.

The decay of $N_2(B)$ and $N_2(C)$ can be decomposed into two phases: *phase 1* where states are depleted mainly by the quenching reactions by O_2 and N_2, and

phase 2 during which pooling reactions (Equations (4.8) and (4.9)) become an important channel of population of $N_2(B)$ and $N_2(C)$, which explains that the decay of these states changes slope at $t > 20$ ns.

4.6.2 Temperature dependence of the dissociative quenching rates of $N_2(B)$ and $N_2(C)$

The decay rate of $N_2(B)$ and $N_2(C)$ can be deduced from the measurements presented in figure 4.18 (e). Different quenching rates are associated with the two phases described earlier. During *phase 1*, from $t = 9$ to $t = 20$ ns, the decay of $N_2(B)$ and $N_2(C)$ occurs with the following measured decay times: τ_{1C}= 2.0 ns, τ_{1B}= 3.8 ns. During *phase 2*, from $t = 20$ ns to $t = 40$ ns (end of measurements), both states decay with approximately the same rate τ_{2C}= 6.3 ns and τ_{2B}= 7.0 ns.

These measurements allow us to determine the rates of the corresponding quenching reactions. Indeed, the decay values of *phase 1* are much shorter than the radiative lifetimes of 6 µs of $N_2(B)$ and 40 ns for $N_2(C)$. Thus, the depletion of these states occurs mainly via fast - nanosecond timescale - dissociation quenching reactions mostly with O_2 and N_2. A non-exhaustive list of the published rates of these quenching reactions can be found in tables 4.4 and 4.5, where the temperature is indicated when known. Most of the data were obtained at ambient temperature, though a few measurements were done at T around 2000 K [65], [68], [69], and [70]. To deduce from our density measurements the quenching rates of $N_2(B)$ and $N_2(C)$ by O_2, the rates of quenching of $N_2(B)$ and $N_2(C)$ by N_2 were taken from the literature, [68], [71], [72], and [73]. The rates for $N_2(B)$ and $N_2(C)$ quenching by O_2 were deduced at 2000 K, which is the approximate temperature of our experiments, in the temporal range 10-20 ns where the decay occurs with the expressions:

$$k_{qN_2(C),O_2} = \left[\frac{1}{\tau_{C,decay,air}} - k_{qN_2(C),N_2} n_{N_2} - \frac{1}{\tau_R}\right] \frac{1}{n_{O_2}} \tag{4.13}$$

$$k_{qN_2(B),O_2} = \left[\frac{1}{\tau_{B,decay,air}} - k_{qN_2(B),N_2} n_{N_2} + \frac{1}{\tau_R}\right] \frac{1}{n_{O_2}} \tag{4.14}$$

where $\tau_R = 36.68$ ns is the rate of radiative deexcitation of $N_2(C)$ state [64]:

$$N_2(C) \quad \rightarrow \quad N_2(B) + h\nu \tag{4.15}$$

We obtained $k_{qN_2(B),O_2} = 2.6\ (\pm\ 0.5)\ \times 10^{-10}$ cm^{-3}. s^{-1} and $k_{qN_2(C),O_2} = 5.0\ (\pm\ 0.5) \times 10^{-10}$ cm^{-3}. s^{-1}.

These values are plotted in figure 4.19, and compared with the other values reported in literature. The reported uncertainties on our measurements take

Table 4.4: N_2(C) quenching rate constants (in 10^{-11}cm^{-3}.s^{-1})

Molecule	T[K]	$N_2(C, v = 0)$	References
N_2	220-500	1	Capitelli *et al* [65], Kossyi *et al* [68]
	300	1.14 ± 0.12	Dilecce *et al* [70]
	300	1.3 ± 0.2	Pancheshnyi *et al*[73]
	300	1.09 ± 0.1	Chen *et al* [69]
	300	1.1 ± 0.6	Millet *et al* [71]
	300	1.12	Mitchell [72]
	1900	2.5 ± 0.3	Bak *et al* [74]
O_2	220-500	30	Capitelli *et al* [65], Kossyi *et al* [68]
	300	30 ± 3	Pancheshnyi *et al* [73]
	300	28 ± 2	Millet *et al* [71]
	300	31.2	Mitchell [72]
	1900	10 ± 0.3	Bak *et al* [74]
	2000	47	Packan [4]
	2000	*50 ± 5*	*Present Work*

Table 4.5: N_2(B) quenching rate constants (in 10^{-11}cm^{-3}.s^{-1})

Molecule	T[K]	$N_2(B, v = 0)$	References
N_2	220-500	5	Kossyi *et al* [68]
	300	3	Capitelli *et al* [65]
	300	1.0 ± 0.8	Piper [75]
	300	0.8	Mitchell [72]
	1900	1.6 ± 0.3	Bak *et al* [74]
O_2	220-500	30	Kossyi *et al*[68]
	1900	4 ± 0.3	Bak *et al* [74]
	2000	*26 ± 5*	*Present Work*

into account the uncertainties on the measured decay time in air and the dispersion on the published quenching rates of $N_2(B)$ and $N_2(C)$ by N_2. More data are available for $N_2(C)$ quenching by O_2 at ambient temperature. From our measurements, the temperature dependence follows a $T/300^{0.3}$ law, which agrees with previous measurements at 2000 K [4]. For $N_2(B)$, the quenching rate at 2000 K seems to be the same as the one at ambient temperature, 3.0 $\times 10^{-10}$cm^{-3}.s^{-1}. The rate of Bak *et al* [74] seems underestimated, probably because the temporal response of their detection system was limited to 5 ns.

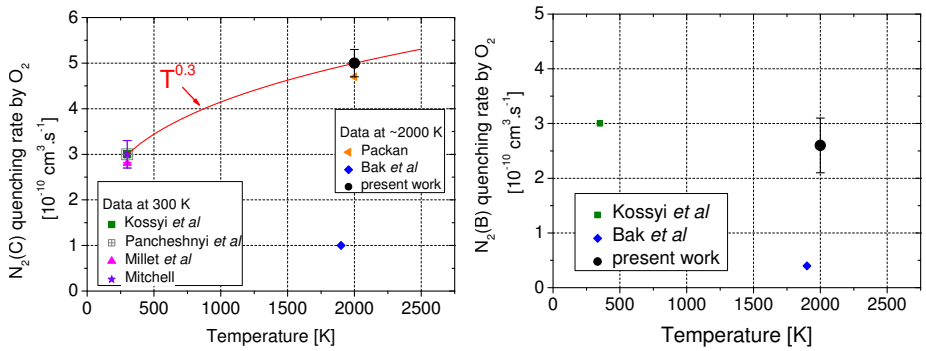

Figure 4.19: Quenching rates of (a) $N_2(C)$ and (b) $N_2(B)$ by O_2. Present work and literature values: Kossyi *et al* [68], Pancheshnyi *et al* [73], Millet *et al* [71], Mitchell [72], Packan [4], and Bak *et al* [74]

In this section, we obtained the time-evolution of the absolute densities of $N_2(B)$ and $N_2(C)$ from experimental spectra, and synchronized them with atomic oxygen TALIF measurements from [6], [49] and electrical measurements. The increase of O and temperature coincides with the decay of $N_2(B)$ and $N_2(C)$, thus validating the two-step mechanism. Finally, we determined for the first time the dissociative quenching rates of $N_2(B)$ and $N_2(C)$ by O_2 at 2000 K.

4.7 Electron density measurements

To provide additional validation data for the two-step mechanism, we now present measurements of the electron number density during the NRP spark discharge. The electron number density can be determined from the FWHM of several Hydrogen Balmer lines such as H_α at 656.3 nm and H_β at 486.1 nm due to Stark broadening of the lineshapes [42]. We have seen on figure 4.4 that H_α was present (over the N_2(B-A) spectrum) due to the presence of H_2O in ambient air. We used the 2400-gr/mm grating and a 50-µm entrance slit of the monochromator to increase the spectral resolution. The broadening of the H_α line is due to several effects: natural broadening, Doppler broadening, collisional broadening, Stark broadening and instrumental broadening, see [42].

In the case of a sufficiently high number density of electrons, Stark broadening dominates, and the FWHM of the line can be easily related to the electron number density. We investigated the FWHM of the H_α line for several spectra for $t = 3$ to 11 ns.

Figure 4.20 presents the experimental spectra of N_2(B-A) with the additional Balmer line H_α for $t = 5$ ns. We added a Specair simulated spectrum of N_2(B-A) on the top figure. The difference of the two spectra gives the H_α lineshape, which is shown on the bottom figure.

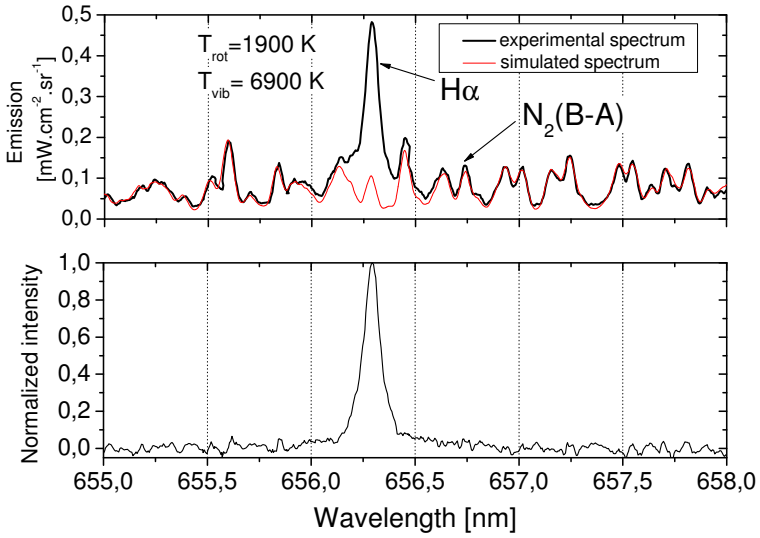

Figure 4.20: Top: Experimental (thick black) and simulated spectra (thin red) obtained for $t = 5$ ns, integrated for 2 ns. Experimental spectra obtained with the 2400 gr/mm grating with a 50-µm slit entrance and calibrated in intensity. Bottom : H_α lineshape obtained from the difference of the two signals shown on the top figure.

From the FWHM of the H_α lineshape, we determined the electron number density through the relation ([42]and [64]):

$$n_e\ [\mathrm{cm}^{-3}] = 9.87 \times 10^{16} \times W_\alpha^{1.65} \text{ with} \tag{4.16}$$

$$W_\alpha = \text{FWHM of } H_\alpha \text{ line [nm]} \tag{4.17}$$

The temporal evolution of the electron number density is presented on figure 4.21 with the number densities of N_2(C) and N_2(B). It was not possible to analyze the spectra for $t > 11$ ns because N_2(B-A) hides the H_α line. The electron density increases during the high voltage pulse up to 3×10^{15} cm^{-3} which is consistent with the electron number density of an NRP spark discharge [2].

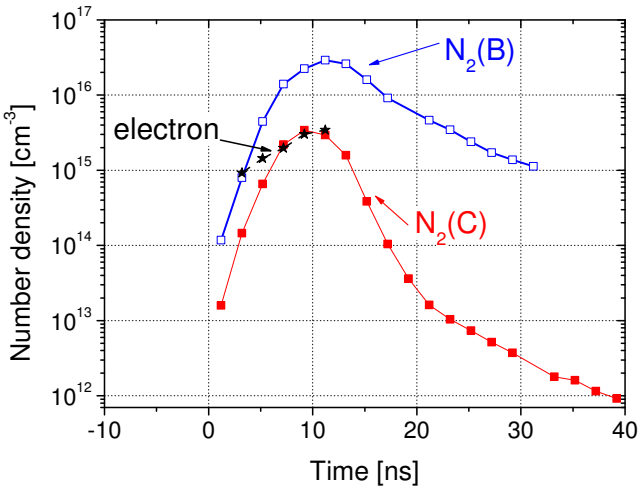

Figure 4.21: Electron number density (black star) determined from the FWHM of the H_α lineshape. The $N_2(C)$ and $N_2(B)$ densities are taken from figure 4.18.

4.8 Conclusions

In this chapter, absolute measurements of the density of excited nitrogen states $N_2(B)$ and $N_2(C)$ created by nanosecond repetitively pulsed discharges in atmospheric pressure air preheated at 1000 K were performed using quantitative Optical Emission Spectroscopy. These measurements were made on the NRP *reference case* spark discharge.

The temporal evolution of the gas temperature was measured using the rotational temperature of the second positive system of nitrogen during the high voltage pulse. An ultrafast heating rate of 5×10^{10} K/s is confirmed. These measurement have been modeled recently by Popov [62], [76], whose model agrees quite well with the absolute densities and temperature measured. A comparison of the evolution of the measured and simulated temperature and O density is shown on figure 4.22.

The diameter of the discharge was studied for the first and second positive system of nitrogen using an Abel inversion of the lateral spectra at the maximum of emission and was found to be 450-500 µm for both states. These measurements were synchronized with previous atomic oxygen measurements [6], [49], and confirm that the dissociation of molecular oxygen within the first 20 ns coincides with the quenching reactions of $N_2(B)$ and $N_2(C)$. The quenching rates of $N_2(B)$ and $N_2(C)$ by O_2 were determined from the decay times of the density of these species and from the published quenching rates of $N_2(B)$ and $N_2(C)$ by N_2, and are respectively equal to 2.6 ($\pm$ 0.5) $\times 10^{-10}$ cm^{-3}. s^{-1} and

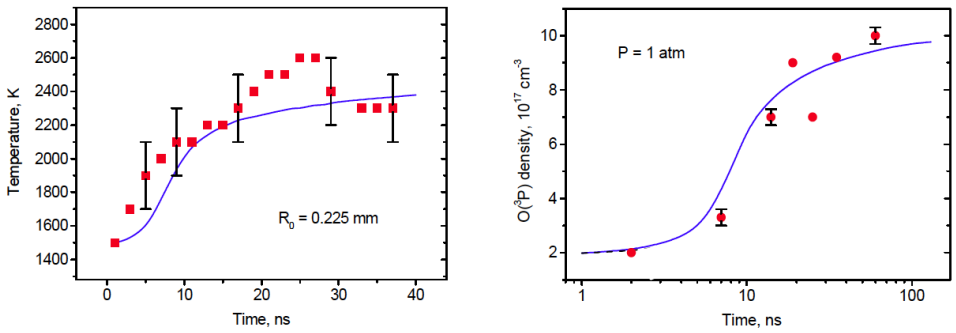

Figure 4.22: Comparison of experimental data (red square) and simulations (blue line) for time evolution of (left) temperature and (right) O density measured by TALIF [6], [49]. Courtesy of Dr Nikolay Popov [76].

5.0 ($\pm$ 0.5)$\times 10^{-10}$ cm^{-3}. s^{-1} at 2000 K. Finally, the temporal evolution of the electron density was deduced from the FWHM of the H_α line, with a peak at 3 $\times 10^{15}$ cm^{-3}.

The new data obtained in this thesis provides a comprehensive data set that will be useful to further validate the two-step mechanism. For this further validation, one should examine on the basis of the results presented here (profiles of E/N, N_2(B), N_2(C), electrons, O, T_{vib} and T_{rot}):

- the relative importance of electron-impact dissociation of O_2,
- the two-step mechanism - which also involves other states such as the N_2(a) state,
- the importance of the pooling reactions that produce N_2(B) and N_2(C) from N_2(A),
- the formation of electronically excited O atoms, etc.

Chapter 5

Influence of R and T_g on Discharge Regimes and Properties

5.1 Introduction

In this chapter, we perform a parametric study of the existence of the glow regime with respect to the radius of curvature of the tip of the electrode R and the gas temperature T_g, in order to validate the model proposed by Pai *et al* [1] and presented in section 2.9. In section 5.2, we detail the experimental conditions used in this chapter and chapter 6. In section 5.3, we characterize the glow discharge at $T_g = 1000$ K with ICCD images, before studying the influence of the radius of curvature of the electrode tip on the spatial structure of the discharge in section 5.4. In section 5.5, we present the domains of existence of the glow regime and show that the model fits the experimental voltage transitions for $T_g > 700$ K. We show that the minimum distance for the existence of the glow regime decreases with decreasing R for a given gas temperature T_g. In section 5.6, we study the spatial structure of the discharge as a function of the temperature and we highlight a new regime, the Multi-Channel Glow (MCG) regime, which has the same characteristics as the glow regime except that several streamers leave the anode. Finally, in section 5.7 we show that we can obtain glow discharges at $T_g = 300$ K with $R = 20$ µm, that have the same features as glow discharges at $T_g = 1000$ K.

5.2 Experimental conditions

We use an Intensified Charge-Coupled Device (ICCD) camera which was synchronized to the NRP discharges to acquire time-resolved images of the plasma with gate width as small as 2 ns. Sections 3.2 and 3.8 provide details on the

experimental setup. This diagnostic allows us to determine the dynamics of the discharge and its spatial configuration. The luminosity of glow discharges is quite low, so in order to have high intensity images, we did not use any filter between the discharge and the camera. The images presented in this thesis characterize the emission coming from all species within the discharge. However, in a glow discharge the light emission is dominated by the emission of $N_2(C)$, see [2]. The gain of the ICCD camera was kept constant and equal to 255 - maximum value possible - for all the images presented in this chapter, except for figure 5.1 (k) for which the gain was reduced to 70. In order to show images with good contrast, we introduce the parameter *Intensity* (I) which represents the value by which we multiply the signal received on the ICCD. It gives an indication of the real intensity of the discharge and was adjusted to visualize each discharge optimally.

In all the ICCD images of this thesis, except when mentioned otherwise, the top electrode is the anode, connected to positive high voltage and the bottom electrode - the cathode - is grounded. We use electrodes of calibrated radius of curvature as explained in section 3.4. We use Pulse Generator 1 in the whole chapter. In this chapter, the flow is axial and blown from the bottom to the top; the flow rate is kept constant and the velocity of air is approximately equal to 1.5 $m.s^{-1}$.

5.3 Characterization of the glow discharge at 1000 K

In this section, we investigate the characterization of the glow discharge obtained at $T_g = 1000$ K with *Delmo* electrodes, the electrodes used by Pai in [2]. The radius of curvature of the electrodes is approximately equal to 200 µm. Figure 5.1 presents images integrated over 25 ns of different types of NRP discharges, corona (top images (a)-(e)), glow (middle images (f)-(j)) and spark (bottom image (k)) depending on the voltage V_p applied on the electrodes. The delay of the camera was set so as to get the signal of one discharge. We notice that the discharges are not perfectly vertical. This is due to the difficulty to align the electrodes at high temperature ($T_g > 800$ K) because of thermal distortion of the electrodes. The corona discharges are not perfectly symmetric on figure 5.1 (d) and (e) because of the roughness of the electrodes and their misalignment.

On the integrated images of the glow regime, we clearly see that the luminosity is not uniform along the inter-electrode axis. The luminosity is higher close to the cathode, especially when the applied voltage V_p is low. The luminosity of the inter-electrode gap close to the anode increases when the voltage increases. In order to understand the spatial structure of the glow discharge, its dynamics was studied with ICCD images integrated for 2 ns - lowest gate width of the camera

- for two different glow regimes, one qualified as "weak glow" for $V_p = 4.8$ kV, just above the C-G transition, and one "strong glow", for $V_p = 5.2$ kV, just below the G-S transition. These images are shown on figure 5.2. By convention, in the following work, time $t = 0$ ns is defined as the time when the rising edge of the pulse measured by the voltage probe reaches 50 % of its maximum value.

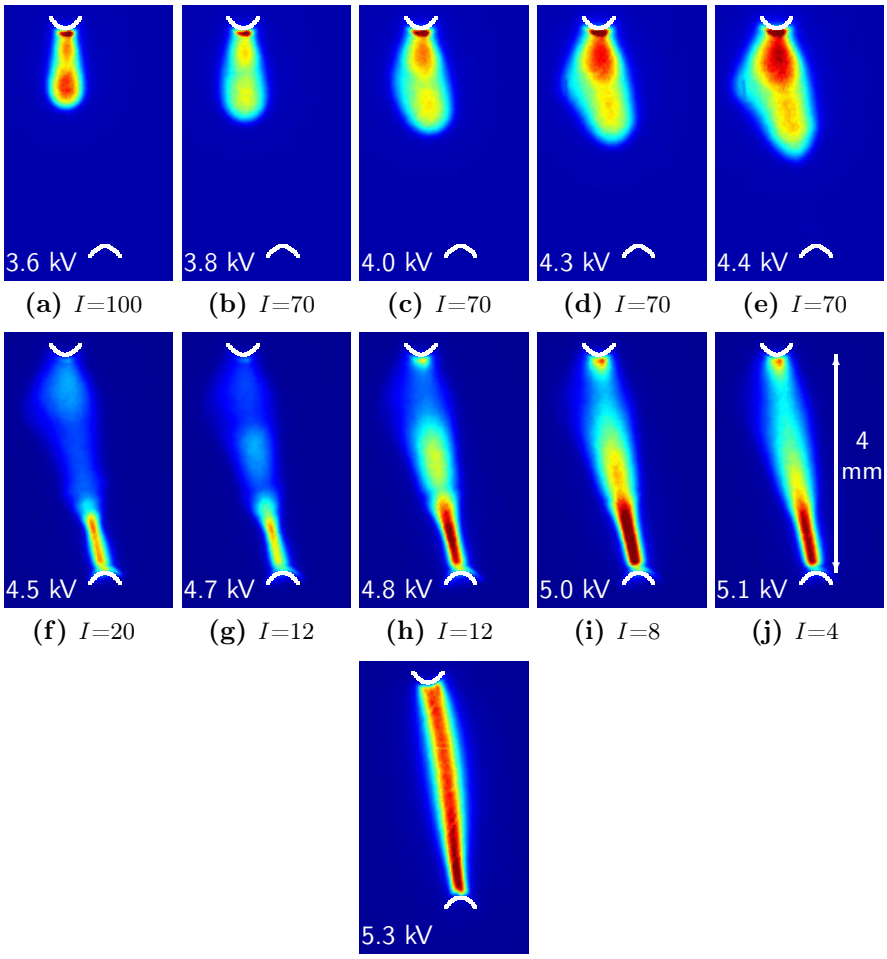

(a) I=100 **(b)** I=70 **(c)** I=70 **(d)** I=70 **(e)** I=70

(f) I=20 **(g)** I=12 **(h)** I=12 **(i)** I=8 **(j)** I=4

(k)

Figure 5.1: Images of a corona discharge (top images (a)-(e)), glow discharge (middle images (f)-(j)), and spark discharge (bottom image (k)) integrated over 25 ns, averaged on several discharges. The gain was equal to its maximum - 255 for the corona and glow regimes and reduced to 70 for the spark regime, to avoid saturation. The electrode shapes are outlined in white.
T_g = 1000 K, *Delmo* electrodes, d = 4 mm, PRF = 10 kHz and $v \approx 1.5\ \mathrm{m.s^{-1}}$.

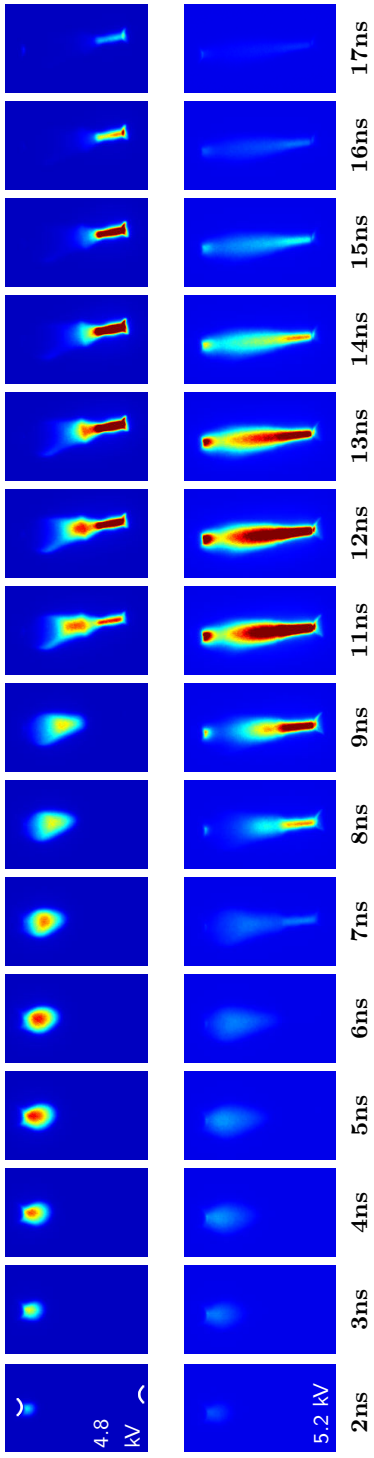

Figure 5.2: Temporal evolution of the glow discharge. Top: "weak" glow regime, Intensity: 150, bottom: "strong" glow regime, Intensity: 25. Images integrated over 2 ns, averaged on several discharges. $T_g = 1000$ K, *Delmo* electrodes, $d = 4$ mm, $PRF = 10$ kHz and $v \approx 1.5$ m.s^{-1}

For the strong glow regime, we clearly distinguish the two phases of discharge formation as described in [2] and [36]. First, the luminosity - which conveys the presence of $N_2(C)$, is generated at the anode initially, at about t = 2 ns and propagates across the gap, reaching the cathode for t = 7-8 ns. The second phase consists in the return stroke, starting from the cathode at about t = 10-11 ns and reaching the anode at t = 12 ns. This tow-step behavior is consistent with the previous studies from Pai *et al* [2] and [36] and shows that the glow regime studied in the present work is physically similar to the one previously described. We also note that the speed of the first wave, about 1×10^8 cm.s^{-1} is typical of the velocity of streamers in air at atmospheric pressure.

For the weak glow regime, we also notice the first phase where the luminosity is first emitted at the anode and propagates to the cathode. However, the connection of the positive streamer and the cathode happens for t = 7-8 ns for the strong glow regime and at t = 10 ns for the weak glow regime. The connection time decreases with the voltage which is consistent with Tholin *et al* [57]. We do not clearly see the return stroke for the weak glow regime. Figure 5.3 shows the measured total emission along the inter-electrode axis for the two NRP glow discharges described in figure 5.2. These images are consistent with the results obtained by Pai, where the 2^{nd} peak intensity which characterizes the second stroke at the anode is proportional to the square of the applied voltage. At low voltages, just above the C-G transition, the second peak at the anode is not observed in [2] and [36]. This also confirms that the emission of the discharge is dominated by the emission of $N_2(C)$, since the total emission along the inter-electrode axis is really similar to the N_2(C-B) (0-0) emission obtained in a similar case [36], see figure 2.18 (a).

In this section, we have shown that at T_g = 1000 K, we could observe glow discharges that had slightly different temporal aspects, namely "strong" and "weak" glow discharges. **Both can be called glow discharges because they are characterized by a light emission on a whole inter-electrode gap distance in a diffuse manner and a low conduction current. That is the criteria that will be used to determine whether a discharge is a glow discharge in the following section.** Furthermore, we have shown that the obtained glow discharges are physically similar to the one found by Pai [2]; they are characterized by the same sequence of physical phenomena for similar measured voltage and current.

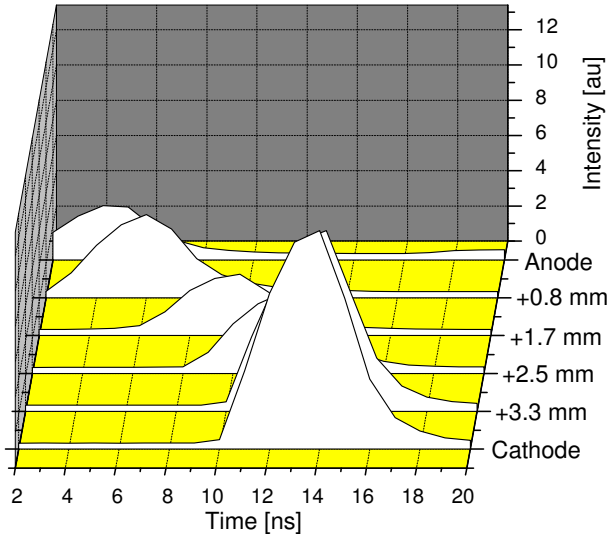

(a) Weak glow $V_p = 4.8$ kV

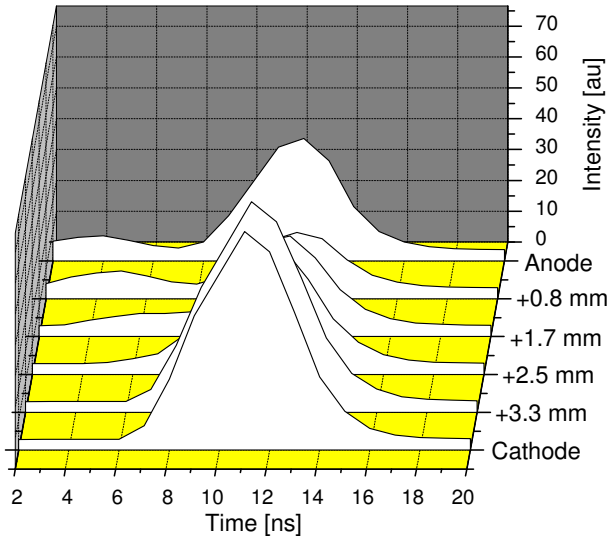

(b) Strong glow $V_p = 5.2$ kV

Figure 5.3: Measured total emission along the inter-electrode axis for an NRP glow discharge with T_g = 1000 K, *Delmo* electrodes, d = 4 mm, PRF = 10 kHz, and $v \approx$ 1.5 m.s^{-1}, (a) "weak" glow V_p = 4.8 kV and (b) "strong" glow V_p = 5.2 kV. Each value is time-integrated over 2 ns.

5.4 Influence of the radius of curvature R on the structure of the glow discharge at T_g = 1000 K

We have already determined precisely what we would call a glow discharge on an ICCD image (see section 5.3). In this section, we present the study of the influence of the radius of curvature R of the electrode tip on the dynamics and the spatial aspect of the glow discharge. We use the *Delta Precis* electrodes R = 50 µm and R = 500 µm described in section 3.4. The distance l was kept constant, l = 8 mm in this section. The glow discharge studied here is typically a "weak" glow discharge, that is to say just above the C-G transition.

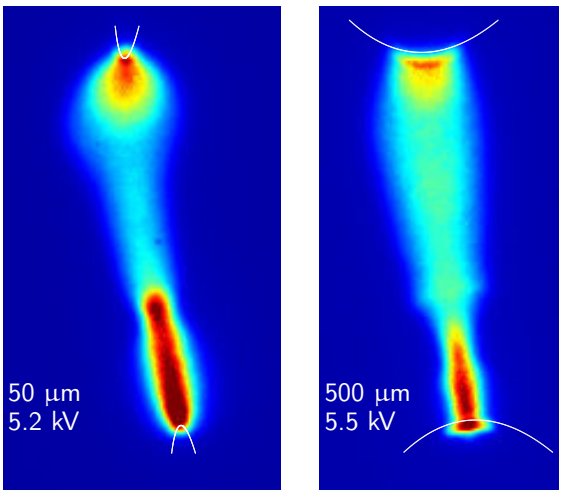

(a) Intensity = 32 **(b)** Intensity = 50

Figure 5.4: Images integrated over 25 ns of a glow discharge for two radii of curvature, (a) R = 50 µm, V_p = 5.2 kV, Intensity = 32 and (b) R = 500 µm, V_p = 5.5 kV, Intensity = 50.
T_g = 1000 K, d = 5 mm, l= 8 mm, PRF = 10 kHz, and $v \approx$ 1.5 m.s^{-1}. The electrodes shapes are outlined in white.

Figure 5.4 shows images of glow discharges integrated during 25 ns, averaged on 400 discharges, for two different radii of curvature, R = 50 µm on the left and R = 500 µm on the right. The voltage is slightly higher for R = 500 µm - V_p = 5.5 kV- than for R= 50 µm -V_p = 5.2 kV- and is just over the C-G transition in each case. The spatial structure of the discharge depends on the radius of curvature of the electrode. Figure 5.5 represents the normalized intensity of the discharge as a function of the distance along the radial extent - 1 mm corresponds to the center of the discharge - for two radii of curvature, R = 50 µm (thin black) and R = 500 µm (thick green) at four different positions.

For R = 50 µm, the size of the plasma is not constant on the whole gap, the

radial extent of the plasma is wider close to the anode, ρ = 0.85 mm and decreases abruptly in the middle of the gap ρ = 0.52 mm. When R = 500 µm, the size of the plasma decreases much more smoothly from the anode to the middle of the gap, the FWHM of the light intensity goes from ρ = 0.90 mm close to the anode to ρ = 0.77 mm in the middle of the gap. The radial width of the discharge close to the pin electrode increases as R decreases, which is due to the increase of the radial component of the Laplacian field close to the pin as R decreases. For both radii of curvature, the global luminosity is similar, the cathode luminosity is strong compared to the luminosity in the middle of the gap. For both radii of curvature, we notice a striction at a distance equal to 3.5 mm from the anode (approximately two-third of the inter-electrode gap distance d), which corresponds to the connection point of the positive and negative streamer (see [57]).

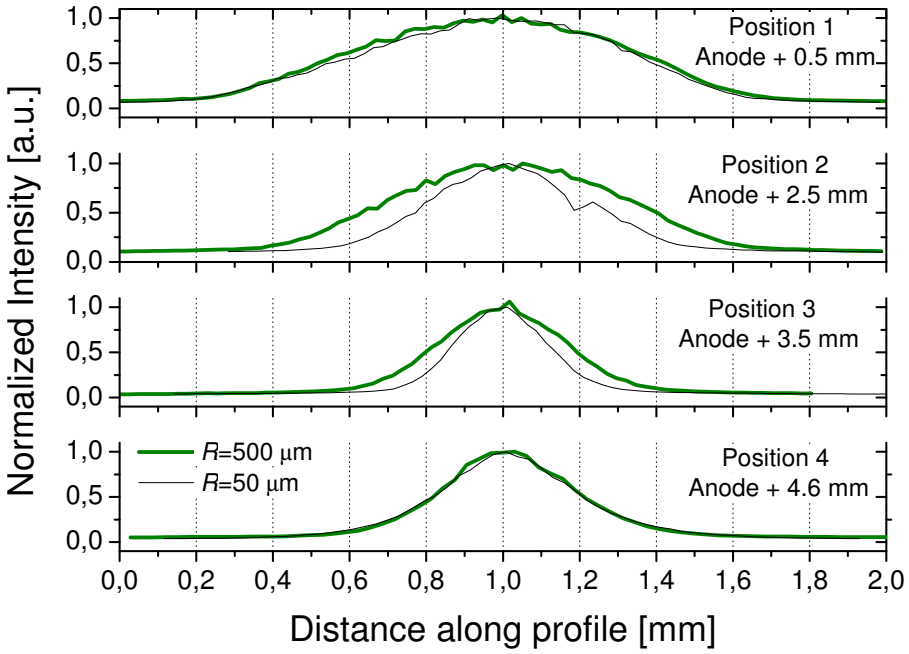

Figure 5.5: Normalized intensity as a function of the distance along the radial extent for two electrode radii of curvature, R = 50 µm, V_p = 5.2 kV (thin black) and R = 500 µm, V_p = 5.5 kV (thick green) at four different positions on the inter-electrode axis.

Figure 5.6 shows the intensity along the inter-electrode axis for R = 50 and 500 µm taken from the images of figure 5.4. We notice the same shape of luminosity. The luminosity at the anode is high, decreases towards the center of the gap before increasing again at the cathode. The luminosity is higher for R = 50 µm, which can still be explained by the higher value of the electric field at the tip. Figure 5.7 shows time-resolved images of a glow discharge - with a

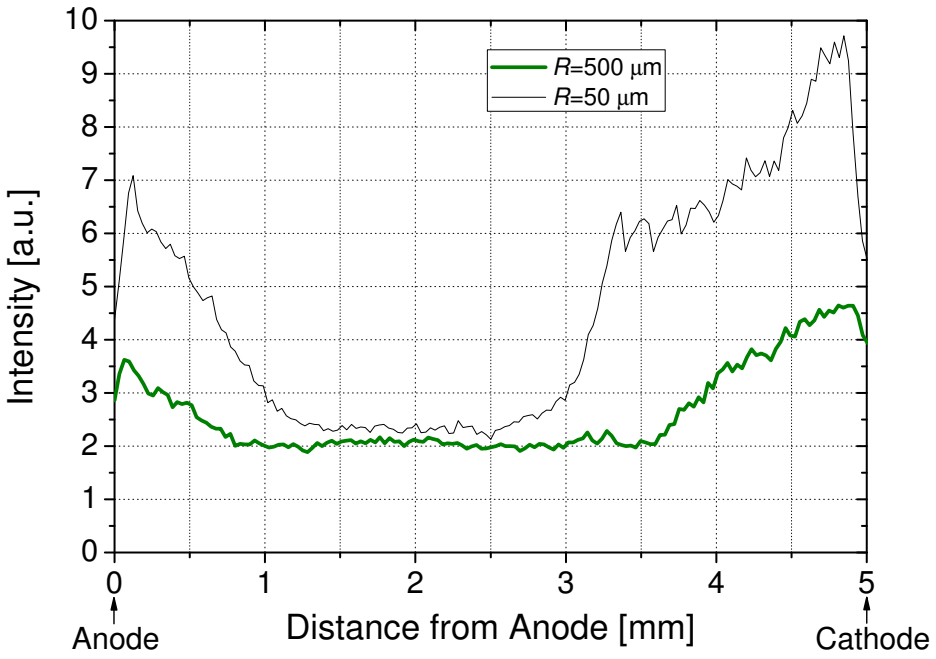

Figure 5.6: Intensity along the inter-electrode axis for two electrode radii of curvature, integrated over pulse duration (25 ns), $R = 50$ µm (thin black) and R= 500 µm (thick green).

time-step of 2 ns - integrated during 2 ns, averaged over 2000 discharges for two different radii of curvature, $R = 50$ µm (top) and $R = 500$ µm (bottom). We see that the shape of the streamer leaving the anode depends on the radius of curvature, as was previously observed on the images integrated over the whole discharge on figure 5.4. For $R = 50$ µm, the radius of the positive streamer varies very steeply during its propagation: the radius decreases by more than 40% from the anode to the mid gap. For $R = 500$ µm, the radius of the positive streamer varies much less - it only decreases by 15 % - and more smoothly than for $R = 50$ µm. For both radii of curvature, we observe a striction that corresponds to the point of connection of the positive and negative streamers.

The connection time is 2-ns shorter for $R = 50$ µm than for $R = 500$ µm: $t = 9$ ns for $R = 50$ µm and $t = 11$ ns for $R = 500$ µm. This is consistent with the increase of the electric field near the anode when the radius of curvature decreases. In [57], for $T_g = 1000$ K, $d = 5$ mm, and $V_p = 5$ kV, the connection time is 4 ns shorter when $R = 50$ µm than when $R = 300$ µm.

Thus, the measurements and simulations are qualitatively in agreement. Also, for a similar applied voltage V_p, the light intensity at the cathode for $t = 11$ ns

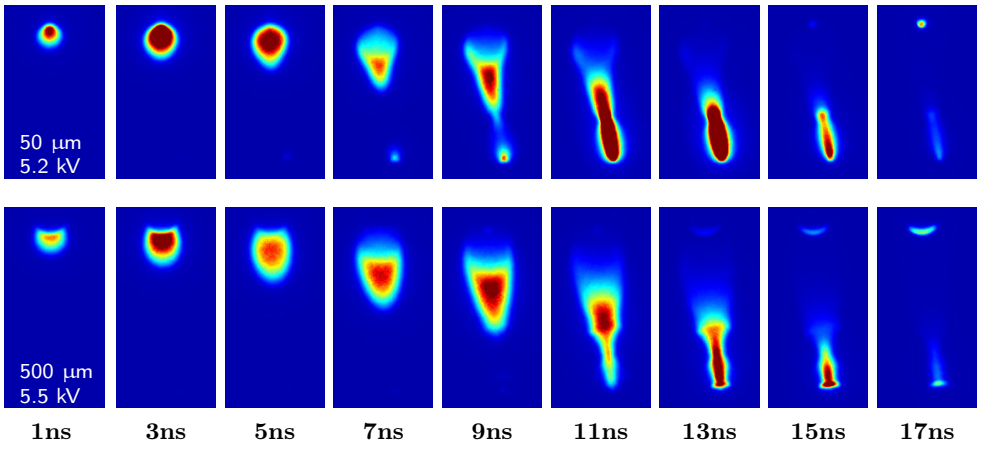

Figure 5.7: Images of a glow discharge temporal development for two radii of curvature, integrated over 2 ns and averaged on several discharges. Top: $R = 50$ µm, $V_p = 5.2$ kV, and bottom: $R = 500$ µm, $V_p = 5.5$ kV. Intensity: 100.

and 13 ns is much higher - 3.5 times higher - for $R = 50$ µm than for $R = 500$ µm. This is because the reduced electric field close to the tip increases when the radius of curvature decreases for the same applied voltage V_p (see section 2.9), thus increasing the production of excited species, and especially $N_2(C)$.

Table 5.1 summarizes the main differences between the structure of a glow discharge for $R = 50$ µm and $R = 500$ µm. In this section, we have shown that for different radii of curvature R of the electrode tip, glow discharges are characterized by the same sequence of physical steps. However, the radius of curvature has a significant influence on the spatial structure of glow discharges. All these conclusions confirm the recent results from 2D-axisymmetric simulations from Tholin *et al* [57].

5.5 Influence of the temperature on the domains of existence of the corona, glow and spark regimes

In this section, we study the influence of the gas temperature T_g on the existence of the glow regime with respect to the radius of curvature of the tip of the electrode R, in order to validate the model presented in section 2.9. This model was developed using hyperboloid electrodes. The electrodes we use in

Table 5.1: Main differences between the structure of the glow discharge studied on figure 5.4 and 5.7 for $R = 50$ µm and $R = 500$ µm.

Radius of Curvature	$R = 50$ µm	$R = 500$ µm
Applied voltage V_p [kV]	5.2	5.5
Connection delay time [ns]	9	11
Radius of the streamer in the mid-gap [mm]	0.52	0.77
Intensity at the cathode for $t = 13$ ns [a.u.]	3.5	1
Streamer radial aspect	varying steeply by 40% during propagation	varying smoothly by 15 % during propagation

the experiments are circular at the tip, and they tangentially join the straight profile, so that the electrode does not show any prominent angle, see section 3.4. However, the difference between the two geometries is very slight, see figure 3.18 and its seems relevant to test the validity of the model on the electrodes we used.

We investigate the transition voltages No discharge-to-Corona (N-C), Corona-to-Glow (C-G) and Glow-to-Spark (G-S) as a function of the gas temperature T_g for a given inter-electrode gap distance d and as a function of d for a given T_g, for various radii of curvature. For each study, we measure the C-G transition voltage V_{CG} and G-S transition voltage V_{GS} using the Lecroy PPE 20 kV high-voltage probe as the applied voltage V_p was slowly increased from 0 V. The discharge regime was estimated watching the discharge with the naked-eye. This method is similar to the method used by Pai in [2]. In the corona regime, the emission zone in the anode region progressively enlarges across the discharge gap as V_p increases until if fully connects with the cathode, and then transitions to the glow regime. This can be seen on figure 5.1. The G-S transition is also distinct, as the luminosity and current greatly increase, accompanied by a crackling sound. We assemble the transition voltage data measured for each temperature T_g into a regime "map" of the discharge regimes as a function of the temperature, as was done in [2]. We have also performed the same study for a given T_g varying d. We were able to investigate the regime from 0 V to approximately 8.6 kV which was the maximum output voltage of Pulser 1 in our experimental conditions. As was done in [2], we stop operating the high-voltage pulse generator immediately after the spark regime is attained to minimize electrode damage. For all these measurements, we set the frequency to $PRF = 30$ kHz.

5.5.1 Existence of the corona, glow and spark regimes for $R = 200$ µm

Figure 5.8 presents the regime map in applied voltage as a function of the gap distance d with $T_g = 1000$ K, $PRF = 30$ kHz, and $v \approx 1.5$ m.s^{-1} for electrodes of radius of curvature $R = 200$ µm. The upper limit of the regime maps corresponds to the maximum applied voltage reachable with Pulser 1, $V_p = 8.6$ kV in our experiments. Under $d = 3$ mm, only the spark regime occurs. We notice the similarity with the regime map obtained by Pai *et al* in [2] and reproduced on figure 2.31 in chapter 2. Figure 5.9 shows the regime map in applied voltage as a function of temperature with $d = 5$ mm, $PRF = 30$ kHz, and $v \approx 1.5$ m.s^{-1} for the electrode of radius of curvature $R = 200$ µm. We notice the similarity with the regime map obtained in [2] at high temperature $T_g > 700$ K and shown in figure 2.28. However, Pai [2] obtained the glow regime only for $T_g > 700$ K.

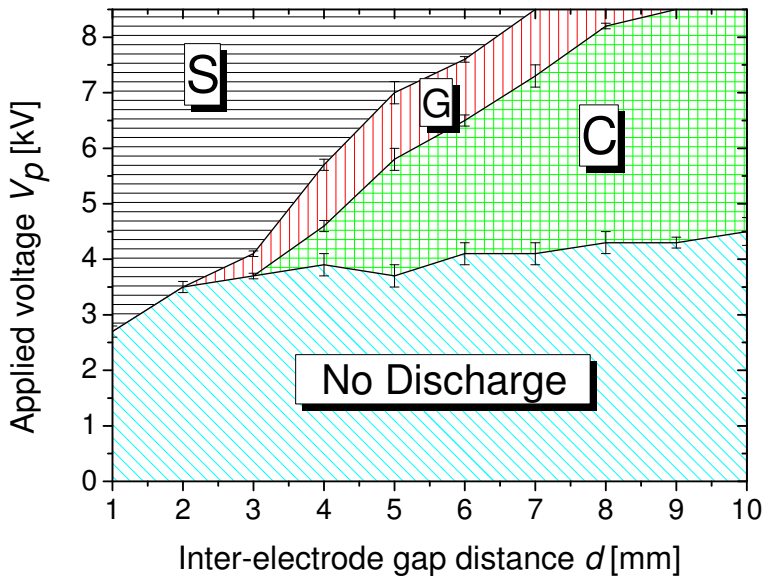

Figure 5.8: Discharge regime map - applied voltage V_p vs gap distance. $T_g = 1000$ K, $R = 200$ µm, $l = 8$ mm, $PRF = 30$ kHz, and $v \approx 1.5$ m.s^{-1}.

This can be interpreted as a consequence of the better symmetry of the electrode and the smoother surface of the material - without asperity. We should add that for 500 K $< T_g <$ 700 K, the glow discharge structure is wider than the one we obtained at higher temperature. This will be investigated in section 5.6.

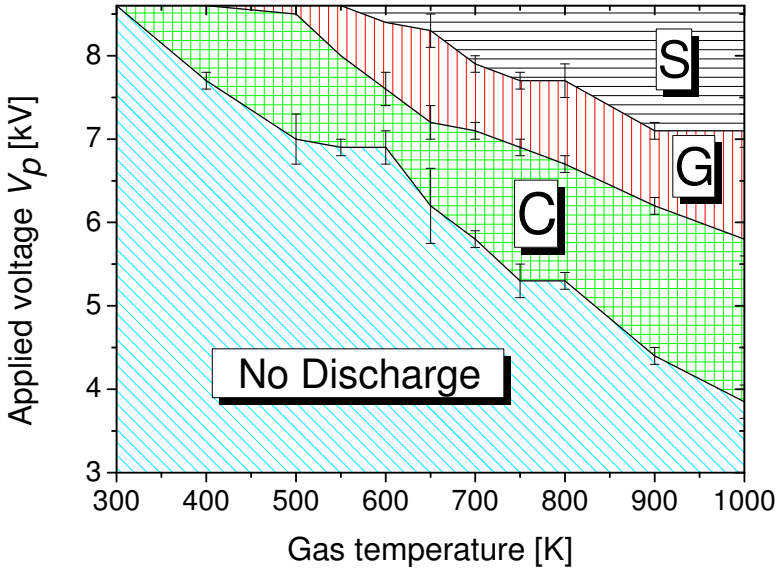

Figure 5.9: Discharge regime map - applied voltage V_p vs gas temperature. R = 200 µm, d = 5 mm, l = 8 mm, PRF = 30 kHz, and $v \approx$ 1.5 m.s^{-1}.

5.5.2 Existence of the corona, glow and spark regimes for various radii of curvature R as a function of gas temperature T_g

We then investigate the same transition voltages for different radii of curvature of the electrode tip: R = 50, 100, 200, and 500 µm as a function of temperature T_g for a given inter-electrode gap distance d = 5 mm. Figure 5.10 displays the results for the two extreme radii of curvature available: (a) R = 50 µm and (b) R = 500 µm. With R = 500 µm, we do not obtain glow discharges for $T_g <$ 800 K within the range of applied voltage reachable with the pulse generator used. With R = 50 µm, we obtain a glow discharge for $T_g \geq$ 500 K. Thus the glow discharge was obtained at much lower temperature for R = 50 µm than for R = 500 µm, confirming the prediction of the model presented in section 2.9.

5.5.3 Comparison with the transition voltage model

We compare our measured transition voltages for different radii of curvature R of the electrodes with the transition voltages predicted by the model of Pai *et al* [1] summarized in section 2.9.

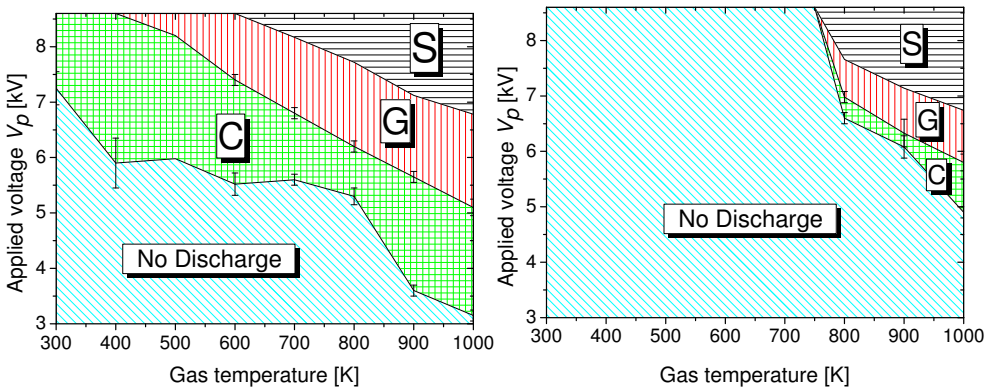

(a) R= 50 µm **(b)** R= 500 µm

Figure 5.10: Discharge regime map - applied voltage V_p vs gas temperature for two radii of curvature. (a) R = 50 µm, and (b) R = 500 µm. d = 5 mm, l = 8 mm, PRF= 30 kHz, and $v \approx$ 1.5 m.s^{-1}.

Corona-to-Glow V_{CG} transition voltage

Figure 5.11 shows the Corona-to-Glow transition voltages V_{CG} measured as a function of (a) gas temperature T_g for d = 5 mm, (b-c) inter-electrode gap distance d for given gas temperatures T_g. (b) shows the transition voltages for different radii of curvature R and T_g = 1000 K, and (c) the transition voltages for R = 100 µm and T_g = 800 and 700 K. We use the transition voltage model V_{CG} obtained using Equation (2.12) assuming that the C-G transition voltage corresponds to the breakdown voltage. Figure 5.11 (a) shows that this model fits quite well the experimental data V_{CG} for T_g >700 K. The cathode fall varies from 1.2 kV - R = 50 and 100 µm to 1.8 kV - R = 500 µm. For R = 200 µm, the cathode fall seems to be equal to 1.8 kV for $T_g \leq$ 800 K and decreases down to 1.2 kV for T_g = 700 K. However, the experimental data departs from the model for 500 K < T_g < 700 K. The experimental values of V_{CG} are significantly smaller than the values determined by the model. This will be explained in section 5.6. On figure 5.11 (b) and (c), we see good correspondence as well between the model and the experimental data for V_{CG} for R = 100 µm and T_g = 800 K and 700 K.

Glow-to-Spark V_{GS} transition voltage

Figure 5.12 shows the Glow-to-Spark transition voltages V_{GS} determined experimentally as a function of the inter-electrode gap distance for (a) R = 200 µm,

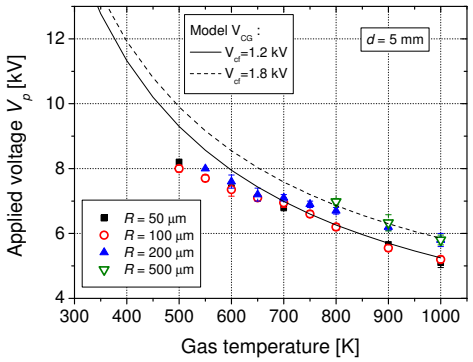

(a) $d = 5$ mm

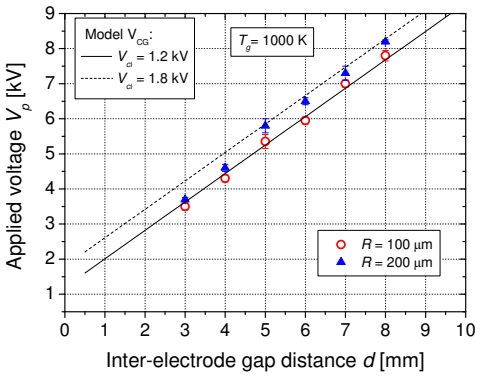

(b) $T_g = 1000$ K

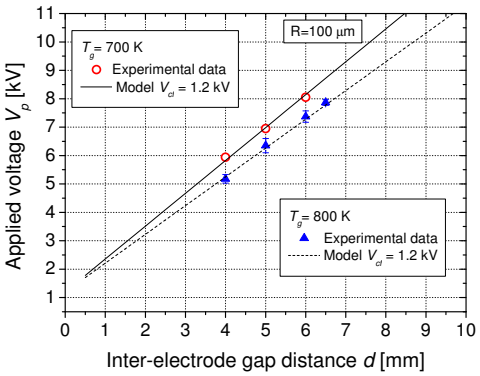

(c) $T_g = 800$ K and 700 K

Figure 5.11: Corona-to-Glow transition voltages V_{CG} for various radii of curvature as a function of (a) gas temperature T_g for $d = 5$ mm, (b) inter-electrode gap distance d for different radii of curvature of the electrode tip and $T_g = 1000$ K, and (c) inter-electrode gap distance d for $R = 100$ µm and $T_g = 800$ and 700 K.
$l = 8$ mm, $PRF = 30$ kHz and $v \approx$ 1.5 m.s^{-1}.

$T_g = 1000$ K, (b) $R = 100$ µm, $T_g = 1000$ K, and (c) $R = 100$ µm, $T_g = 800$ K. We represent as well the modeled V_{GS}, obtained using Equation (2.14) and V_{AST}, obtained using Equation (2.10). We notice that the experimental data agree well with the models. For $d < d_{min}$, the N-S transition is observed, and the transition voltage is correctly predicted by the theoretical AST curve. For $d > d_{min}$, the G-S transition is observed, and the transition voltage is correctly modeled by the theoretical V_{GS} curve. Note that V_{GS} varies linearly with d.

The value of $\left(\frac{E}{N}\right)_{GS}$ can be obtained using figure 5.12 (b) from the slope of V_{GS} for $R = 100$ µm at $d = 5$ mm. V_{cf} can be deduced from the same figure by extrapolating V_{GS} to $d = 0$. The value we take is 1.0 kV. Furthermore, we use the elevated temperature. For each initial gas temperature, we esti-

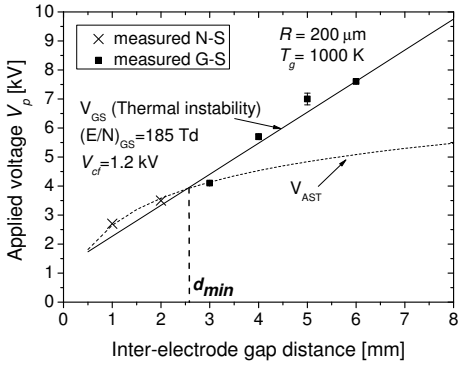

(a) $R = 200$ µm, $T_g = 1000$ K

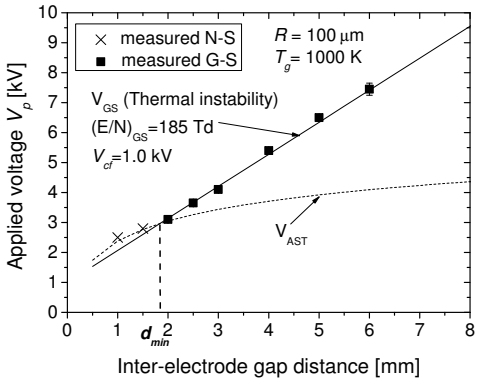

(b) $R = 100$ µm, $T_g = 1000$ K

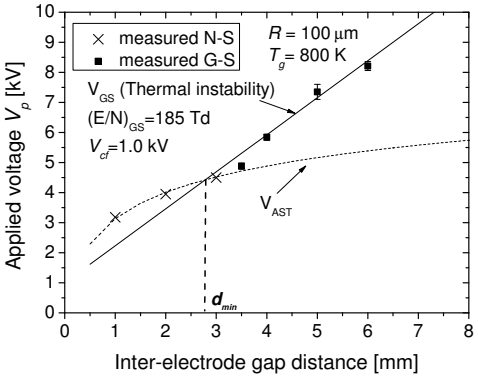

(c) $R = 100$ µm, $T_g = 800$ K

Figure 5.12: Glow-to-Spark transition voltages V_{GS} and No-Discharge-to-Spark transition voltages V_{NS} for various radii of curvature as a function of inter-electrode gap distance d.
(a) $R = 200$ µm, $T_g = 1000$ K (b) $R = 100$ µm, $T_g = 1000$ K (c) $R = 100$ µm, $T_g = 800$ K.
$l = 8$ mm, $PRF = 30$ kHz, and $v \approx 1.5$ m.s^{-1}

mate the elevated temperature writing the energy balance to the gas, using the value of energy deposited into a typical glow discharge - 10 µJ, as explained in [1]. The field in the positive column is equal to $E_{pc} = \left(\frac{E}{N}\right)_{GS} N$, which gives $\left(\frac{E}{N}\right)_{GS} = 185$ Td.

The curves of V_{AST} were calculated using α_{AST} deduced from the experimental values of V_{min}. We notice that there is a significative change in the shape of the transition voltage curve when d is decreased and the transition changes from a G-S to a N-G. The transition voltage curve varies linearly with d for V_{GS} and non-linearly for V_{NS}, which is appropriately predicted by the models detailed above.

Figure 5.13 presents the modeled V_{GS} - solid lines, and V_{AST} - dotted lines, as a function of the inter-electrode gap distance d for various radii of curvature R and T_g = 1000 K. The intersection of V_{GS} and V_{AST} corresponds to the theoretical value of the minimum distance d_{min} for the existence of the glow regime. We see that V_{AST} increases with R, which explains why d_{min} increases with R. d_{min} corresponds to a cathode fall V_{cf} = 1.1 kV for R =50, 100 and 200 µm and V_{cf} =1.3 kV for R = 500 µm.

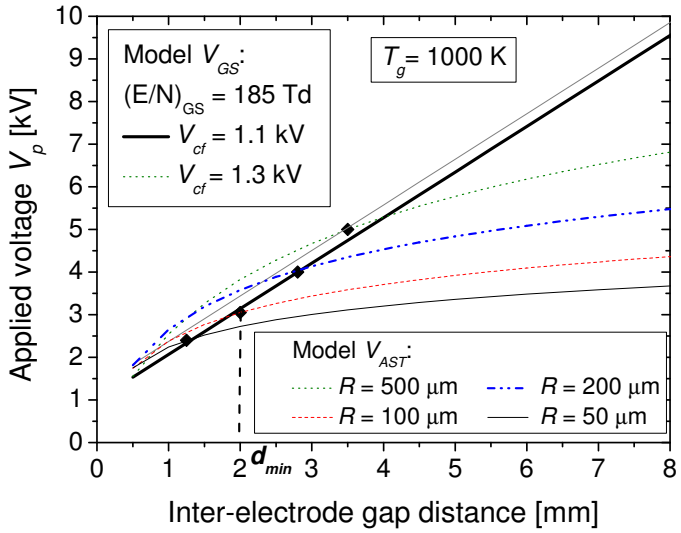

Figure 5.13: Predicted V_{GS} and V_{AST} for various radii of curvature, as a function of inter-electrode gap distance d. The intersection of V_{GS} and V_{AST} gives the experimental values of d_{min} represented as a square for each value of R. T_g = 1000 K, l = 8 mm, PRF = 30 kHz, and $v \approx$ 1.5 m.s^{-1}.

5.5.4 Minimum distance d_{min} and corresponding minimum voltage V_{min} for the existence of the glow regime

As was seen in previous sections, we can determine the minimum distance d_{min} for the existence of the glow regime from the map of the various discharge regimes as a function of d for a given temperature T_g. However, making this map is time-consuming and even if we stop operating just after getting the spark discharge, we still damage the electrodes each time we produce a spark discharge. Indeed, even after a few spark discharges (less than 10 s in total), the cathode is seriously damaged by ion bombardment and heating as can be seen on figure 5.14. Since the purpose of this work was to study the influence of the radius of curvature of the electrodes, we needed perfectly calibrated radii of curvature to have reproducible experiments.

Thus, in the rest of the study, we limit ourselves to the determination of the

minimum distance d_{min} and corresponding minimum voltage V_{min} for which glow discharges exist as function of gas temperature T_g and do not investigate further the influence of the radius of curvature on the G-S transition voltage V_{GS}.

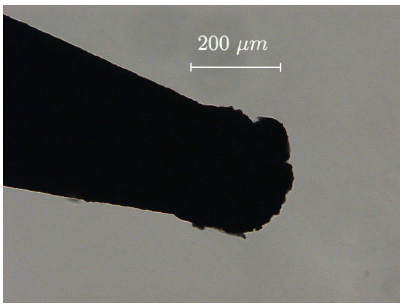

Figure 5.14: Cathode of initial radius of curvature $R_0 = 100$ µm after a few spark discharges. Image obtained with a BX51 Olympus microscope.

Figure 5.15 shows the influence of the radius of curvature on the existence of the glow regime. Figure 5.15 (a) represents the minimum distance d_{min} and (b) the corresponding minimum voltage V_{min} for the existence of the glow regime as a function of temperature T_g for various radii of curvature.

We see that the glow regime exists for $T_g \geq 700$ K for $R = 500$ µm, $T_g \geq 500$ K for $R = 200$ and 100 µm and $T_g \geq 300$ K for $R = 50$ µm. Furthermore, d_{min} decreases with R for a given gas temperature T_g. Consequently, the glow regime exists at lower temperature with small radius of curvature. On figure 5.15 (a), we also show the predicted d_{min} as a function of temperature T_g. As explained in section 2.9, we used a semi-empirical model for α_{AST}. From V_{min}, we calculate α_{AST} using Equation (2.10) setting $V_{AST} = V_{min}$. Then we deduce d_{min} as function of T_g using Equation (2.16). Figure 5.15 (b) shows the value of the voltage V_{min} obtained at d_{min}, and we see that this voltage increases with decreasing T_g for a given R. Furthermore, for a given gas temperature T_g, V_{min} decreases with decreasing R, which confirms that glow regime is promoted with small radius of curvature R.

In conclusion, using electrodes with small radius of curvature $R = 50$ µm, we succeeded in obtaining glow discharges at $T_g = 300$ K, which was one of the primary objectives of this thesis. We should emphasize that this study is based on visual observations of the discharge. In the next section, imaging diagnostics will be used to analyze the temporal development of the glow discharges obtained.

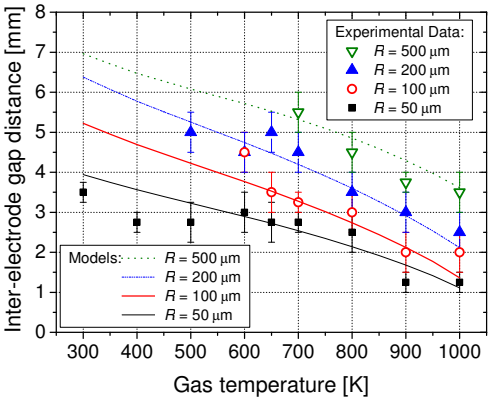

(a) Minimum distance d_{min}

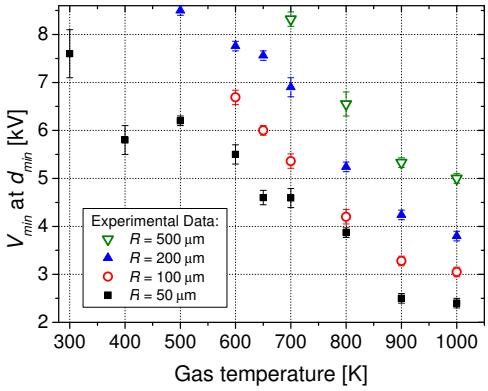

(b) Minimum voltage V_{min}

Figure 5.15: (a) Minimum distance d_{min} and (b) corresponding minimum voltage V_{min} for the existence of the glow regime as a function of temperature T_g for various radii of curvature. l = 8 mm, PRF = 30 kHz, and $v \approx 1.5$ m.s^{-1}.

5.6 Influence of the temperature on the structure of the glow discharge

In this section, we present images of glow discharges for different temperatures. In the previous section, we presented the domain of existence of the glow regime as a function of the gas temperature T_g. This study was done with the naked eye. While studying the various domains of existence of the regimes, we noticed that for low temperatures $500 < T_g < 700$ K, the spatial structure of the glow discharges was rather different from the structure for $T_g = 1000$ K. In order to verify that the glow discharges that we observed had the same dynamic behavior than the one studied at $T_g = 1000$ K, we investigate the structure of the glow discharge using ICCD imaging (see section 5.2 for the experimental details).

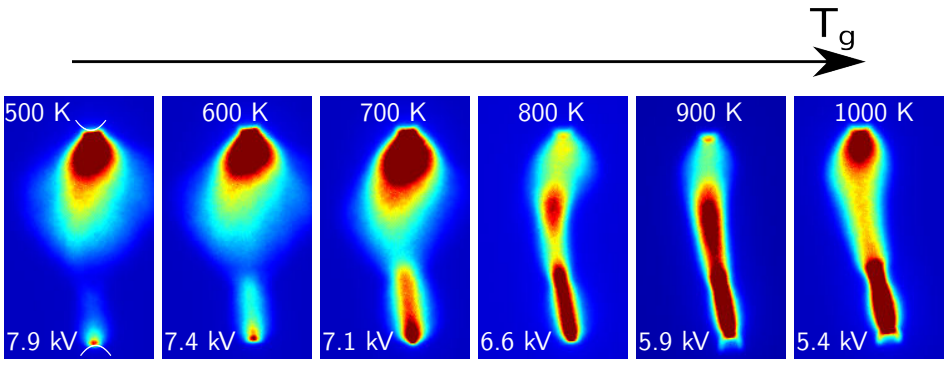

(a) $I = 60$ **(b)** $I = 60$ **(c)** $I = 60$ **(d)** $I = 20$ **(e)** $I = 20$ **(f)** $I = 60$

Figure 5.16: Images integrated during 25 ns of a glow discharge as function of gas temperature T_g. Emission averaged over several discharges. $R = 200$ µm, $d = 5$ mm, $l = 8$ mm, $PRF = 10$ kHz and $v \approx 1.5$ m.s^{-1}.

Figure 5.16 shows time-integrated images of the structure of a glow discharge from $T_g = 500$ K (left) to 1000 K (right) for the same inter-electrode gap distance $d = 5$ mm and same $PRF = 10$ kHz. In each case, the image corresponds to a weak glow regime just above the C-G transition. As the temperature decreased, the applied voltage V_p had to be raised to get the glow regime, which is consistent with the temperature dependence of the Corona-to-Glow transition voltage V_{CG}, see section 5.5.3.

For $800 < T_g < 1000$ K, the glow discharge structure is similar to the discharge structure of a glow regime obtained using *Delmo* electrodes, see section 5.3 or obtained in the previous work of Pai [2]. For $500 < T_g < 700$ K, the plasma appears to be diffuse and homogeneous when the optical emission is integrated over 100 accumulations. However, when we observe the discharge, we notice individual filaments in the volume of emission. To investigate the behavior of each discharge individually, images of single discharges were acquired with an

integration time of 25 ns.

Figure 5.17 presents single-shot images of a glow discharge from T_g = 500 K (left) to 800 K (right) for the same experimental parameters as in figure 5.16. Several typical samples of single-shot images are presented vertically. For T_g = 800 K, only one single-shot image is presented since all acquisitions were similar.

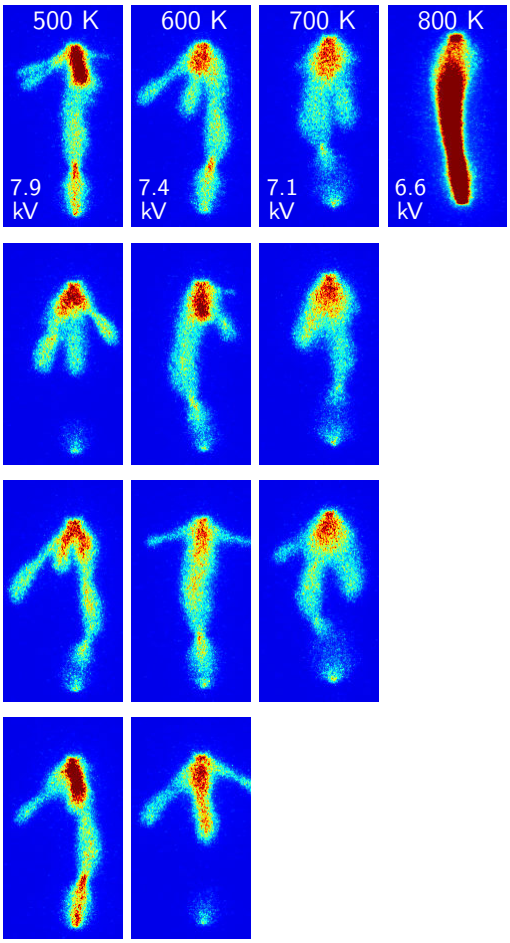

Figure 5.17: Single-shot images integrated during 25 ns of a glow discharge as function of gas temperature T_g. Intensity I = 25.

These images reveal that the plasma is actually composed of filamentary streamer discharges with a branching structure. The high repetition rate and the variability in position of the numerous streamers give a diffuse appearance to the eye. Figure 5.18 presents time-resolved images - integrated during 2 ns - of this new kind of radially extended glow discharge, that we will call Multi-Channel Glow (MCG) discharge. Several typical samples of single-shot images are pre-

sented vertically for each time t. Recall that we cannot capture more than one image per discharge event. Therefore, the images presented here are all from separate discharges.

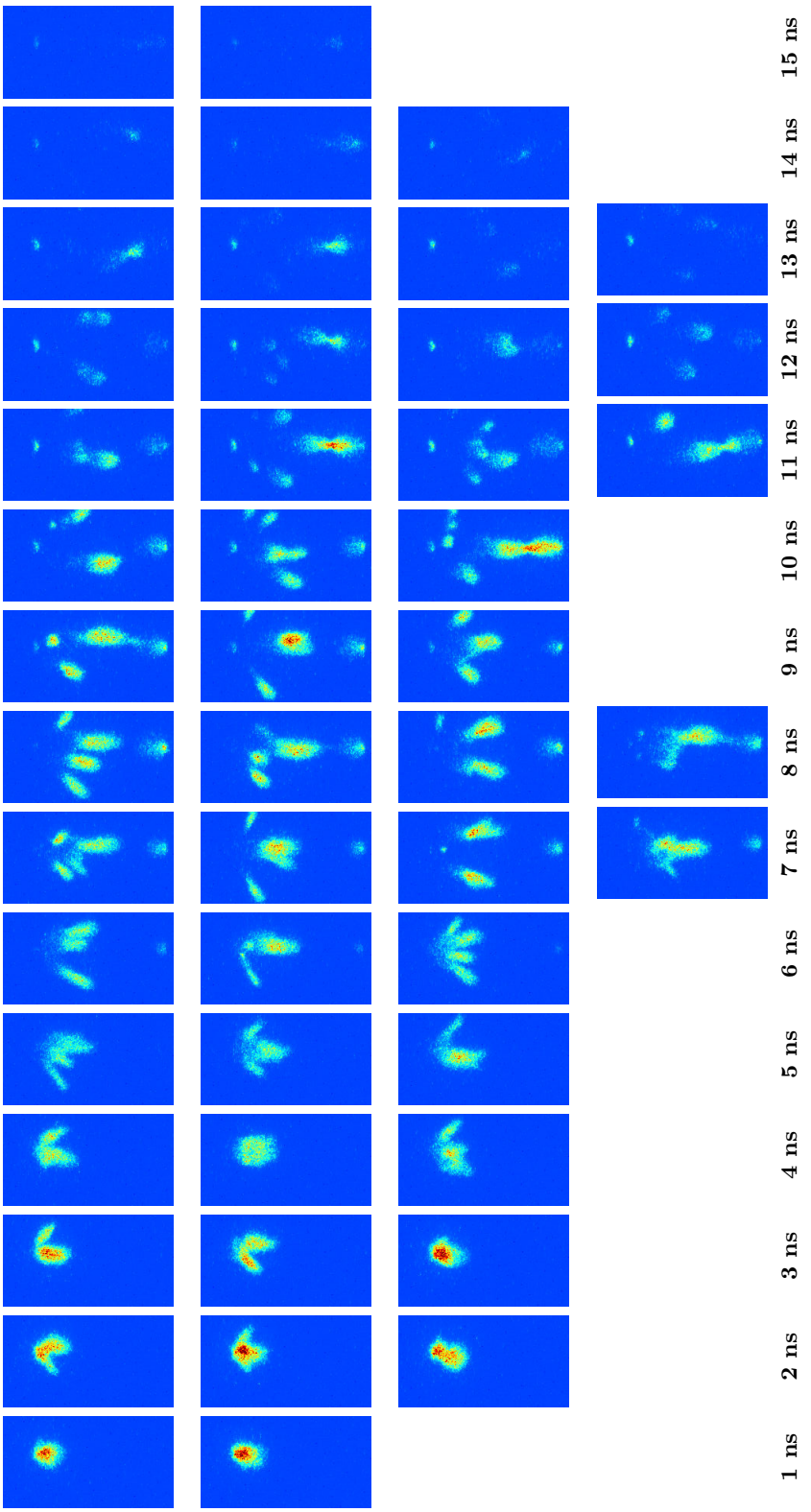

Figure 5.18: Single-shot images integrated during 2 ns of an NRP multi-channel glow discharge. $T_g = 500$ K, $R = 200$ µm, $d = 5$ mm, $V_p = 7.9$ kV, $l = 8$ mm, $PRF = 10$ kHz and $v \approx 1.5$ m.s^{-1}. Intensity $I = 45$.

5.6.1 Dynamic description

The dynamics of this radially extended glow discharge are very similar to the dynamics of a common glow discharge, see figure 5.2. First, the luminosity which is indicative of the presence of $N_2(C)$ is generated at the anode initially, at about $t = 1$ ns and propagates across the gap, reaching the cathode at $t = 7$-8 ns. This connection time is similar to the one in a common glow discharge, around 6-8 ns. The connection time seems to be a little longer in the case of the multi-channel discharge, even though the voltage is higher than for the glow discharge at $T_g = 1000$ K. This may be because the streamers take a curved path in the MCG discharge. We cannot distinguish a return stroke, as for a weak glow discharge.

Unlike the weak glow discharge at $T_g = 1000$ K, we distinguish several paths of light emission. The excited species responsible for the luminosity, mainly $N_2(C)$, can take different paths from one discharge to the other. The connection between the anode and the cathode does not always occur along the same path: the main streamer that leaves the anode connects the cathode axially, but additional streamers leave from the side of the anode. In other words, from one discharge to the other, several streamers leave the anode at the same time and/or the streamer does not always take the same axial path.

5.6.2 Electrical characteristics of glow and Multi-Channel Glow (MCG) regime

Figure 5.19 shows the voltage and the total current measured for a glow regime for $T_g = 1000$ K and $d = 5$ mm and a multi-channel regime for $T_g = 300$ K and $d = 3.5$ mm. The applied voltage is higher at low temperature (see section 5.5.1), but the shape is similar for both discharges. The total current is fairly similar in both discharges. The similarity in voltage and current of these two regimes makes them impossible to distinguish using only electrical measurements. As will be shown in section 6.8, the energy deposited is practically the same for both regimes.

5.6.3 Multi-channel glow regime, as a 3D version of the glow regime

The images of figures 5.17 and 5.18 confirm that we have found a 3D phenomenon occuring at temperatures $T_g < 700$ K with electrodes of radius of curvature $R = 200$ µm and an inter-electrode gap distance $d = 4$ mm, which has not been observed previously in our experimental reactor. This might have been due to the different nature of the electrodes. Pai *et al* [1], [2], [36] used *Delmo* industrial electrodes whose shape was not completely symmetric, whereas we use calibrated *Delta Precis* electrodes. Furthermore, the difference between the two regimes is only a difference in their spatial structure and can only be de-

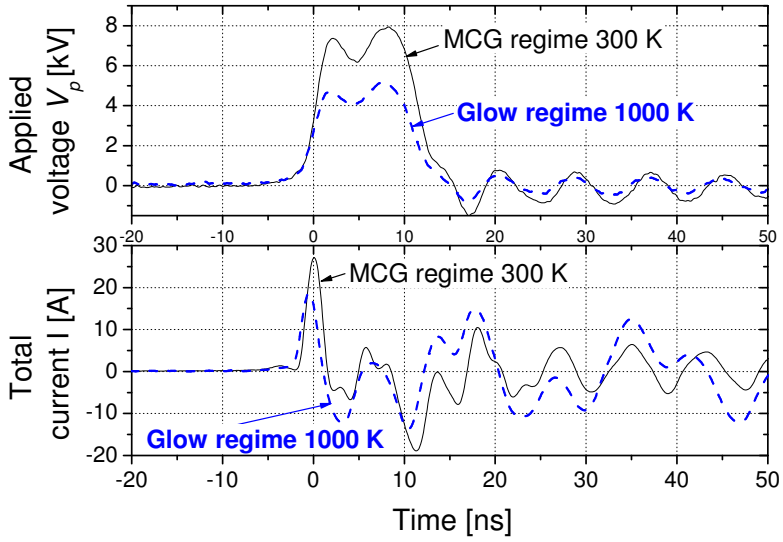

Figure 5.19: Typical voltage and current waveforms for a glow regime (dash blue) and an MCG regime (solid black).

tected with ICCD images, a diagnostic that had not been implemented by Pai. However, from our experiments, we cannot invalidate the 1D-model developed in section 5.5. As long as an axial glow discharge is observed, this model is valid. Thus, this MCG regime appears to be simply a 3D version of the glow regime defined and studied in [1], [2], and [36]. All the characteristics of the multi-channel regime except its spatial distribution are identical to the glow regime characteristics.

5.6.4 Definition of the Multi-Channel Glow (MCG) regime

We may now define precisely what will be called a glow regime and what will be called a MCG regime. For both the MCG and glow discharges, light is emitted in diffuse manner, and the conduction current is very small. In addition, a streamer connects the anode and the cathode. These features are common to the MCG and glow regimes. However, the spatial structure of a glow and MCG discharge is different. In the glow regime, only one streamer joins the anode and the cathode. Figure 5.20 shows several samples of single-shot images of a MCG discharge, integrated over 25 ns. A variety of situations is possible:

- an axial connection between the anode and the cathode
- an axial connection with additional streamers leaving the anode
- two off-axis connections, two different streamers reach the cathode
- an off-axis connection with additional streamers

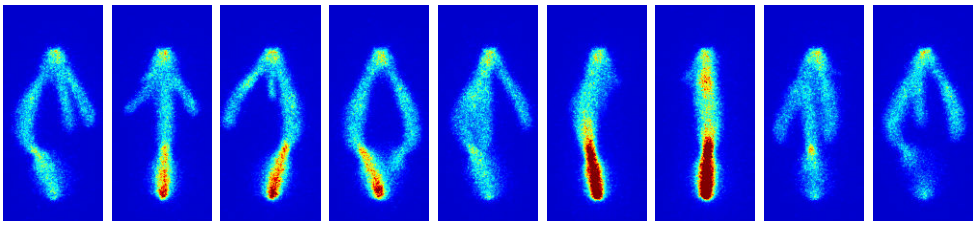

Figure 5.20: Samples of single-shot images of a MCG discharge, integrated over 25 ns. T_g **= 600 K,** R **= 200 µm,** d **= 5 mm,** V_p **= 7.4 kV,** l **= 4 mm,** PRF **= 10 kHz and** $v \approx$ 1.5 m.s^{-1}**. Intensity** I **= 18.**

Figure 5.21 shows the intensity along the axis of symmetry of the electrodes, for T_g = 1000 K and T_g = 600 K. We notice important differences between those two profiles. For the glow discharge at 1000 K, the intensity is high at the anode, decreases along the inter-electrode axis, is constant from $d/5$ to $3d/5$ (distance from the anode), and increases again toward the cathode. The intensity is higher at the cathode than at the anode. For the MCG discharge at 600 K, the intensity is high at the anode and decreases from the anode to the distance $3d/5$ from the anode. This is because not all streamers join the cathode, unlike for a glow discharge. Finally, the intensity increases slightly towards the cathode, reaching 3/10 of the intensity at the anode. We see that the two profiles are quite different. However, we should not rely on the time-averaged intensity profiles to distinguish glow or MCG discharges because their intensity profiles can be similar. Instead, it is recommended to rely on the analysis of time-evolution images or the single-shot images.

When the gas temperature is decreased from T_g = 1000 K to T_g = 500 K, the MCG regime tends to be favored over the glow regime, see figure 5.17. On figures 5.9 and 5.10 (a), we had obtained a glow regime at lower temperatures than Pai *et al* and [1] and [2]. But because these maps were obtained by watching the discharge, we were unable to discriminate a glow discharge from a MCG discharge. Thus, the domains indicated on the various maps presented in section 5.5 may correspond to either a glow or a MCG regime. For example, for R = 200 µm, glow regime exists for $T_g > 700$ K, and the MCG regime for $T_g \leq 700$ K. Furthermore, this 3D structure of the discharge may explains why the experimental data slightly departs from the model on figure 5.11.

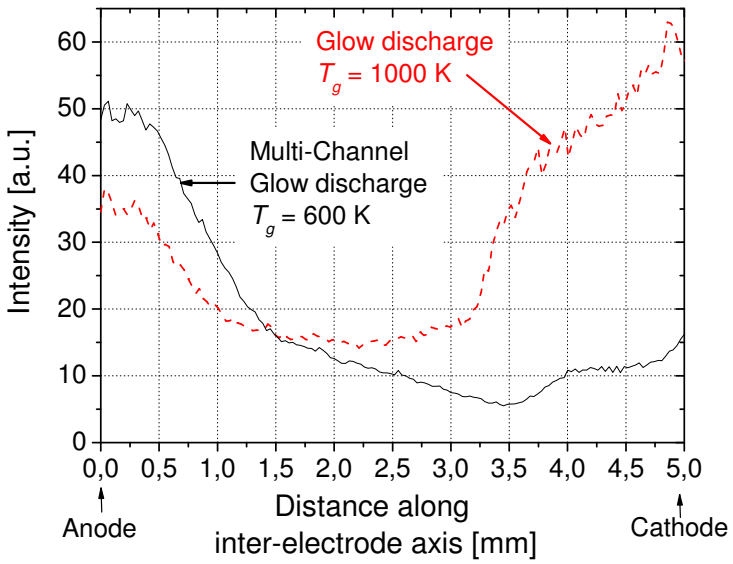

Figure 5.21: Intensity of the averaged discharges as function of distance along inter-electrode axis for T_g = 1000 K and V_p = 5.4 kV (thick dash red) from figure 5.16 (f) and T_g = 600 K and V_p = 7.4 kV (thin solid black), from figure 5.16 (b).
R = 200 µm, d = 5 mm, , l = 4 mm, PRF = 10 kHz and $v \approx$ 1.5 m.s^{-1}!.

5.6.5 Multi-channel regime in other experimental setups

This branching structure regime was previously observed in other experimental conditions. In [77], Nijdam obtained multi-streamer discharges in air at atmospheric pressure and ambient temperature. He used a so-called "C -supply" pulse generator that provides pulses of amplitude around 18 kV, rise time of 15-24 ns and fall time of approximately 10 µs, in a pin (anode)-plane (cathode) configuration separated by an inter-electrode gap distance of 40 mm.

In these experimental conditions, we see in figure 5.22 a very strong multi-channel regime: about 10 streamers are initiated at the anode and then separate in more than 50 different streamers at d = 20 mm from the anode. When the pressure is decreased down to 50 mbar, the branching structure is not present anymore, but we see instead a diffuse discharge with uniform luminosity from the anode to the cathode. Similar effects were obtained in [59] where negative pulses of amplitude around 12 kV, rise time of 8 ns and FWHM of 22 ns, in a pin (anode)-plane (cathode) configuration separated by an inter-electrode gap distance of 30 mm have been applied in air at pressures between 300 and 760 torr.

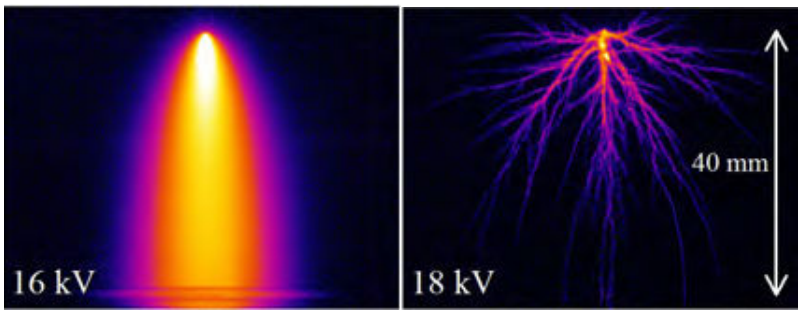

(a) P = 50 mbar **(b)** P = 1000 mbar

Figure 5.22: ICCD images integrated for more than 1000 ns of a "streamer discharge" in air in a pin-plane configuration for two different values of pressure. T_g = 300 K. d = 40 mm. Camera gain is varied between the images, discharges are brighter at lower pressure. Images taken from [77].

Similar effects of the pressure have been seen in [78] where pulses of amplitude around 45 kV, rise time of 5 ns and FWHM of 10 ns, in a pin (anode)-plane (cathode) configuration separated by an inter-electrode gap distance of 15 mm have been applied in air at pressures between 1 and 9 bars.

The evolution of the spatial structure of the discharge of Nijdam [77] and Tardiveau *et al* [78], when the pressure is increased in their experimental setup, is identical to the evolution of the spatial structure of the discharge in our present work when the temperature is increased. This suggest that the spatial structure of the discharge depends on the reduced electric field E/N within the discharge, N being the density of the gas.

5.7 Glow discharges from T_g = 1000 K to T_g = 300 K

In section 5.6, we mentioned that a MCG regime appears when the reduced electric field is decreased from a situation where a glow discharge exists. To obtain glow discharges at low temperature $T < 500$ K, we will see in section 6.2 that the inter-electrode gap distance d must be decreased.

To keep the reduced electric field E/N approximately constant, we started from a glow discharge at T_g = 1000 K and d = 4 mm and progressively decreased the gas temperature T_g and the inter-electrode gap distance d. The experimental parameters varied in this study are presented in table 5.2. We repeat this experiment for electrodes of five different radii of curvature: *Delta Precis* electrodes with R = 50, 100, 200 and 500 µm and *Axfil* electrodes with R = 20 µm.

Table 5.2: Inter-electrode gap distance d and corresponding gas temperature T_g for each NRP glow discharge shown in figure 5.23.

Gas temperature T_g [K]	Inter-electrode gap distance d [mm]
300, 400	2.5
500, 600	3.0
700, 800	3.5
900, 1000	4.0

Figure 5.23 presents time-integrated images of glow discharges (integrated on several discharges) for different radii of curvature R = 20, 50, 100, 200 and 500 µm and different temperatures. The radius of curvature R is decreased from top to bottom, the top line corresponds to 500 µm and the bottom two lines correspond to 20 µm. Each temperature corresponds to a column, T_g = 300 K is on the left and T_g = 1000 K on the right. Each discharge recorded corresponds to a weak glow discharge, as defined in section 5.3. For every set of parameters both single-shot and averaged images were taken. The structure of each discharge appears similar in the averaged and single-shot images. In other words, we observe a glow regime and not a MCG regime, as defined in section 5.6. For instance, the last line of figure 5.23 presents single-shot images for R = 20 µm while the line immediately above presents averaged images of the same discharge.

For R = 500 µm and T_g = 800 K, the transition N-S is observed for an applied voltage $V_p \approx$ 6.3 kV, and no glow discharge is seen for $T_g <$ 900 K. This is consistent with the minimum distance d_{min} of existence of the glow regime with respect to the gas temperature T_g, see figure 5.15. For R = 500 µm and T_g = 800 K, the predicted d_{min} is 4.5 mm which is larger than our gap distance of 4 mm in this experiment. For R = 200 and 100 µm, at T_g = 500 K, an unstable glow is observed for $V_p \approx$ 6.0 kV transitioning from time to time to a spark regime. For this reason, this regime was not considered to be a glow regime and was not recorded with the ICCD camera (sparks can damage the camera). Each time a glow regime was recorded, we checked that it was a weak glow regime by a careful examination of the 2-ns time-resolved images of the discharge and by checking on the single-shot images that it was not a MCG discharge.

All images presented in figure 5.23 show glow discharges, from T_g = 900 K to T_g = 1000 K for R = 500 µm, from T_g = 500 K to T_g = 1000 K for R = 200 and 100 µm, and from T_g = 300 K to T_g = 1000 K for R = 50 and 20 µm. This is consistent with the model developed in [1], [2], and [36] and presented in 2.9. For a given temperature, decreasing the radius of curvature promotes the existence of the glow regime. With large radii of curvature, only the transitions

from "No Discharge" to spark regime are observed.

An example of time-resolved images of two glow discharges - one obtained at 1000 K and one at 300 K for the same radius of curvature $R = 20$ µm is presented on figure 5.24. The experimental parameters are the same as those of figure 5.23. In particular, $d = 4$ mm for $T_g = 1000$ K and $d = 2.5$ mm for $T_g = 300$ K. On this figure, the intensity of the images is higher for the images at higher temperature. This was observed for all the images of figure 5.23. Nevertheless, we notice the same succession of physical processes than in the weak glow discharge as defined in section 5.3. This allows us to conclude that we have evidenced the existence of the glow regime at 300 K, as was defined previously on the discharge at 1000 K in [2].

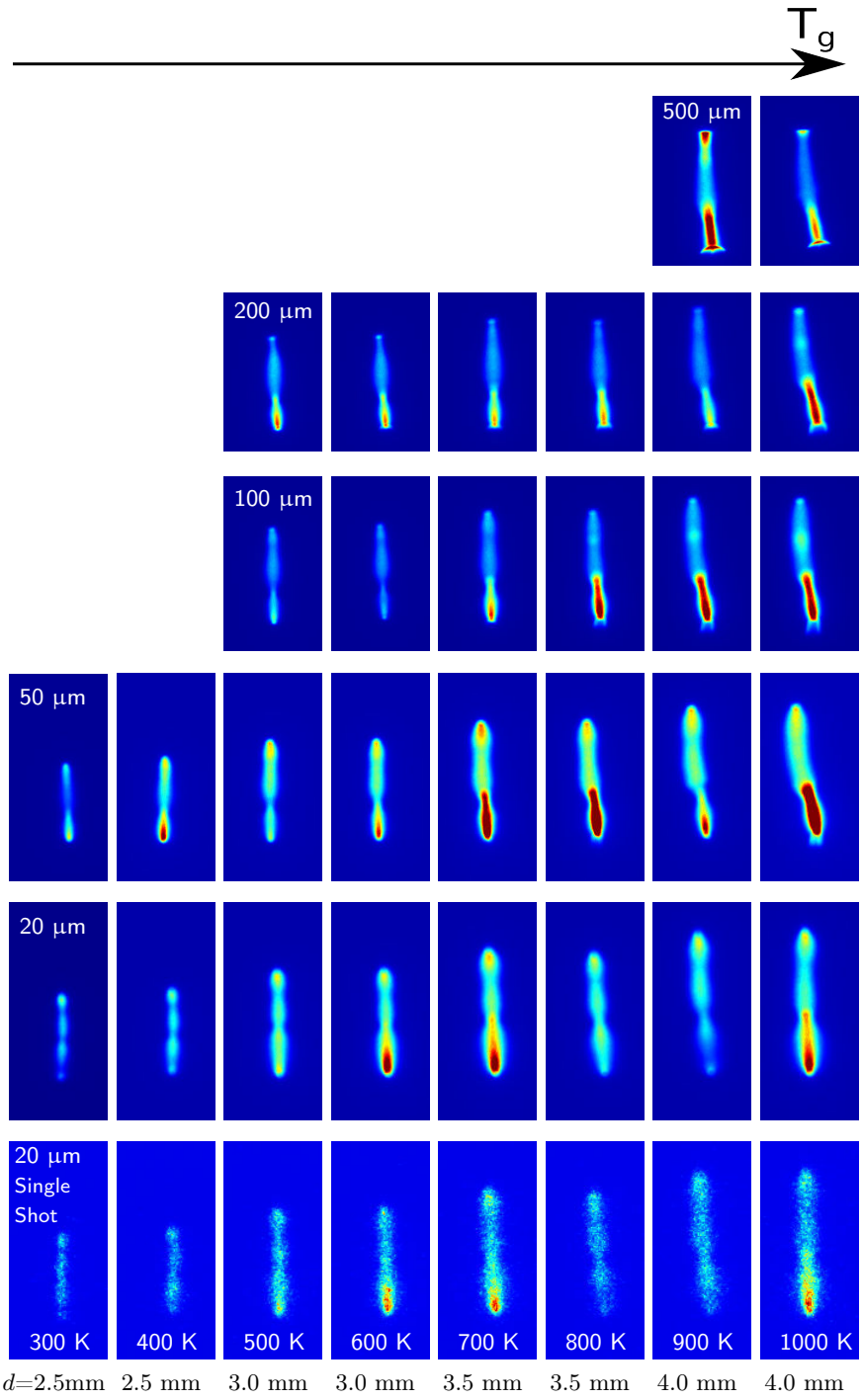

Figure 5.23: Images integrated during 25 ns of a glow discharge at different temperatures and radii of curvature. The images are averaged over several discharges except for the last row, which corresponds to single-shot discharges. l = 3.5 mm (l is defined on figure 3.16), PRF = 10 kHz, and $v \approx$ 1.5 m.s^{-1}. Top 3 rows: Intensity I = 25, Rows 4,5: Intensity I = 50, Bottom row: Intensity I = 25.

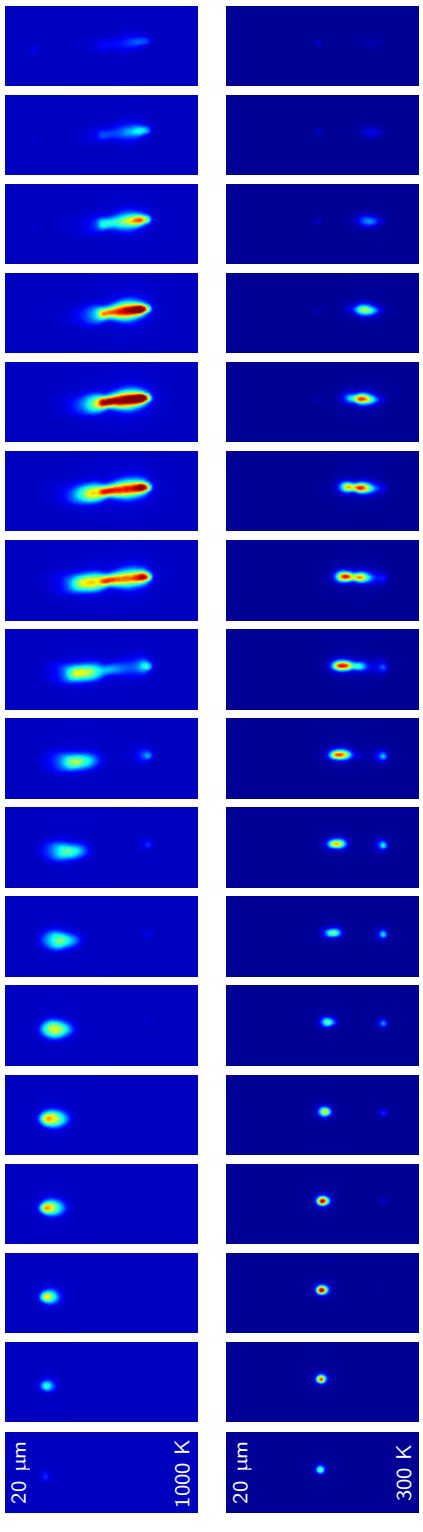

Figure 5.24: Images integrated during 2 ns of a glow discharge for (top) T_g = 1000 K, d = 4.0 mm, and V_p = 4.0 kV and (bottom) T_g = 300 K, d = 2.5 mm, and V_p = 4.7 kV (bottom). Images are averaged over several discharges. R = 20 µm, l = 3.5 mm, PRF = 10 kHz, and $v \approx$ 1.5 m.s^{-1}. Intensity I = 150 (top) and I = 250 (bottom).

5.8 Conclusions

In this chapter, we have first determined with ICCD - camera images the spatial and temporal structure of a glow discharge at $T_g = 1000$ K. We confirmed the existence of different kinds of glow regimes, a so-called "weak glow" regime and a "strong glow" regime, the first regime being just above the onset voltage of the return stroke. We studied the influence of the radius of curvature of the electrodes on the spatial structure of the discharge at $T_g = 1000$ K. For $R = 50$ µm, the streamer radius decreases while it propagates, whereas for $R = 500$ µm, the radius of the streamer is approximately constant. We then studied the influence of the radius of curvature of the tip of the electrodes on the limits of existence of the glow regime. This study confirmed the model proposed by Pai in [1] and confirmed that at a given gas temperature T_g, the minimum distance for the existence of the glow regime d_{min} decreases when the radius of curvature of the electrode decreases.

We studied the influence of the gas temperature on the spatial structure of the discharge at a given radius of curvature with ICCD-camera imaging. On single-shots images, we evidenced a regime spatially different from the glow regime, called the Multi-Channel Glow (MCG) regime. This regime has the same properties as the glow regime but it features several positive streamers within a single discharge.

Finally, we have determined a set of parameters for which the glow regime exists for different temperatures and different radii of curvature provided we decrease the inter-electrode gap distance d while decreasing the gas temperature T_g.

We have succeeded in obtaining a glow regime at $T_g = 300$ K with electrodes of small radii of curvature $R = 20$ and 50 µm, as was predicted by Pai *et al* in [1]. The configuration of the electrode is not exactly pin-pin, since we introduced a plane behind the electrodes. The influence of the length l between the tip of the electrode and the plane will be studied in the next chapter.

Chapter 6

Parametric Study of the NRP Glow regime at $T_g = 300$ K

6.1 Introduction

In the previous chapter, we established the existence of NRP Glow (G) discharges at $T_g = 300$ K. To get such a regime, electrodes of small radius of curvature $R = 20$ or 50 µm are needed, with a relatively small inter-electrode gap distance (around 2.5 mm). The existence of a Multi-Channel Glow (MCG) regime with a 3D branching structure was also established.

The purpose of this chapter is to establish the parameters that are important to promote the NRP glow regime with respect to the NRP Multi-Channel Glow (MCG) regime.

In the first part, we study the influence of geometrical parameters. In section 6.2, we study the influence of the inter-electrode gap distance d and in section 6.3, that of the flow direction on the nature of the discharge regime. Then, in section 6.4, we study the influence of the length l between the tip of the electrode and the plane behind it. The definition of the length l is given on figure 3.16 in section 3.4.

In the second part, we will study in section 6.5 the influence of the Pulse Repetition Frequency PRF and in section 6.6 the influence of the velocity of the flow on the nature of the discharge regime. In section 6.7, we discuss the physical explanation for the transitions from MCG and glow regimes. Then, we show in section 6.8 an estimation of the energy put into the glow and MCG discharges. Finally, in section 6.9, we investigate the importance of the plane behind the pin electrodes with additional experiments.

In this chapter, we used Pulse Generators 1 and 2 and electrodes of small radius

of curvature at the tip $R =$ 50 µm or 20 µm at $T_g = 300$ K. We use the system described in section 3.2, but we do not preheat the gas and work at room temperature $T_g = 300$ K.

6.2 Influence of the inter-electrode gap distance d

In this section, we study the influence of the inter-electrode gap distance d on the structure of the discharge at $T_g = 300$ K. We use Pulse Generator 1 at $PRF = 10$ kHz with electrodes of radius of curvature at the tip $R =$ 50 µm. We work with an axial flow of velocity v equal to 0.5 m.s^{-1}. The length l is kept constant, $l = 3$ mm. As the operator increases the voltage from 0 V, the discharge is observed with the naked-eye. Images of glow-like discharges are captured as soon as a luminous junction is realized between the electrodes. Glow-like discharges when observed with the naked eye may either be glow discharges or MCG discharges.

Figure 6.1 presents on the first line averaged images of glow-like discharges for several inter-electrode gap distances d. The applied voltage V_p is increased when the gap d increases. These images are integrated over 25 ns and averaged over 1000 discharges. We notice that the radius ρ of the discharge at the mid-gap decreases with decreasing d, and that the discharge luminosity structure seems different for the different inter-electrode gap distances d. To discriminate MCG and glow regimes, we also took single-shot images that are shown under the averaged images. Several typical samples of single-shot images are presented vertically on the second, third and fourth lines of figure 6.1. The various samples do not appear with the same frequency. For instance, for $d = 2.5$ mm, most of the discharges are similar to the images of figure 6.1 (h) or (n), which explains why the plasma has a relatively small radial extent on the averaged image of figure 6.1 (b), and figure 6.1 (t) rarely occurs. For $d \geq 3.0$ mm, the structure is that of an MCG discharge, several streamers leave the anode, and for $d \leq 2.5$ mm, the discharge is a glow discharge, only one streamer leaves the anode. This explains why the radius of the plasma is much larger for large values of d than for small values of d.

We have seen that decreasing the inter-electrode gap distance d promotes the existence of the glow regime with respect to the MCG regime. The evolution of the discharge structure is similar when d is increased on figure 6.1 and when T_g is decreased on figure 5.16. This confirms that the relevant parameter that controls the transition between the two regimes glow and MCG is the reduced Laplacian electric field between the electrodes. When the reduced electric field on the axis of symmetry of the discharge is too low (d is large or T_g is small), the model presented in section 2.9 is not valid anymore and the discharge develops a 3D branching structure. This will be detailed in section 6.7.

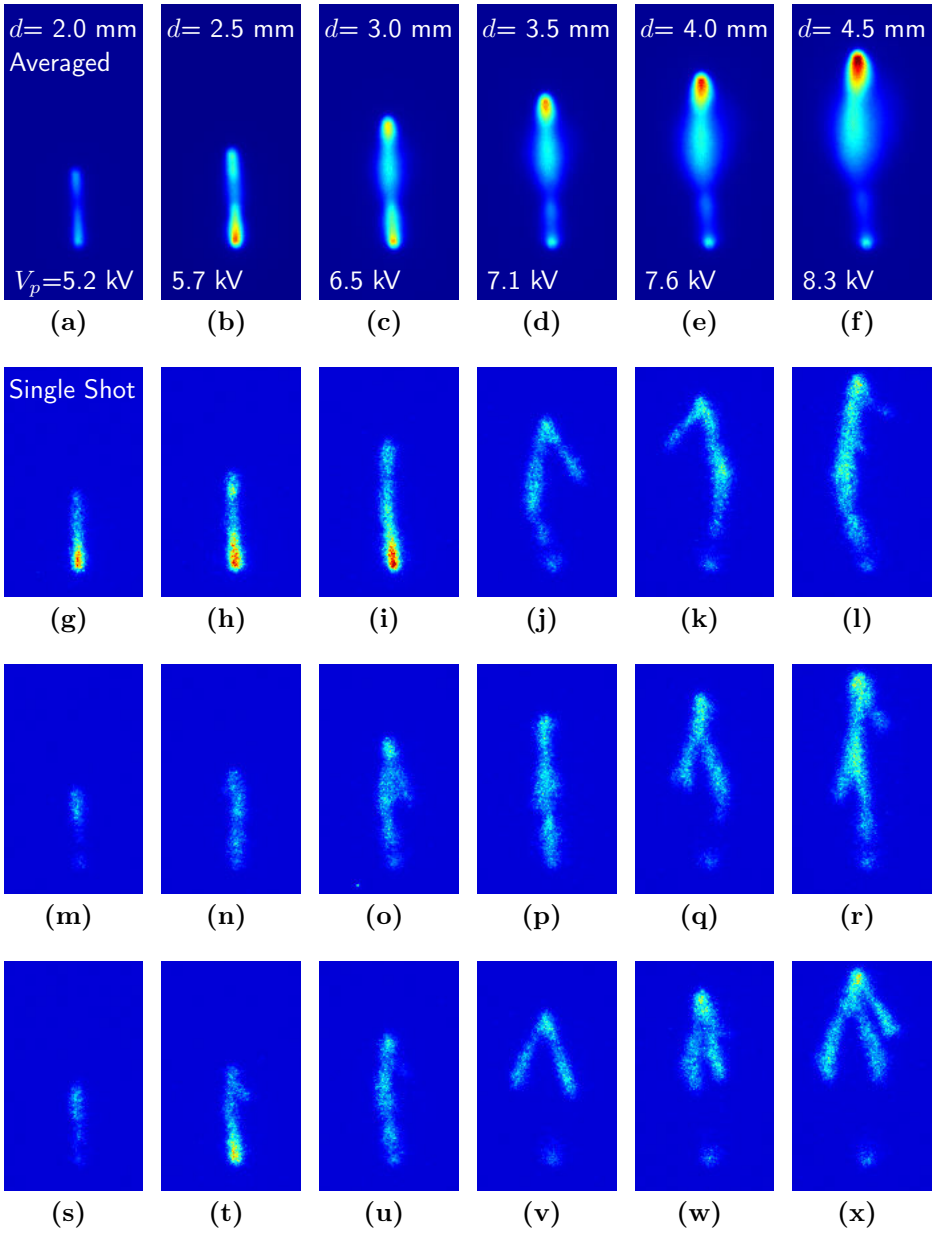

Figure 6.1: Images integrated over 25 ns of glow-like discharges with respect to the inter-electrode gap distance d. d is increased from left to right in steps of 0.5 mm from d = 2.0 mm to d = 4.5 mm. The first row corresponds to images averaged over several discharges (Intensity I = 50) and the last three rows are examples of single-shot images (Intensity I = 20). T_g = 300 K, R = 50 µm, l = 3 mm, PRF = 10 kHz and v = 0.5 m.s^{-1}.

6.3 Influence of the flow direction

In this section, we detail the influence of the flow direction on the structure of the glow discharge. We placed an additional metallic piece in between the carrying *Delmo* electrodes and the *Delta Precis* or *Axfil* electrodes, as was explained in section 3.4. Consequently, we introduced a plane behind the pin electrodes, which modifies the structure of the Laplacian electric field between the electrodes. Furthermore, the metallic piece is an obstacle to the air flow. The size of this metallic piece is 6-8 mm in a flow of velocity $v \approx 0.5$ m.s^{-1}. Therefore, the Reynolds number is around 180-200 for $T_g = 300$ K, which means that behind the obstacle the flow is vortical. The schematic diagram in figure 6.2 shows the flow field before and after the obstacle.

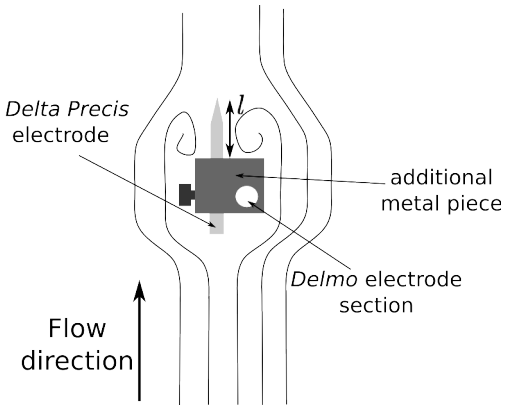

Figure 6.2: Schematic diagram presenting the nature of the flow before and after the obstacle. The carrying *Delmo* electrode direction is orthogonal to the figure plane.

In the upcoming section 6.4, we will study the influence of the length l between the tip of the electrodes and the plane on the structure of the discharge. But changing the position of the discharge with respect to the plane would change the position of the plasma in the flow. Thus, it would be difficult to decouple the influence of the Laplacian electric field on the discharge and the influence of the nature of the flow. Consequently, studying the impact of the parameter l on the discharge is more relevant in a transverse flow configuration.

This leads to consider whether the direction of the flow may have an influence on the regime transitions. Preliminary experiments showed that a transverse flow has a tendency to blow more the discharge than an axial flow. However, the various behaviors established in the previous chapter, the influence of R and T_g on the structure of the discharge, should be similar. Consequently, in a first approach, we did not make a complete study of the impact of the direction of the flow on the discharge structure. We have simply analyzed one test case, a typical glow discharge at $T_g = 300$ K, for two perpendicular directions of the

flow.

The experimental setup for the study of NRP discharges in a transverse flow was detailed in section 3.2. The electrodes are positioned approximately 15 mm above the output of the metal tube blowing air. Figure 6.3 presents images averaged on several glow discharges for two perpendicular directions of the flow. On the left (a) is the same image as in figure 5.23 for $T_g = 300$ K and $R = 20$ µm. The right image corresponds to the same experimental parameters except that the flow is blown perpendicularly to the axis of the electrodes. We used the same air blowing tube in the two experiments. To change the axis of the flow, we had to change the direction of the inter-electrode axis. For figure 6.3 (a), the flow is blown from the bottom (cathode) to the top (anode) and the electrodes are vertical. Figure 6.3 (b) represents the image of an horizontal discharge rotated of 90° clockwise. Thus, the flow comes from the left, as indicated on the image. This rotation was made to compare easily the two images.

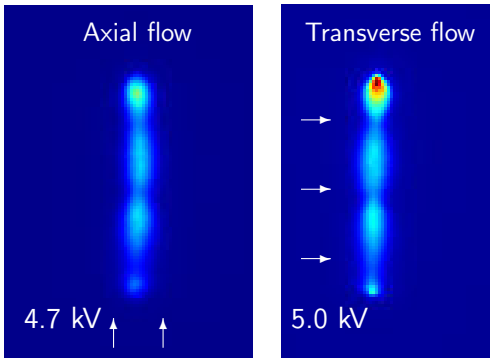

(a) **(b)**

Figure 6.3: Averaged images integrated over 25 ns of glow discharges. (a) corresponds to an axial flow, blown from the bottom to the top $V_p = 4.7$ kV, (b) corresponds to a transverse flow, blown from the left to the right $V_p = 5.0$ kV.
$T_g = 300$ K, $R = 20$ µm, $d = 2.5$ mm, $l = 3.5$ mm, $PRF = 10$ kHz and $v = 0.5$ m.s^{-1}. Intensity $I = 50$.

We notice the same structure of the discharge. Both are glow discharges, and present a global luminosity that is homogeneous. The geometric structures of the discharge are similar. When the flow is transverse, we have to increase the applied voltage to get a glow regime from 4.7 kV to 5.0 kV for figure 6.3 (b). Thus, the luminosity is stronger at the anode on figure 6.3 (b) than on figure 6.3 (a). This confirms that the regime transitions are only slightly different for a transverse flow.

We also took single-shot images in the same conditions. The images obtained

are identical to the averaged images, except they are less luminous. Figure A.1 in appendix A presents time-resolved images of the glow discharge in a transverse flow at T_g = 300 K of figure 6.3 (b). We notice the same succession of physical steps that in a typical glow discharge in an axial flow at T_g = 1000 K (figure 5.2) or T_g = 300 K (figure 5.24).

The study of this single test case suggests that changing the flow direction does not significantly affect the domain of existence of the various regimes for the velocity considered here. For a given set of parameters, a discharge might be a glow for an axial flow and a corona for a transverse flow. However, it is reasonable to consider that the influence of the various parameters studied in the previous chapter (radius of curvature of the electrode R, gas temperature T_g...) on the discharge structure will not be greatly modified by changing the direction of the flow. Consequently, until the end of the thesis, we will work in a transverse flow and use the results previously obtained in axial flow.

6.4 Influence of the distance l

The purpose of this section is to establish the influence of the length l between the tip of the electrodes and the plane, varying l from 1 mm to several millimeters. The axis of the flow is perpendicular to the inter-electrode axis. Using Pulse Generator 1, and short length l (l = 1 or 2 mm), we did not manage to get a glow discharge for the maximum output voltage reachable by the pulser. Therefore, we used Pulse Generator 2, that was characterized in section 3.3. The main difference that impacts the structure of the discharge and the regime transitions is the duration of the pulse. We used both channels of the pulser, Channel 1 that creates pulses of Full Width at Half Maximum (FWHM) of 23 ns, and Channel 2 that creates pulses of FWHM of 6 ns, in the configuration studied.

In the first part of the section, we study the effect of the length l on the glow regime or MCG regime. In the second part, we present experiments performed with constant applied voltage V_p. These experiments will be used to discuss the physical reasons behind the branching structure of MCG discharges.

6.4.1 Promote the glow regime increasing length l

Figure 6.4 presents images of glow-like discharges for various lengths l, l = 1 to 5 mm. These images were recorded as soon as a luminous junction was realized between the electrodes, when increasing the voltage from 0 V and observing the plasma with the naked-eye. The first line shows averaged images of several discharges and the second and third lines are samples of single-shot images.

First, the minimum voltage to get glow-like discharges is higher with Pulser 2

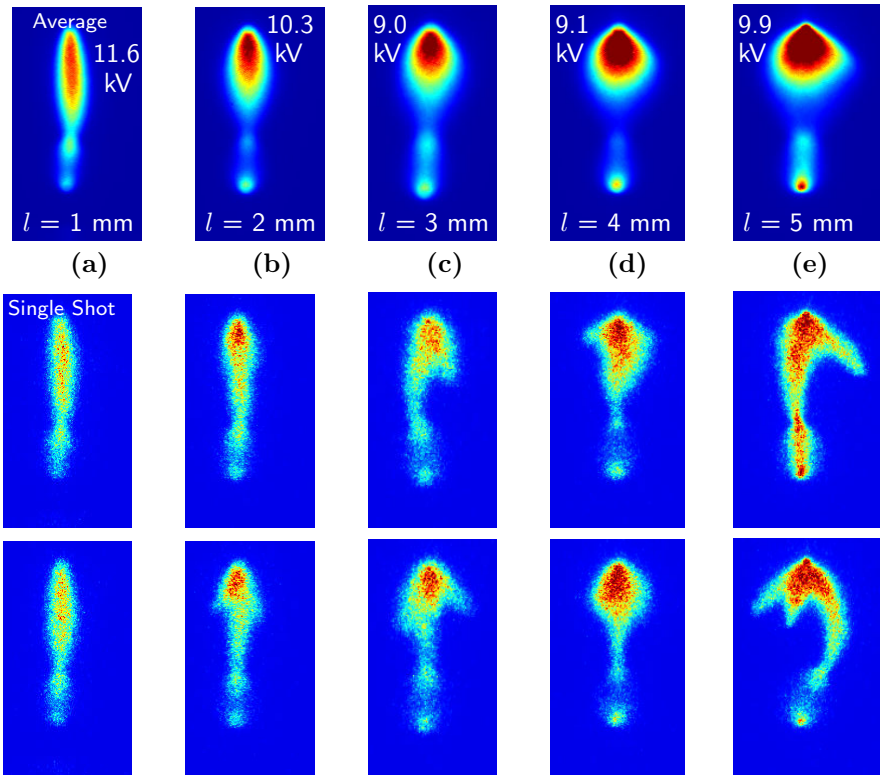

Figure 6.4: Images integrated over 20 ns of glow-like discharges for l = 1 to 5 mm. The images on the first line averaged over several discharges (I= 40) and those on the second and third lines are samples of single-shot images (I= 25).
T_g = 300 K, R = 50 µm, d = 4 mm, PRF = 10 kHz and transverse flow $v = 0.5$ m.s^{-1}**.**

Channel 2 than with Pulser 1. The conditions of figure 6.1 (e) are identical to the conditions of figure 6.4 (c) except that the flow is transverse on the latter image. In this case, the applied voltage V_p = 9.0 kV is higher than the applied voltage in the first case, V_p = 7.6 kV. The difference between the two applied voltages seems too high to be only due to the change of flow direction. Another reason is the shorter duration of the pulse obtained with Pulser 2 Channel 2, see section 3.3. We had to increase the applied voltage to have the same effects on the plasma, since the voltage is applied during a shorter period of time. Another consequence of the shorter duration of the pulse is that the luminous emission is significant during a shorter period. Then, it is sufficient to integrate the images on 20 ns (vs 25 ns for Pulser 1) to get the whole discharge.

Second, the structure of the discharge changes when l is decreased, the radial extent of the discharge is much larger when the length l is larger. As in the previous sections - sections 5.6 and 6.2, this might be a sign of the existence

of an MCG regime. From the single-shot images of the same discharges, on the second and third lines of figure 6.4, it is clear that for l = 3 to 5 mm, the structure is that of an MCG discharge, and for l = 1 mm, the discharge is a glow discharge. l = 2 mm is an intermediate case between a glow and MCG discharge. Time-resolved images of the glow discharge for l = 1 mm were taken and confirmed the glow nature of the discharge. A single streamer leaves the anode on the inter-electrode axis and joins the cathode, as was seen on figure 5.24. The differences in spatial structure for different values of l will be explained in section 6.4.2.

A third interesting result is the evolution of the minimum applied voltage V_p to get a luminous junction between the electrodes - either a glow or MCG regime - when the length l is decreased. For 1 mm $< l <$ 3 mm, we had to increase the applied voltage V_p to get a luminous junction between the electrodes when l was decreased. This can be understood easily with a simple model of the Laplacian electric field between the electrodes in this geometry. Even if the plane is of finite dimension, the additional axial component of the electric field created by the plane will increase the total value of the axial electric field at mid gap. Since $\vec{E} = -\vec{\nabla}V$, the integral of the z-component of the electric field along the inter-electrode axis is equal to the potential difference between the anode and the cathode. If the field is enhanced at mid-gap and the applied voltage V_p is constant, the electric field at the tip is reduced. A glow discharge will only develop if the electric field is high enough at the tip to ignite the streamer. Consequently, we have to increase the applied voltage V_p as l is decreased. This is illustrated on figure 6.5. It schematically represents the influence of the reduction of the length l on the axial electric field $E_L(z)$ keeping the integral of $E_L(z)$ over z constant.

6.4.2 Interpretation of the influence of l on the structure of a glow-like discharge

The influence of the parameter l on the structure of the discharge leads us to analyze the physical causes of branching. Although the purpose of this work is not to make a detailed study of the causes of branching, we will show how we can interpret our experiments.

The exact mechanism that leads to streamer branching has been under discussion for a long time now. Several explanations were given. Branching could be due to a fundamental Laplacian instability in the streamer front. This explanation was proposed in various works of Arrayas *et al* [79], Meulenbroek *et al* [80], Rocco *et al* [81], and Liu and Pasko [82]. Another older explanation is based on the concepts of Raether [83]. Branching could be due to the stochastic behavior of secondary avalanches in front of the streamer head. Pancheshnyi [84] observed from 3D simulations that the non-uniformity of the distribution

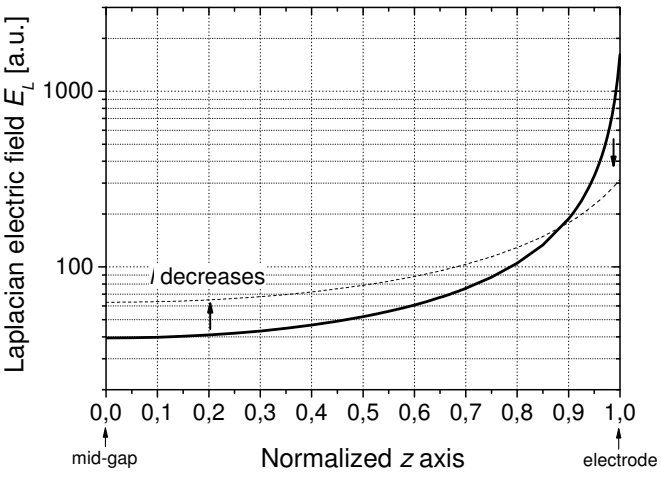

Figure 6.5: Schematic diagram presenting the influence of the plane behind the electrodes on the axial Laplacian electric field at constant applied voltage V_p. The field E_L at mid-gap ($z = 0$) is enhanced whereas the field at the tip of the electrode is decreased.

of the seed charges had an effect on the streamer head formation and could lead to a branching phenomena. However the level of seed charges considered in [84] was really low, 10^2-10^3 cm^{-3}. This is much smaller than the level of pre-ionization in our experiments, which can be considered equal to 10^9-10^{11} cm^{-3}. Thus, this explanation might be relevant in low density environments but not in media such as plasmas created by NRP in atmospheric pressure, where the background ionization - charges left from the previous pulses - and free electrons created by photoionization are high.

Let's prove this estimation of the pre-ionization level by evaluating the density of charged species before the beginning of a new pulse, following references [4], [85], [86], and [87]. In the case of a gas with no electronegative component, the electron density $n_e = n_+$ decays according to the law (see references [85] and [87]):

$$\frac{dn_e}{dt} = -\beta n_e n_+ \tag{6.1}$$

$$n_e(t) = \frac{n_e^{max}}{1 + \beta n_e^{max} t} \tag{6.2}$$

The electron-ion recombination coefficient is typically equal to $\beta = 10^{-6} - 10^{-7}$ cm^{-3}s^{-1} for $T_g = 300$ K (see references [65] and [85]). In the case where $n_e^{max} = 10^{13}$ cm^{-3} [2], $\beta n_e^{max} t > 1$ for $t > 1$ µs. In the case of NRP discharges of this work, the repetition frequency PRF of the pulses is between 1 and 30 kHz, which corresponds to a minimum duration between the pulses of 33 µs. Consequently, the previous condition is valid in the present work and equation

(6.2) becomes:

$$n_e(t) \approx \frac{1}{\beta t} \tag{6.3}$$

The pre-ionization level in terms of electrons is approximately equal to $10^9 - 10^{11}$ cm^{-3} depending on the PRF.

However, in a gas with an electronegative component such as air with O_2, attachment is an important depletion mechanism for electrons [85]. In cold air, without electric field, the dominant process is [85]:

$$e + O_2 + M \rightarrow \ O_2^- + M \ (M = O_2 \text{ or } N_2) \tag{6.4}$$

The main negative ion formed during the inter-pulse is considered to be O_2^- [85], [84] though this has been questioned recently [88]. The electron lifetime with respect to attachment is $\tau_a = 1.1 \times 10^{-8}$ s^{-1} [85].

For T_g = 1000 K or above, attachment can be considered negligible [4] and [89]. Consequently, the background pre-ionization is of different nature depending on the temperature. For $T_g \geq$ 1000 K, pre-ionization consists in electrons and negative ions such as O_2^- in equivalent proportions, but for T_g = 300 K, pre-ionization mainly consists of negative ions. Still the pre-ionization level is similar [89] as the one found using Equation (6.3) even if the nature of the charges is different at low temperature. Consequently, at room temperature, the pre-ionization level is equal to 10^9-10^{11} cm^{-3} in terms of negative ions.

To verify the foregoing arguments, it is necessary to test the influence of the Laplacian field created by the plane on the structure of the discharges (glow or MCG). To this end, we have conducted experiments in which we kept the applied voltage and gap distance constant, and just varied the length l. Keeping d and V_p constant implies that the Laplacian electric field remains about constant near the tip of the electrodes, even when l is varied, because the field at the tip is mostly determined by the radius of curvature of the electrodes. In contrast, the Laplacian field at mid-gap varies much more with the distance l, because the Laplacian field created by the plane is comparable in magnitude to the Laplacian field produced by the electrodes at mid gap. Furthermore, for reasons that will become apparent after Section 6.5 where we study the influence of the PRF, we chose to work with a PRF of 1 kHz.

The first series of experiments was conducted with short pulses produced by Pulser 2 Channel 2, and with electrodes of radius of curvature R = 20 µm. From the averaged images obtained at l = 1, 3 and 4 mm (see figure 6.6), and from an analysis of single-shot images (not shown), we can conclude that we have a glow discharge for l = 1 mm, and MCG discharges for l= 3 and 4 mm.

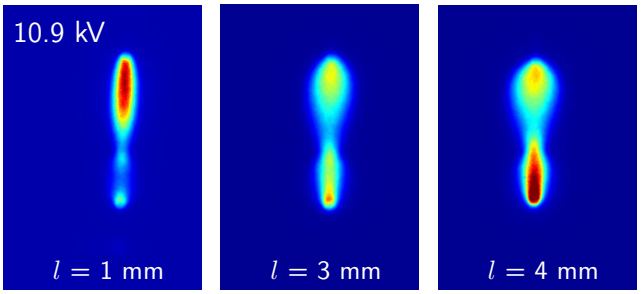

(a) $I = 50$ **(b)** $I = 20$ **(c)** $I = 20$

Figure 6.6: Images integrated over 20 ns of glow-like discharges to the eye for l= 1, 3 and 4 mm. The applied voltage is kept constant at 10.9 kV. T_g = 300 K, R = 20 µm, d = 4 mm, V_p = 10.9 kV, PRF = 1 kHz and v = 0.5 m.s^{-1}.

Thus we see that increasing the Laplacian field created by the plane promotes the occurrence of glow discharges over MCG discharges.

This effect is even clearer on longer gap discharges, obtained with a longer gap $d = 6$ mm and longer pulse durations (hence using Pulser 2 Channel 1). Images obtained for $l = 3$ and 4 mm at constant applied voltage are shown in Figure 6.7. Here we clearly see the difference between the glow discharge obtained for $l = 1$ mm and the MCG discharge obtained for $l = 3$ mm.

Thus, these studies at constant applied voltage demonstrate that the Laplacian field created by the plane plays a key role on the branching in our discharges. Because the level of pre-ionization is similar in both cases, the cause of branching cannot be related to stochastic effects. Instead, we believe that branching is prevented when the electric field is oriented along the z-axis, which is not the case when the field is just created by a pin electrode of small radius of curvature. The use of a plane reinforces the field along the z-axis, thus guiding the streamers along that axis, hence preventing branching.

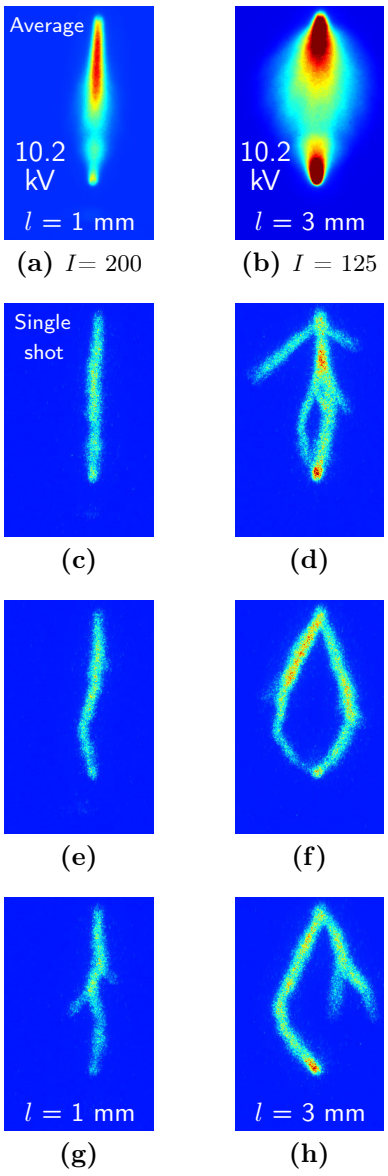

(a) I= 200 **(b)** I = 125

(c) **(d)**

(e) **(f)**

(g) **(h)**

Figure 6.7: Images integrated over 50 ns of glow-like discharges for l = 1 and 3 mm. The applied voltage is kept constant at 10.2 kV. The first line displays images averaged over several discharges. The second, third and fourth lines display samples of single-shot images (I = 35).
T_g = 300 K, R = 20 µm, d = 6 mm, V_p = 10.2 kV, PRF = 1 kHz and v = 0.5 m.s^{-1}.

6.5 Influence of the Pulse Repetition Frequency

In this section, we study the influence of the Pulse Repetition Frequency (PRF) on the structure of the discharge. We used Pulse Generator 2 on Channel 2 with $R = 20$ µm electrodes with a given inter-electrode gap distance $d = 4$ mm. Two values of the length l were investigated, $l = 1$ and 4 mm. The choice of l is important, when l is small, glow discharges will be promoted, as was seen in section 6.4.

Figure 6.8 shows the influence of the PRF on the structure of the discharge for $l = 1$ and 4 mm. For the two sets of values of l, we increase the PRF from 1 to 30 kHz. All other parameters are kept constant. The first line displays averaged images. The second and third lines display samples of single-shot images. For $l = 1$ mm, only one sample is shown since all the discharges had an identical spatial structure. In order to decouple the impact of the PRF and the impact of the flow on the discharge, we work in motionless ambient air. The influence of the flow rate on the discharge structure will be studied in section 6.6.

First of all, we had to increase the applied voltage to get glow-like discharges while decreasing the frequency. This has already been observed by Pai [2]. For $l = 1$ mm, the discharge is of the glow type at all PRF. For $l = 4$ mm, the discharge changes from an MCG at 1 kHz to a glow at 10 and 30 kHz.

In the case $l = 1$ mm, the field is strongly enhanced by the plane behind the electrodes (see section 6.4), and this effect seems sufficient to promote glow discharges at all frenquencies investigated. However, when l is larger, $l = 4$ mm, the structure of the discharge depends greatly on the PRF. The conclusions must not be drawn too quickly. It is known that the branching frequency decreases when the pulse repetition rate is increased [84]. The reason suggested in [84] is that a higher frequency leads to a higher density and a better homogeneity of seed charges. Consequently, low frequency leads to a stochastic non-uniformity that causes branching. This might be an acceptable argument for low pulse repetition frequencies below 1-10 Hz, but in our case, where the difference is observed between 1 kHz and 30 kHz, this is not relevant.

Indeed, as we saw in section 6.4.2, the level of pre-ionization in terms of negative ions is as high as 10^9-10^{11} cm^{-3} for frequencies 1-30 kHz. For such high levels of pre-ionization in terms of negative ions O_2^-, it seems very unlikely that stochastic processes can explain the difference in spatial structure of the discharges as observed in figure 6.8. Other explanations are necessary. A first argument might be that even if the densities of charged species are uniform, the lower the density in front of the streamer head, the harder it is for the streamer to propagate. An interesting result can be taken from [86]. They calculated the propagation velocity of streamers for different levels of background

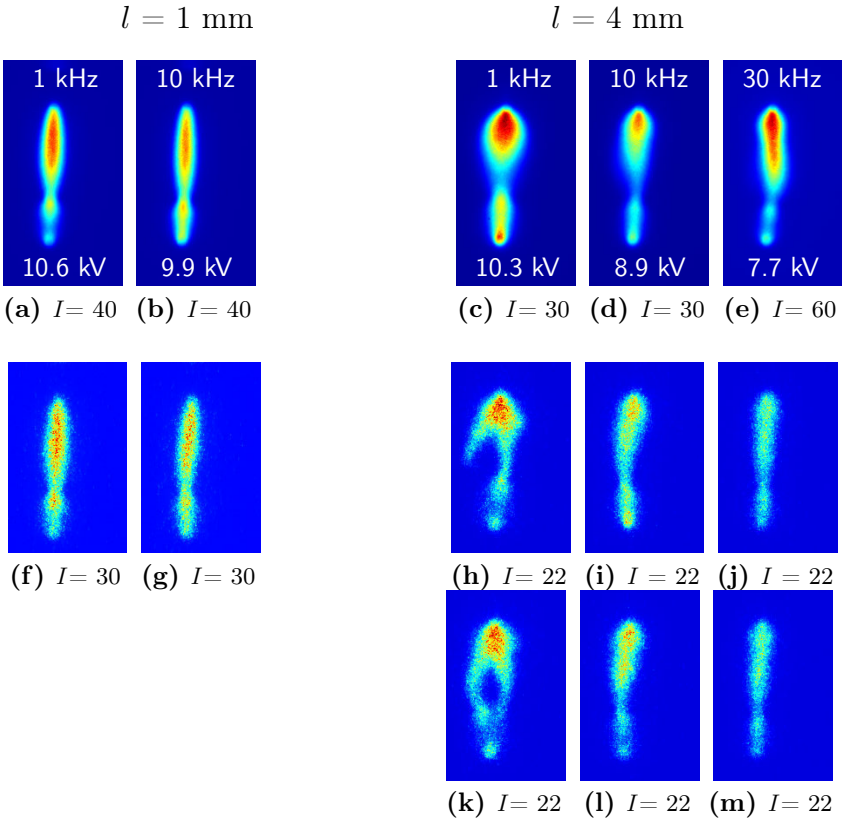

Figure 6.8: Images integrated over 20 ns of glow-like discharges with respect to PRF. Two values of l are investigated, l = 1 mm on the left and l = 4 mm on the right. For the two sets of values of l, we increase the PRF from 1 kHz from the left (a) and (c) to 10 kHz middle (b) and (d) and finally 30 kHz right (e) - only for l = 4 mm. The other parameters are kept constant. The first line displays images averaged over several discharges. Second and third lines displays samples of single-shot images.
T_g = 300 K, R = 20 µm, d = 4 mm, and static room air.

ionization. For background ionization level of 0 and 10^9 cm^{-3} for O_2^-, the velocity of the streamer is similar. Streamers propagate by photo-ionization but are quite insensitive to the background ionization. But for an initial density of O_2^- of 10^{11} cm^{-3}, the velocity of the streamer increases, which indicates that the propagation of the streamer becomes easier for such a high ionization background.

Another argument might be that at high repetition frequencies, there might not be enough time for diffusion of the residual ions. This could result in a memory effect, with streamers taking the same path on consecutive discharges. In [84], Pancheshnyi gives the diffusion coefficient for atmospheric negative ions

$D_{ion} = 5 \times 10^{-2}$ cm^2. s^{-1}. For a plasma of diameter 500 µm, the characteristic diffusion time is approximately equal to 12 ms. This timescale is comparable with the duration between two pulses at low frequencies used in this work - 1 kHz corresponds to 1 ms. In [90], Tholin *et al* detail the simulated distribution of the electron density at the beginning of the eigth first pulses of an NRP discharge at 10 kHz and 1000 K. The discharge tends to a permanent regime after the second pulse in agreement with the experimental observation of Pai [2]. In this regime, the electron density is uniform in a domain of diameter 2 mm around the axis of symmetry of the discharge. Diffusion of electrons is negligible between pulses. We can infer that the same effect will happen for negative ions at room temperature.

These results confirm the importance of the PRF in NRP discharges, here on the discharge structure. Using a high repetition rate of the pulses - $PRF > 10$ kHz - is favorable to the development of glow discharges.

As a conclusion, we have seen that increasing the frequency of the pulses promotes the glow regime with respect to the MCG regime. Two main explanations were given. The first is that the level of pre-ionization in terms of negative ions is lower for 1 kHz than for 30 kHz, which makes the propagation of the streamer harder. The second explanation is that for repetition rates as high as 30 kHz, the charged species may not have time to diffuse from the path that was created from the previous discharge.

6.6 Influence of the flow rate

In this section, we consider the influence of the flow on the structure of the glow discharge at room temperature. To our knowledge, this aspect has never been studied in a pin-pin NRP configuration in air at atmospheric pressure. Glow discharges at room temperature were obtained after a study with respect to the temperature of the gas, see section 5.6. In preheated air, NRP discharges were obtained in an air flow. This explains why the first NRP glow discharges at room temperature that we got were obtained in an air flow (either transverse or axial). Furthermore, this flow of air could be important in biomedical applications: the carrier gas brings the active species (ions, radicals) into the zone to treat. Consequently, it seems relevant to study the importance of the flow rate on the nature of the NRP glow discharge.

Figure 6.9 presents images of glow-like discharges in a transverse air flow and in ambient static room air, both at 300 K, for $l = 3$ and 5 mm. Indeed, as was seen in section 6.4, when the value of l is small, the glow regime is promoted with respect to the MCG regime. The first row presents averaged images and the last two rows show samples of single-shot images. The first and third columns

correspond to a discharge in a transverse air flow of velocity $v = 0.5$ m.s^{-1}, and the second and fourth columns correspond to images in ambient static room air. We worked with a Pulse Repetition Frequency $PRF = 10$ kHz with Pulser 2 Channel 2. In both cases, the applied voltage is increased from 0 V until we detect by eye a luminous junction between the electrodes,

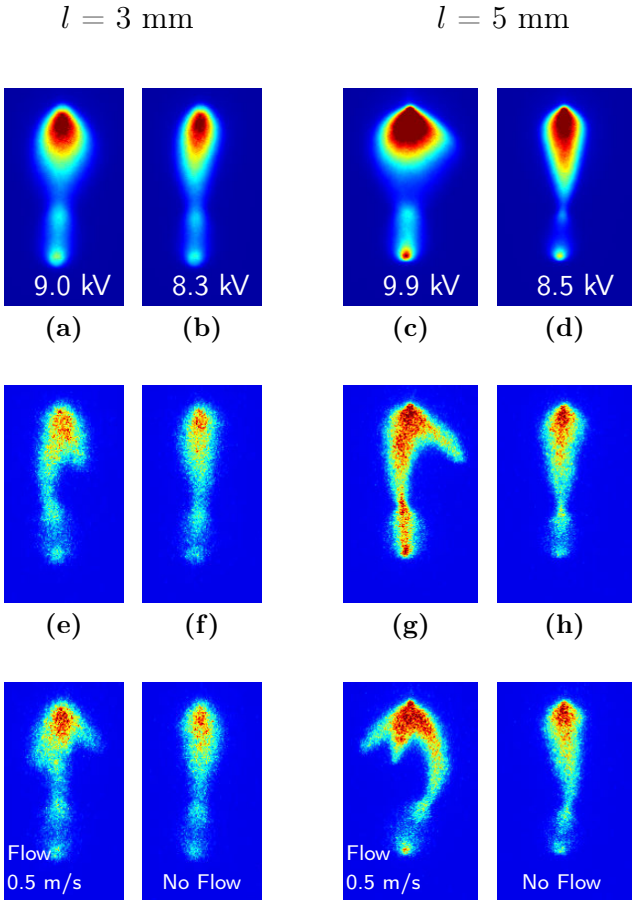

Figure 6.9: Images integrated over 20 ns of glow-like discharges for different values of the transverse air flow for l = 3 and 5 mm. The first row displays images averaged over several discharges (I=40) and the last two rows are single shot images (I=25). Two samples of single shot images are presented vertically. The first and third columns correspond to a discharge in a transverse air flow of velocity $v = 0.5$ m.s^{-1}, and the second and fourth columns correspond to images in ambient room air.
T_g = 300 K, R = 50 µm, d = 4 mm, and PRF = 10 kHz.

For both values of l, the applied voltage V_p for which the glow-like regime is obtained is smaller for a discharge in static ambient room air. This is consistent

with the already mentioned fact that the flow tends to blow NRP discharges, especially in a transverse configuration. Furthermore, the structure of the discharge changes in static or moving air. In an air flow of relatively low velocity, the discharge tends to be an MCG discharge, with a streamer leaving the anode away from the axis of symmetry of the electrodes. In static air, the discharge is much more axial and corresponds to a glow regime.

The air flow has two main effects: first, it evacuates the neutral particles that may have been slightly heated by the discharge. A streamer may develop more easily in a slightly heated media. Glow discharges at $T_g = 1000$ K were found to heat the gas by $\Delta T < 200$ K [2], [36] and it is likely that glow discharges at 300 K heat similarly. This small increase of the temperature on the axis of symmetry of the system can promote this direction for subsequent pulses.

The air flow also evacuates the charged species (ions, electrons). In a discharge where the charged particles have not been evacuated during the inter-pulse duration, the streamer tends to leave the anode in the axial direction, where the charged particles are. Thus, both factors could be important.

We now vary the flow velocity $v = 0.3$, 0.5 and 0.8 m.s^{-1}. For similar experimental parameters as those of figure 6.9, glow discharges in static air becomes MCG discharges at the three different velocities that we tested. The corresponding images are shown on figure A.2 in appendix A. Even for a flow at a velocity as small as $v = 0.3$ m.s^{-1}, the discharge structure is affected by the evacuation of the heat and/or the charged particles.

Next, in order to compare the structure of the discharge for the same applied voltage V_p, we studied what happens when the air flow in which a discharge is created is suddenly stopped. Figure 6.10 shows images of either corona or glow-like discharges recorded when the plasma is created in a transverse air flow and when the flow was stopped keeping all other parameters constant, in particular the applied voltage. Two cases were studied, one for $PRF = 1$ kHz, (a) and (b), and one for $PRF = 30$ kHz, images (c), (d), and (e). At 1 kHz, we start from an MCG discharge (a). At 30 kHz, we start either from a corona discharge (c) or from an MCG discharge (e). Image (f) was not recorded since it was a spark discharge.

The results differ greatly for the two frequencies. At low frequency $PRF = 1$ kHz, the discharge structure remains an MCG discharge when the transverse air flow at $v = 0.8$ m.s^{-1} is stopped. For $PRF = 30$ kHz, the structure of the discharge is affected when the air flow is stopped. Starting from a corona in the transverse flow (c), the discharge evolves towards a more directional corona (d) or even a glow. Starting from an MCG discharge in the

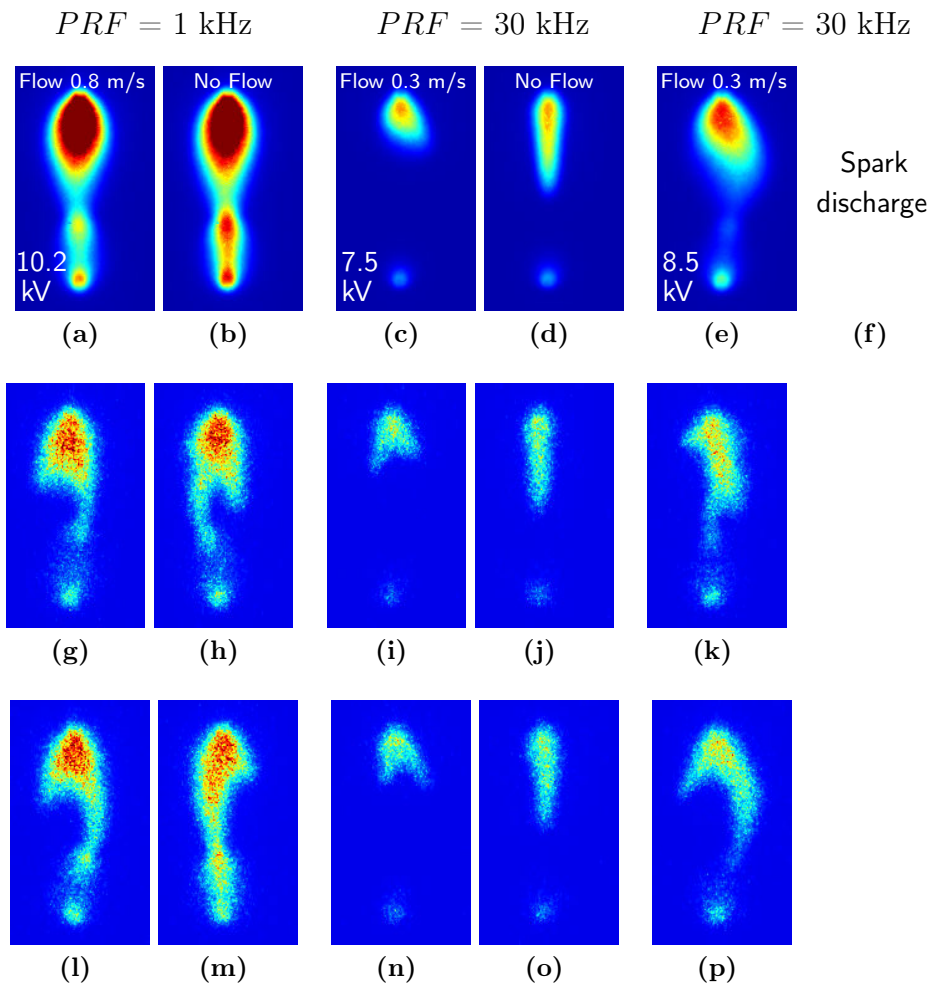

Figure 6.10: Images integrated over 20 ns of glow-like discharges in a transverse air flow and after stopping the air flow. For each couple of images, the flow is stopped between image (a) and (b), (c) and (d), and (e) and (f), all other parameters are kept constant. The first row corresponds to images averaged over several discharges (I= 60) and the last two rows are single-shot images (I= 25). The image of spark discharge is not represented.
T_g = 300 K, R = 20 µm, d = 4 mm, l = 3 mm.

transverse flow (e), the discharge turns into a spark when the flow is stopped.

This confirms what we already established in section 6.5. At low frequency, there is no "memory effect" even in a static flow. The particles are evacuated by diffusion and the discharge develops in a media with hardly no memory

of the previous pulses. The branching structure only depends in the relative ratio of the axial and radial Laplacian electric field. At high frequency, even if the axial Laplacian reduced electric field is relatively small, memory effects come into play. The discharge always develops axially because of the small time between the pulses: particles have no time to evacuate.

Thus, the nature of the flow has a strong influence on the discharge spatial structure and the discharge transition voltages. These two cases of frequencies can be analyzed in terms of characteristic times of the various phenomena at stake. What brings energy into the system - high voltage pulses - is applied at a frequency PRF. Let's call $T = 1/PRF$ the duration between the pulses. What takes energy out of the system is the convection by the air flow. Since the flow is transverse, we consider that a particle is totally evacuated from the discharge when it has run approximately the diameter of the plasma D. We consider $D \approx 500$ µm. The residence time τ_{res} for a particle within the plasma can be defined by $\tau_{res} = D/v$. We can evaluate the Damköhler number Da defined as the ratio of the energy deposited into the system by the energy evacuated by a convective flow.

$$Da = \frac{\tau_{res}}{T} \tag{6.5}$$

For the static flow, we can evaluate similarly the Damköhler number Da using the characteristic diffusion timescale determined in section 6.5. The numerical values of the residence time τ_{res}, the inter-pulse duration T and the ratio τ_{res}/T of the discharges in a transverse air flow and in static air are summarized in table 6.1.

Table 6.1: Characteristic timescales of the energy deposited and evacuated by convection and diffusion in the NRP discharges studied on figure 6.10.

		Flow				No Flow		
PRF [kHz]	T [µs]	v [m.s^{-1}]	τ_{res} [µs]	τ_{res}/T	Regime	τ_{dif} [µs]	τ_{dif}/T	Regime
30	33	0.3	1667	50	MCG	10000	300	spark
1	1000	0.8	625	0.625	MCG	10000	10	MCG

For small values of the Damköhler number, the discharges tend to be of the MCG kind. For $PRF = 30$ kHz with a flow at $v = 0.3$ m.s^{-1} and for $PRF = 1$ kHz with and without flow, $Da \leq 50$ and the discharges are MCG discharges (figure 6.10). However, when $Da \approx 300$, the large number of pulses seen by the particles has a significant influence on the nature of the discharge; "memory effects" come into play, and glow discharges are privileged. The transition Damköhler number for which the axial path is privileged because of the high number of pulses seen by the particles is between 50 and 300

In this section, we have seen the importance of the flow on the structure of the discharge. We have established that at low repetition frequencies, the flow has no influence on the discharge structure. At high frequencies, the flow has a strong influence on the structure of the discharge: a glow discharge becomes an MCG in the presence of a transverse flow. This underscores the importance of memory effect in NRP discharges. At low frequencies the flow evacuates the charged particles and heat. There is no privileged path for the streamer and an MCG regime develops. At high frequencies, the flow has no time to evacuate charged particles and heat between two pulses, and the axial path where the charged particles from the previous pulses are is a privileged axis for the development of a new streamer: a glow regime develops.

6.7 Glow - MCG transition

The parametric study of the glow and MCG regimes enables us to highlight the main reason why an MCG discharge develops when the model (see section 2.9) predicts a glow discharge. The appearance of the branching structures of an MCG regime is due to the low value of the axial component of the Laplacian reduced electric field compared to the radial component within the gap between the electrodes. This was not predicted by the model of section 2.9, since this model was not a 3D model. In an MCG discharge, additional streamers propagate outwards the axis of symmetry of the electrodes.

This was the case in several independent studies that we led:

- when the temperature was decreased from 1000 K to 300 K see section 5.6
- when the inter-electrode gap distance d was increased see section 6.2
- when the length l between the tip of the electrode and the plane behind was increased see section 6.4

In these three cases, the axial Laplacian reduced electric field value is lowered and this decrease is accompanied by the appearance of the branching structure.

Furthermore, the radial dependence of the field is changed. By varying the length l for instance, we affected the value of the Laplacian electric field on the axis of symmetry (see figure 6.5) but we also affected the radial dependence of the field. To see the effect of the variation of l, we performed a 2D-axisymmetric simulation for two values of the length l corresponding to the experiments of figure 6.6, except that we considered a symmetric case where $V_+ = +10.9$ kV and $V_- =$ -10.9 kV. Figure 6.11 shows the equipotentials between the electrodes. The step between them is equal to 1/20 of the voltage differences between the two electrodes.

The calculation domain is 3 cm wide and 1 cm high with Dirichlet conditions

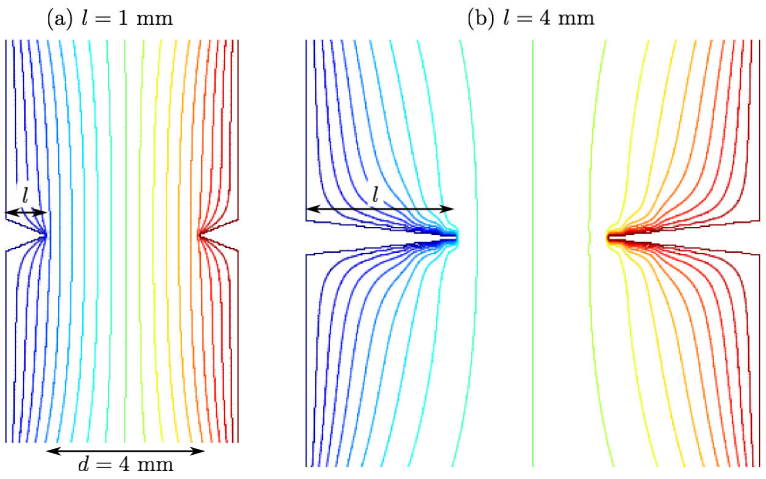

Figure 6.11: Simulated equipotentials for two values of the length l, corresponding to the experiments of figure 6.6, except that $V_+ = +10.9$ kV and $V_- =$ -10.9 kV.

($V = 0$) on the border, and the images shown are zoomed on the electrodes. We see that the equipotentials are much smoother when $l = 1$ mm. When $l = 4$ mm, the field tends to be spherical at the tip of the electrode, the radial component is increased compared to the axial component, thus confirming our conclusion on the influence of the radial component of the electric field on the nature of the glow-like regime. When the radial dependence of the electric field is very peaked, streamers tend to leave on the side; branching and an MCG discharge develop.

However, in some cases at high frequencies, we still observe glow discharges whereas in the same experimental conditions we get MCG discharge at low frequencies. This is due to a "memory effect" at high frequencies. This was seen when we decreased the repetition frequency (see section 6.5) and when we decreased the flow rate in section 6.6. When the time between pulses is large (low frequencies), charged particles and heat are evacuated either by diffusion or convection, which prevents any path from being privileged, and an MCG discharge develops. When the time between pulses is smaller (high frequencies), charged particles and heat are less evacuated, which explains why the subsequent discharge takes the axial path: glow discharges develop. This confirms the importance of the repetitive aspect of the pulses on the nature of the discharge.

6.8 Energy measurements

A full characterization of the glow and MCG regimes at room temperature, in terms of degree of gas heating, density of active species produced, energy deposited is clearly warranted at this point, but is beyond the scope of this thesis. Nevertheless, to gain some insight into the properties of the glow and MCG discharges at 300 K, we have attempted to estimate the energy deposited per pulse. This is the object of this chapter. The details of the measurements are given in appendix C. Here we will comment the main results.

Estimation of the energy of a glow Regime at T_g = 300 K

Figure 6.12 presents the total energy as a function of the applied voltage V_p for three different regimes: no discharge, corona, and glow. The total energy in a typical glow regime at room temperature is around 120 µJ. However, most of this energy is composed of parasitic losses - that we were not able to evaluate - if we compare with the case of a glow regime obtained at T_g = 1000 K, see section C.2. Furthermore, if we consider the energy increase when no discharge is observed, from V_p= 0 to 7 kV, it seems really unlikely that the plasma energy represents more than a few µJ for a glow regime. We can thus only determine the order of magnitude of the energy of the glow regime at T_g = 300 K, and its value should be between a few µJ and a few tens of microjoules.

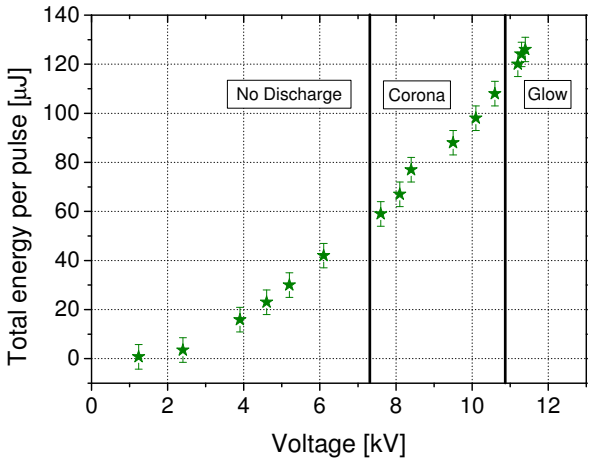

Figure 6.12: Total energy per pulse as function of the applied voltage V_p at room temperature. The parameters are set - l = 1 mm - so as to get a glow discharge at high voltage.

Comparison of the energy of a glow regime and an MCG regime at $T_g = 300$ K

Still, we can investigate the differences in the total energies of the two regimes studied in chapters 5 and 6, the glow regime and the MCG regime at room temperature. Figure 6.13 shows the total energy measured as function of applied voltage V_p in two different experimental cases.

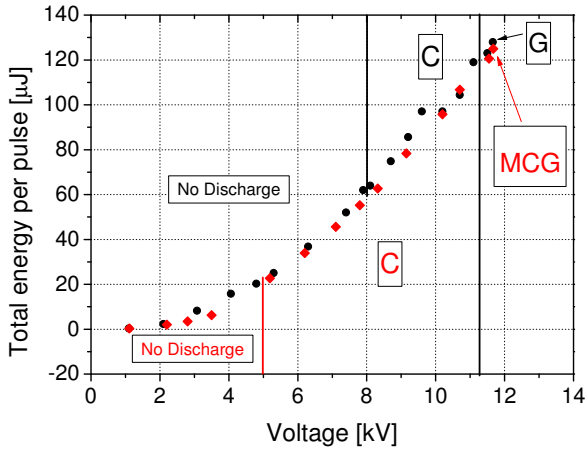

Figure 6.13: Total energy per pulse as function of the applied voltage V_p in the same experimental conditions except l that was varied - black circle $l = 1$ mm, red diamond $l = 4$ mm. The corona regime is obtained at lower voltage for $l = 4$ mm. For $V_p = 11.4$ kV, we obtain either a glow ($l = 1$ mm) or a Multi-Channel Glow regime ($l = 4$ mm).

For $V_p = 11.7$ kV, we obtain a glow regime in one case and an MCG regime in the other case. We use the same delay in both case $\tau = +0.3$ ns. These experiments were done in the same conditions: Pulser 2 Channel 2, in a transverse flow of velocity $v = 0.5$ m.s^{-1}, $T_g = 300$ K, $R = 20$ µm, $d = 4$ mm, and $PRF = 10$ kHz. The only parameter that was varied was the length l, $l = 1$ mm for the glow regime and $l = 4$ mm for the MCG regime. The total energies E_{total} are equal ($\pm$ 1 µJ) for the two regimes. It is strongly unlikely that the parasitic losses are different in these two cases, since they only depend on the electric circuit. However, based on figure 6.12 and section C.2, the parasitic losses $E_{no-plasma}$ seem to be important. Using

$$E_{plasma} = E_{total} - E_{no-plasma} \tag{6.6}$$

(see equation (C.1) of appendix C for details), it is difficult to evaluate if the resulting energy of the plasma E_{plasma} is similar for the two regimes. It seems very unlikely that the parasitic losses differ by an order of magnitude. The difference in the parasitic losses might only be of a few µJ for the two regimes.

Consequently, the energies E_{plasma} should be within a few µJ and a few tens of microjoules for the glow and the MCG regimes.

In this section, we estimated the order of magnitude of the energy deposited into the plasma E_{plasma} for a glow regime at T_g = 300 K to be between a few µJ and a few tens of µJ and that it should be similar for the glow regime and the Multi-Channel Glow regime.

6.9 Importance of the plane behind the pin electrodes

In this section, we confirm the importance of the plane behind the electrodes with two additional experiments.

First, we study discharges between tungsten wires of 50 µm diameter. We used Pulse Generator 2 with Channel 1 - FWHM around 25 ns - at PRF = 10 kHz. There is no conducting plane behind the electrodes. A picture of the experimental setup can be found on figure 6.14.

Figure 6.15 displays images of the discharge obtained: clearly, the branching phenomenon is enhanced. We see a developed branching structure with four channels leaving the anode. The channels then divide again in more than four channels for some of them. This enables to confirm that branching is enhanced in a pin-pin configuration with small radius of curvature.

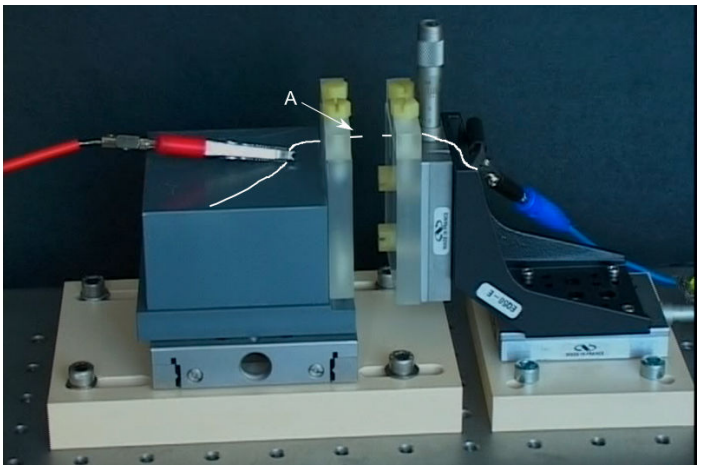

Figure 6.14: Experimental reactor enabling to work in a pin-pin configuration at room temperature. The electrodes are made of 50 µm diameter tungsten wires and are outlined in white. No conducting plane is placed behind the electrode unlike in the case of the parametric study of chapters 5 and 6. The holders are PVC, non-conducting planes. The flow of air was transverse.

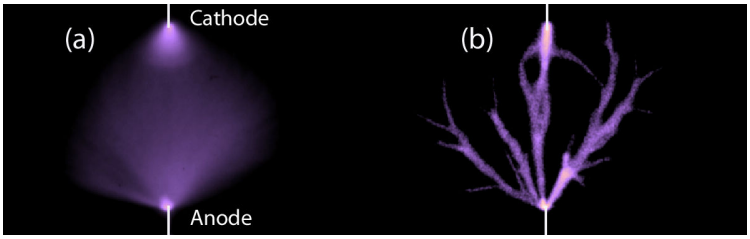

Figure 6.15: Images of MCG discharges obtained in the experimental setup of figure 6.14. (a) Image integrated over 30 ns averaged over several discharges and (b) single-shot image integrated over 20 ns. The electrodes are outlined in white. Unlike for the other images of this work, the anode is at the bottom and the cathode at the top.
Transverse Flow, T_g = 300 K, $R \approx$ 50 µm, d = 8 mm, $V_p \approx$ 14 kV, PRF = 10 kHz and $v \approx$ 1 m.s^{-1}.

The second example is the complete opposite of the first one. Here, we created a reactor using several sets of pin-pin electrodes set on large steel planes. The experimental setup is shown in figure 6.16.

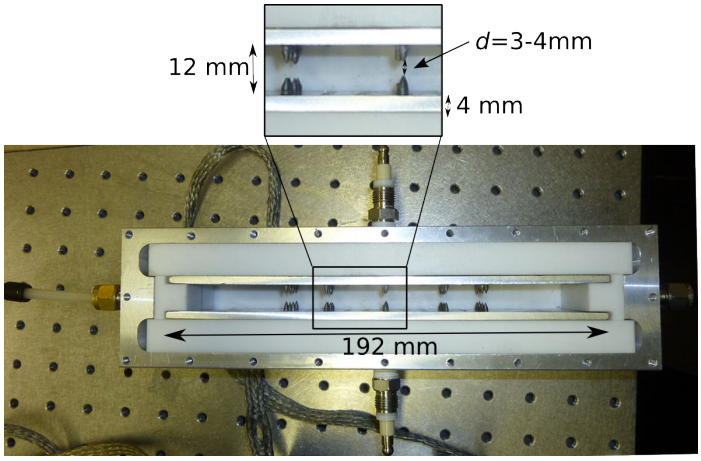

Figure 6.16: Experimental reactor for the multi-pin configuration.

The distance between the two planes was 12 mm and the typical inter-electrode gap distance used was around 4 mm. The electrodes used were radius of curvature around 100-200 µm. Preliminary studies [91] indicate that, in this configuration, glow discharges are much easier to obtain than in the pin-pin configuration or with the small plane of size around 6 mm used in the previous sections. With a transverse air flow or in static air at atmospheric pressure, for an applied voltage of 7-8 kV and for two pairs of electrodes, we easily obtained a glow regime. In this configuration, the axial component of the Laplacian electric field is high which prevents branching.

These two additional experiments confirm the importance of axial component of the Laplacian electric field compared to the radial component in order to get glow discharges in room temperature air.

6.10 Conclusions

In this chapter, we have investigated the nature of glow-like discharges that we obtain at room temperature with respect to several parameters. We have seen that decreasing the inter-electrode gap distance d promotes the existence of the glow regime with respect to the Multi-Channel Glow (MCG) regime. We have highlighted the importance of the plane behind the electrode. Decreasing the length l promotes the glow regime with respect to the MCG regime. Using a larger plane compared to the inter-electrode gap distance d promotes the glow regime.

Then, we have investigated the influence of the Pulse Repetition Frequency, PRF and we have noticed that increasing the frequency promotes the glow regime. We have investigated the influence of the flow rate: it has no influence on the nature of the discharge at low frequencies but a strong influence at higher frequencies due to memory effects. In static air at high frequencies, the inter-pulse duration is too small for the evacuation of heat and/or charged particles: glow discharges are privileged. We have suggested reasons to explain the branching structures detected in cases where the model predicted a glow discharge: a low value of the axial Laplacian reduced electric field between the electrodes, and a very peaked distribution of the radial electric field as a function of radius from the center of discharge. We have not been able to give more than an order of magnitude of the energy of a glow discharge at room temperature: between a few µJ and few tens of µJ.

For the sake of completeness, in appendix B, we show a comparison of time-resolved images of a glow discharge at room temperature with simulations and we see a good agreement.

We have established that glow discharges can be created at room temperature using pin electrodes of small radius of curvature R = 20-50 µm, with a plane located very close behind the pin. Another alternative would be to use an intermediate radius of curvature R = 100-150 µm. The Laplacian electric field would be strong enough at the tip of the electrode, and the radial distribution of the Laplacian electric field would be quite smooth. This would prevent the MCG regime from developing. In such a case, we should increase the applied voltage (as was seen in section 5.5) and consequently increase the inter-electrode gap distance to approximately d = 10 mm. An applied voltage of about 15 kV would be needed, which was at the limit of Pulser 2 used with the additional

capacitor.

We detailed the effects of the various parameters of our experiments on the nature of glow-like discharges. The goal of this work was to establish the conditions of existence of the glow regime at ambient temperature. Thus, we emphasized the ways to promote the existence of glow regime over the MCG regime. However, depending on the application, both glow-like discharges could be interesting. A glow discharge would be interesting because every discharge is located at the same location in space which can concentrate the effect on a zone to treat, the specific energy is higher. A MCG discharge could be interesting if a large volume of gas needs to be treated.

Chapter 7

Conclusion

7.1 Contributions of this thesis

In this thesis, the NRP method was implemented to generate either NRP spark or glow discharges into preheated atmospheric pressure air (T_g = 300-1000 K) between two steel electrodes of controlled radius of curvature which were either perpendicular or parallel to the flow. The plasma was created using short (5-30 ns of FWHM) high-voltage (up to 8.5 or 14 kV depending on the pulse generator) pulses repeated at Pulse Repetition Frequencies (PRF) from 1 to 30 kHz for an inter-electrode gap distance from 1 to 8 mm. The radii of curvature of the electrodes studied were from 20 to 500 µm and for some experiments we used a steel plane of 6 mm × 8 mm behind each pin electrode.

We have used calibrated Optical Emission Spectroscopy (OES) to examine the densities of two excited states of nitrogen - N_2(B) and N_2(C) during and after an NRP spark discharge in order to validate the two-step mechanism proposed to explain the ultrafast heating enhanced in NRP spark discharges. We realized 2-ns-long time-resolved measurements of the absolute number densities of N_2(B) and N_2(C) from which we deduced the gas temperature evolution. We measured the radius of the discharge for those two species. We performed highly time-resolved imaging (single shot and averaged images) with ICCD camera of NRP glow discharges for different radii of curvature and gas temperature and highlighted the existence of a 3D regime that we called NRP Multi-Channel Glow (MCG) regime. Finally, we investigated how to promote the NRP glow and MCG regime with a parametrical study at T_g = 300 K.

Ultrafast heating of NRP spark discharges

We defined an NRP *reference case* spark discharge with similar experimental condictions to those of previous atomic oxygen measurements [6], [49]. The diameter of the discharge was studied from the first and second positive system of nitrogen using an Abel inversion of the lateral spectra at the maximum of

emission and was found to be 450-500 µm for both states. Time resolved measurements of the absolute number densities of N_2(B) and N_2(C) were realized and from the N_2(C-B) spectra, we determined the temporal evolution of the gas temperature during and after the high voltage pulse. The gas temperature increases from 1500 K to 2400 K within 20 ns, thus confirming ultrafast heating. Synchronizing those measurements with previous atomic oxygen measurements [6], [49], we have shown that the dissociation of molecular oxygen within the first 20 ns is mainly due to the quenching reactions of N_2(B) and N_2(C). The quenching rates of N_2(B) and N_2(C) by O_2 were determined from the decay times of the density of these species and from the published quenching rates of N_2(B) and N_2(C) by N_2, and are respectively equal to 2.6 ($\pm$ 0.5) $\times 10^{-10}$ $cm^{-3}.s^{-1}$ and 5.0 ($\pm$ 0.5)$\times 10^{-10}$ $cm^{-3}.s^{-1}$ at 2000 K. Finally, the temporal evolution of the electron density was deduced from the FWHM of the H_α line, with a peak at 3 $\times 10^{15}$ cm^{-3}.

Influence of the radius of curvature of the electrode and gas temperature on the NRP glow regime

We studied the NRP glow regime at T_g = 1000 K and confirmed the existence of different glow regimes, a so-called "weak glow" regime and a "strong glow" regime. The weak glow regime is just above the onset voltage of the return stroke, and the strong glow regime shows a developed return stroke from the cathode to the anode. At the same temperature, we notice that for a radius of curvature of the electrode of R = 50 µm, the streamer radius decreases while it is propagating, while for R = 500 µm, the radius of the streamer is approximately constant. The influence of the radius of curvature of the tip of the electrode on the limits of existence of the glow regime confirms the model established by Pai *et al* in [1] and confirms that at a given gas temperature T_g, the minimum distance for the existence of the glow regime d_{min} decreases when the radius of curvature of the electrode decreases. Finally, we have shown a set of parameters for which the NRP glow regime exists for different temperatures and different radii of curvature. We obtain a glow regime at T_g = 300 K with small radii of curvature R = 20 and 50 µm, as was predicted by Pai *et al* in [1]. However, we added a steel plane (6 mm × 8 mm) behind each pin electrode.

Existence of an NRP Multi-Channel Glow (MCG) regime

While decreasing the gas temperature, we have seen emerging a spatially different regime from the glow regime, that we named the Multi-Channel Glow (MCG) regime. This regime is characterized by the same features as the glow regime - low conduction current, low light intensity, same discharge dynamics, but the streamer can leave the anode on another direction than the inter-electrode direction or several streamers leave the anode within a single discharge. Depending on the application, both glow-like discharges could be in-

teresting. An NRP glow discharge could be interesting when the application requires a concentrate effect on a zone to treat; the specific energy is higher. A MCG discharge could be interesting if a large volume of gas needs to be treated.

NRP glow and MCG regime at T_g = 300 K

Decreasing the inter-electrode gap distance d promotes the existence of NRP glow regime with respect to NRP MCG regime. The importance of the plane behind the electrode was shown: decreasing the length l between the plane and the electrode tip promotes the NRP glow regime with respect to NRP MCG. We have also shown that increasing the frequency promotes the NRP glow regime. We have investigated the influence of the flow rate on the nature of the discharge: the flow has no influence on the nature of the discharge at low frequencies but a strong influence at higher frequencies due to memory effects. In static air at high frequencies, the inter-pulse duration is too small for the evacuation of heat and/or charged particles: glow discharges are privileged. We gave an order of magnitude of the energy of a glow discharge at room temperature: between a few µJ and few tens of µJ. Finally, we have suggested reasons that might explain the branching structures that we have detected in cases where the model predicted an NRP glow discharge. It could be due to a low value of the axial Laplacian reduced electric field between the electrodes, and to a very peaked distribution of the radial electric field as function of radius from center of discharge.

7.2 Recommendations and perspectives

Concerning the establishment of the existence of the glow regime at 300 K, several studies should be undertaken. First, it is important to verify that the NRP glow discharge does not heat the ambient gas, which is a required condition to use it in temperature sensitive applications. The difference between the NRP glow and MCG regime should be investigated in terms of energy deposited into the plasma, temperature increase and production of atomic oxygen. The latter study can be realized with TALIF measurements as was previously done at T_g = 1000 K [6], [49]. It is important to know whether the energy deposited into the plasma is different for glow discharges and MCG discharges. One method to determine the parasitic losses $E_{noplasma}$ in a glow discharge at T_g = 300 K would be to keep all the parameters constant but to increase the inter-electrode gap distance. The parasitic losses should only depend on the electric circuit. In such conditions, we would detect no plasma and the energy measured would only correspond to the parasitic losses.

We have demonstrated the existence of NRP glow discharges at room temperature using pin electrodes of small radius of curvature of the electrodes R = 20-50 µm, with a plane very close (1-3 mm) behind the pin. Another al-

ternative would be to use an intermediate radius of curvature R = 100-150 µm. The Laplacian electric field would be strong enough at the tip of the electrode and would not decrease too steeply, and the radial distribution of the Laplacian electric field would be quite smooth. This would prevent MCG regime from developing. In such a case, we should increase the applied voltage as was seen in section 5.5 and consequently increase the inter-electrode gap distance to approximately d = 10 mm. An applied voltage of about 15 kV would be needed which was at the limit of Pulser 2.

Concerning the ultrafast heating during an NRP spark discharge, the data obtained in this thesis provides a comprehension data set that will be useful to further validate the two-step mechanism. For this further validation, one should examine on the basis of the results presented here (profiles of E/N, N_2(B), N_2(C), electrons, O, T_{vib} and T_{rot}):

- the relative importance of electron-impact dissociation of O_2,
- the two-step mechanism - which also involves other states such as the N_2(a) state,
- the importance of the pooling reactions that produce N_2(B) and N_2(C) from N_2(A),
- the formation of electronically excited O atoms, etc.

Another challenge is to understand if this ultrafast heating occurs as well when the initial gas temperature is decreased. From Schlieren measurements [51], it was shown that in ambient temperature room air, the temperature behind the shock wave was almost constant and equal to the initial temperature. Complementary measurement of gas temperature with Optical Emission Spectroscopy should be realized at the EM2C laboratory in order to verify this conclusion.

Appendix A

Additional images of NRP glow discharges at $T_g = 300$ K

A.1 Time-resolved images in a transverse flow

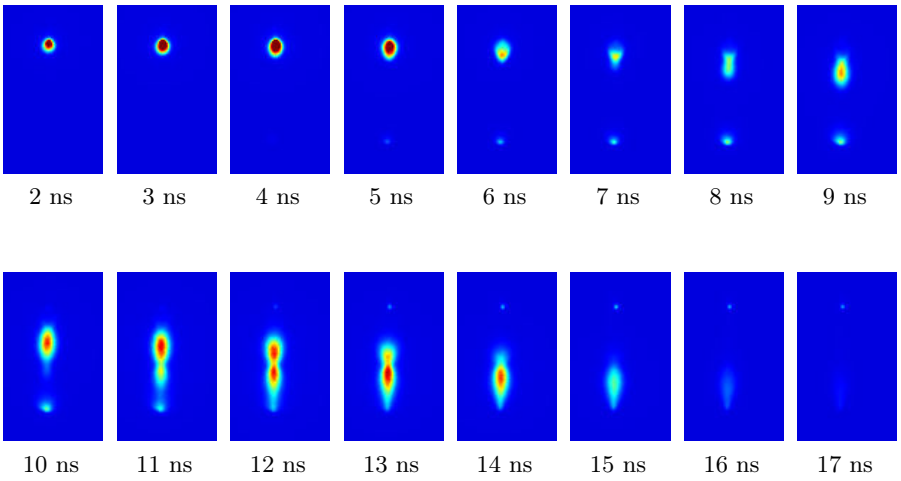

Figure A.1: Images integrated over 2 ns of an NRP glow discharge at ambient temperature, averaged over several discharges. Flow is blown from left to right on the images. The experimental parameters corresponds to the image of figure 6.3 (b).
$T_g = 300$ K, $R = 20$ µm, $d = 2.5$ mm, $V_p = 5.0$ kV, $l = 3.5$ mm, $PRF = 10$ kHz and $v = 0.5$ m.s^{-1}. Intensity I= 220.

A.2 Influence of the transverse flow velocity on the NRP glow discharge structure

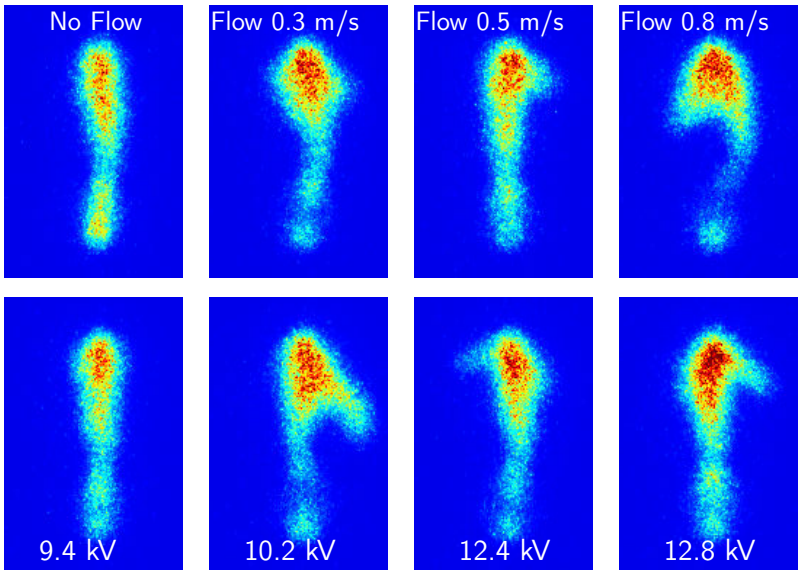

Figure A.2: Single-shot images integrated over 20 ns of glow-like discharges for different values of the air flow. Two samples of images are presented vertically. The first column corresponds to a discharge realized in static ambient room air. The following columns correspond to discharges realized in a transverse flow of air increased from $v = 0.3$ m.s^{-1} to $v = 0.8$ m.s^{-1}. T_g = 300 K, R = 50 µm, d = 4 mm, d = 3.5 mm. Intensity: I = 25.

Appendix B

NRP glow discharges at ambient temperature - comparison with simulations

The purpose of this appendix is to show additional experiments that were done with another pulse generator and to compare them with simulations. We used a third Pulser FID FPG30-100MS, called Pulse Generator 3, which is different from Pulser 1 and Pulser 2 as it delivers symmetric pulses, i.e. that the anode is at potential $V_+ = V_p$ and the cathode at potential $V_- = -V_p$. Pulser 3 characteristics are described in [40]. Because the symmetry of pulses, the Laplacian electric field is less perturbed by surrounding objets at ground potential. This pulse generator has been used in previous works [23] and [40]. From preliminary experiments, we had noticed that it seems easier to obtain glow discharges at room temperature with this pulse generator. Consequently, we took a few images in this configuration. We used an air flow at 10 m.s^{-1} with $d = 5$ mm. The electrodes were *Delmo* electrodes with a radius of curvature around 100 µm, though the shape may not have been symmetric. The FWHM of the pulse was approximately 15 ns, and we worked at $PRF = 1$ kHz.

Figure B.1 shows a comparison between time-resolved images of a glow discharge obtained in the conditions detailed above and simulations - performed by Tholin, Bourdon and Celestin of the emission of the second positive system of N_2 integrated over the line of sight. Images of both series are integrated over 2 ns. The anode is at the top and the cathode at the bottom of the images. These data were published in [92]. Rather good agreement is obtained between the experimental and simulated images. A striction happens on both the experimental and simulated images for t_0+ 2 ns and t_0+ 3 ns. If we compare these images with the images of figure 5.24, we see that the different processes that happen during a glow discharge are quite similar: development of a streamer at the anode, connection of the streamer with the cathode, striction of the dis-

charge approximately at mid-gap. The only difference consists in the significant emission of $N_2(C)$ that we see at the cathode in the case of Pulser 3 that we did not see in the case of Pulser 1 and Pulser 2.

These additional images show that we can obtain glow discharges at room temperature with both types of pulser, a pulse generator delivering symmetric pulses $V_+ = V_p$ and $V_- = -V_p$ such as Pulser 3 and a pulse generator delivering positive high voltage pulses $V_+ = V_p$ and $V_- = 0$ V such as Pulser 1 and Pulser 2. Finally, we have compared images of an NRP glow discharge at room temperature with simulations and found a rather good agreement.

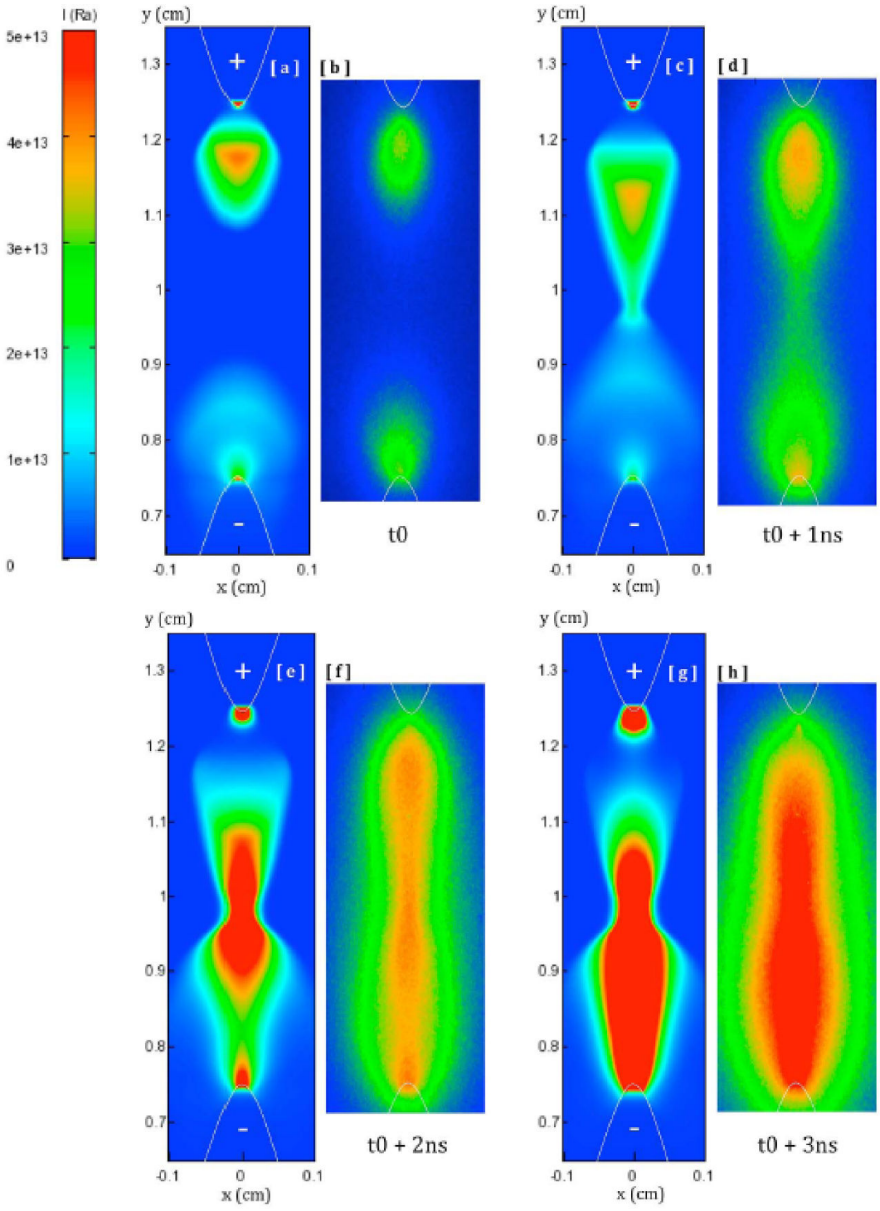

Figure B.1: Images integrated over 2 ns averaged over 50 discharges of a glow discharge taken every 1 ns (b, d, f, and h). Spatial distribution of calculated line of sight of the second positive system of N_2 emission time integrated over 2 ns (a, c, e, and g). The scale is linear. Experimental conditions: axial flow, T_g = 300 K, $R \approx$ 100 µm, d = 5 mm, $V_p = V_+ = \mid V_- \mid$ = 9 kV, PRF = 1 kHz and $v \approx$ 10 $\mathrm{m.s^{-1}}$. Images taken from [92].

Appendix C

Electrical characterization of glow and MCG discharges at ambient temperature

In this appendix, we present measurements of the discharge voltage and current during application of the high voltage pulse to determine the electrical characteristics of the glow regime at $T_g = 300$ K. A comparison of the high voltage pulses delivered by Pulser 1 and Pulser 2 was presented in section 3.3 and a detailed study of the influence of the position of the voltage probe on the measured voltage for a glow discharge was realized in section 3.9. So, in this appendix, we focus on current measurements and energy determination.

C.1 Determination of the current using Pearson probes

The Pearson probes that were used to measure the discharge current were described in section 3.2. Figure C.1 shows the positions of the current probes for the two pulsers used in the present work.

Pulser 1 highest reachable voltage was limited to 8.6 kV, in our experiment. Pulser 2 can go to higher voltage, around 20 kV in an open circuit, and 15 kV if we use an additional capacitor, as explained in section 3.3. In these high applied voltage, the discharge may create electromagnetic noise likely to perturb the measured current. Figure C.2 shows, with the same high-voltage Pulser 2 settings, the current when the probe was around the cable and when it was just beside for a typical glow discharge. The residual current (noise current) that we measured when the probe was not around the cathode cable is not zero, but is negligible compared to the useful signal.

The measured total current I_{tot} is ideally only a displacement current in ambient air at low voltage where no discharge is observed. Figure C.3 shows the

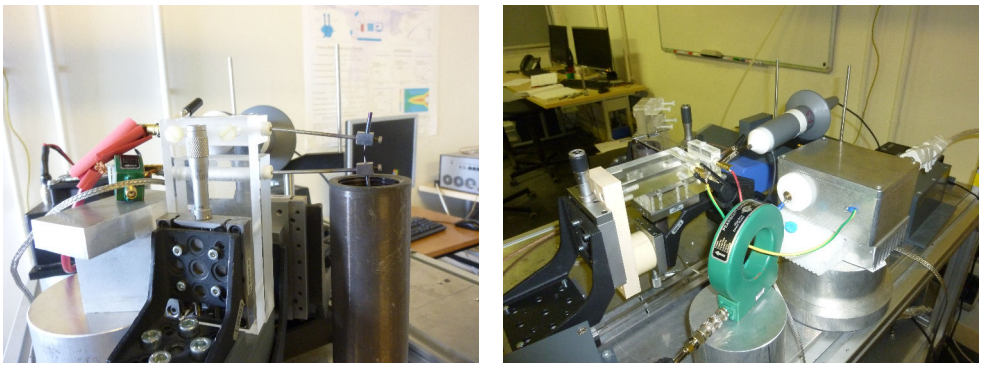

(a) (b)

Figure C.1: Position of the current probe for (a) Pulser 1 and (b) Pulser 2. The 2877 Pearson current probe is not connected on the left picture.

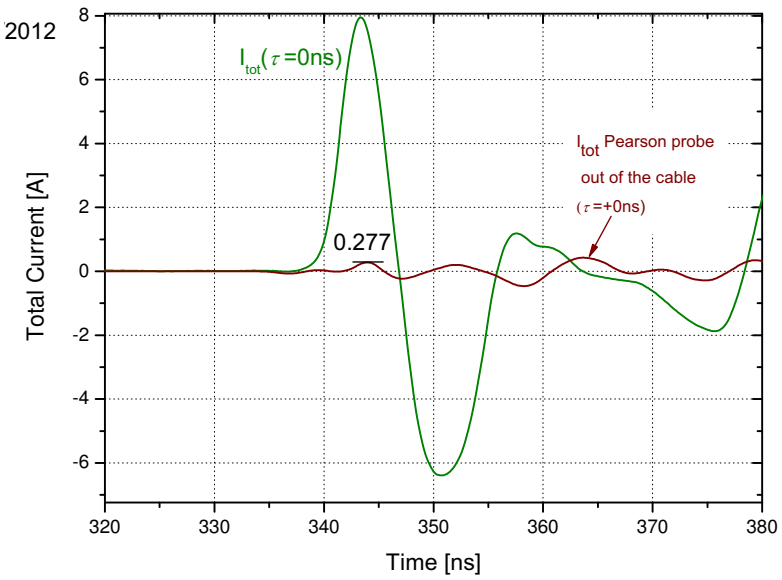

Figure C.2: Measured current through the Pearson coil when the probe is around the cable and when it is just beside the cable for a typical glow discharge at T_g = 300 K.

calculated I_{disp} derived from the applied voltage measured by the Lecroy probe for a typical no discharge state, with Pulser 1 on the left (a) and Pulser 2 Channel 1 on the right (b).

$$I_{disp} = C\frac{dV_p}{dt}$$

We should emphasize the importance of the delay between the waveforms. Indeed, the signals delivered by the voltage and current probes are synchronized.

This delay depends on the lengths of the various cables used, the intrinsic delay between the various channels of the scope, and the triggering mode used.

To synchronize the current and voltage probes, we match the total current and the derivative of the applied voltage V_p with no discharge present (in this case the electrodes behave as a simple capacitor). For instance, in the case of figure C.3 (a), the delay τ between the current I_{tot} and I_{disp} determined from voltage measurements is equal to -2.35ns. We can see on figure C.4 that using Pulser 2 and Channel 2 (short pulses), the signal given by the Pearson probe seems to decrease slower than dV_p/dt, which might be due to a slow decrease time of the probe. Indeed, this phenomenon only happens with very short pulses of FWHM around 5 ns. Yet, we still see that the electrode impedance Z_{elec} is dominated by the capacitance of the cables. In the example of figure C.4, the capacitance was chosen as to scale the calculated displacement current I_{disp} to the same maximum value as the measured current I_{tot}. Using this scaling method, the electrode capacitance was measured for different applied voltages in a regime where no plasma was present at room temperature, and the electrode capacitance was found to be in the range: 2.7-3.5 pF for $l = 1$ mm and $d = 4$ mm (figure C.5).

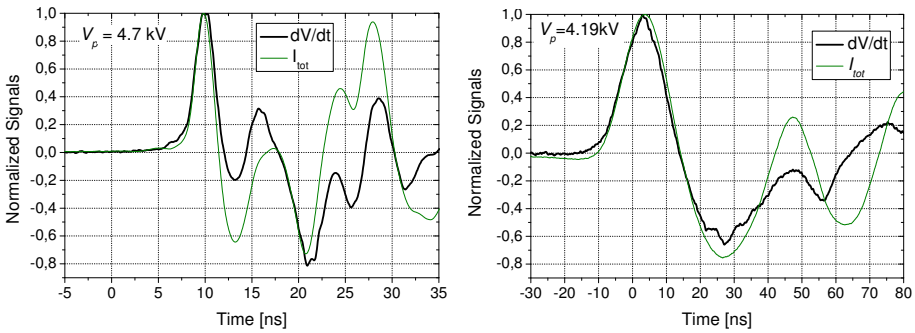

(a) **(b)**

Figure C.3: Normalized displacement current and normalized total current with (a) Pulser 1 and (b) Pulser 2 Channel 1 when no plasma is observed at room temperature.

In this section, we have verified that the noise current measured by the Pearson probe was not significant. We have checked that the current was displacement current when no discharge was observed, for all pulse generators used in this work.

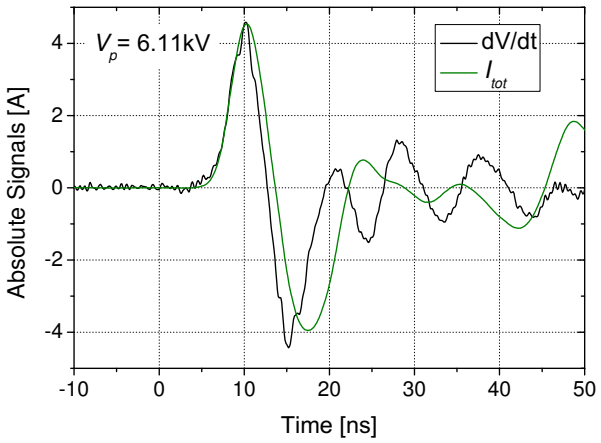

Figure C.4: Displacement current and total current with Pulser 2 Channel 2 when no plasma is observed at room temperature.

C.2 Energy determination

In this section, we discuss the energy deposited per pulse in the plasma for typical glow discharges. We will first explain the principle of the method on a glow discharge at $T_g = 1000$ K and show the importance of the delay between total current and voltage. The determination of the energy for a typical glow or MCG discharge at $T_g = 300$ K is done in section 6.8.

Principle of the method

To obtain the energy, the applied voltage and discharge current were measured as explained in section C.1. The total energy is calculated by multiplying the measured voltage and current waveforms to obtain the power, which is then integrated in time during the pulse duration to yield the energy. The value we take into account is the value of the energy obtained after the first pulse which correspond to the energy at $t = 20$ ns. The delay that we apply to the current is determined by synchronizing the total current I_{tot} and displacement current dV_p/dt when no plasma is observed.

Pai presented this method to calculate the energy of a glow discharge at 1000 K [2]. It is slightly different from the process described in section 4.3 to determine the energy of an NRP spark discharge. The energy determined for a glow regime at $T_g = 1000$ K, E_{total} is compared to "no-plasma" energy $E_{no-plasma}$, that is to say to the energy measured with the high voltage pulse generator operated using the same settings but in ambient air such that no discharge is created. In the case of a spark discharge, $E_{no-plasma} \ll E_{plasma}$. The energy deposited within the discharge is equal to

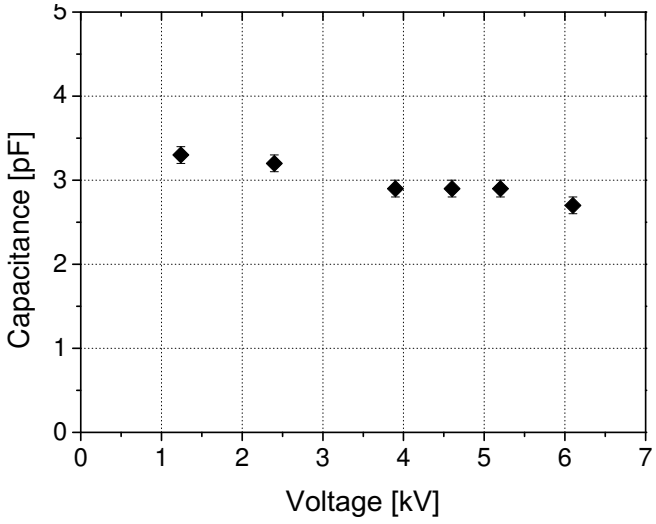

Figure C.5: Electrode capacitance C as a function of the applied voltage for different "no discharge" state at room temperature.

$$E_{plasma} = E_{total} - E_{no-plasma} \tag{C.1}$$

Figure C.6 shows the energy per pulse for glow discharges at different applied voltages V_p. The data taken from [2] are compared with results obtained in the present work with Pulser 2 Channel 2 and different types of electrodes (*Delmo* electrodes for Pai, and *Delta Precis* electrodes in the present work). The energy per pulse is slightly smaller than the one found by Pai. We find 0.8 µJ while Pai found 1.4 µJ when the applied voltage was 5.9 kV. These results are consistent recalling that the FWHM of the high-voltage pulse with Pulser 2 Channel 2 is shorter than with Pulser 1 (see Table 3.3), which was used for Pai's study. To calculate the energy deposited per pulse in a glow regime at ambient temperature, we cannot strictly use the same method. We determined first the total energy in the discharge for different voltages corresponding to "No discharge", corona and glow regime.

Influence of the delay on the total energy

The delay τ has a strong influence on the determination of the total energy. We need to synchronize the total current and voltage very precisely: a change of 0.2-0.3 ns in the delay τ has a 50% influence on the energy of a typical glow regime at $T_g = 1000$ K, see figure C.7. However, what is important is the difference between the total energy and the energy when no plasma is observed, which corresponds to the energy of the parasitic losses, see equation (C.1). Changing slightly the delay τ changes both the values E_{total} and $E_{no-plasma}$

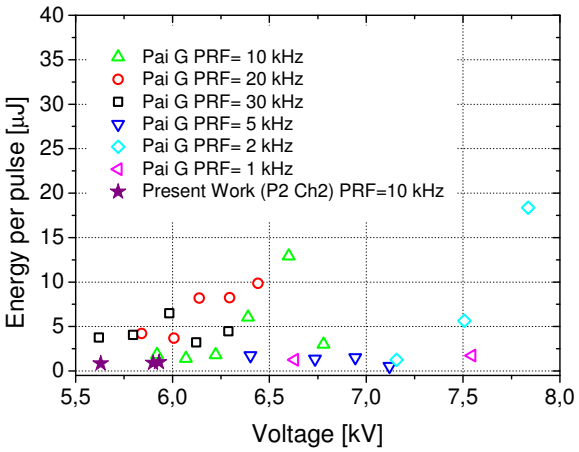

Figure C.6: Measured energy per pulse for the glow regime as function of applied voltage for PRF =1-30 kHz and T_g = 1000 K.
Pai 's data: P1, d = 4 mm, v = 1.6 m.s^{-1} taken from [2], Present Work: Pulser 2 Channel 2, d = 4 - 5 mm, v = 1.7 – 2.6 m.s^{-1}

but scarcely affects the difference E_{plasma}. In the rest of this work, we choose to synchronize I_{disp} and I_{tot} when no discharge is applied at low voltage and ambient temperature.

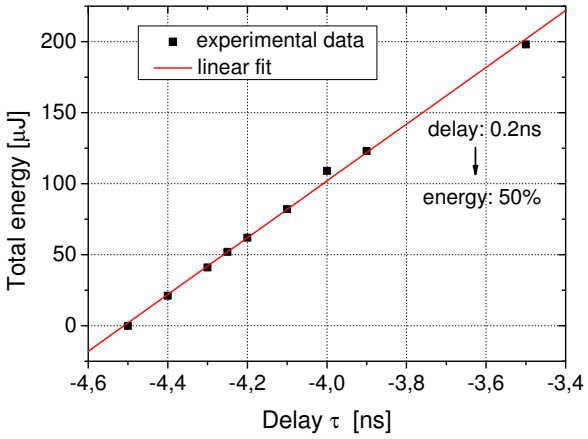

Figure C.7: Energy per pulse in a typical glow discharge at ambient temperature as function of the delay τ between the total current and displacement current.

In this section, we have shown that the delay τ between the current and the voltage has a strong influence on the total energy E_{total} of a glow discharge. For a typical glow state at T_g = 300 K, the energy increases of 50 % if the delay changes of 0.3 ns.

Bibliography

[1] D. Pai, D. A. Lacoste, and C. O. Laux, "Transitions between corona, glow, and spark regimes of nanosecond repetitively pulsed discharges in air at atmospheric pressure," *Journal of Applied Physics*, vol. 107, p. 093303, 2010. p. vi, x, 3, 4, 6, 18, 19, 30, 32, 33, 35, 36, 38, 39, 40, 41, 42, 43, 44, 45, 46, 47, 119, 132, 135, 143, 144, 145, 148, 152, 182

[2] D. Pai, *Nanosecond Repetitively Pulsed Plasmas in Preheated Air at Atmospheric Pressure*. PhD thesis, Ecole Centrale Paris, France, 2008. p. vi, 2, 4, 6, 13, 14, 15, 16, 17, 18, 19, 24, 30, 31, 32, 33, 35, 36, 45, 47, 51, 52, 63, 73, 77, 78, 88, 89, 90, 99, 101, 115, 120, 124, 130, 131, 139, 143, 144, 145, 148, 149, 161, 165, 167, 169, 194, 195, 196

[3] S. Macheret, M. Shneider, and R. Miles, "Modeling of discharges generated by electron beams in dense gases: Fountain and thunderstorm regimes," *Physics of Plasmas*, vol. 8, pp. 1518–1528, May 2001. p. 2, 14

[4] D. M. Packan, *Repetitively Pulsed Glow Discharge in Atmospheric Pressure Air*. PhD thesis, Stanford University, 2002. p. 2, 16, 17, 18, 113, 114, 161, 162

[5] N. A. Popov, "Investigation of the mechanism for rapid heating of nitrogen and air in gas discharges," *Plasma Physics Reports*, vol. 27, pp. 886–896, 2001. p. 3, 26

[6] G. D. Stancu, F. Kaddouri, D. A. Lacoste, and C. O. Laux, "Atmospheric pressure plasma diagnostics by OES, CRDS and TALIF," *Journal of Physics D: Applied Physics*, vol. 43, p. 124002, 2010. p. 3, 4, 26, 29, 66, 87, 88, 91, 101, 106, 107, 109, 110, 111, 114, 116, 117, 181, 182, 183

[7] M. G. Kong, G. Kroesen, G. Morfill, T. Nosenko, T. Shimizu, J. van Dijk, and J. L. Zimmermann, "Plasma medicine: an introductory review," *New Journal of Physics*, vol. 11, Nov 26 2009. p. 6

[8] G. Fridman, M. Peddinghaus, M. Balasubramanian, H. Ayan, A. Fridman, A. Gutsol, and A. Brooks, "Blood coagulation and living tissue sterilization by floating-electrode dielectric barrier discharge in air," *Plasma Chemistry and Plasma Processing*, vol. 26, pp. 425–442, 2006. 10.1007/s11090-006-9024-4. p. 6, 7

[9] J. L. Walsh and M. G. Kong, "Portable nanosecond pulsed air plasma jet," *Applied Physics Letters*, vol. 99, Aug 22 2011. p. 7

[10] A.-M. Pointu, A. Ricard, E. Odic, and M. Ganciu, "Nitrogen atmospheric

pressure post discharges for surface biological decontamination inside small diameter tubes," *Plasma Processes and Polymers*, vol. 5, pp. 559–568, Aug 15 2008. p. 8

[11] Z. Machala, L. Chladekova, and M. Pelach, "Plasma agents in bio-decontamination by DC discharges in atmospheric air," *Journal of Physics D - Applied Physics*, vol. 43, Jun 9 2010. p. 8, 30

[12] E. Es-Sebbar, S.-B. C, N. Naudé, F. Massines, and G. N., "Absolute nitrogen atom density measurements by two-photon laser-induced fluorescence spectroscopy in atmospheric pressure dielectric barrier discharge of pure nitrogen," *Journal of Applied Physics*, vol. 106, 2009. p. 9

[13] O. Guaitella, M. Huebner, D. Marinov, V. Guerra, C. D. Pintassilgo, S. Welzel, J. Roepcke, and A. Rousseau, "Oxidation of NO into NO_2 by Surface Adsorbed O Atoms," *Contributions to Plasma Physics*, vol. 51, pp. 176–181, Mar 2011. p. 9

[14] A. Debien, N. Benard, and E. Moreau, "Streamer inhibition for improving force and electric wind produced by DBD actuators," *Journal of Physics D - Applied Physics*, vol. 45, May 30 2012. p. 9

[15] D. F. Colas, A. Ferret, D. Z. Pai, D. A. Lacoste, and C. O. Laux, "Ionic wind generation by a wire-cylinder-plate corona discharge in air at atmospheric pressure," *Journal of Applied Physics*, vol. 108, Nov 15 2010. p. 9

[16] Y. Lagmich, T. Callegari, L. C. Pitchford, and J. P. Boeuf, "Model description of surface dielectric barrier discharges for flow control," *Journal of Physics D - Applied Physics*, vol. 41, May 7 2008. p. 9

[17] A. V. Likhanskii, M. N. Shneider, S. O. Macheret, and R. B. Miles, "Modeling of dielectric barrier discharge plasma actuator in air," *Journal of Applied Physics*, vol. 103, Mar 1 2008. p. 9

[18] M. Nishihara, K. Takashima, J. W. Rich, and I. V. Adamovich, "Mach 5 bow shock control by a nanosecond pulse surface dielectric barrier discharge," *Physics of Fluids*, vol. 23, Jun 2011. p. 10

[19] I. Levchenko, K. Ostrikov, and D. Mariotti, "The production of self-organized carbon connections between Ag nanoparticles using atmospheric microplasma synthesis," *Carbon*, vol. 47, pp. 344–347, Jan 2009. p. 10, 11

[20] K. K. Ostrikov, U. Cvelbar, and A. B. Murphy, "Plasma nanoscience: setting directions, tackling grand challenges," *Journal of Physics D - Applied Physics*, vol. 44, May 4 2011. p. 10

[21] D. Z. Pai, S. Kumar, I. Levchenko, D. A. Lacoste, C. O. Laux, and K. Ostrikov, "Atmospheric-Pressure Discharges for the Fabrication of Surface-Based Metal Nanostructures," *IEEE Transactions on Plasma Science*, vol. 39, pp. 2814–2815, Nov 2011. p. 11

[22] R. C. Steele, A. C. Jarrett, P. C. Malte, J. H. Tonouchi, and D. G. Nicol, "Variables affecting nox formation in lean-premixed combustion," *Journal of Engineering for Gas Turbines and Power-Transactions of the ASME*, vol. 119, no. 1, pp. 102–107, 1997. p. 11, 26

[23] G. Pilla, D. Galley, D. A. Lacoste, F. Lacas, D. Veynante, and C. O. Laux,

"Stabilization of a turbulent premixed flame using a nanosecond repetitively pulsed plasma," *IEEE Transactions on Plasma Science*, vol. 34, no. 6, 2006. p. 11, 26, 187

[24] N. L. Aleksandrov, S. V. Kindysheva, E. N. Kukaev, S. M. Starikovskaya, and A. Y. Starikovskii, "Simulation of the ignition of a methane-air mixture by a high-voltage nanosecond discharge," *Plasma Physics Reports*, vol. 35, pp. 867–882, Oct 2009. p. 11

[25] D. A. Lacoste, D. A. Xu, J. P. Moeck, and C. O. Laux, "Dynamic response of a weakly turbulent lean-premixed flame to nanosecond repetitively pulsed discharges," *Proceedings of the Combustion Institute*, 2012. p. 12

[26] A. Starikovskiy and N. Aleksandrov, "Plasma-assisted ignition and combustion," *Progress in Energy and Combustion Science*, vol. 74, pp. 337–347, 2002. p. 12

[27] L. Yu, C. Laux, D. Packan, and C. Kruger, "Direct-current glow discharges in atmospheric pressure air plasmas," *Journal of Applied Physics*, vol. 91, pp. 2678–2686, Mar 1 2002. p. 13

[28] J. Kim and K. Terashima, "2.45 GHz microwave-excited atmospheric pressure air microplasmas based on microstrip technology," *Applied Physics Letters*, vol. 86, May 9 2005. p. 13

[29] F. Massines, P. Segur, N. Gherardi, C. Khamphan, and A. Ricard, "Physics and chemistry in a glow dielectric barrier discharge at atmospheric pressure: diagnostics and modelling," *Surface & Coatings Technology*, vol. 174, pp. 8–14, Sep-Oct 2003. 8th International Conference on Plasma Surface Engineering, Garmisch Partenki, Germany, SEP 09-13, 2002. p. 14, 30

[30] A. Yalin, Z. Yu, O. Stan, K. Hoshimiya, A. Rahman, V. Surla, and G. Collins, "Electrical and optical emission characteristics of radio-frequency-driven hollow slot microplasmas operating in open air," *Applied Physics Letters*, vol. 83, pp. 2766–2768, Oct 6 2003. p. 14

[31] I. Adamovich, "Control of electron recombination rate and electron density in optically-pumped non-equilibrium plasmas," *Journal of Physics D - Applied Physics*, vol. 34, pp. 319–325, Feb 7 2001. p. 14

[32] N. Aleksandrov, V. F. I., R. S. Islamov, I. V. Kochetov, A. P. Napartovich, and V. G. Peygov, "essai," *Teplofiz. Vys. Tempp (translated in High Temperature)*, vol. 19, pp. 22–27, 1981. p. 16

[33] W. L. Nighan, "Electron energy distributions and collision rates in electrically excited n_2, co, and co_2," *Phys. Rev. A*, vol. 2, pp. 1989–2000, Nov 1970. p. 16

[34] C. H. Kruger, C. Laux, L. Yu, D. M. Packan, and L. Pierrot, "Nonequilibrium discharges in air and nitrogen plasmas at atmospheric pressure," *Pure and Applied Chemistry*, vol. 74, pp. 337–347, 2002. p. 17

[35] M. Nagulapally, G. Candler, C. O. Laux, L. Yu, D. M. Packan, C. H. Kruger, S. R., and S. K. H. in *31th AIAA Plasmadynamics and Laser Conference*, vol. 2000-2417, (Denver, Colorado), 2000. p. 17

[36] D. Z. Pai, G. D. Stancu, D. A. Lacoste, and C. O. Laux, "Nanosecond repetitively pulsed discharges in air at atmospheric pressure - the glow regime," *Plasma Sources Science Technology*, vol. 18, pp. 045030–37, 2009. p. 17, 18, 19, 20, 29, 47, 124, 143, 144, 148, 169

[37] D. Z. Pai, D. A. Lacoste, and C. O. Laux, "Nanosecond repetitively pulsed discharges in air at atmospheric pressure - the spark regime," *Plasma Sources Science Technology*, vol. 19, pp. 065015–25, 2010. p. 18, 19, 20, 21, 22, 23, 24, 25, 26, 47, 105

[38] T. Shao, C. Zhang, Z. Niu, P. Yan, V. F. Tarasenko, E. K. Baksht, A. G. Burahenko, and Y. V. Shut'ko, "Diffuse discharge, runaway electron, and x-ray in atmospheric pressure air in an inhomogeneous electrical field in repetitive pulsed modes," *Applied Physics Letters*, vol. 98, Jan 10 2011. p. 19

[39] D.-z. Yang, W.-c. Wang, L. Jia, D.-x. Nie, and H.-c. Shi, "Production of atmospheric pressure diffuse nanosecond pulsed dielectric barrier discharge using the array needles-plate electrode in air," *Journal of Applied Physics*, vol. 109, Apr 1 2011. p. 20

[40] G. Pilla, *Etude expérimentale de la stabilisation de flammes propane-air de pré-mélange par décharges nanosecondes impulsionnelles répétitives.* PhD thesis, Ecole Centrale Paris, 2008. p. 22, 187

[41] `www.specair-radiation.net`. p. 24, 92

[42] C. O. Laux, T. G. Spence, C. H. Kruger, and R. N. Zare, "Optical diagnostics of atmospheric pressure plasmas," *Plasma Sources Science and Technology*, vol. 12, no. 2, pp. 125–138, 2003. p. 24, 92, 114, 115

[43] S. Babayan, J. Y. Jeong, S. A., V. J. Tu, M. Moravej, G. Selwyn, and R. F. Hicks, "Deposition of silicon dioxide films with a non-equilibrium atmospheric pressure plasma jet," *Plasma Sources Science & Technology*, vol. 10, pp. 573–578, 2001. p. 26

[44] U. Cvelbar, K. Ostrikov, and M. Mozetic, "Reactive oxygen plasma-enabled synthesis of nanostructured cdo: tailoring nanostructures through plasma-surface interactions," *Nanotechnology*, vol. 19, 2008. p. 26

[45] D. Z. Pai, "Nanomaterials synthesis at atmospheric pressure using nanosecond discharges," *Journal of Physics D: Applied Physics*, vol. 44, p. 174024, 2011. p. 26

[46] W. Kim, M. G. Mungal, and M. A. Cappelli, "Formation and role of cool flames in plasma-assisted premixed combustion," *Applied Physics Letters*, vol. 92, no. 5, 2008. p. 26

[47] E. Mintusov, A. Serdyuchenko, I. Choi, W. R. Lempert, and I. V. Adamovich, "Mechanism of plasma assisted oxidation and ignition of ethylene-air flows by a repetitively pulsed nanosecond discharge," *Proceedings of the Combustion Institute*, vol. 32, 2009. p. 26

[48] G. D. Stancu, M. Janda, F. Kaddouri, D. A. Lacoste, and C. O. Laux, "Time resolved CRDS measurements of the $N_2(A)$ density produced by nanosecond discharges in atmospheric pressure nitrogen and air," *Journal*

of Physical Chemistry A, vol. 114, no. 1, 2010. p. 26, 66, 88

[49] G. D. Stancu, M. Janda, F. Kaddouri, D. Pai, D. A. Lacoste, J. C. Rolon, and C. O. Laux, "Investigation of the mechanism for rapid heating of nitrogen and air in gas discharges," in *39th Plasmadynamics and Laser Conference AIAA*, (Seattle,Washington), 2008. p. 26, 27, 88, 110, 111, 114, 116, 117, 181, 182, 183

[50] F. Kaddouri, G. D. Stancu, D. Pai, D. A. Lacoste, and C. O. Laux, "Energy release and fast heating process study in nanosecond repetitively pulsed air discharges at atmospheric pressure," in *63rd Gaseous Electronics Conference*, (Paris, France), 2010. p. 26, 88, 105

[51] D. A. Xu, D. A. Lacoste, D. L. Rusterholtz, P.-Q. Elias, G. D. Stancu, and C. O. Laux, "Experimental study of the hydrodynamic expansion following a nanosecond repetitively pulsed discharge in air," *Applied Physics Letters*, vol. 99, p. 121502, 2011. p. 27, 28, 29, 91, 105, 184

[52] E. Stoffels, I. Kieft, R. Sladek, D. Slaaf, E. van der Laan, P. Jimenez-Moreno, and M. Steinbuch, "Towards plasma surgery: Plasma treatment of living cells," in *Physics of Ionized Gases* (Hadzievski, L, ed.), vol. 740 of *AIP Conference Proceedings*, pp. 309–314, 2004. 22nd Summer School and International Symposium on the Physics of Ionized Gases, Tara Natl Pk, Yugoslavia, Aug 23-27, 2004. p. 30

[53] S. Perni, G. Shama, J. L. Hobman, P. A. Lund, C. J. Kershaw, G. A. Hidalgo-Arroyo, C. W. Penn, X. T. Deng, J. L. Walsh, and M. G. Kong, "Probing bactericidal mechanisms induced by cold atmospheric plasmas with Escherichia coli mutants," *Applied Physics Letters*, vol. 90, Feb 12 2007. p. 30

[54] A. Schutze, J. Y. Jeong, S. Babayan, G. Selwyn, and R. F. Hicks, "Deposition of silicon dioxide films with a non-equilibrium atmospheric pressure plasma jet," *IEEE*, vol. 26, pp. 1685–1694, 1998. p. 30

[55] E. M. Bazelyan and Y. P. Raizer, *Spark Discharge*. CRC Press, Boca-raton, New York, 1998. p. 39

[56] S. Celestin, *Study of the dynamics of streamers in air at atmospheric pressure*. PhD thesis, Ecole Centrale Paris, France, 2008. p. 39

[57] F. Tholin and A. Bourdon, "Influence of temperature on the glow regime of a discharge in air at atmospheric pressure between two point electrodes," *Journal of Physics D: Applied Physics*, vol. 44, pp. 385203–385220, 2011. p. 39, 90, 124, 127, 128, 129

[58] C. Montijn and E. U., "Diffusion correction to the Raether-Meek criterion for the avalanche-to-streamer transition," *Journal of Physics D: Applied Physics*, vol. 39, no. 2979, 2006. p. 40

[59] S. Pancheshnyi, M. Nudnova, and A. Starikovskii, "Development of a cathode-directed streamer discharge in air at different pressures: experiment and comparison with direct numerical simulation," *Physical Review E*, vol. 71, no. 016407, 2005. p. 44, 146

[60] *Princeton Instruments PI-MAX System*. p. 69

[61] C. O. Laux, R. J. Gessman, B. Hilbert, and C. H. Kruger, "Experimental study and modeling of infrared air plasma radiation," in *AIAA Conference*, vol. 2124, 1995. p. 75

[62] N. A. Popov, "Kinetic processes initiated by a nanosecond high-current discharge in hot air," *Plasma Physics Reports*, vol. 37, pp. 807–815, 2011. p. 96, 105, 116

[63] K. P. Huber and G. Herzberg, *Molecular Spectra and Molecular Structure IV. Constants of Diatomic Molecules. IV*, vol. IV. New York: Van Nostrand Reinhold Company, 1979. p. 96

[64] C. O. Laux, *Optical Diagnostics and Radiative Emission of Air Plasmas*. PhD thesis, Stanford University, 1993. p. 96, 97, 112, 115

[65] M. Capitelli, C. M. Ferreira, B. F. Gordiets, and A. I. Osipov, *Plasma Kinetics in Atmospheric Gases*. Atomic, Optical and Plasma Physics, Berlin: Springer-Verlag, 2000. p. 96, 97, 98, 112, 113, 161

[66] C. A. Brau and R. M. Jonkman, "Classical theory of rotational relaxation in diatomic gases," *Journal of Chemical Physics*, vol. 52, no. 2, pp. 477–484, 1970. p. 97, 98

[67] C. Park, "Rotational relaxation of N_2 behind a strong shock wave," *Journal of Thermophysics and Heat Transfer*, vol. 18, no. 4, pp. 527–533, 2004. p. 97, 98

[68] I. A. Kossyi, A. Y. Kostinsky, A. A. Matveyev, and V. P. Silakov, "Kinetic scheme of the nonequilibrium discharge in nitrogen-oxygen mixtures," *Plasma Sources Science and Technology*, vol. 1, pp. 207–220, 1992. p. 112, 113, 114

[69] C. H. Chen, M. G. Payne, G. S. Hurst, and J. P. Judish, "Kinetic studies of N_2 and N_2-SF_6 following proton excitation," *Journal of Chemical Physics*, vol. 65, p. 3863, 1976. p. 112, 113

[70] G. Dilecce, P. F. Ambrico, and S. De Benedictis, "New N_2 collision quenching and vibrational relaxation rate constants: 2. PG emission diagnostics of high-pressure discharges," *Plasma Sources Science and Technology*, vol. 16, pp. S45–S51, 2007. p. 112, 113

[71] P. Millet, Y. Salamero, H. Brunet, J. Galy, D. Blanc, and J. L. Teyssier, "Deexcitation of N_2(C, v'=0 and 1) levels in mixtures of oxygen and nitrogen," *Journal of Chemical Physics*, vol. 58, no. 12, pp. 5839–5841, 1973. p. 112, 113, 114

[72] K. B. Mitchell, "Fluorescence efficiency and collisional deactivation rates for N_2 and N_2^+ bands excited by soft x rays," *Journal of Chemical Physics*, vol. 53, no. 5, pp. 1795–1802, 1976. p. 112, 113, 114

[73] S. V. Pancheshnyi, S. M. Starikovskaia, and A. Y. Starikovskii, "Collisional deactivation of N_2(C, v=0,1,2,3) states by N_2, O_2, H_2 and H_2O molecules," *Chemical Physics*, vol. 262, 2000. p. 112, 113, 114

[74] M. S. Bak, W. Kim, and M. Cappelli, "On the quenching of excited electronic states of molecular nitrogen in nanosecond pulsed discharges in atmospheric pressure air," *Applied Physics Letters*, vol. 98, p. 011502, 2011.

p. 113, 114
[75] L. G. Piper, "State-to-state $N_2(A)$ energy pooling reactions. II the formation and quenching of N_2(B,v=1-12)," *Journal of Chemical Physics*, vol. 88, no. 11, 1988. p. 113
[76] N. Popov, "Fast gas heating initiated by pulse nanosecond discharge in atmospheric pressure air," in *19th International Conference on Gas Discharges and Their Applications*, (China), 2012. p. 116, 117
[77] S. Nijdam, *Experimental investigations on the physics of streamers*. PhD thesis, TU Eindhoven, The Netherlands, 2011. p. 146, 147
[78] P. Tardiveau, N. Moreau, F. Jorand, C. Postel, S. Pasquiers, and P. Vervisch, "Nanosecond scale discharge dynamics in high pressure air," *IEEE Transactions on plasma Science*, vol. 36, no. 4, 2008. p. 147
[79] M. Arrayás, U. Ebert, and W. Hundsdorfer, "Spontaneous branching of anode-directed streamers between planar electrodes," *Phys. Rev. Lett.*, vol. 88, p. 174502, Apr 2002. p. 160
[80] B. Meulenbroek, A. Rocco, and U. Ebert, "Streamer branching rationalized by conformal mapping technique," *Physical Review E*, vol. 69, 2004. p. 160
[81] A. Rocco, U. Ebert, and W. Hundsdorfer, "Streamer branching of negative streamers in free flight," *Physical Review E*, vol. 66, 2002. p. 160
[82] N. Liu and V. Pasko, "Effects of photoionization on propagation and branching of positive and negative streamers in sprite," *Journal of Geophysical Research*, vol. 109, 2004. p. 160
[83] H. Raether, "Die entwicklung der elektronenlawine in den funkenkanal," *Zeitschrift für Physik A Hadrons and Nuclei*, vol. 112, pp. 464–489, 1939. p. 160
[84] S. Pancheshnyi, "Role of electronegative gas admixtures in streamer part, propagation and branching phenomena," *Plasma Sources Science & Technology*, vol. 14, no. 4, 2005. p. 160, 161, 162, 165, 166
[85] Y. P. Raizer, *Gas discharge physics*. Springer-Verlag, 1991. p. 161, 162
[86] G. Wormeester, S. Pancheshnyi, A. Luque, S. Nijdam, and U. Ebert, "Probing photo-ionization: simulations of positive streamers in varying N_2:O_2 mixtures," *Journal of Physics D: Applied Physics*, vol. 43, p. 505201, 2010. p. 161, 165
[87] Y. Akishev, G. Aponin, A. Balakirev, M. Grushin, V. Karalnik, A. Petryakov, and N. Trushkin, "Memory and sustention of microdischarges in a steady-state dbd: volume plasma or discharge plasma?," *Plasma Sources Science & Technology*, vol. 20, p. 024005, 2011. p. 161
[88] N. A. Popov, "Evolution of the negative ion composition in the afterglow of a streamer discharge in air," *Plasma Physics Reports*, vol. 36, no. 9, pp. 812–818, 2010. p. 162
[89] F. Tholin and A. Bourdon, "Influence of the preionization on the dynamics of an air discharge between two point electrodes at atmospheric pressure," in *30th ICPIG*, (Belfast, UK), 2011. p. 162
[90] F. Tholin and A. Bourdon, "Numerical simulation of successive nanosecond

pulsed discharges in air at atmospheric pressure," in *ESCAMPIG XXI*, (Viana do Castelo, Portugal), 2012. p. 167

[91] F. Girschig, S. Mannai, and P. Toniato, "Creating hydrogen with NRP plasma: Final report." Projet Innovation P5A111BD, 2012. p. 177

[92] F. Tholin, D. L. Rusterholtz, D. A. Lacoste, D. Z. Pai, S. Celestin, J. Jarrige, G. D. Stancu, A. Bourdon, and C. O. Laux, "Images of a nanosecond repetitively pulsed glow discharge between two point electrodes in air at 300 k and at atmospheric pressure," *IEEE Transactions on Plasma Science*, vol. 39, pp. 2254–2255, 2011. p. 187, 189